

# High performance solid-state mesoscopic solar cells

THÈSE N° 6006 (2013)

PRÉSENTÉE LE 27 NOVEMBRE 2013

À LA FACULTÉ DES SCIENCES DE BASE

LABORATOIRE DE PHOTONIQUE ET INTERFACES

PROGRAMME DOCTORAL EN CHIMIE ET GÉNIE CHIMIQUE

ÉCOLE POLYTECHNIQUE FÉDÉRALE DE LAUSANNE

POUR L'OBTENTION DU GRADE DE DOCTEUR ÈS SCIENCES

PAR

Julian BURSCHKA

acceptée sur proposition du jury:

Prof. J.-E. Moser, président du jury

Prof. M. Graetzel, directeur de thèse

Prof. U. Bach, rapporteur

Prof. A. Fontcuberta i Morral, rapporteur

Dr H. Snaith, rapporteur



ÉCOLE POLYTECHNIQUE  
FÉDÉRALE DE LAUSANNE

Suisse  
2013





# Abstract

Mesoscopic sensitized solar cells are one of the most promising third-generation photovoltaic technologies. Dye-sensitized solar cells (DSCs), imitating the photosynthesis of green plants, were the first photovoltaic devices to utilize a mesoscopic heterojunction for the conversion of solar irradiation into electrical power. Solid-state dye-sensitized solar cells (ssDSCs), that employ an organic hole-transporting material in place of a liquid redox electrolyte, have evolved as viable contenders to conventional liquid DSCs.

A typical ssDSC is composed of a mesostructured wide-bandgap metal oxide semiconductor that is sensitized with a light-absorbing chromophore and infiltrated with a molecular organic hole-transporter, usually by solution-processing. In this device, photoexcitation of the sensitizer and subsequent ultrafast electron injection into the conduction band of the metal oxide semiconductor is followed by hole transfer from the oxidized sensitizer to the organic hole-transporter. Charge transport of both the electron and the hole through the two bicontinuous phases, followed by charge migration through the external circuit, completes the photovoltaic operation of the cell.

Despite more than 15 years of development, ssDSCs have always been lagging behind their liquid counterparts in terms of both power conversion efficiency and long-term stability. My thesis presents three different approaches that are aimed at contributing to the development of high-performance solid-state mesoscopic solar cells.

Firstly, I present a new class of Co(III) complexes as solution-processable *p*-type dopants for triarylamine-based hole-conductors such as the commonly employed 2,2',7,7'-tetrakis-*N,N*-di-*para*-methoxyphenylamine-9,9'-spirobifluorene (spiro-MeOTAD). The proposed Co(III) complexes were characterized in detail using optical and electrochemical techniques. The application of the new *p*-dopants in ssDSC rendered it possible to directly relate the conductivity of the doped hole-transporter to the photovoltaic performance of the devices. The work shows that chemical *p*-doping is a powerful tool to control the charge transport properties of spiro-MeOTAD in ssDSCs, capable of replacing the commonly employed photo-doping, i.e. the light-assisted one-electron oxidation of spiro-MeOTAD by ambient oxygen. Combining this strategy with a state-of-the-art organic D- $\pi$ -A sensitizer allowed us to achieve power conversion efficiencies of up to 7.2%—a new record for this kind of device architecture.

Secondly, I investigated a series of new molecular hole-transporters based on the triarylamine-substituted 9,9'-spirobifluorene core. In total, we synthesized seven new materials and characterized them in detail using electrical and electrochemical techniques. Organic-field effect transistors were fabricated employing these materials in order to evaluate their hole mobilities. From the comparison of different substituents on the hole-conducting triarylamine moieties, a structure–property relationship was derived, highlighting the importance of processability and hole mobility of the hole-transporting material for an efficient application in a ssDSC configuration. We encountered the purity of the new materials as a key parameter for a proper functioning of the device and identified the use of functionalized metal-scavenging polystyrene beads as a valuable purification step.

Thirdly, a new technique is introduced that allows to realize functional composites of a mesoporous metal oxide and the organic–inorganic hybrid perovskite  $\text{CH}_3\text{NH}_3\text{PbI}_3$ .  $\text{CH}_3\text{NH}_3\text{PbI}_3$  has recently attracted great attention as a light-harvesting pigment in mesoscopic solar cells. We propose a two-step technique to deposit the perovskite absorber:  $\text{PbI}_2$  is first applied on a substrate by solution-processing and subsequently exposed to a solution of  $\text{CH}_3\text{NH}_3\text{I}$ . It was evidenced that the desired hybrid perovskite forms within seconds after contacting the two precursors. Scanning electron microscopy was employed to elucidate the changes in crystal morphology during the transformation reaction. The kinetics of the reaction was investigated in detail using X-ray diffraction and optical spectroscopy. Employing the two-step technique for the fabrication of mesoscopic perovskite-based solar cells enabled new record power conversion efficiencies of up to 15%.

By following three different strategies, this thesis could contribute significantly to the development of high-performance solid-state mesoscopic solar cells. The power conversion efficiencies of 7.2% and 15%, achieved with a molecular dye and an organic–inorganic perovskite pigment, respectively, represent important milestones for the design of third-generation photovoltaic cells that hopefully one day can compete with the conventional silicon-based solar cell technology.

**Keywords:** organic electronics, photovoltaics, solid-state dye-sensitized solar cell, hybrid solar cell, hole-transporting material, organic field-effect transistor, p-type doping, Co(III) complex, photo-doping, organic–inorganic hybrid perovskite, sequential deposition, spiro-MeOTAD, methylammonium lead iodide.

# Zusammenfassung

Die nanostrukturierte, Farbstoff-sensibilisierte Solarzelle—nach ihrem Erfinder Professor Michael Grätzel auch Grätzel-Zelle genannt—ist einer der wichtigsten Vertreter der Solarzellen der sogenannten dritten Generation. Inspiriert durch die photosynthetischen Vorgänge in grünen Pflanzen wird in der Farbstoffsolarzelle das sichtbare Licht durch einen molekularen Farbstoff absorbiert. Die Farbstoffsolarzelle war eines der ersten photovoltaischen Systeme, bei dem Sonnenenergie mit Hilfe einer mesoskopischen, dreidimensionalen Heterostruktur in elektrische Energie umgewandelt wird. Feststoff-Farbstoffsolarzellen, die auf einem festen, organischen p-Halbleiter basieren, haben sich als bemerkenswerte Alternative zu den klassischen Farbstoffsolarzellen etabliert in welchen ein flüssiger Redoxelektrolyt zum Einsatz kommt. Einer der am weitesten verbreiteten organischen Lochleiter, die in Feststoff-Farbstoffsolarzellen Verwendung finden, ist 2,2',7,7'-tetrakis-*N,N*-di-*para*-methoxyphenylamine-9,9'-spirobifluorene (spiro-MeOTAD). Trotz einer Entwicklungszeit von mehr als 15 Jahren lag der Wirkungsgrad und die Langzeitstabilität der Feststoff-Farbstoffsolarzelle stets weit hinter der konventionellen Elektrolyt-Farbstoffsolarzelle. Die vorliegende Arbeit befasst sich damit, die Limitierungen der Feststoff-Farbstoffsolarzelle zu verstehen und Lösungsansätze zu bieten, die es ermöglichen, den Wirkungsgrad und die Langzeitstabilität der Solarzelle weiter zu verbessern. Insgesamt wurden drei verschiedene Ansätze verfolgt:

Der erste Teil der Arbeit präsentiert eine Reihe von metallorganischen Co(III) Komplexen, die für die *p*-Dotierung von Triarylamin-basierten organischen Lochleitern, wie zum Beispiel spiro-MeOTAD, entwickelt wurden. Die Co(III) Komplexe können zusammen mit dem Lochleiter aus Lösung prozessiert werden. Sie eignen sich daher für den Einsatz in Feststoff-Farbstoffsolarzellen, um die Leitfähigkeit von spiro-MeOTAD zu erhöhen und besser kontrollieren zu können. Die Co(III) Komplexe wurden mithilfe optischer sowie elektrochemischer Methoden charakterisiert. Eine Anwendung der Co(III) Komplexe in Feststoff-Farbstoffsolarzellen zeigte, dass sich die Leitfähigkeit des Lochleiters direkt mit dem Wirkungsgrad der Solarzellen korrelieren lässt. Des weiteren demonstriert diese Arbeit, dass die Methode der chemischen Dotierung in der Tat hilfreich ist und mit der—normalerweise üblichen und eher unkontrollierten—sogenannten Photodotierung, das heisst der Licht-induzierten Oxidation von spiro-MeOTAD durch Luftsauerstoff, konkurrieren kann. In Verbindung mit einem organischen Farbstoff ermöglichte dieses Konzept die Herstellung von Feststoff-Farbstoffsolarzellen mit Wirkungsgraden von bis zu 7.2%.

Der zweite Teil der Arbeit befasst sich mit einer Reihe neuer, Triarylamin-basierter molekularer Lochleiter und ihrer Anwendung in Farbstoffsolarzellen. Insgesamt wurde sieben neue Materialien synthetisiert sowie mithilfe elektrischer und elektrochemischer Methoden charakterisiert. Eines der Ziele der vorliegenden Arbeit war die Darstellung von Lochleitern mit einem—im Vergleich zu spiro-MeOTAD—höheren Oxidationspotential. Dies wurde mit zwei der neuen Verbindungen erreicht. Organische Feldeffekttransistoren auf Basis der neuen Lochleiter wurde angefertigt, um die Ladungsträgerbeweglichkeiten der Materialien zu bestimmen. Der Vergleich verschiedener Substituenten an den peripheren Triarylamin-Einheiten erlaubte es, eine Struktur-Eigenschafts-Beziehung abzuleiten, sowie die Wichtigkeit von Prozessierbarkeit und Ladungsträgerbeweglichkeit des Lochleiters für eine effiziente Funktionsweise der Solarzelle aufzuzeigen. Als einer der problematischsten Faktoren hat sich die Reinheit der neuen Materialien herausgestellt. In diesem Zusammenhang wurde der Einsatz funktionalisierter Polystyrolpartikel als Metall-Scavenger untersucht, um die Reinheit der Lochleiter zu verbessern.

Der dritte Teil der Arbeit stellt eine neue Methode zur Herstellung von Nanoverbundmaterialien aus einer Metalloxidstruktur und der organisch-anorganischen Hybridverbindung  $\text{CH}_3\text{NH}_3\text{PbI}_3$  vor.  $\text{CH}_3\text{NH}_3\text{PbI}_3$  kristallisiert in einer Perowskitstruktur und hat innerhalb der letzten zwei Jahre großes Aufsehen erregt, da das Material in Solarzellen Wirkungsgrade von mehr als 15% erreichte. Wir präsentieren eine Methode um den Perowskit-Lichtabsorber nicht direkt sondern in zwei Schritten aufzubringen: Zunächst wird  $\text{PbI}_2$  aus einer Lösung auf ein Substrat aufgetragen. Anschließend wird der trockene  $\text{PbI}_2$  Film in eine Lösung von  $\text{CH}_3\text{NH}_3\text{I}$  getaucht. Unsere Experimente zeigen, dass sich die gewünschte Perowskitstruktur innerhalb weniger Sekunden bildet, sobald die beiden Vorstufen miteinander in Kontakt treten. Die Änderung der Morphologie der dünnen  $\text{PbI}_2$  Schicht während der Reaktion wurde mithilfe von Rasterelektronenmikroskopie im Detail untersucht. Ein großer Teil der Arbeit befasst sich mit der Geschwindigkeit der Umwandlung von  $\text{PbI}_2$  zu  $\text{CH}_3\text{NH}_3\text{I}$ , die mithilfe von optischer Spektroskopie und Röntgenpulverdiffraktometrie untersucht wurde. Die Verwendung der beschriebenen Methode für die Herstellung von nanostrukturierten Solarzellen ermöglichte Wirkungsgrade von bis zu 15%.

Alle drei Studien konnten signifikant zur Entwicklung der nanostrukturierten Solarzellen beitragen. Besonders die hohen Wirkungsgrade von 7.2% und 15%, die mit Hilfe von Solarzellen auf Basis eines molekularen Farbstoffes beziehungsweise eines organisch-anorganischen Hybridabsorbers erreicht wurden, stellen wichtige Meilensteine auf dem Weg zu einer technisch ausgereiften und konkurrenzfähigen Photovoltaiktechnologie dar.

*Schlüsselwörter:* Organische Elektronik, Photovoltaik, Feststoff-Farbstoffsolarzelle, Hybrid-Solarzelle, organische Halbleiter, Lochleiter, organischer Feldeffekttransistor, p-Dotierung, Co(III) Komplex, Photodotierung, Organisch-anorganischer Hybrid Perowskit, spiro-MeOTAD, Methylammoniumblei(II)iodid.

# Contents

<b>Abstract / Zusammenfassung</b>	<b>iii</b>
<b>Nomenclature</b>	<b>xi</b>
<b>1 Introduction</b>	<b>1</b>
1.1 Dye-sensitized solar cells (DSCs)	1
1.2 Solid-state dye-sensitized solar cells (ssDSCs)	3
1.3 Electronic processes in DSCs	4
1.4 Solar cell characterization	6
1.4.1 Reference solar spectral irradiance	6
1.4.2 Current–voltage characteristics	7
1.4.3 Quantum efficiency measurements	10
1.5 The important ssDSC components	11
1.5.1 The compact metal oxide blocking layer	11
1.5.2 The mesoporous metal oxide film	11
1.5.3 The hole-transporting material	12
1.5.4 The sensitizer	14
1.5.5 The back contact	17
1.6 Motivation and strategies	19
<b>2 Co(III) complexes as <i>p</i>-dopants in solid-state DSCs</b>	<b>21</b>
2.1 Introduction	21
2.1.1 <i>p</i> -Type doping of organic semiconductors	21
2.1.2 Background and motivation	23
2.1.3 Co(III) complexes as <i>p</i> -type dopants	24
2.2 Results and discussion	26
2.2.1 First generation Co(III) <i>p</i> -dopant: FK102	26
2.2.1.1 Electrochemical characterization of FK102	26
2.2.1.2 Oxidation of spiro-MeOTAD using FK102	27
2.2.1.3 Charge transport properties of <i>p</i> -doped spiro-MeOTAD	28
2.2.1.4 Application of FK102 in ssDSCs	29
2.2.2 Second generation Co(III) <i>p</i> -dopants: FK209 and FK269	33
2.2.2.1 Motivation and strategy	33
2.2.2.2 Characterization of FK209 and FK269	34

2.2.2.3	Estimation of a Co(III)-to-spiro-MeOTAD <sup>•+</sup> conversion yield . . . . .	36
2.2.2.4	Influence of the type of dopant on PV performance . . . . .	38
2.2.2.5	Investigation of high doping levels . . . . .	39
2.3	Conclusion and perspective . . . . .	39
<b>3</b>	<b>9,9'-spirobifluorene based hole-transporters for ssDSC applications</b>	<b>41</b>
3.1	Introduction . . . . .	41
3.1.1	Inorganic <i>p</i> -type semiconductors . . . . .	41
3.1.2	Organic <i>p</i> -type semiconductors . . . . .	42
3.1.3	Basic requirements for the HTM in ssDSCs . . . . .	45
3.1.3.1	Semiconducting properties . . . . .	45
3.1.3.2	Processability and pore infiltration . . . . .	46
3.1.3.3	Morphology . . . . .	47
3.1.3.4	Optical properties . . . . .	47
3.1.3.5	Stability . . . . .	48
3.1.4	Motivation and strategy . . . . .	48
3.2	Results and discussion . . . . .	48
3.2.1	Design of new 9,9'-spirobifluorene based HTMs . . . . .	48
3.2.2	Electrochemical characterization . . . . .	50
3.2.2.1	Electrochemical measurements in solution . . . . .	51
3.2.2.2	Photoelectron spectroscopy in air (PESA) . . . . .	53
3.2.3	Charge transport properties investigated by FET measurements . . . . .	55
3.2.3.1	Techniques to determine charge carrier mobilities . . . . .	55
3.2.3.2	Characterization of organic field-effect transistors . . . . .	57
3.2.3.3	OFETs based on spiro-MeOTAD . . . . .	59
3.2.3.4	OFETs based on new 9,9'-spirobifluorene derivatives . . . . .	63
3.2.4	ssDSC device performance of new HTMs . . . . .	66
3.2.5	Influence of the material's purity . . . . .	70
3.3	Conclusion and perspective . . . . .	75
<b>4</b>	<b>Mesoscopic perovskite-sensitized solar cells</b>	<b>77</b>
4.1	Introduction . . . . .	77
4.1.1	Inorganic absorbers in ssDSCs . . . . .	78
4.1.2	Organic-inorganic hybrid perovskites . . . . .	79
4.1.3	Methyl ammonium lead iodide – CH <sub>3</sub> NH <sub>3</sub> PbI <sub>3</sub> . . . . .	80
4.1.4	Motivation and strategy . . . . .	82
4.2	Results and discussion . . . . .	83
4.2.1	CH <sub>3</sub> NH <sub>3</sub> PbI <sub>3</sub> formed by sequential deposition . . . . .	83
4.2.2	Perovskite morphology investigated by scanning electron microscopy . . . . .	85
4.2.3	Kinetics of the transformation reaction . . . . .	90
4.2.3.1	Investigations on flat TiO <sub>2</sub> /FTO films . . . . .	91
4.2.3.2	Investigations on porous TiO <sub>2</sub> . . . . .	93
4.2.4	X-ray diffraction spectroscopy . . . . .	95

4.2.5	Perovskite-sensitized solar cells . . . . .	97
4.2.5.1	Photovoltaic characterization . . . . .	99
4.2.5.2	Long-term stability . . . . .	101
4.2.5.3	Optimization of photovoltaic performance . . . . .	102
4.2.5.4	High performance devices . . . . .	106
4.3	Conclusion and Perspective . . . . .	107
<b>5</b>	<b>Conclusion &amp; perspective</b>	<b>111</b>
<b>6</b>	<b>Experimental Section</b>	<b>115</b>
6.1	Materials and synthesis . . . . .	115
6.1.1	Synthesis of new HTMs . . . . .	115
6.1.2	Synthesis of cobalt complexes . . . . .	117
6.2	Optical spectroscopy . . . . .	118
6.3	Electrochemical characterization . . . . .	119
6.4	Photoelectron spectroscopy in air . . . . .	119
6.5	Conductivity measurements . . . . .	119
6.6	OFET fabrication and characterization . . . . .	120
6.7	Fabrication and characterization of solar cells . . . . .	121
6.7.1	Fabrication of solid-state dye-sensitized solar cells . . . . .	121
6.7.2	Fabrication of perovskite-based solar cells . . . . .	122
6.7.3	Characterization of solar cells . . . . .	123
6.7.4	Long-term stability testing . . . . .	123
6.8	X-ray diffraction spectroscopy . . . . .	124
	<b>Appendix</b>	<b>125</b>
	<b>Bibliography</b>	<b>129</b>
	<b>Acknowledgements</b>	<b>143</b>
	<b>Curriculum Vitae / List of publications</b>	<b>145</b>





# Nomenclature

## List of Abbreviations

2D	Two dimensional
2H	Nomenclature for the most common $\text{PbI}_2$ polytype
3D	Three dimensional
AM	Air mass
AM1.5G	Reference solar spectral irradiance according to ASTM G-173-03
APCE	Absorbed photon-to-electron conversion efficiency
ASTM	American Society for Testing and Materials
C220	A D- $\pi$ -A sensitizer (cf. Figure 1.9 on page 18)
CB	Conduction band
Co(bpy)	Tris(2,2'-bipyridyl)cobalt(III)
Co(bpy-pz)	Tris(6-(1 <i>H</i> -pyrazol-1-yl)-2,2'-bipyridine)cobalt(III)
Co(phen)	Tris(1,10-phenanthroline)cobalt(III)
cps	Counts per second
CV	Cyclic voltammetry
D- $\pi$ -A	Donor- $\pi$ -Bridge-Acceptor
DMeO-TPD	A hole-transporting material (cf. Figure 3.1 on page 43)
DMF	<i>N,N</i> -dimethylformamide
DOS	Density of states
DPV	Differential pulse voltammetry
DSC	Dye-sensitized solar cell

## Nomenclature

---

EC	Electrochemistry
EQE	External quantum efficiency
F <sub>4</sub> -TCNQ	2,3,5,6-tetrafluoro-7,7,8,8-tetracyanoquinodimethane
Fc <sup>+</sup> /Fc	Ferrocenium/Ferrocene redox couple
FET	Field-effect transistor
FF	Fill factor
FK102	A Co(III) complex (cf. Figure 2.11 on page 33)
FK209	A Co(III) complex (cf. Figure 2.11 on page 33)
FK269	A Co(III) complex (cf. Figure 2.11 on page 33)
FRET	Förster resonance energy transfer
FTO	Fluorine-doped tin oxide
G	Global
GBL	γ-butyrolactone
Hex	Hexyl
HM	Homemade
HM-spiro-MeOTAD	Homemade spiro-MeOTAD (made at LPI, EPFL)
HOMO	Highest occupied molecular orbital
HTM	Hole-transporting material
IPCE	Incident photon-to-electron conversion efficiency
IQE	Internal quantum efficiency
IR	Infrared
ITO	Tin-doped indium oxide
LED	Light-emitting diode
LHE	Light-harvesting efficiency
LiTFSI	Lithium bis(trifluoromethylsulfonyl)imide
LUMO	Lowest unoccupied molecular orbital
Me	Methyl

MLCT	Metal-to-ligand charge transfer
MO	Metal oxide
mp-TiO <sub>2</sub>	Mesoporous TiO <sub>2</sub>
MPP	Maximum power point
NHE	Normal hydrogen electrode
NMR	Nuclear magnetic resonance
OFET	Organic field-effect transistor
OLED	Organic light-emitting diode
P3HT	Poly(3-hexylthiophen-2,5-diyl)
PCBM	[6,6]-phenyl-C <sub>61</sub> -butyric acid methyl ester
PCE	Solar-to-electrical power conversion efficiency
PCPDTBT	Poly[2,6-(4,4-bis-(2-ethylhexyl)-4H-cyclopenta[2,1-b;3,4-b']dithio phene)-alt-4,7-(2,1,3-benzothiadiazole)]
PEDOT	Poly(3,4-ethylenedioxythiophene)
PESA	Photoelectron spectroscopy in air
PFF	Pore-filling-fraction
PL	Photoluminescence
ppm	Parts per million
PTES	Phenyl(triethoxy)silane
PV	Photovoltaic
PW	Pre-wetting
QD	Quantum dot
QP	Quadrapure <sup>TM</sup>
rpm	Revolutions per minute
RT	Room temperature
SCLC	Space-charge limited current
SEM	Scanning electron microscopy

## Nomenclature

---

sp-TiO <sub>2</sub>	Flat TiO <sub>2</sub> deposited by spray-pyrolysis
spiro-3,5-MeO	A hole-transporting material (cf. Figure 3.2 on page 49)
spiro-3,5-mixed	A hole-transporting material (cf. Figure 3.2 on page 49)
spiro-3,5-tBut	A hole-transporting material (cf. Figure 3.2 on page 49)
spiro-m-MeO	A hole-transporting material (cf. Figure 3.2 on page 49)
spiro-MeO-TPA	A hole-transporting material (cf. Figure 3.2 on page 49)
spiro-MeOTAD	A hole-transporting material (cf. Figure 3.2 on page 49)
spiro-p-HexO	A hole-transporting material (cf. Figure 3.2 on page 49)
spiro-p-tBut	A hole-transporting material (cf. Figure 3.2 on page 49)
ssDSC	Solid-state dye sensitized solar cell
TBP	4- <i>tert</i> -butylpyridine
TCO	Transparent conductive oxide
TFSI <sup>-</sup>	Bis(trifluoromethylsulfonyl)imide anion
TOF	Time of flight
TU	Thiourea functionality
UV	Ultraviolet
VB	Valence band
Vis	Visible
XRD	X-ray diffraction spectroscopy
Y123	A D- $\pi$ -A sensitizer (cf. Figure 1.9 on page 18)

## List of Symbols

$\beta$	Poole-Frenkel coefficient
$\delta$	Chemical shift
$\epsilon$	Permittivity
$\eta_{coll}$	Charge collection efficiency
$\eta_{inj}$	Charge injection efficiency

---

$\mu$	Mobility
$\mu_0$	Zero-field mobility
$\mu_{sat}$	Saturation mobility
$\rho$	Mass density
$\tau$	Transit time (SCLC model) / Decay time of an exponential fit
$\theta$	Diffraction angle (XRD) / Factor that considers the presence of charge carrier traps (SCLC model)
$\varepsilon$	Molar extinction coefficient
$C_i$	Capacitance of the gate dielectric of a field-effect transistor
$d$	Film thickness
$e$	Elementary charge
$E_{Fermi}$	Position of the Fermi level
$E_{HOMO}$	Position of the HOMO level
$E_{ox}$	Redox potential
$F$	Electric field strength
$I$	Current
$I_{DS}$	Source–drain current
$I_{ON/OFF}$	ON/OFF current ratio
$J$	Current density / Coupling constant (NMR)
$J_{MPP}$	Current density at the maximum power point
$J_{ph}$	Photocurrent density
$J_{sat}$	Saturation current density
$J_{SCLC}$	Space-charge limited current density
$J_{SC}$	Short-circuit photocurrent density
$k$	Boltzmann constant
$k_{rec}$	Recombination rate constant
$k_{trans}$	Transport rate constant

## Nomenclature

---

$L$	Transistor channel length
$M$	Molar mass
$m$	Diode ideality factor
$P_{el}$	Electrical power
$P_{in}$	Incident solar power
$R_p$	Parallel (shunt) resistance
$R_s$	Series resistance
$T$	Temperature
$V$	Voltage / Volume
$V_{DS}$	Source–drain voltage
$V_{GS}$	Source–gate voltage
$V_{MPP}$	Voltage at the maximum power point
$V_{OC}$	Open-circuit voltage
$V_{Th}$	Threshold voltage
$W$	Transistor channel width
$Z$	Number of formula units per unit cell

# 1 Introduction

Energy is one of the essential needs of our modern society. The ever increasing world energy consumption entails the depletion of fossil energy resources. The excessive emission of greenhouse gases, caused by burning fossil fuel, results in global warming, threatening Earth's ecosystem. Unacceptable global risks and a problem of waste disposal eliminate nuclear power as a viable alternative to carbon-based fuel. Consequently, we are witnessing a growing quest for the development of low cost renewable energy sources. Substantial scientific endeavors have focused on the design of technologies that utilize one of the four primary renewable energy resources—wind, water, biomass and solar irradiation—for power generation. Due to the immense amount of energy that the Earth receives daily from the Sun, solar energy is seen as a top candidate to alleviate World's energy crisis.

One of the most prominent strategies to utilize solar power is the direct conversion of solar energy into electricity using photovoltaic (PV) devices. Conventional silicon-based solar cell technologies that permit an efficient conversion of solar energy into electrical power were developed and commercialized many years ago. However, cost-intensive purification and fabrication processes and the resulting long energy payback time impair the deployment of such solar cells on a terawatt scale.

During the last three decades, several promising alternatives based on cost-efficient organic materials have been proposed. The potential advantage of these emerging photovoltaic technologies is their use of abundant low-cost materials that can be processed from solution, enabling the application of large-area printing techniques to reduce the fabrication costs and the energy payback time. Amongst them dye-sensitized solar cells (DSCs) have gained notable attention imitating Nature's amazing energy conversion machinery—photosynthesis.

## 1.1 Dye-sensitized solar cells (DSCs)

The device architecture of a typical dye-sensitized solar cell as it has been developed more than 25 years ago, is depicted in Figure 1.1 [1]. The DSC embodiment comprises a molecu-

lar chromophore that is responsible for light-harvesting—similarly to chlorophyll in green plants. The chromophore—also referred to as dye or sensitizer—is chemically anchored to a mesostructured wide-bandgap *n*-type metal oxide semiconductor that acts as a scaffold for the sensitizer and takes up the role of a transport channel for the photogenerated electrons. Upon visible light excitation the sensitizer injects an electron into the conduction band of the semiconductor. This photoinduced electron injection and the resulting one electron oxidation of the sensitizer represent the key step of the photovoltaic device—the charge separation. This step also comprehends two major particularities that distinguish the DSC from any other PV technology. Firstly, the DSC separates the light-harvesting unit (dye) from the charge-transporting unit (metal oxide), whereas in most other PV devices the absorber material takes up a dual role of light absorption and charge transport. Secondly, the charge separation in a DSC occurs by kinetic competition and not by a built-in electric field as in conventional silicon solar cells.

Following the charge separation, the dye radical cation is regenerated by electron donation from a redox couple in the electrolyte that infiltrates the mesoporous structure and is in contact with the sensitized junction. Due to a concentration gradient, the reduced redox-active species present in the electrolyte subsequently diffuse away from the junction to the backside of the device, where they are restored by interfacial electron transfer at the back electrode (counter-electrode). At the same time, the photogenerated electrons move through the continuous semiconductor network until they reach the current-collecting front electrode (photoanode). Charge migration through the external circuit completes the photovoltaic device. In its simplest configuration (Figure 1.1), both the front and the back electrode are made of transparent conductive oxide (TCO) coated glass, enabling light to enter the cell from either side.

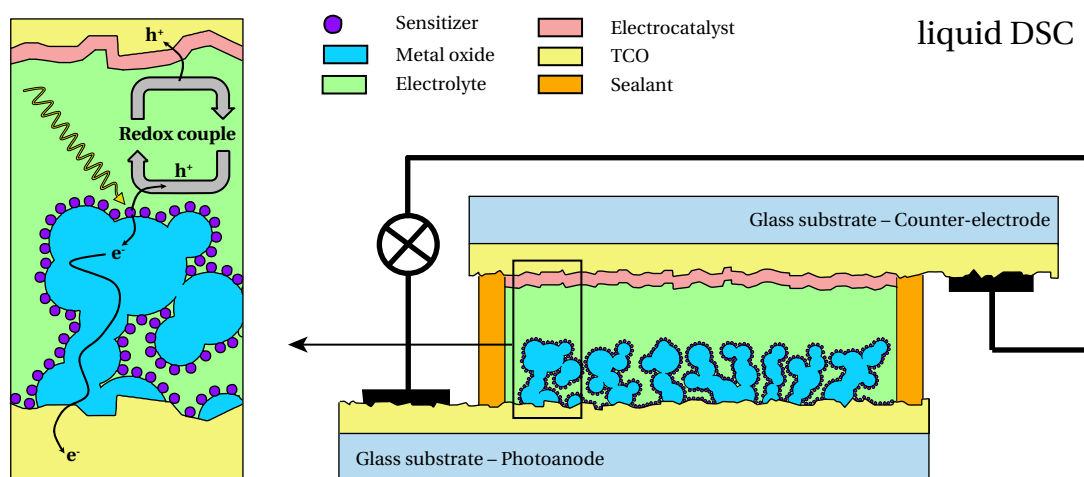


**Figure 1.1** — Device architecture of a typical liquid DSC (not to scale). TCO—transparent conductive oxide.



## 1.2 Solid-state dye-sensitized solar cells (ssDSCs)

Although power conversion efficiencies (*PCEs*) of over 13% could be achieved with the above-mentioned device architecture, potential stability issues due to electrolyte leakage have led to the development of dye solar cells where the liquid redox electrolyte is replaced by a solid hole-transporting material (HTM). The design of so-called solid-state dye-sensitized solar cells (ssDSC) differs slightly from their liquid counterparts, even though the basic principles of the device operation remain identical. A schematic representation of a typical ssDSC device architecture is given in Figure 1.2. Four main structural differences between a liquid and solid-state DSC can be identified:

- Compared to a typical liquid DSC, that is usually constructed by assembling two separate electrodes together with the liquid electrolyte filling the space in between them, a ssDSC is fabricated using a monolithic device architecture and built upon a single TCO substrate.
- The solid HTM is deposited by solution-processing, e.g. spin-coating. During the deposition, the HTM solution infiltrates the sensitized, mesoporous metal oxide structure and the subsequent evaporation of the solvent leaves the HTM in its solid form.
- The back electrode is usually deposited by shadow mask evaporation of a thin layer of gold or silver directly onto the solid HTM.
- The formation of an ohmic contact between the HTM and the TCO, requires the presence of a blocking layer covering the TCO and avoiding any direct contact to the HTM.

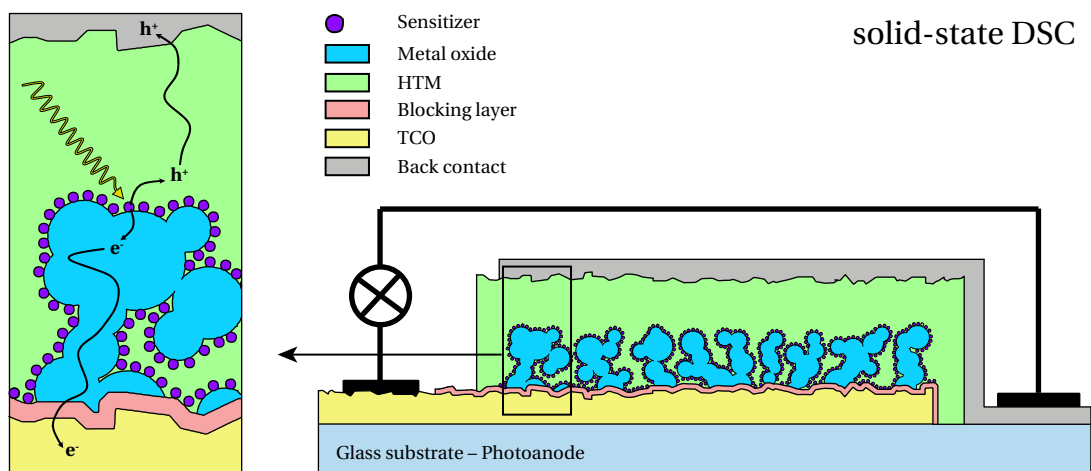


**Figure 1.2** — Device architecture of a typical solid-state DSC (not to scale). TCO—transparent conductive oxide, HTM—hole-transporting material.

### 1.3 Electronic processes in DSCs

Solid-state DSCs represent the general topic of the present thesis. Therefore, the focus of this introductory section lies on ssDSCs, although many of the aspects discussed here are equally valid for liquid DSCs. Figure 1.3 illustrates the electronic processes that take place during the operation of a DSC.

As mentioned previously, the first step to occur is the light absorption and excitation of the sensitizer anchored to the porous metal oxide (MO). In the simplest case the excitation corresponds to a promotion of an electron from the highest occupied molecular orbital (HOMO) to the lowest unoccupied molecular orbital (LUMO) of the sensitizer. Following the excitation, the sensitizer can undergo radiative or non-radiative relaxation, restoring its initial ground state. Alternatively, the photoexcited state of the dye can be quenched by electron transfer from the HOMO level of the dye to the conduction band (CB) of the metal oxide semiconductor. This process leads to separated charges and is referred to as *electron injection*. If the metal oxide is carefully chosen and the sensitizer properly engineered, the electron injection occurs on a femtosecond timescale. The factors that govern the electron injection kinetics will be discussed in more detail in Section 1.5.4. As the relaxation of the photoexcited dye is orders of magnitude slower than the electron injection, the charge separation occurs almost quantitatively. It is this favorable kinetic bias within the system that is intrinsic for an efficient functioning of the device. The fraction of electrons that are injected into the metal oxide after the excitation of the sensitizer is given by the charge separation efficiency or

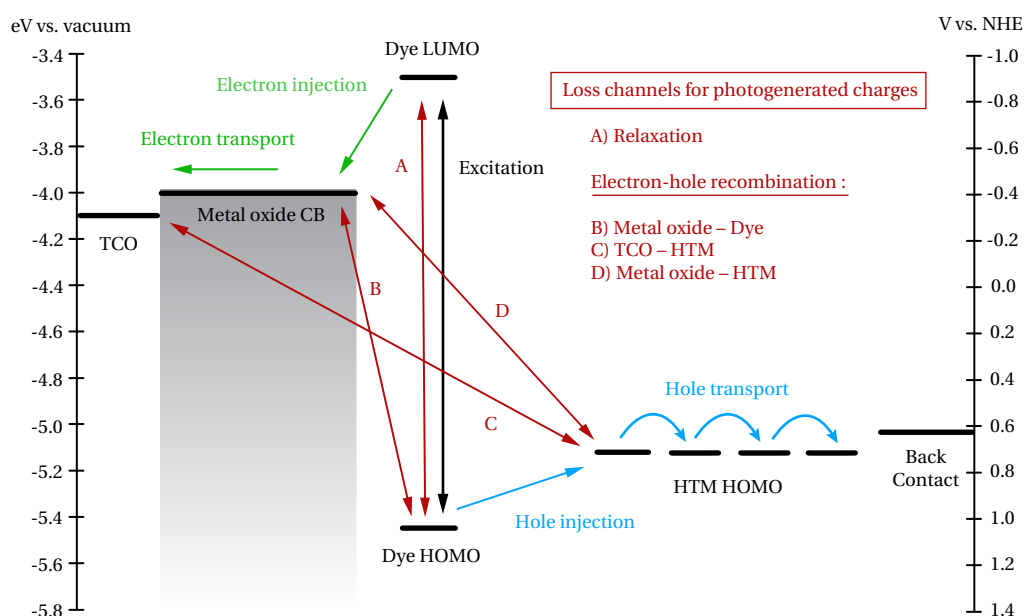


**Figure 1.3** — Energy scheme, illustrating the electronic processes that occur in an ssDSC. CB—conduction band, NHE—normal hydrogen electrode.

charge injection efficiency  $\eta_{inj}$ . Subsequent to the charge separation, the oxidized sensitizer is regenerated by electron transfer from the HTM to the dye. In the case of ssDSCs, this process is usually referred to as *hole injection*, as a hole is transferred from the oxidized sensitizer to the HTM. The kinetics of the hole injection depends mainly on the energy level offset between the HOMO of the dye and the HOMO of the HTM. Yet, a certain chemical compatibility such as favorable orbital overlap and/or similar hydrophobicity between the dye and the HTM may also play an important role. Moreover, efficient charge transfer between the dye and the HTM requires an intimate contact between both materials. This requirement is not straightforward as the solid HTM has to be infiltrated into the metal oxide structure. These problems will be discussed in more detail at the beginning of Chapter 3.

It is important to note that the preceding paragraphs describe an idealized representation of the basic device operation. The rate constants of the different electron transfer processes strongly depend on the materials employed. One aspect that has been discussed is that the electron injection in a ssDSC is much slower compared to liquid DSCs. In contrast to that, the hole injection from the oxidized dye to the HTM (dye-regeneration) is usually much faster in the solid-state case. This may lead to a process referred to as *reductive quenching*, where the excited state of the dye is quenched by hole injection into the HTM before the electron injection into the metal oxide can occur. This process leads to the formation of a dye radical anion as the intermediate species. The dye radical anion can then undergo electron injection into the metal oxide conduction band, regenerating the dye in its neutral form. Both pathways—the oxidative and the reductive quenching of the photoexcited state of the dye—yield the same result, but differ in the nature of the intermediate species.

After the charge separation (electron injection) has occurred, electron–hole recombination can lead to the loss of photogenerated charge carriers. In total, four different loss channels can be identified:

- A) Radiative or non-radiative relaxation of the photoexcited state of the dye, directly after excitation (*relaxation*)
- B) Recombination between electrons in the metal oxide conduction band and oxidized dye molecules (*recombination MO–Dye*)
- C) Recombination between electrons in the TCO and holes in the hole-transporting material (*recombination TCO–HTM*)
- D) Recombination between electrons in the metal oxide conduction band and holes in the hole-transporting material (*recombination MO–HTM*)

The recombination pathways B, C and D stand in direct competition with the transport of photogenerated electrons through the metal oxide film. Therefore, they determine the charge collection efficiency  $\eta_{coll}$ , i.e. the fraction of photogenerated charges that reach the current-collecting front electrode without recombining. The relaxation (A) that occurs before the

charge separation, is usually separated from the electron–hole recombination pathways (B–D), which happen after the charge separation. The relaxation is quantified by  $\eta_{inj}$  as described earlier.

In a first approximation, the charge collection efficiency  $\eta_{coll}$  can be expressed according to Equation 1.1, where  $k_{rec}$  is the global recombination rate constant,  $k_X$  ( $X = B, C, D$ ) are the rate constants for the different recombination pathways and  $k_{trans}$  is the rate constant for the charge transport through the metal oxide film.

$$\eta_{coll} = 1 - \frac{k_{rec}}{k_{trans}} \quad \text{with} \quad k_{rec} = k_B + k_C + k_D \quad (1.1)$$

The recombination between electrons in the metal oxide conduction band and the oxidized dye molecules (pathway B) stands in direct kinetic competition with the hole injection into the HTM, and can therefore be avoided when the latter is sufficiently fast. It can also be influenced by a proper engineering of the sensitizer, as has been shown in the literature for liquid DSCs [2]. The electron flow from the TCO to the HTM (pathway C) can be hindered through the use of a blocking layer that completely covers the TCO substrate, inhibiting any direct exposure of the TCO to the HTM. The TCO is usually coated with the same metal oxide as the one the porous structure is composed of. In fact, the absence of the blocking layer would disrupt the proper functioning of the device, as the contact between the TCO and the HTM is ohmic.

The recombination pathway D (recombination MO–HTM) represents one of the major problems in ssDSCs and DSCs in general. The corresponding rate constant  $k_D$  is usually consider much larger compared to  $k_B$  and  $k_C$ , justifying the approximation  $k_{rec} \approx k_D$ . However,  $k_{rec}$  lies in the same range as  $k_{trans}$ , potentially leading to carrier losses and collection efficiencies < 100%. Compared to liquid DSCs,  $k_{rec}$  is about 10–100 times faster in ssDSCs, resulting in much shorter average carrier diffusion lengths. In order to ensure an efficient charge collection, the thickness of the mesoporous metal oxide film is limited to about 2–3  $\mu\text{m}$  in ssDSCs.

## 1.4 Solar cell characterization

### 1.4.1 Reference solar spectral irradiance

One of the most important aspects of the solar cell characterization is the solar spectrum that is employed to evaluate the photovoltaic performance of a device. The solar spectral irradiance is standardized by the American Society for Testing and Materials (ASTM). The extraterrestrial solar spectrum denoted as Air Mass Zero (AM0) and depicted in Figure 1.4 (red spectrum) is defined by the ASTM E-490 standard. The unit 'Air Mass' defines the optical path length that light has to travel through Earth's atmosphere. The Air Mass is zero for the extraterrestrial irradiance. The integrated spectral irradiance of the AM0 standard is  $1366.1 \text{ W m}^{-2}$ .

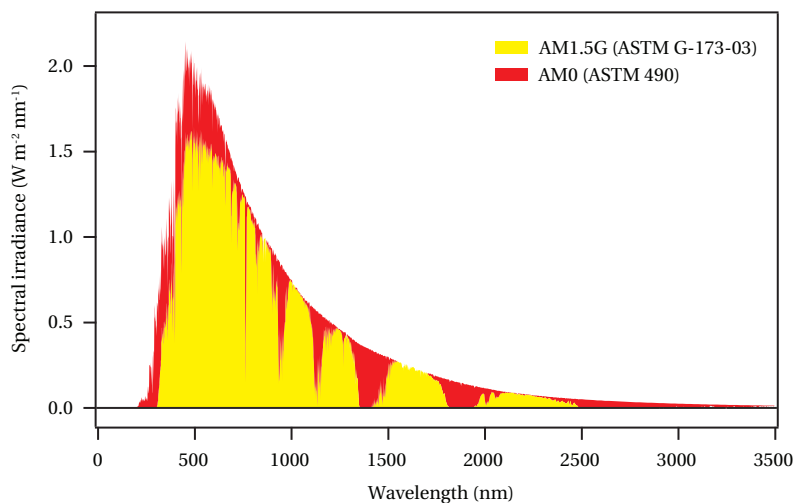


**Figure 1.4** — Reference solar spectral irradiance according to the standards ASTM E-490 (AM0) and ASTM G-173-03 (AM1.5G). ASTM—American Society for Testing and Materials.

Upon passing through the atmosphere, the solar irradiance is attenuated as a result of absorption and scattering processes. The solar spectral irradiance reaching Earth's surface is described by the ASTM G-173-03 standard and herein denoted as AM1.5G (yellow spectrum in Figure 1.4). This standard defines the solar spectral irradiance for a solar zenith angle of  $48.19^\circ$ —that corresponds to an Air Mass of 1.5—and for specific atmospheric conditions. The incident plane is defined as a Sun-facing inclined plane, tilted at  $37^\circ$  towards the Equator. Moreover, the solar irradiance defined by the ASTM G-173-03 standard is the hemispherical—global (G)—irradiance that consists of both direct and diffuse light. The integrated spectral irradiance of the AM1.5G standard is  $1000.4 \text{ W m}^{-2}$ .

### 1.4.2 Current–voltage characteristics

In order to evaluate the performance of a solar cell, the current density—voltage ( $J$ – $V$ ) characteristics of the device are measured. Practically, this is done by applying an external potential bias to cell while measuring the current response. The  $J$ – $V$  characteristics are measured in the dark and under illumination. The applied potential is referred to as forward bias, when electrons are injected into the device from the photoanode side and reverse bias, when electrons are injected from the counter-electrode (back contact) side.

In the dark, an ideal dye-sensitized solar cell shows typical diode behavior. The corresponding  $J$ – $V$  curve is referred to as dark current curve. A typical dark current curve is displayed in Figure 1.5 a. At low applied potential, no—or very little—current flows through the device due to the low conductivity of the metal oxide semiconductor, resulting from a low charge density. Further increase of the applied potential increases the charge density and raises the quasi Fermi level in the metal oxide. When the quasi Fermi level approaches the conduction band of

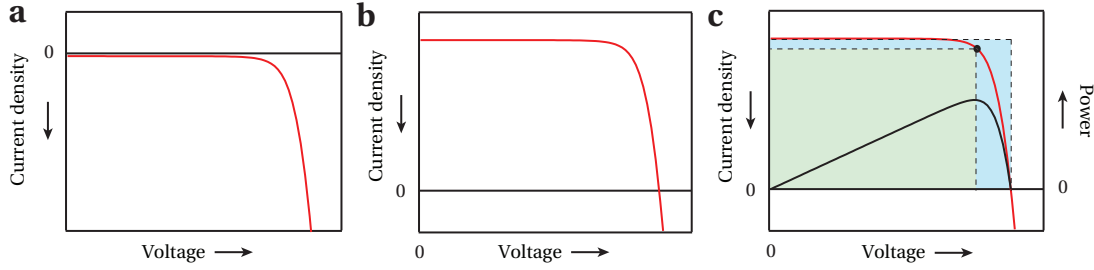


**Figure 1.5** — a) A typical  $J$ - $V$  of a solar cell measured in the dark. b) A typical  $J$ - $V$  of a solar cell measured under illumination. c) A typical  $J$ - $V$  of a solar cell measured under illumination and the corresponding power curve (right-hand axis, black curve). The black dot on the  $J$ - $V$  curve marks the point where the electrical power output is maximum.

the semiconductor, the dark current increases steeply as electrons can flow unhindered to the HTM (or liquid redox electrolyte). Note that in the dark, electrons are injected into the metal oxide and recombine with holes in the HTM. Therefore, the dark current is governed by the same electron-hole recombination process that leads to the loss of photogenerated charge carriers under illumination.

Under illumination, a photocurrent that flows opposite to the diode (dark) current is generated: the solar cell acts as a current source. A typical  $J$ - $V$  curve measured under illumination is displayed in Figure 1.5 b. The shape of the  $J$ - $V$  curve is governed by two competing processes: the generation of photocurrent and the electron-hole recombination. At low forward bias, most of the photogenerated charge carriers are collected before they recombine. In this region, the photocurrent is almost independent of the applied potential. Upon further increasing the applied bias, the recombination becomes more and more prominent, finally leading to a loss of photogenerated charge carriers. At this point, the  $J$ - $V$  starts to drop until it reaches the point where no net current is flowing, as all photogenerated charge carriers recombine. This limiting point is denoted as the open-circuit potential ( $V_{OC}$ ). The second limiting condition is the short-circuit photocurrent ( $J_{SC}$ ), defined as the point where the external bias applied to the cell is zero.

Several other parameters that characterize the performance of a solar cell can be derived from the  $J$ - $V$  characteristics:

The power conversion efficiency ( $PCE$ ), i.e. the fraction of the incident power  $P_{in}$  that is converted into electrical power  $P_{el}$ , is calculated from the power curve. The electrical power is defined as the product of  $J$  and  $V$ . A typical  $J$ - $V$  curve (red curve) and the corresponding power curve (black curve), i.e. the output power of the solar cell as a function of applied voltage, are displayed in Figure 1.5 c. As can be seen from the figure, the power curve shows a maximum that lies in the range of the curvature of the  $J$ - $V$  curve. The maximum of the power curve is called the maximum power point (MPP). The corresponding voltage and current are

denoted as  $J_{MPP}$  and  $V_{MPP}$ , respectively. The  $PCE$  is then defined according to Equation 1.2.

$$PCE = \frac{P_{el}}{P_{in}} = \frac{J_{MPP} V_{MPP}}{P_{in}} \quad (1.2)$$

$$FF = \frac{J_{MPP} V_{MPP}}{J_{SC} V_{OC}} \quad (1.3)$$

$$PCE = \frac{J_{SC} V_{OC} FF}{P_{in}} \quad (1.4)$$

Another important parameter of the solar cell is the fill factor  $FF$ . It is defined as the ratio between the product of  $J_{MPP}$  and  $V_{MPP}$ , and  $J_{SC}$  and  $V_{OC}$  according to Equation 1.3. It can be depicted as the ratio between the two rectangles spanned by  $J_{MPP}$  and  $V_{MPP}$ , and  $J_{SC}$  and  $V_{OC}$ , as illustrated in Figure 1.5 c. The  $FF$  describes the ‘squareness’ of the  $J$ – $V$  curve. Using the definition of the  $FF$ , Equation 1.2 can be rewritten as Equation 1.4.

In a simple approximation, the  $J$ – $V$  curve of a solar cell can be described by the ideal diode equation (Equation 1.5) where  $J_{ph}$  is the generated photocurrent,  $J_{sat}$  is the saturation current,  $e$  is the elementary charge,  $k$  the Boltzmann constant and  $T$  the temperature [3]. Due to a non-ideal behavior of the solar cell, an ideality factor  $m$  is introduced ( $m = 1$  for an ideal diode) [4]. Furthermore, a series resistance  $R_S$  and a parallel resistance  $R_P$ , also referred to as shunt resistance, can be added to the equivalent circuit of the solar cell in order to account for resistive losses. The equivalent circuit with the parasitic resistances  $R_S$  and  $R_P$  is illustrated in Figure 1.6 a. Considering  $m$ ,  $R_S$  and  $R_P$ , the diode equation is modified to Equation 1.6. Practically,  $R_S$  results, for example, from the connections made to the solar cell and/or the sheet resistance of the conductive substrate. In ssDSCs,  $R_S$  is additionally affected by the transport resistance of the HTM. In contrast to that,  $R_P$  arises from loss processes within the solar cell, leading to a leakage current. In ssDSC the leakage current could, for instance, result from a flawed metal oxide compact layer that does not entirely prevent the contact

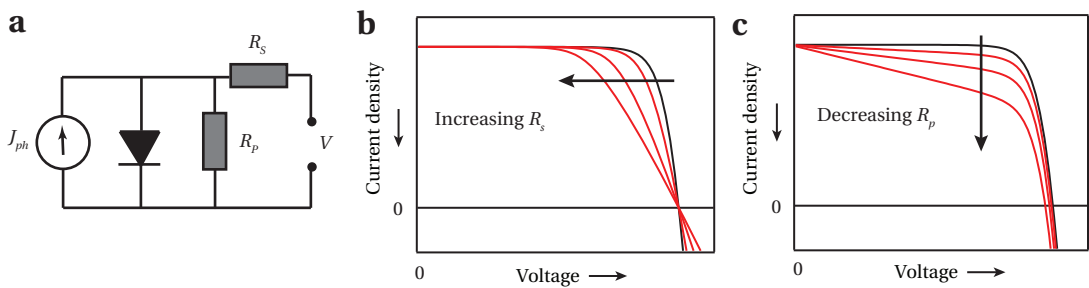


**Figure 1.6** — a) Equivalent circuit of a solar cell. a, b) Influence of a) an increasing series resistance  $R_S$  and b) a decreasing parallel resistance  $R_P$  on the  $J$ – $V$  characteristics of a solar cell.

between the TCO and the HTM. The influence of these parasitic resistances on the  $J$ - $V$  characteristics of a solar cell is schematically illustrated in Figure 1.6 b, c. As is evident from the figure, an increase in  $R_S$  or a decrease in  $R_P$  both lead to a decrease of the  $FF$  of the device.

$$J = J_{ph} - J_{sat}(\exp(\frac{eV}{kT}) - 1) \quad (1.5)$$

$$J = J_{ph} - J_{sat}(\exp(\frac{e(V + JR_S)}{mkT}) - 1) + \frac{V + JR_S}{R_P} \quad (1.6)$$

### 1.4.3 Quantum efficiency measurements

The quantum efficiency of a solar cell is measured as a function of wavelength and represents the fraction of incident photons which is converted into electrons that reach the external circuit. Two types of quantum efficiencies exist: the external quantum efficiency ( $EQE$ ) and the internal quantum efficiency ( $IQE$ ).

The  $EQE$ , also referred to as incident photon-to-electron conversion efficiency ( $IPCE$ ), considers all photons that are emitted from the solar simulator and that hit the active area of the solar cell. It is accessible by measuring the photocurrent of the solar cell under monochromatic irradiation. From this, the  $IPCE$  can be calculated based on the known photon flux  $J_0$  of the solar simulator according to Equation 1.7, where  $J_{SC}(\lambda)$  is the short-circuit photocurrent density under monochromatic irradiation and  $e$  the elementary charge. Integration of the product of  $IPCE$  and  $J_{SC}(\lambda)$  over the wavelength of the incoming light yields the total short-circuit photocurrent density that is expected to be generated by the solar cell.

The  $IPCE$  can also be expressed by a product of internal efficiencies that quantify the different electronic processes within the device according to Equation 1.8. In Equation 1.8,  $LHE$  is the light-harvesting efficiency,  $\eta_{inj}$  is the electron injection efficiency (or charge separation efficiency) and  $\eta_{coll}$  is the charge collection efficiency. The  $LHE$  equals the absorptance and is easily accessible experimentally by measuring the absorption spectrum of the solar cell. Dividing the  $IPCE$  by the  $LHE$  yields the  $IQE$ , also referred to as absorbed photon-to-electron conversion efficiency ( $APCE$ ), that considers only photons that are absorbed by the device.

$$IPCE(\lambda) = \frac{J_{SC}(\lambda)}{eJ_0} \quad (1.7)$$

$$IPCE(\lambda) = LHE(\lambda) \times \eta_{inj}(\lambda) \times \eta_{coll}(\lambda) \quad (1.8)$$



## 1.5 The important ssDSC components

The following sections aim to discuss the different parts of the ssDSC in more detail. Those aspects of the ssDSC that are more closely related to the work that is presented in this thesis will be discussed extensively in the introductory paragraph of each chapter.

### 1.5.1 The compact metal oxide blocking layer

In conventional liquid DSCs, the interfacial electron transfer from the TCO substrate to the oxidized species of the redox couple is usually rather slow. In contrast to that, a proper functioning of a ssDSC necessitates a thin metal oxide blocking layer that prevents the direct contact between the TCO and the HTM. The metal oxide blocking layer is normally composed of the same material as the mesoporous metal oxide film. In most cases the material of choice for the mesoporous film—and hence the blocking layer—is  $\text{TiO}_2$ . The ideal blocking layer is as thin as possible and fully covers the TCO surface. Practically, the blocking layer has to be as thick as necessary to achieve a full surface coverage, a parameter that strongly depends on the technique that is used to deposit it.

Several techniques have been used to fabricate thin metal oxide films for the application as a blocking layer. The most frequently used technique is the deposition of the metal oxide blocking layer by aerosol spray pyrolysis [5], mainly because it does not require the use of expensive equipment and yields films of relatively good quality. A detailed procedure for the deposition of  $\text{TiO}_2$  via aerosol spray pyrolysis is given in the experimental section (Section 6.7.1). The thickness of the thin metal oxide film can be controlled via the concentration of the precursor solution, the pressure of the carrier gas and the number of spraying cycles. The influence of the different parameters during the deposition of the  $\text{TiO}_2$  blocking layer by spray pyrolysis on the device performance of ssDSCs has been investigated by several groups [6–9]. The typical thickness of a  $\text{TiO}_2$  compact layer prepared by spray-pyrolysis lies in the range of 20–100 nm.

### 1.5.2 The mesoporous metal oxide film

The mesoporous metal oxide film has two main tasks: a) it serves as scaffold for the sensitizer and b) it transports electrons from the sensitized surface to the conductive substrate. In an ideal scenario, the specific surface area of the mesoporous film is covered by a monolayer of dye molecules. It is desirable to maximize the number of dye molecules in the photovoltaic device and hence the amount of generated photocurrent (for a given active area and metal oxide film thickness). This can be achieved by maximizing the specific surface area of the mesoporous metal oxide film. The specific surface area of a particulate, porous film is determined by the average pore and particle size. A smaller particle size generally leads to a higher surface area, but also a smaller pore size. Practically, a compromise between the two parameters has to be found, as the pore size must be sufficiently large in order to allow for an efficient infiltration of

the solid hole-conductor (solid-state DSC) or an efficient diffusion of the redox active species in and out of the pores (liquid DSC). So far, the highest power conversion efficiencies have been achieved with mesoporous films composed of metal oxide nanoparticles with an average particle diameter of around 20 nm. The average pore diameter is usually in the same range or slightly larger (20–40 nm).

So far, the material of choice to achieve good photovoltaic performance has been  $\text{TiO}_2$ .  $\text{TiO}_2$  is a semiconductor with a wide bandgap of approximately 3.2 eV, that is non-toxic, environmentally friendly and naturally abundant. Due to the presence of oxygen vacancies,  $\text{TiO}_2$  is intrinsically *n*-doped.  $\text{TiO}_2$  naturally occurs in three different phases: anatase, rutile and brookite. The phase that is most thermodynamically stable is rutile. However, both anatase and brookite are kinetically stable and only convert to rutile at high temperatures ( $> 600^\circ\text{C}$ ). For DSC applications, the anatase phase has shown the best performance, although the exact reasons have not yet been fully ascertained [10]. Other wide-bandgap semiconductors that have been investigated for ssDSCs are ZnO [11–14] and  $\text{SnO}_2$  [15–17]. Both materials are particularly interesting due to their higher charge carrier mobility in the bulk [18]. The mesoporous  $\text{TiO}_2$  film in an ssDSC is typically 2–3  $\mu\text{m}$  thick.

When using  $\text{TiO}_2$ , the mesoporous  $\text{TiO}_2$  electrode is often treated in an aqueous solution of  $\text{TiCl}_4$  prior to the device fabrication (cf. Section 6.7.1. In many cases such a treatment has been reported to improve the performance of the photovoltaic devices. This effect has been attributed to several phenomena such as an increase in the electron injection rate, a retardation of the electron–hole recombination and/or an increase in the dye loading, i.e. the amount of dye adsorbed on the mesoporous  $\text{TiO}_2$  film. However, the exact mechanism of the improvement is not entirely understood. Additionally to its influence on the device performance, the  $\text{TiO}_2$  treatment improves the necking between adjacent metal oxide nanoparticles and thus the mechanical strength of the mesoporous film. The effect of the  $\text{TiCl}_4$  treatment on the electron transfer dynamics in an ssDSC configuration has recently been investigated by Marchioro et al. [19].

Besides the  $\text{TiCl}_4$  treatment many attempts have been made to coat the mesoporous metal oxide film with a thin layer of an insulating oxide in order to slow down the electron–hole recombination and increase the carrier diffusion length. Ideally, the insulating layer is only a few angstroms thick, so that the electron injection from the sensitizer can occur via quantum-mechanical tunneling. Insulating oxides that have been investigated for this application in ssDSCs are  $\text{ZrO}_2$  [20],  $\text{Al}_2\text{O}_3$  [21–23] and  $\text{MgO}$  [24] on  $\text{TiO}_2$  as well as  $\text{MgO}$  and  $\text{TiO}_2$  on  $\text{SnO}_2$  [15–17].

### 1.5.3 The hole-transporting material

In an ssDSC the hole-transporting material infiltrates the mesoporous metal oxide structure, ensuring a constant regeneration of oxidized dye molecules and transporting charges away from the sensitized interface to the back contact of the solar cell. Various materials have

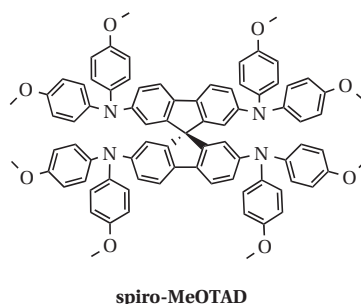


**Figure 1.7** — Molecular structure of 2,2',7,7'-tetrakis-*N,N*-di-*para*-methoxyphenylamine-9,9'-spirobifluorene (spiro-MeOTAD), utilized as the HTM in ssDSCs.

been explored for their utility as HTMs in ssDSCs, ranging from molecular or polymeric organic semiconductors to inorganic semiconductors. A detailed review on the materials that have been investigated, as well as a general discussion about the basic requirements of an HTM for the application in ssDSCs are given at the beginning of Chapter 3. Here, light-harvesting will focus on the most commonly employed HTM in ssDSC—2,2',7,7'-tetrakis-*N,N*-di-*para*-methoxyphenylamine-9,9'-spirobifluorene (spiro-MeOTAD). The molecular structure of spiro-MeOTAD is depicted in Figure 1.7. In 1998 Bach et al. introduced spiro-MeOTAD as a HTM for ssDSCs and since then spiro-MeOTAD has remained as the material of choice when high power conversion efficiencies are demanded [25].

Spiro-MeOTAD is an amorphous organic *p*-type semiconductor. It has a glass transition temperature of 121°C and a melting point of 246°C [26]. Spiro-MeOTAD has a large band-gap and yields almost colourless thin films when deposited from solution. The lowest energy electronic transition results in a strong absorption band at 389 nm (3.2 eV) with a molar extinction coefficient of  $7.2 \times 10^5 \text{ l mol}^{-1} \text{ cm}^{-1}$  (cf. Section 2.2.1.2). The first oxidation potential of spiro-MeOTAD is found to be approximately –5.1 eV as derived from electrochemical and photoelectron spectroscopy measurements (cf. Section 3.2.2). Spiro-MeOTAD exhibits a hole mobility in the range of  $1 \times 10^{-5}$  to  $1 \times 10^{-4} \text{ cm}^2 \text{ V}^{-1} \text{ s}^{-1}$  as determined by various techniques (cf. Section 3.2.3.3). The conductivity of spiro-MeOTAD thin films depends strongly on the presence (or absence) of additives and/or *p*-dopants. The mobility and conductivity of spiro-MeOTAD are discussed in detail in Section 2.1.2 and Section 3.2.3.3, respectively.

Spiro-MeOTAD has a very high solubility in organic solvents such as toluene or chlorobenzene and is usually deposited by spin-coating, although other techniques have been reported [27]. Several additives are commonly added to the spin-coating formulation of spiro-MeOTAD and processed together with the HTM. Typically, these additives are: 4-*tert*-butylpyridine (TBP), lithium bis(trifluoromethylsulfonyl)imide (LiTFSI) and, in some cases, a *p*-dopant (cf. Chapter 2). TBP and  $\text{Li}^+$  ions are also two very common additives in liquid DSCs where they are added to the redox electrolyte. The main effects of the two additives on the device performance can be related to their adsorption on the surface of the mesoporous metal oxide, although the exact mechanism is not fully understood. The net effect of the addition of TBP is

usually believed to be an upward shift of the metal oxide conduction band and/or a retardation of the electron–hole recombination rate, which leads to an increase in the  $V_{OC}$  [28, 29]. A very similar effect has also been observed upon the addition of TBP to the spiro-MeOTAD spin-coating solution for the fabrication of ssDSCs [30]. In contrast to that, the addition of  $\text{Li}^+$  to the liquid electrolyte usually shifts the metal oxide conduction band downwards, expanding the energy difference to the excited state of the sensitizer and hence accelerating the electron injection [29, 31]. The result is an increase in the  $J_{SC}$ . In ssDSCs, the exact mechanism seems to be more complex, although the same net effect is observed [32].

In addition to influencing the surface properties of the metal oxide, the additives can also have an effect on the charge transport in the bulk of the HTM. Snaith et al. observed an effect of LiTFSI on the hole mobility and conductivity of spiro-MeOTAD [33]. However, later it has been found that LiTFSI can act as a *p*-dopant by accelerating the oxidation of spiro-MeOTAD by atmospheric oxygen—a process referred to as photo-doping (cf. Section 2.1.2) [34–36]. Moreover, Abate et al. found that the influence of LiTFSI on the charge transport properties of spiro-MeOTAD is negligible in the absence of oxygen [34]. The influence of TBP on the charge transport of spiro-MeOTAD has not been reported yet, although it is known that TBP helps to solubilize LiTFSI in the spiro-MeOTAD matrix [30].

### 1.5.4 The sensitizer

The sensitizer (dye) makes the wide-bandgap metal oxide sensitive to visible light. A key parameter to obtain an efficient photovoltaic device is to employ a sensitizer that has a broad absorption spectrum, overlapping with the emission spectrum of the Sun as much as possible. In most cases, the transition that is responsible for the absorption of visible light is the transition from the HOMO to the LUMO of the dye, as described previously.

Besides an appropriate absorption spectrum, the position of the sensitizer's energy levels relative to the metal oxide conduction band and the HOMO of the HTM is equally important. These requirements are necessary in order to allow an efficient electron injection into the conduction band of the metal oxide semiconductor and an efficient hole injection into the HTM. On an energy scale, the LUMO level of the dye has to lie above the conduction band of the metal oxide and the HOMO level of the dye has to lie below the HOMO level of the HTM (cf. Figure 1.3). Moreover, electronic conjugation between the dye and the metal oxide is needed for the electron injection to occur efficiently. Practically, this is achieved through the chemisorption of the sensitizer to the metal oxide surface via a suitable anchoring functionality—typically a carboxylic acid group.

In general, the dyes that have been investigated for DSC applications can be divided into two categories: metal complexes and organic dyes. It is worth mentioning that several concepts exist to replace the molecular sensitizer by an inorganic or organic–inorganic hybrid absorber. This strategy is not considered here, but will be discussed extensively in the introductory part of Chapter 4.

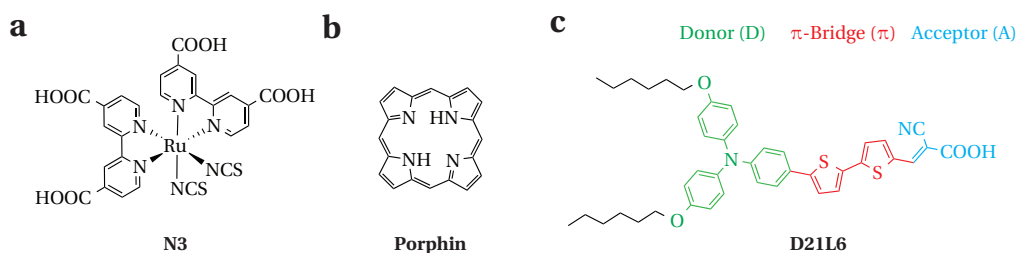


**Figure 1.8** — a) Molecular structure of *cis*-bis(isothiocyanato)bis(2,2'-bipyridyl-4,4'-dicarboxylato)ruthenium(II) (N3). b) Molecular structure of porphin, the basic building block of porphyrin dyes. c) Molecular structure of the D- $\pi$ -A dye D21L6.

**Metal complexes.** Metal complexes based on Ru(II) such as *cis*-bis(isothiocyanato)bis(2,2'-bipyridyl-4,4'-dicarboxylato)ruthenium(II) (N3, Figure 1.8 a) were the first dyes to yield high power conversion efficiencies in liquid DSCs [1]. The dyes of this class have a strong absorption band in the visible region of the electromagnetic spectrum that results from a metal-to-ligand charge transfer (MLCT) transition. This transition promotes an electron from the bonding metal-centered d orbitals ( $t_{2g}$  symmetry) to the anti-bonding ligand-centered  $\pi^*$  orbitals of the complex. The molar extinction coefficient of the MLCT transition is usually about  $1 \times 10^4 \text{ l mol}^{-1} \text{ cm}^{-1}$ —a value that is rather low and necessitates relatively thick metal oxide film of 10–20  $\mu\text{m}$  to ensure complete light absorption. This poses a problem especially for ssDSCs, where the optimum thickness of the mesoporous layer is found to be only 2–3  $\mu\text{m}$ .

**Organic sensitizers.** In contrast to the metal complexes, organic sensitizers are composed purely of organic atoms that form large conjugated  $\pi$ -systems, enabling low energy transitions that lie in the visible region of the electromagnetic spectrum. These  $\pi$ - $\pi^*$  transitions, that usually originate from intramolecular charge-transfer transitions, have much higher molar extinction coefficients compared to the MLCT transitions in metal organic complexes. Several concepts exist to design organic sensitizers suitable for the application in DSCs.

On the one hand, the sensitizer can be based on an organic chromophore that itself absorbs visible light and is highly colored. Prominent examples are chromophores based on porphin (Figure 1.8 b)—called porphyrins—that are naturally occurring, e.g. haem or chlorophyll. In most cases porphyrins occur—or are used—in their doubly deprotonated form. In this state the porphin macrocycle can act as a tetradentate ligand and coordinate divalent metal cations such as  $\text{Zn}^{2+}$ ,  $\text{Fe}^{2+}$  or  $\text{Mg}^{2+}$ . Despite the presence of this metallic cation, porphyrins are still referred to as organic dyes, as the orbitals of the metal cation are not directly involved in the  $\pi$ - $\pi^*$  transition. For DSC applications, the chromophore needs to be substituted with an anchoring group (such as a carboxylic acid group) in order to attach it to the metal oxide surface. Furthermore, other functional groups can be introduced to adapt the properties of the dye to the requirements of the DSC. The design of porphyrin sensitizers for liquid DSCs has recently been reviewed by Li et al. [37]

On the other hand, a sensitizer can be designed through the clever combination of different organic moieties that would be colorless on their own. The most commonly employed concept that has gained a lot of interest in recent years, is the D- $\pi$ -A concept, in which an electron-rich donor unit (D) is connected to an electron-deficient acceptor unit (A) via a conjugated  $\pi$ -bridge ( $\pi$ ). Upon light absorption electron density is transferred from the HOMO, that is mainly localized on the donor unit, to the LUMO, that is mainly localized on the acceptor unit. The resulting intramolecular charge-transfer state is stabilized due to electrostatic attraction and the large delocalization of the positive and negative charge, which leads to a low energy absorption band in the visible. By design, the acceptor unit is also the part of the molecule that anchors to the metal oxide surface. The D- $\pi$ -A design is particularly beneficial due the directionality of the charge transfer during the excitation. Upon light absorption, electron density is vectorised from the donor moiety to the acceptor moiety, i.e. in the direction of the metal oxide surface, facilitating the electron injection into the metal oxide conduction band.

The structure of a typical D- $\pi$ -A dye is depicted in Figure 1.8 c. This dye—denoted as D21L6—pioneered the D- $\pi$ -A concept and was one of the first organic dyes to yield efficient and stable liquid DSCs [38]. Later, it was also employed in ssDSCs [39]. In the case of D21L6, the electron-rich donor is an alkoxy-substituted triphenylamine (green) that is connected to an electron-deficient cyanoacrylate acceptor/anchor (blue) via a conjugated thiophene-based  $\pi$ -bridge (red). A vast number of different building blocks for the design of D- $\pi$ -A dyes for DSC applications has been reported, out of which the most important ones have been comprehensively reviewed by Hagfeldt et al. [40]

**General structural design.** Besides the optimization of the absorption spectrum and/or the tuning of the energy levels, substituents on the sensitizer can have other important functions.

A problem that is frequently encountered in the field of DSCs, is the aggregation of dye molecules that hampers the formation of a dye monolayer on the metal oxide surface. The nature of the aggregates depends strongly on the structure of the dye, but is mainly due to either  $\pi$ - $\pi$  interactions or hydrogen bonding. One way to overcome this problem is to introduce sterically demanding substituents, such as long alkyl chains, that space the dye molecules from each other and hence prevent the aggregation. A second effect of the sterically demanding substituents, that has been reported in the literature, is their shielding of the metal oxide surface [39, 41–44]. Once adsorbed on the metal oxide surface, dye molecules with long alkyl chains have proved to decrease the electron-hole recombination rate. The long alkyl chains efficiently shield the metal oxide surface and avoid the direct contact between the metal oxide and the HTM. Several examples have been reported where other functional substituents are introduced on the dye molecule. Snaith et al. reported on a ruthenium based sensitizer bearing ion-coordinating ethylenedioxy chains that bind  $\text{Li}^+$  ions and keep them close to the surface [45]. Other studies focused on the introduction of hole-conducting triarylamine moieties on the ligands of ruthenium complexes in order to facilitate the interaction between the sensitizer and the HTM [46–50]. An influence of the substituents on the chemical compatibility between dye and HTM has also been reported by Kwon et al. [51]

**Sensitizers used in ssDSCs.** The first record of the application of a Ru(II) metal complex in a ssDSC configuration is the report by Hagen et al. from 1997 [52]. In this work Hagen et al. pioneered the use of organic hole-transporting materials for the fabrication of ssDSCs and achieved a *PCE* of 0.2% using the aforementioned N3 dye. One year later, Bach et al. used the same dye, combined it with spiro-MeOTAD as the HTM and reached a *PCE* of 0.7% [25]. In the subsequent years, careful device engineering allowed for an optimization of this system and an increase of the *PCE* to up to 3.2% in 2002 [26, 30, 53]. Following this work, a further improvement of the device performance was achieved by a slight modification of one of the bipyridine ligands of the ruthenium complex, enabling *PCEs* of up to 4.0% (2005) [54], 4.5% (2007) [41] and 5.0% (2010) [55]. Until today, this efficiency has remained the highest *PCE* achieved with an ssDSC based on a metal complex sensitizer and an organic HTM.

The use of organic sensitizers for ssDSCs was pioneered by Tennakone et al. in 1995 who reached a *PCE* of 0.8% using cyanidin as the sensitizer and *p*-CuI as the HTM. In the following years, this *PCE* was quickly outperformed by the system developed by Bach et al. [25], based on spiro-MeOTAD and the N3 dye. In 2005, Schmidt-Mende et al. were the first to report on the use of an organic sensitizer that was able to supersede the previously employed ruthenium metal complexes and reached a *PCE* of 4.1% [56]. Consecutively, the *PCE* of ssDSCs based on spiro-MeOTAD and organic D- $\pi$ -A dyes have been optimized up to 4.8% (2008) [57], 6.5% (2010) [58] and 7.2% (2011, this work) [59].

It is important to note that this brief overview cites only the important milestones of the development of dyes for ssDSCs. Several other organic sensitizers have been investigated for ssDSC. Besides the aforementioned D- $\pi$ -A dyes, this includes dyes based on chromophores such as porphyrin [60, 61], phthalocyanine [62, 63], squaraine [64–66], rylene [67, 68] or ullazine [69].

Moreover, this literature review shows that the increase in power conversion efficiency that has been achieved in the last years is solely due to the development of new sensitizers, whereas the rest of the device architecture and composition remained almost identical to the one originally proposed by Bach et al. in 1998 [25].

**Sensitizers used in this thesis.** For the studies presented in this thesis, two state-of-the-art D- $\pi$ -A sensitizers denoted as C220 and Y123 were employed. Their molecular structures are shown in Figure 1.9 and their optical and electrochemical properties are summarized in Table 1.1. Using C220, *PCEs* of up to 6.5% were achieved for a ssDSC based on spiro-MeOTAD [58]. The first example of a ssDSC based on the Y123 dye is presented in this work (cf. Section 2.2.1.4). By employing Y123, a record power conversion efficiency of 7.2% was achieved [59].

### 1.5.5 The back contact

The back contact of a ssDSC is usually formed by thermal evaporation of a noble metal with a high work function, such as gold or silver. Besides being less expensive and having a



## Chapter 1. Introduction

**Table 1.1** — Electrochemical and optical properties of the D- $\pi$ -A dyes Y123 and C220.

Dye	$\lambda_{max}^a$ nm	$\epsilon^a$ l mol <sup>-1</sup> cm <sup>-1</sup>	$E_{ox}^b$ V vs. Fc <sup>+</sup> /Fc	$E(HOMO)^c$ eV vs. vacuum
C220	555	$5.5 \times 10^4$	0.17	-5.27
Y123	542	$5.1 \times 10^4$	0.28	-5.38

<sup>a</sup> Data taken from reference [58] (C220) and [70] (Y123).

<sup>b</sup> Data determined from electrochemical measurements in dichloromethane solution. The applied potential was internally referenced using the Ferrocenium/Ferrocene (Fc<sup>+</sup>/Fc) redox couple (cf. Section 6.3 for details).

<sup>c</sup> Derived from  $E_{ox}$  using a conversion factor of -5.1 eV for the Fc<sup>+</sup>/Fc standard.

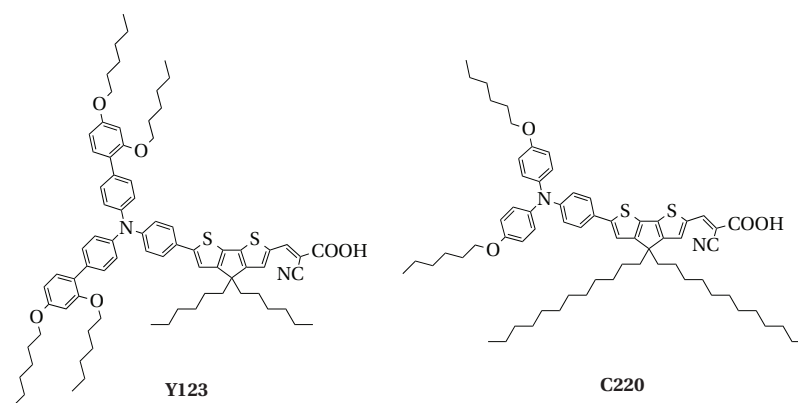


**Figure 1.9** — Molecular structures of the D- $\pi$ -A sensitizers C220 and Y123.

higher conductivity, silver has proved to yield higher short-circuit photocurrents [41]. This was attributed to the higher reflectivity of silver, that is particularly helpful for thin metal oxide films where the incident light is not entirely absorbed. Few examples exist where the evaporated metal contact has been replaced by an alternative electrode material. Chiang et al. fabricated a bifacial transparent ssDSC by using a back contact composed of a thin layer of a conductive polymer and tin-doped indium oxide (ITO) deposited by sputtering [71]. Similar devices were fabricated by Hardin et al. and Margulis et al. who used a transparent array of silver nanowires as the back contact [72, 73]. Xu et al. reported on the use of a carbon-based back contact that was deposited via screen-printing [74].



## 1.6 Motivation and strategies

Despite more than 15 years of development, solid-state dye-sensitized solar cells have always been lagging behind their liquid counterparts. For many years, the PCE of ssDSCs has stagnated in the range of 4-6%, compared to liquid DSCs that nowadays reach power conversion efficiencies of up to 13%. Partly, this can be attributed to a rather poor reproducibility of the photovoltaic performance of ssDSCs. Additionally, the parameters that limit the device performance were not entirely understood, hampering the development of new materials and/or device architectures.

The studies presented in this thesis aimed at helping to solve the above-described issues. In general, I followed three different strategies:

In Chapter 2 I present a new strategy to control the charge-transport properties of the widely used hole-transporting material spiro-MeOTAD and introduce a new class of molecular p-type dopants based on Co(III) complexes for organic semiconductors. These new materials were designed to be processed from a solution and allow for a better control of the conductivity of spiro-MeOTAD compared to the commonly employed photo-doping. It is shown how the dopants can be engineered in order to match their properties to the requirements that are needed for an efficient application in ssDSCs. In combination with a new organic sensitizer, these dopants enabled a new record power conversion efficiency of 7.2%.

Chapter 3 describes the development of new molecular hole-transporting materials for the application in ssDSCs. We synthesized seven new HTMs that are based on a triarylamine-substituted 9,9'-spirobifluorene core. The new materials were characterized by electrical and electrochemical techniques in order to evaluate their properties. Organic-field effect transistors were fabricated based on the new materials in order to determine their hole mobility and develop a structure-property relationship. The comparison of different peripheral substituents on the triarylamine moieties allowed to highlight the importance of the processability of the HTM for an application in ssDSCs. In general, we encountered the purity of the new materials as one of the major issues, but were able to present a purification method to (partly) circumvent this problem.

Chapter 4 is based on the use of a new hybrid organic-inorganic perovskite sensitizer ( $\text{CH}_3\text{NH}_3\text{PbI}_3$ ) to replace the molecular dye in ssDSCs. This material has recently aroused great interest in the scientific community, as it enabled power-conversion efficiencies of over 12%. I introduce a new technique to realize the nanoscopic perovskite morphology that is required for the fabrication of efficient solar cells. This technique relies on the deposition of the perovskite in two steps:  $\text{PbI}_2$  is first applied on a substrate by solution-processing and subsequently exposed to a solution of  $\text{CH}_3\text{NH}_3\text{I}$ . The desired hybrid perovskite forms within seconds after contacting the two precursors. The kinetics of the reaction is evidenced in detail using scanning electron microscopy as well as X-ray diffraction and optical spectroscopy. Employing the sequential deposition method for the fabrication of solar cells enabled a new record power conversion efficiency of 15%.



## 2 Co(III) complexes as *p*-dopants in solid-state DSCs

*The following chapter describes the use of cobalt(III) complexes as *p*-type dopants for triaryl-amine-based organic semiconductors such as spiro-MeOTAD and their use in solid-state dye-sensitized solar cells. The work presented in this chapter is partially based on two articles that have been published in peer-reviewed journals [59, 75]. The synthesis of all Co(III) complexes presented in this chapter has been carried out by Dr. Florian Kessler, LPI, EPFL.*

### 2.1 Introduction

Spiro-MeOTAD is one of the most commonly used hole-transporting materials in ssDSCs (cf. Section 1.5.3). Several desirable properties, e.g. a favorable glass transition temperature, solubility, ionization potential, absorption spectrum and solid-state morphology, make spiro-MeOTAD a suitable candidate for this application. However, similarly to other wide-bandgap organic hole-conductors, spiro-MeOTAD suffers from a relatively low conductivity in its pristine form. In order to overcome this problem, additional charge carriers are generated by doping—a common technique used to tune the electrical properties of both, organic and inorganic semiconductors.

#### 2.1.1 *p*-Type doping of organic semiconductors

Electronic doping is a powerful tool to carefully control the type and density of charge carriers in both organic and inorganic semiconducting materials [76, 77]. Doping of organic semiconductors is usually based on a charge-transfer reaction between the organic host and the dopant, the latter being either a donor (*n*-type doping) or acceptor (*p*-type doping) species that leaves part of the host molecules in a reduced or oxidized state. The doping process is illustrated in Figure 2.1. The introduction of additional charge carriers—either holes or electrons—leads to an increased charge carrier density in the host material, resulting in a higher conductivity according to Equation 2.1, where  $\sigma$  is the conductivity,  $e$  the elementary charge and  $n_x$  and  $\mu_x$  are the density and mobility of the positive (index p) and negative

(index *n*) charge carriers, respectively.

$$\sigma = \sigma_n + \sigma_p = (n_n e \mu_n) + (n_p e \mu_p) \quad (2.1)$$

It has to be noted, that the increase in the conductivity is not necessarily proportional to the increase in the charge carrier density, as the mobility is often affected by the doping. The influence of the doping on charge carrier mobility has been reported for a variety of host materials, including other triarylamine-based hole-conductors [78–80]. However, the literature shows, that several effects have to be considered and therefore *p*-doping can result in an increase or a decrease in charge carrier mobility [81].

The key parameter for efficient doping is the position of the ionization potential or electron affinity of the dopant with respect to the host's energy levels. However, depending on the application, other features, such as ease of processing, may become equally important, finally rendering a dopant only suitable for a specific type of device architecture and/or fabrication process.

Various materials have been reported for their use as *p*-dopants, ranging from strongly electron-accepting fluorinated organic molecules, such as 2,3,5,6-tetrafluoro-7,7,8,8-tetracyanoquinodimethane (F<sub>4</sub>-TCNQ) [82, 83], to transition metal oxides (e.g. WO<sub>3</sub> [84, 85] or MoO<sub>3</sub> [86, 87]), metal complexes (e.g. molybdenum tris[1,2-bis(trifluoromethyl)ethane-1,2-dithiolene] [88]), and redox active salts (e.g. NOBF<sub>4</sub> [89] or *p*-(BrC<sub>6</sub>H<sub>4</sub>)<sub>3</sub>NSbCl<sub>6</sub> [89]). Many of these materials are typically applied by vacuum deposition techniques and exhibit low solubility in organic solvents, while others are facing stability issues or are too reactive and prone to side reactions.

Materials such as MoO<sub>3</sub> or WO<sub>3</sub>, both being extensively studied *p*-type dopants, are remarkably performing when thermally evaporated onto or together with the organic semiconductor, but

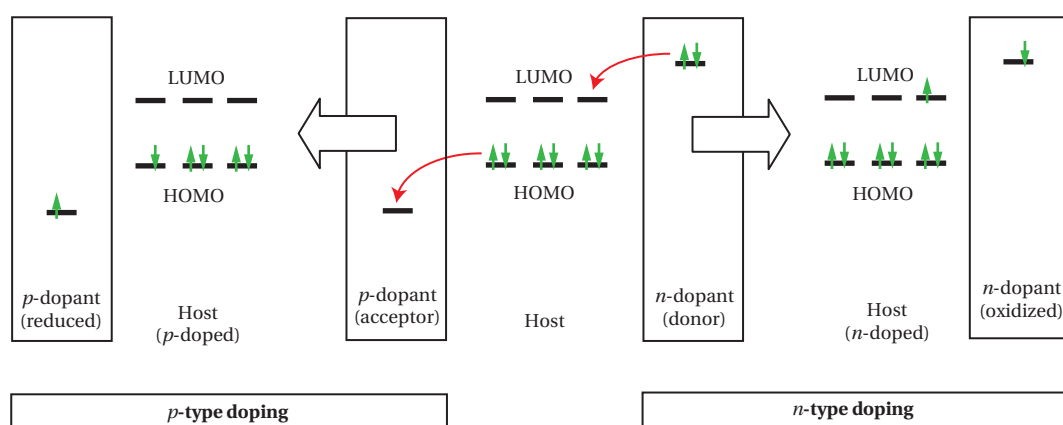


**Figure 2.1** — Scheme illustrating the doping of an organic semiconductor (host) by using either an acceptor species (*p*-type doping) or a donor species (*n*-type doping).

suffer from a lack of solubility when solution-processing is required. Solubility problems are also encountered for molybdenum tris[1,2-bis(trifluoromethyl)ethane-1,2-dithiolene] and F<sub>4</sub>-TCNQ, as these materials have been developed to be thermally evaporated. However, a recent report shows that F<sub>4</sub>-TCNQ can indeed be used as *p*-type dopant for spiro-MeOTAD in ssDSCs [83]. *p*-(BrC<sub>6</sub>H<sub>4</sub>)<sub>3</sub>NSbCl<sub>6</sub> is the dopant that has initially been proposed by Bach et al. [25] in their seminal publication on spiro-MeOTAD-based ssDSCs and has also widely been employed in organic light-emitting devices (OLEDs) [90]. In addition to containing toxic antimony, the compound however exhibits poor stability and degrades within days when in solution, demanding a suitable alternative to be identified.

### 2.1.2 Background and motivation

While *p*-type doping of spiro-MeOTAD was proposed many years ago [25], no detailed study on *p*-type doping in ssDSCs has been reported so far. In fact, most of the recent publications on spiro-MeOTAD-based ssDSCs do not follow this strategy [91, 92]. The reason why high power conversion efficiencies could nevertheless be achieved, is that the devices were typically fabricated under aerobic conditions, enabling the facile one-electron oxidation of spiro-MeOTAD with molecular oxygen under illumination to proceed—a process referred to as photo-doping. While it has been clear for many years, that the photo-doping of spiro-MeOTAD occurs in the presence of oxygen, the exact mechanism is still poorly understood. Only recently, several studies have focused on investigating the pivotal role of oxygen on ssDSC device performance. Studies presented by Cappel et al. [35] and Abate et al. [34] show that the photo-doping is catalyzed by the presence of Li<sup>+</sup> that is commonly introduced into the HTM matrix.

The influence of photo-doping on device performance is illustrated in Figure 2.2. This data shows, how the *J*–*V* characteristics of a ssDSC change upon repeated measurements. During the device fabrication, carried out under aerobic conditions (dry air), a particular attention was paid to avoid excessive illumination of the cell with light  $\lambda < 600$  nm that would lead to photo-doping. However, the intrinsic charge carrier density in spiro-MeOTAD is low, resulting in a low conductivity of the hole transporter, a high series resistance of the photovoltaic device, a low *FF* and hence a poor initial device performance (curve No. 1 in Figure 2.2 a).

During the repeated measurements under continuous illumination, spiro-MeOTAD—that is exposed to the ambient atmosphere—becomes oxidized by photo-doping, leading to an increase in its conductivity, a decrease in the solar cell's series resistance, an increase in the *FF* and hence an increase in the overall PV performance. The evolution of the different photovoltaic parameters that were extracted from the *J*–*V* characteristics during the continuous measurements is shown in Figure 2.2 b–e. This data clearly reveals growing trends for *V*<sub>OC</sub>, *FF* and *PCE*. Only the *J*<sub>SC</sub> first increases upon the photo-doping, then reaches a maximum and finally decreases at higher doping levels. Due to this decrease in the *J*<sub>SC</sub>, the *PCE* reaches a plateau at high photo-doping. These trends will be further discussed in Section 2.2.1.4.

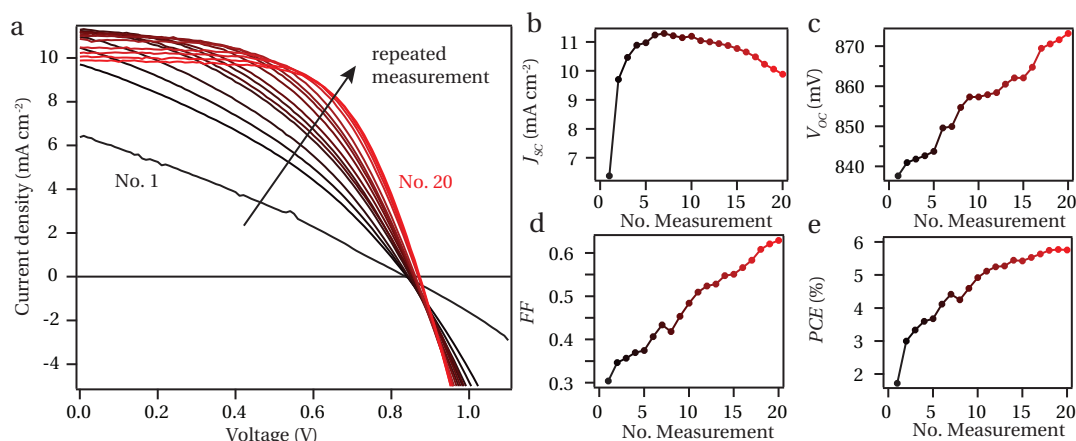


**Figure 2.2** — a)  $J$ - $V$  characteristics measured under simulated AM1.5G solar irradiance ( $100 \text{ mW cm}^{-2}$ ). The measurement was repeated 20 times as indicated by the colour code from black (measurement No. 1) to red (measurement No. 20). The device has been fabricated without the addition of any chemical dopant and in the absence of light with  $\lambda < 600 \text{ nm}$ . b-e) Change of the photovoltaic parameters extracted from the  $J$ - $V$  characteristics as a function of measurement number.

However, very similar trends have recently been reported by Wang et al. [93], who also studied the effect of photo-doping on the solar cell performance.

The data presented above shows that high power-conversion efficiencies can indeed be achieved employing photo-doped spiro-MeOTAD. Therefore, chemical *p*-doping is not necessarily the key to high performance, but it is expected to be crucial to achieve reproducible results, the fabrication of stable ssDSCs using photo-doping being clearly difficult to control. Moreover, the addition of a chemical *p*-type dopant becomes essential when the photovoltaic devices are fabricated under inert atmosphere.

Before the study presented in this chapter was commenced, reproducibility of photovoltaic device performance had been one of the major issues in the field of ssDSCs. We suspected the influence of atmospheric oxygen on the device performance and the uncontrolled oxidation of spiro-MeOTAD during the device fabrication to be one possible cause. Hence, I decided to revisit the concept of using chemical *p*-dopants to control the doping level of spiro-MeOTAD in ssDSCs.

### 2.1.3 Co(III) complexes as *p*-type dopants

From the above-presented short literature review, it becomes evident that none of the dopants that are described in the literature is suitable for the use in solid-state DSCs, mainly because a deposition from solution together with the organic HTM would be favorable.

The following list summarizes the various properties an ideal dopant should possess for its successful application in ssDSCs.

- The oxidation potential of the dopant should be sufficiently high to oxidize spiro-MeOTAD and other potential HTMs in order to ensure an efficient *p*-doping.
- The dopant should have a good solubility in organic solvents and particularly in the spiro-MeOTAD spin-coating formulation in order to be suitable for solution-processing.
- The dopant should be colorless in order to avoid any competition with the sensitizer for light-harvesting.
- The dopant should be air-stable and chemically inert towards HTM, sensitizer and metal oxide semiconductor.
- The structure of the dopant should allow for a synthetically facile tunability of the chemical and physical properties.

Our strategy was therefore to develop a new class of *p*-dopants that fulfill the above-listed criteria, allowing for a detailed investigation of the influence of chemical *p*-doping on ssDSCs device performance. We identified polypyridyl cobalt(III) complexes as possible candidates. Complexes such as tris(2,2'-bipyridyl)cobalt(III), tris(1,10-phenanthroline)cobalt(III) or tris(6-(1*H*-pyrazol-1-yl)-2,2'-bipyridyl)cobalt(III)—all depicted in Figure 2.3—have been successfully used as redox mediators in liquid DSCs replacing the conventional triiodide/iodide redox couple [94–96]. They are straightforward and easy to synthesize, air stable and almost colorless. Moreover, the organic ligands allow for a facile tuning of their physical, chemical and electrochemical properties, helping to adapt them for the desired application.

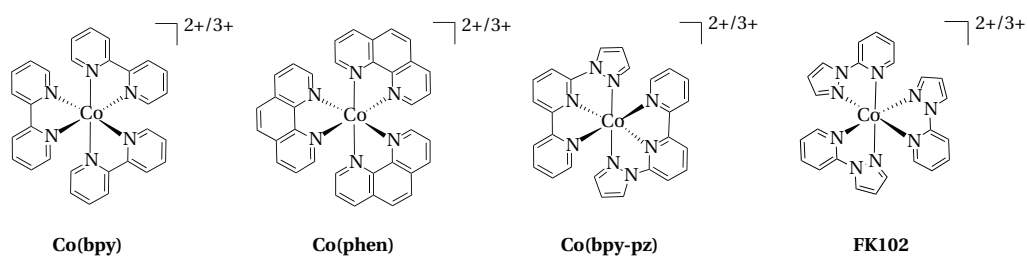


**Figure 2.3** — Molecular structures of the cobalt complexes tris(2,2'-bipyridyl)cobalt(III) (Co(bpy)), tris(1,10-phenanthroline)cobalt(III) (Co(phen)), tris(6-(1*H*-pyrazol-1-yl)-2,2'-bipyridyl)cobalt(III) (Co(bpy-pz)) and tris(2-(1*H*-pyrazol-1-yl)pyridine)cobalt(III) hexafluorophosphate (FK102) that have been employed as redox shuttles in liquid DSCs.

## 2.2 Results and discussion

### 2.2.1 First generation Co(III) *p*-dopant: FK102

Our first choice for the doping application was tris(2-(1*H*-pyrazol-1-yl)pyridine)cobalt(III) hexafluorophosphate denoted as FK102 and depicted in Figure 2.3. FK102 had originally been developed as a redox shuttle for liquid DSCs, but its oxidation potential turned out to be too high for an efficient regeneration of oxidized dye molecules [97], which, interestingly, made it attractive for the *p*-doping discussed herein. It is worth mentioning that this is the first time that Co(III) complexes are used for doping applications and in general, metal complexes so far have mostly been employed as electron donors, i.e. n-type dopants [98–100].

#### 2.2.1.1 Electrochemical characterization of FK102

The main criterion to select a Co(III) complex suitable for the use as *p*-dopant a sufficient driving force for the one-electron oxidation of spiro-MeOTAD. Cyclic voltammetry (CV) and differential pulse voltammetry (DPV) was employed to characterize the HTM and the Co(III) complex in a dichloromethane solution, using the ferrocenium/ferrocene ( $\text{Fc}^+/\text{Fc}$ ) redox couple as an internal reference. The results from the electrochemical analysis are presented in Figure 2.4. As expected and in agreement with the literature [26, 101], the measurements yield three fully reversible oxidation/reduction waves for spiro-MeOTAD (black curves in Figure 2.4), corresponding to four oxidation states that arise from the oxidation of the four methoxy-substituted triarylamine moieties. The first two oxidation/reduction waves situated at 0.01 V vs.  $\text{Fc}^+/\text{Fc}$  and 0.14 V vs.  $\text{Fc}^+/\text{Fc}$ , result from the first and second oxidation state, respectively, whereas the third oxidation/reduction wave situated at 0.35 V vs.  $\text{Fc}^+/\text{Fc}$  is a two electron oxidation, corresponding to the third and fourth oxidation state of spiro-MeOTAD. As for the FK102 cobalt complex, a poorly reversible oxidation/reduction wave at about 0.38 V vs.

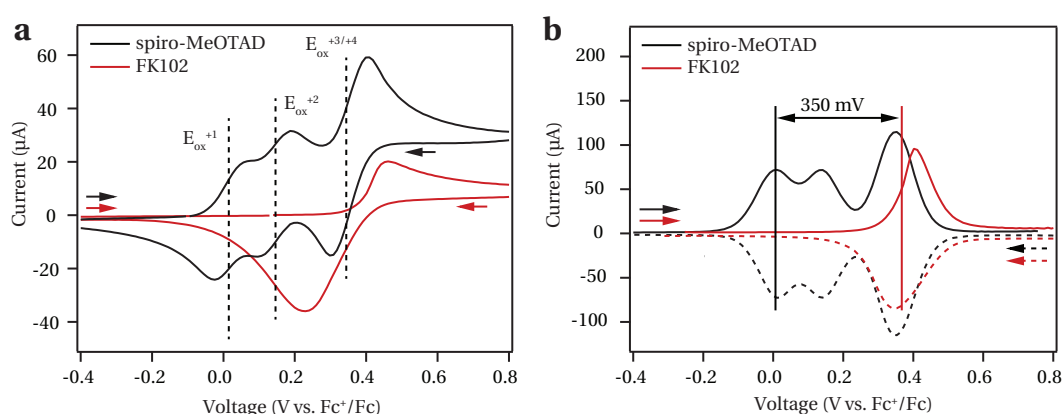


**Figure 2.4** — Electrochemical characterization of spiro-MeOTAD and FK102 using a) cyclic voltammetry and b) differential pulse voltammetry in dichloromethane solution, containing 0.1 M tetrabutylammonium hexafluorophosphate. The applied potential was internally referenced using the  $\text{Fc}^+/\text{Fc}$  redox couple.



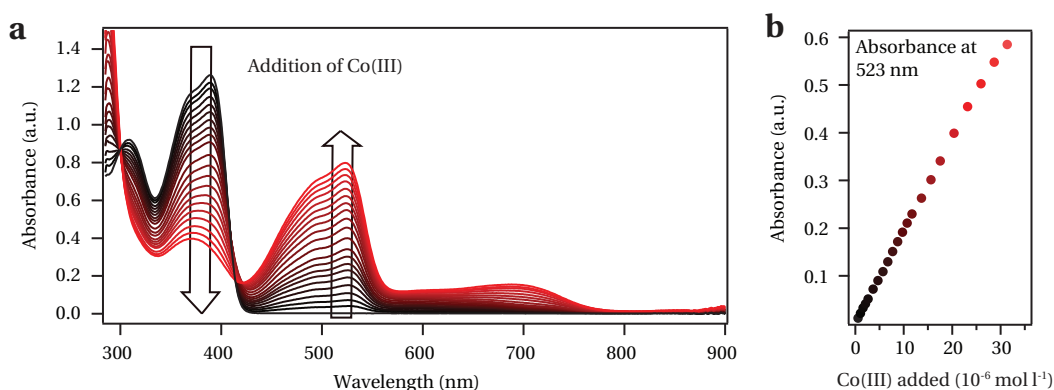


**Figure 2.5** — a) Change in the UV-vis absorption spectrum of a spiro-MeOTAD chlorobenzene solution upon the gradual addition of the FK102 Co(III) complex. The gradual addition of the oxidant is illustrated through the colour gradient from black (pure spiro-MeOTAD) to red. b) Absorbance at 523 nm as a function of the amount of Co(III) oxidant added.

$\text{Fc}^+/\text{Fc}$  is observed, corresponding to the Co(III)/Co(II) redox couple. From the comparison with data obtained for spiro-MeOTAD, a driving force of roughly 350 mV for the spiro-MeOTAD one-electron oxidation reaction was derived. This value is expected to be largely sufficient for efficient *p*-doping.

#### 2.2.1.2 Oxidation of spiro-MeOTAD using FK102

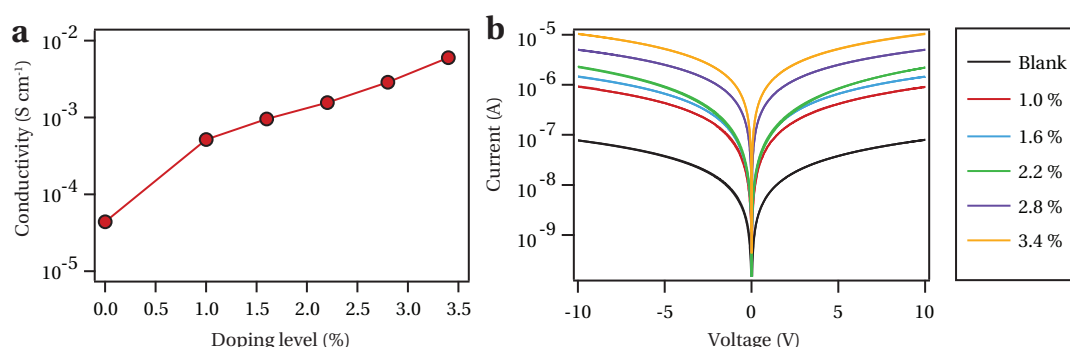
I employed UV-vis optical absorption spectroscopy to investigate the oxidation of spiro-MeOTAD by the Co(III) complex. This strategy has previously been used and is straightforward due to the deep red color of the appearing spiro-MeOTAD $^{\bullet+}$  cation radical. Figure 2.5 a shows how the UV-vis absorption spectrum of a spiro-MeOTAD solution in chlorobenzene gradually changes upon the addition of a solution of FK102. The addition of FK102 decreases the absorption peak of the neutral spiro-MeOTAD at 388 nm and gives rise to two new absorption bands at 520 nm and 687 nm, which can be attributed to the mono cation radical of spiro-MeOTAD. Even though energetically possible, the formation of the doubly oxidized form is not expected, unless more than one equivalent of oxidizing agent is added. However, it is difficult to distinguish these two by simple optical absorption measurements. Figure 2.5 b represents a plot of the absorbance at 523 nm as a function of the amount of FK102 added to the spiro-MeOTAD solution. As expected, the absorbance increases linearly upon the gradual addition of FK102. This data allows for the estimation of a Co(III)-to-spiro-MeOTAD $^{\bullet+}$  conversion yield that will be discussed in more detail in Section 2.2.2.3.

2.2.1.3 Charge transport properties of *p*-doped spiro-MeOTAD

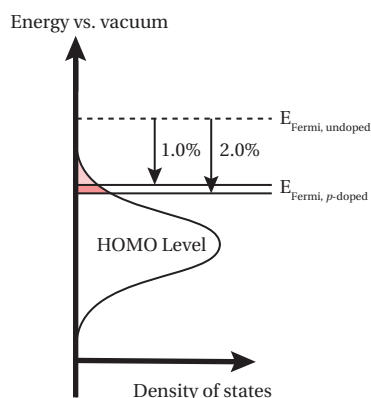
As the successful oxidation of spiro-MeOTAD by FK102 has been confirmed, the benefit of the doping, i.e. an increased conductivity, has to be proved. Therefore we measured linear current–voltage curves of thin spiro-MeOTAD films between two separated gold electrodes for different doping concentrations and extracted the conductivity of the films using Ohm's Law. The results are shown in Figure 2.6. The thin films have been prepared by spin-coating spiro-MeOTAD from a chloroform solution containing spiro-MeOTAD, FK102, TBP and LiTFSI. The two latter additives are commonly introduced in ssDSCs (cf. Section 1.5.3) and are known to influence on the charge-transport properties of spiro-MeOTAD. Hence they were also used here.

Figure 2.6 a depicts the change in conductivity as a function of doping ratio. For a reference sample that does not contain any *p*-dopant, a conductivity of  $4.4 \times 10^{-5} \text{ S cm}^{-1}$  was obtained. Snaith et al. [33] had previously reported a conductivity of  $2.0 \times 10^{-5} \text{ S cm}^{-1}$  for the undoped spiro-MeOTAD—a value that is in agreement with the findings reported here, taking into account that a slightly different concentration of LiTFSI was used. Upon the addition of 1.0% FK102 the conductivity of the spiro-MeOTAD thin film steeply increases by one order of magnitude to  $5.3 \times 10^{-4} \text{ S cm}^{-1}$ . A further exponential increase in conductivity is observed for higher doping ratios as shown in Figure 2.6 a, although the slope of this increase is smaller. From Equation 2.1 in Section 2.1.1 we would expect that the conductivity is proportional to the hole carrier density. The superlinear increase of the conductivity with the doping ratio must therefore result from a change in the mobility. As discussed in the introductory section of this chapter, such a dependence of the mobility on the doping level is frequently observed for organic semiconductors.

The origin of the two regimes in conductivity plot can be rationalized by the Gaussian shape of the density of states (DOS) that is typical for disordered organic semiconductors and that is illustrated in Figure 2.7. Starting from an intrinsic (undoped) semiconductor, the introduction of 1.0% of *p*-dopant represents a very large relative increase of carrier concentration, leading



**Figure 2.6** — a) Plot of the conductivity of *p*-doped spiro-MeOTAD thin films as a function of doping ratio. b) Current–voltage curves of *p*-doped spiro-MeOTAD thin films and an undoped reference (Blank) from which the conductivities were derived according to Ohm's Law.



**Figure 2.7** — Scheme to illustrate how the position of the Fermi level shifts ( $E_{\text{Fermi}}$ ) upon the introduction of 1.0% and 2.0% of a *p*-dopant.

to a strong shift of the Fermi level, as the additional charge carriers fill up the tail of the DOS. A further increase of the doping ratio causes only a small shift of the Fermi level, as it now reaches the region of a large density of states. Similar trends have been observed for other systems [102].

Generally, it has to be noted that the given doping ratios correspond to the molar percentage of FK102 that has been added to the spiro-MeOTAD solution prior to spin-coating, but not necessarily to the resulting doping concentration within the amorphous film. Nevertheless, the results presented here clearly show that the proposed Co(III) complex can indeed be used to efficiently *p*-dope spiro-MeOTAD.

#### 2.2.1.4 Application of FK102 in ssDSCs

In order to prove that the increase in conductivity upon *p*-doping spiro-MeOTAD is beneficial for practical applications, solid-state dye-sensitized solar cells were fabricated, employing spiro-MeOTAD as a hole conductor and FK102 as a *p*-dopant. The latter was added to the spiro-MeOTAD solution prior to the spin-coating. To avoid excessive photo-doping of the HTM and focus solely on the effect of chemical doping, these photovoltaic devices were fabricated under red light illumination ( $\lambda > 600$  nm). Three different doping ratios of 1.0%, 1.6% and 2.2% were investigated and compared to an undoped reference (blank). Hereby, the devices were based on an organic D- $\pi$ -A sensitizer coded Y123 (cf. Section 1.5.4 and Figure 1.9). This work shows for the first time that the Y123 sensitizer also performs well in spiro-MeOTAD-based ssDSCs, as it has previously only been employed in liquid DSCs [103].

**Photovoltaic device performance.**  $J$ - $V$  characteristics measured under simulated AM1.5G solar irradiance of approximately  $100 \text{ mW cm}^{-2}$  intensity are presented in Figure 2.8 and the extracted photovoltaic parameters summarized in Table 2.1. For the undoped reference I found an open-circuit potential  $V_{\text{OC}}$ , short-circuit current density  $J_{\text{SC}}$  and fill factor  $FF$  of 878 mV,

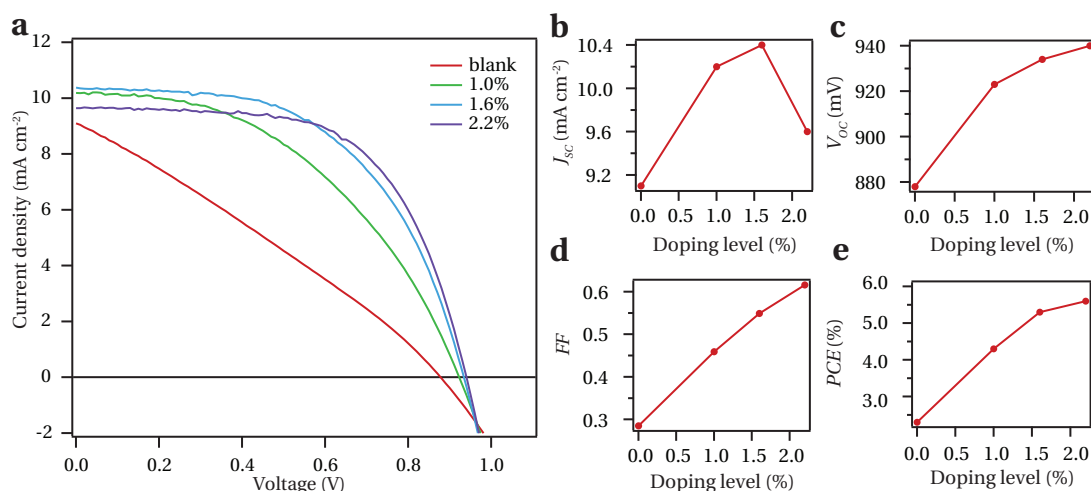


**Figure 2.8** — a)  $J$ - $V$  characteristics measured under simulated AM1.5G solar irradiance ( $100 \text{ mW cm}^{-2}$ ) for *p*-doped devices and an undoped reference (Blank). The devices are based on the Y123 sensitizer. b-e) Change of the photovoltaic parameters extracted from the  $J$ - $V$  Characteristics as a function of doping ratio.

9.1  $\text{mA cm}^{-2}$  and 0.29, respectively, yielding an overall  $PCE$  of 2.3%. This device suffers from a low  $FF$  that can be attributed to the low conductivity and therefore high charge-transport resistance of the undoped spiro-MeOTAD film, contributing to a high series resistance of the solar cell. Upon the addition of 1.0%, 1.6% and 2.2% FK102, the  $FF$  improves to 0.46, 0.55 and 0.62, respectively, resulting in  $PCE$ s of 4.3%, 5.3% and 5.6%. The addition of FK102 initially increases the  $J_{sc}$  to 10.2  $\text{mA cm}^{-2}$  (1.0% FK102) and 10.4  $\text{mA cm}^{-2}$  (1.6% FK102), which is then followed by a decrease to 9.6  $\text{mA cm}^{-2}$  (2.2% FK102) at higher doping levels. The exact reason for this decrease in  $J_{sc}$  at high doping levels remains to be explored but might arise from a filtering of the incoming light by the spiro-MeOTAD cation radical which strongly absorbs at 520 nm ( $\epsilon = 4.0 \times 10^4 \text{ l mol}^{-1} \text{ cm}^{-1}$ ) and therefore competes with the sensitizer for light-harvesting. However, besides the filtering effect of the spiro-MeOTAD cation radical, the  $J_{sc}$  could also be affected by higher recombination kinetics resulting from a higher hole density in the spiro-MeOTAD phase or an influence of the increased hole density on the regeneration of oxidized dye molecules.

The open-circuit potential increases to 923 mV upon the addition of 1.0% FK102 and, surprisingly, increases further to 934 and 940 mV when the doping ratio is raised to 1.6% and 2.2%, respectively. This trend is contradictory to our expectations, as a higher hole density in the spiro-MeOTAD film should lead to augmented recombination between holes and conduction band electrons and consequently a decrease in  $V_{oc}$ , especially at high doping levels. However, this effect might be compensated by a lowering of the Fermi level in the spiro-MeOTAD film when the dopant is added, expanding the energy difference to the quasi Fermi level of the  $\text{TiO}_2$ , enabling higher  $V_{oc}$  values to be realized. Moreover, the higher conductivity of the HTM facilitates charge extraction and consequently obviates the accumulation of holes near the sensitized junction. Nevertheless, further in-depth studies are required to elucidate the

## 2.2. Results and discussion

**Table 2.1** — Photovoltaic parameters of *p*-doped devices derived from *J*–*V* measurements at 100 mW cm<sup>−2</sup> simulated AM1.5G irradiance before and after ageing.

			Blank	1.0%	1.6%	2.2%
<b>Fresh</b>	$V_{OC}$	(mV)	878	923	934	940
	$J_{SC}$	(mA cm <sup>−2</sup> )	9.1	10.2	10.4	9.6
	$FF$	(%)	0.29	0.46	0.55	0.62
	$PCE$	(%)	2.3	4.3	5.3	5.6
<b>Aged</b>	$V_{OC}$	(mV)	887	925	943	947
	$J_{SC}$	(mA cm <sup>−2</sup> )	9.9	10.3	10.2	9.8
	$FF$	(%)	0.30	0.54	0.63	0.65
	$PCE$	(%)	2.6	5.2	6.1	6.1

detailed effect of *p*-doping on the electron–hole recombination kinetics and the cause for the observed trend in  $V_{OC}$ . A maximum power conversion efficiency of 5.6% is achieved for the device containing 2.2% FK102, measured directly after the device fabrication.

It is important to note, that the trends of  $V_{OC}$ ,  $J_{SC}$ ,  $FF$  and  $PCE$  for different concentrations of the chemical *p*-dopant observed here, correspond very well to what was previously obtained for photo-doping (Section 2.1.2). This clearly suggests, that the observed trends are exclusively due to the *p*-doping effect of spiro-MeOTAD and that the chemical *p*-doping is capable of replacing the commonly employed photo-doping. In general, it is observed that the power conversion efficiency of solar cells based on the aforementioned system increases significantly over time when the devices are stored under dark. The comparison between *J*–*V* data measured several days after the device fabrication and the photovoltaic parameters initially obtained, reveals that this performance boost mainly results from an increase in  $FF$  (Table 2.1). We attribute this phenomenon to an improved contact behavior at the interface between spiro-MeOTAD and the silver back contact. However, so far it is unclear whether this

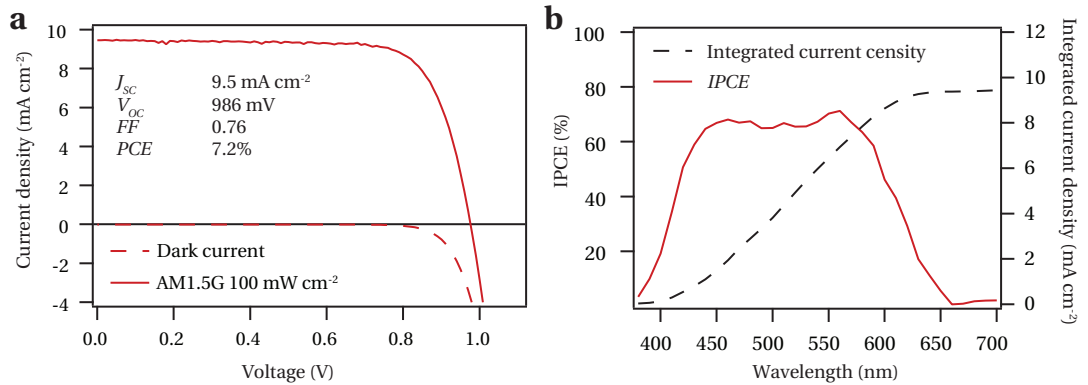


**Figure 2.9** — a) *J*–*V* characteristics of the best performing device measured under 100 mW cm<sup>−2</sup> simulated AM1.5G irradiation (solid line) and in the dark (dashed line). b) IPCE spectrum. The right hand axis indicates the integrated current density that is expected to be generated under AM1.5G illumination.

process involves any reaction with oxygen or moisture, or if it is of pure morphological nature. An influence of oxygen on the charge collection efficiency at the metallic back contact has been previously suspected [41, 72], although a detailed mechanism has not yet been proven. Devices based on the system presented herein generally reach power conversion efficiencies between 6–7%, measured 1–2 weeks after their fabrication. For the best performing device containing 1.6% FK102 dopant an unprecedented and very promising power conversion efficiency of 7.2% was achieved. To the best of my knowledge, this was the first time that such a high *PCE* has been obtained for an all solid-state dye-sensitized solar cell. For this device, the values of the photovoltaic parameters  $V_{OC}$ ,  $J_{SC}$ , and *FF* were 986 mV, 9.5 mA cm<sup>-2</sup> and 0.76, respectively. The corresponding *J*–*V* characteristics are illustrated in Figure 2.9 a. Compared to previously reported highly efficient ssDSCs, our system particularly benefits from the high open-circuit potential of close to 1 V, a property that can be attributed to the Y123 sensitizer. Figure 2.9 b shows the spectrum of the incident-photon to current conversion efficiency (IPCE) of this device. The IPCE spectrum reaches peak values of about 65–70% in the region of 430–580 nm. The right-hand axis of the graph in Figure 2.9 b shows the photocurrent obtained by integrating the overlap between the IPCE spectrum and the AM1.5G solar photon flux. The resulting photocurrent is in very good agreement with the one derived from the *J*–*V* characteristics.

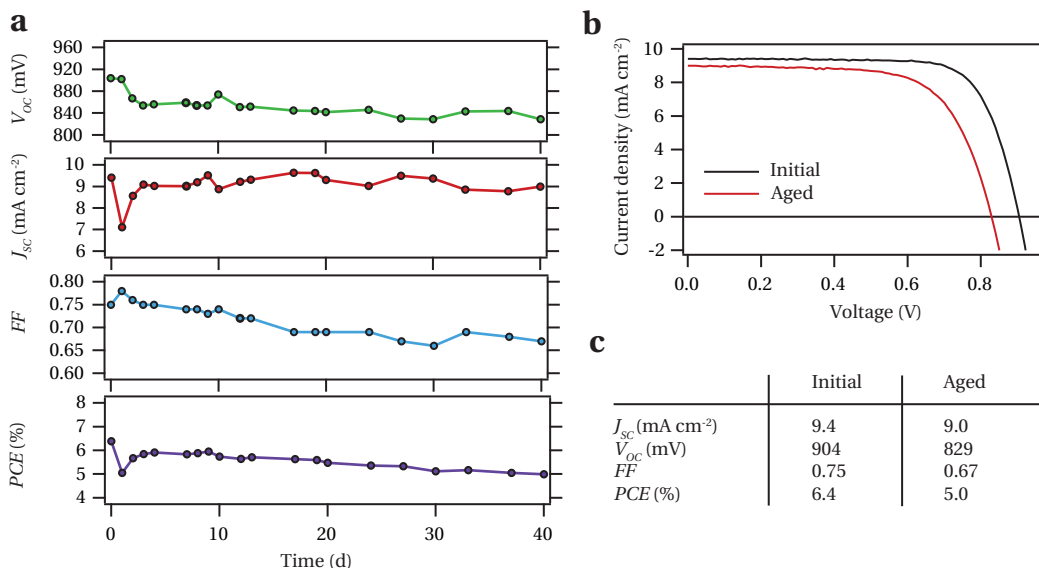


**Figure 2.10** — Long-term stability of a photovoltaic device based on *p*-doped spiro-MeOTAD (0.7%) and the C220 sensitizer. The device was sealed with epoxy resin, equipped with a  $\lambda < 420$  nm filter and kept at 60°C, 100 mW cm<sup>-2</sup> AM1.5G illumination and open-circuit. a) Evolution of photovoltaic parameters during the ageing. b) *J*–*V* curves measured before and after the ageing of 40 days. c) Photovoltaic parameters before and after the ageing.

**Long-term stability of photovoltaic devices.** Besides excellent performance, good long-term stability of photovoltaic devices is highly desirable, but very few studies have been performed on spiro-MeOTAD-based ssDSCs. The influence of the *p*-doping by FK102 on the device stability was therefore investigated. Cells employing the organic D- $\pi$ -A sensitizer coded C220 (cf. Section 1.5.4 and Figure 1.9), were subjected to standard light-soaking conditions (60°C, 100 mW cm<sup>-2</sup> AM1.5G). In order to avoid undesired photo-doping, the devices were hermetically sealed and equipped with a  $\lambda < 420$  nm filter. Under these conditions, photovoltaic cells maintained over 80% of their initial performance during a period of 40 days (Figure 2.10). The  $J_{SC}$  stayed constant during this period, as did the  $V_{OC}$  after an initial drop of 60 mV. Therefore the gradual decrease of the  $FF$  is mainly responsible for the loss of  $PCE$ . Nevertheless, these preliminary results are promising, as they clearly indicate that the proposed *p*-type dopant is not harmful for device stability. Furthermore, these findings are even more remarkable as, to the best my knowledge, this was the first time that a  $PCE$  of 5% could be maintained for a ssDSC under prolonged test conditions.

## 2.2.2 Second generation Co(III) *p*-dopants: FK209 and FK269

### 2.2.2.1 Motivation and strategy

Although the above-mentioned cobalt complex FK102 can be used as an efficient *p*-dopant, I encountered its solubility as one of the major limiting factors, e.g. impeding the investigation of high doping ratios. For this reason we sought to develop other Co(III) complexes that exhibit much better solubility in the spiro-MeOTAD spin-coating formulation.

The main reason for the relatively low solubility of FK102 in organic solvents is its PF<sub>6</sub><sup>-</sup> counterion, whereas salts of bis(trifluoromethylsulfonyl)imide (TFSI<sup>-</sup>) are usually much more soluble. In addition to the change of the counterion, we also introduced a solubilizing *tert*-butyl group on the pyridine-pyrazole (py-pz) ligand. The 2-(1*H*-pyrazol-1-yl)-4-*tert*-butylpyridine

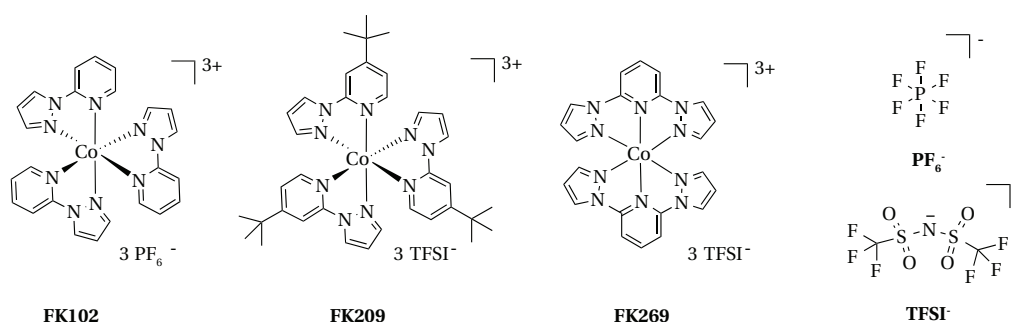


**Figure 2.11** — Molecular structures of FK102 and the two new cobalt(III) complexes tris(2-(1*H*-pyrazol-1-yl)-4-*tert*-butylpyridine)cobalt(III) bis(trifluoromethylsulfonyl)imide (FK209) and bis(2,6-di(1*H*-pyrazol-1-yl)pyridine)cobalt(III) bis(trifluoromethylsulfonyl)imide (FK269), as well as the anions PF<sub>6</sub><sup>-</sup> and bis(trifluoromethylsulfonyl)imide (TFSI<sup>-</sup>).



ligand has previously been successfully used for improved solubility of cationic Ir(III) complexes [104]. The TFSI<sup>−</sup> salt of the Co(III) complex bearing this ligand is denoted as FK209 (Figure 2.11). Apart from the solubility, we also increased the oxidation potential of the dopant in order to maximize the driving force for the doping reaction and to make it suitable for a larger number of host materials. This was done by changing the aromatic ligand. Compared to pyridine (py), pyrazol (pz) is a weaker  $\sigma$ -donor as well as a weaker  $\pi$ -acceptor [105]. Therefore we replaced the three bidentate py-pz ligands by two tridentate pz-py-pz ligands which is expected to stabilize the metal-centered HOMO level of the complex. The TFSI<sup>−</sup> salt of the corresponding Co(III) complex is denoted as FK269 (Figure 2.11). The Co(II) analog of FK269 has previously been reported and characterized by Holland et al. [106] and Ayers et al. [107].

### 2.2.2.2 Characterization of FK209 and FK269

**General characterization.** All the three Co(III) complexes FK102, FK209 and FK269 are diamagnetic low-spin complexes. The diamagnetism is confirmed by <sup>1</sup>H NMR spectroscopy and the appearance of the peaks from the aromatic ligands in the region < 10 ppm. Upon the reduction to Co(II), all three complexes become paramagnetic in agreement with a strong downfield shift (FK269) or complete disappearance (FK102 and FK209) of the <sup>1</sup>H NMR signals. Holland et al. [106] found that the Co(II) analog of FK269 takes up a high spin quartet configuration, which results from the weak splitting of the metal d-orbitals induced by the pyrazole-based ligands. A high spin configuration was also confirmed by Saha et al. [108] for a Co(II) complex bearing a methyl-substituted py-pz ligand.

**Optical characterization of FK102, FK209 and FK269.** All three complexes appear as orange/red solids and give slightly orange colored solutions in organic solvents. UV-vis absorption spectra taken from acetonitrile solutions are shown in Figure 2.12. All complexes show strong absorption bands in the UV region below 350 nm arising from ligand centered  $\pi$ - $\pi^*$  transitions. The orange color, however, results from the very weak d-d transition that lies in the region between 400–600 nm, having a molar extinction coefficient ( $\epsilon$ ) of less than 30 and 600 l mol<sup>−1</sup> cm<sup>−1</sup> in the case of the Co(II) and Co(III) species, respectively. Both new complexes are therefore very suitable for doping applications due to their visible transparency that avoids filtering of incoming light by the dopant in the photovoltaic device.

**Electrochemical characterization of FK209 and FK269.** The two new complexes were also characterized by DPV and CV measurements in order to evaluate their redox potentials and compare them to FK102. Results are given in Figure 2.13. As expected, the complexes show oxidation/reduction waves in dichloromethane that correspond to the Co(III)/Co(II) redox couple situated in the region of 0.2–0.8 V vs. the Fc<sup>+</sup>/Fc standard. As in the case of FK102, the redox process is irreversible for FK269, but can be considered quasi-reversible in the case of FK209. From the DPV measurements, the redox potentials of FK209 and FK269 were estimated to be around 0.32 and 0.58 V vs. Fc<sup>+</sup>/Fc, respectively. As mentioned in Section 2.2.1.1 the redox potential of FK102 is about 0.38 V vs Fc<sup>+</sup>/Fc. The lower redox potential



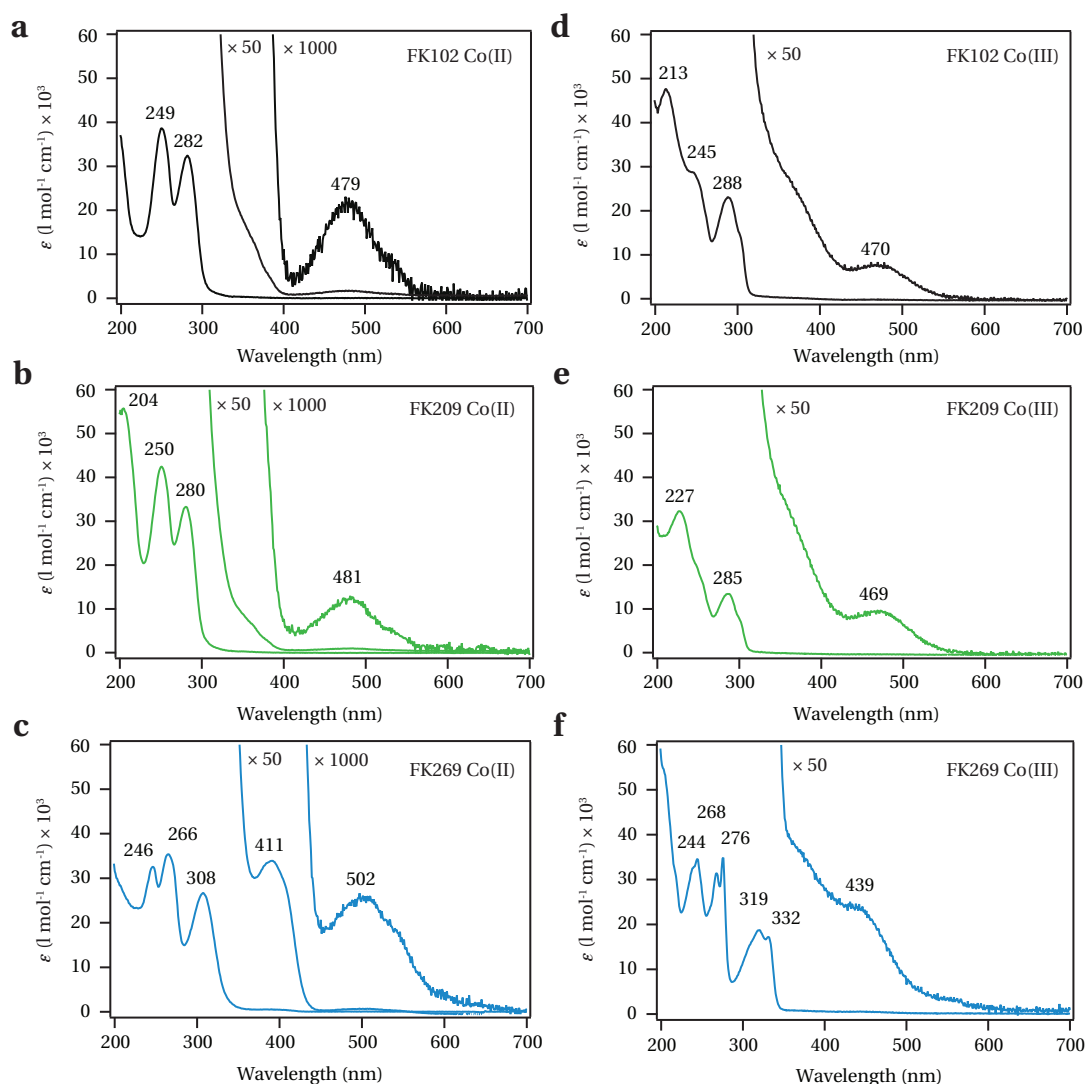


**Figure 2.12** — Absorption spectra of the Co(III) dopants FK102, FK209 and FK269 (d–f) and their Co(II) analogues (a–c) measured in acetonitrile solution. Two magnifications are given for the Co(II) complexes and one for the Co(III) complexes. Numbers on the graphs indicate the peak positions in nm.  $\epsilon$ —molar extinction coefficient.

of FK209 compared to FK102 can be rationalized by the inductive electron-donating effect of the *tert*-butyl groups on the py-pz ligand that destabilizes the HOMO of the complex. In agreement with our predictions, the change from a total number of 3 py/3 pz rings (FK102, FK209) to 2 py/4 pz rings (FK269) coordinated to the Co(III) metal center increases the redox potential, even though the large shift of roughly 200 mV was unexpected. Considering the first redox potential of spiro-MeOTAD at 0.01 V vs.  $\text{Fc}^+/\text{Fc}$ , all three dopants exhibit a driving force of more than 300 mV for the one-electron oxidation of spiro-MeOTAD.

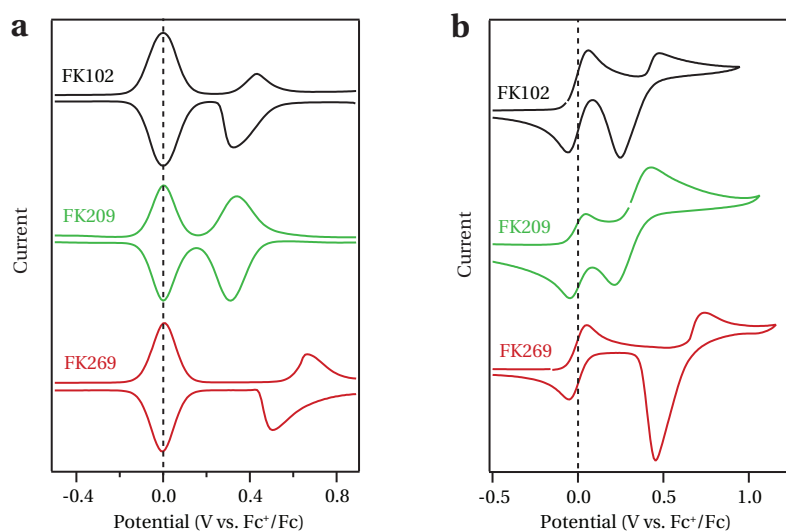


**Figure 2.13** — Electrochemical characterization of FK209 and FK269 in dichloromethane solution using a) differential pulse voltammetry and b) cyclic voltammetry. 0.1 M tetrabutylammonium hexafluorophosphate has been added as a supporting electrolyte. The applied potential was internally referenced using the  $\text{Fc}^+/\text{Fc}$  redox couple. The electrochemical data of FK102 is shown for comparison.

### 2.2.2.3 Estimation of a Co(III)–to–spiro-MeOTAD $^{\bullet+}$ conversion yield

The oxidation of spiro-MeOTAD by the two new Co(III) complexes was confirmed by UV–vis absorption spectroscopy in chlorobenzene solution. The gradual addition of any of the three complexes to a spiro-MeOTAD solution causes a decrease of the absorption band of spiro-MeOTAD at 389 nm together with a rise of the two absorption bands at 523 and 689 nm corresponding to the spiro-MeOTAD $^{\bullet+}$  cation radical (Figure 2.14). It is important to note that the addition of the Co(II) analogue of any of the complexes to a spiro-MeOTAD solution does not lead to the formation of spiro-MeOTAD $^{\bullet+}$ , as confirmed by UV–vis absorption measurements. This proves that the oxidation of spiro-MeOTAD is linked to the reduction of Co(III) to Co(II), as expected.

Monitoring the appearance of the absorption peak at 523 nm or the disappearance of the peak at 389 nm allows for the calculation of a Co(III)–to–spiro-MeOTAD $^{\bullet+}$  conversion yield. For the neutral spiro-MeOTAD molecule an average molar extinction coefficient of  $7.2 \times 10^4 \text{ l mol}^{-1} \text{ cm}^{-1}$ , was found—a value that is in good agreement with previously reported data [26]. From the disappearance of the peak at 389 nm I calculated conversion yields of 59%, 62% and 71% for the three different oxidants FK102, FK209 and FK269, respectively. However, this calculation might underestimate the conversion yield as it does not take into account any possible contribution from absorption by the reaction products, i.e. the spiro-MeOTAD $^{\bullet+}$  cation radical and the generated Co(II) complex at this wavelength. Therefore monitoring the appearance of the absorption band at 523 nm is preferred even though values for the extinction coefficient of spiro-MeOTAD $^{\bullet+}$  reported in the literature range from 2.7 to

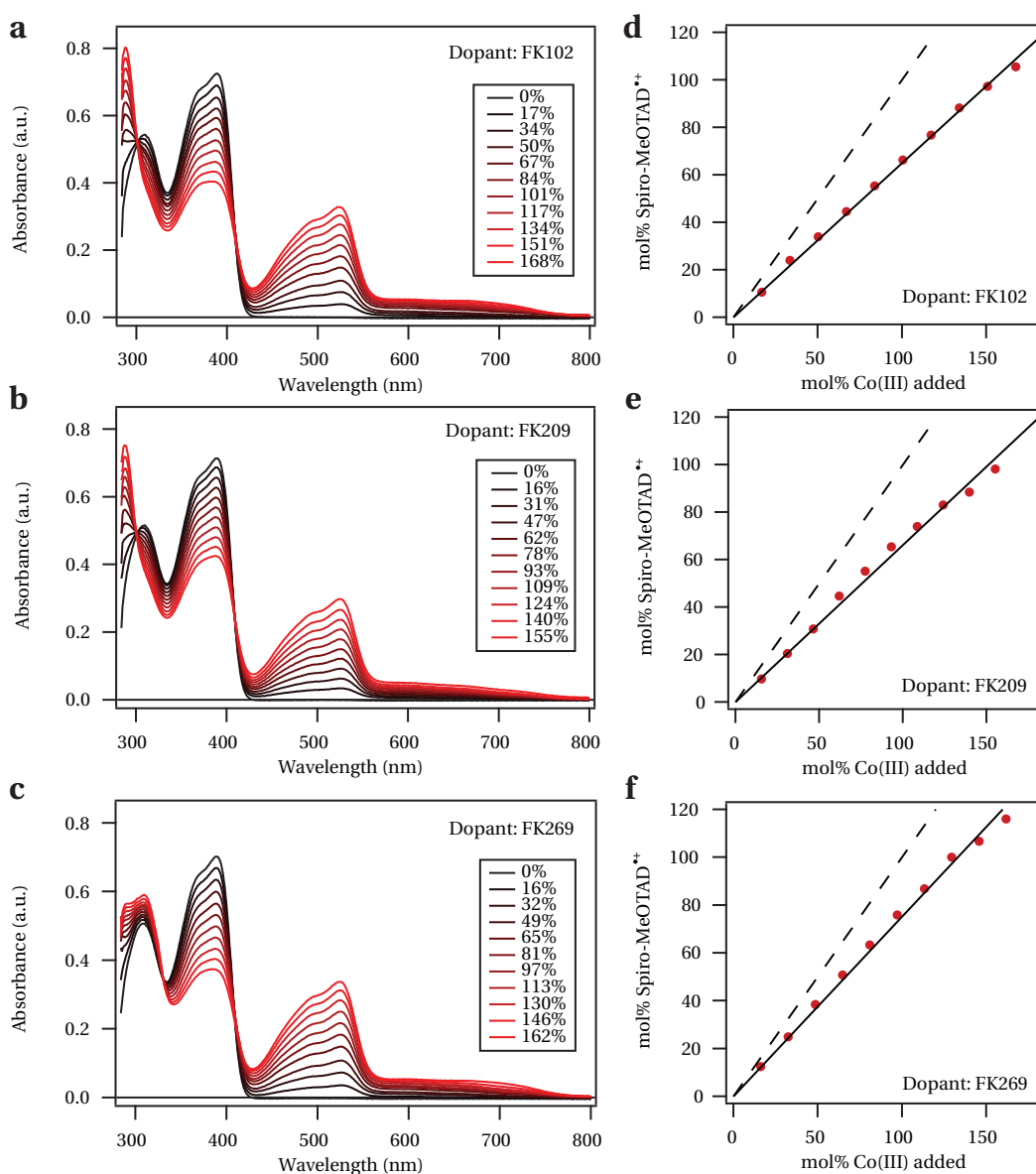


**Figure 2.14** — a-c) Change of the UV-vis absorption spectrum of a spiro-MeOTAD solution in chlorobenzene upon the gradual addition of either of the three dopants a) FK102, b) FK209 or c) FK269. The change in coloration from black to red corresponds to increasing Co(III) levels, with black being pure spiro-MeOTAD in chlorobenzene. Percentages given in the legend are the amount of Co(III) added to the solution in mol% relative to spiro-MeOTAD. d-f) Plots of the amount of oxidized spiro-MeOTAD (mol%) calculated from the absorbance at 523 nm using a molar extinction coefficient of  $3.4 \times 10^4 \text{ l mol}^{-1} \text{ cm}^{-1}$  vs. the amount of Co(III) added to the solution (mol%). Solid lines are linear fits, dashed lines indicate a theoretically expected conversion of 100%.

$4.1 \times 10^4 \text{ l mol}^{-1} \text{ cm}^{-1}$  [26, 35, 109]. Using an average value of  $3.4 \times 10^4 \text{ l mol}^{-1} \text{ cm}^{-1}$ , the conversion yields were estimated to be 65%, 68% and 78% for FK102, FK209 and FK269, respectively. The results indicate similar conversion yields for FK102 and FK209 and a significantly higher yield for FK269, a trend that can be rationalized by the difference in driving force for

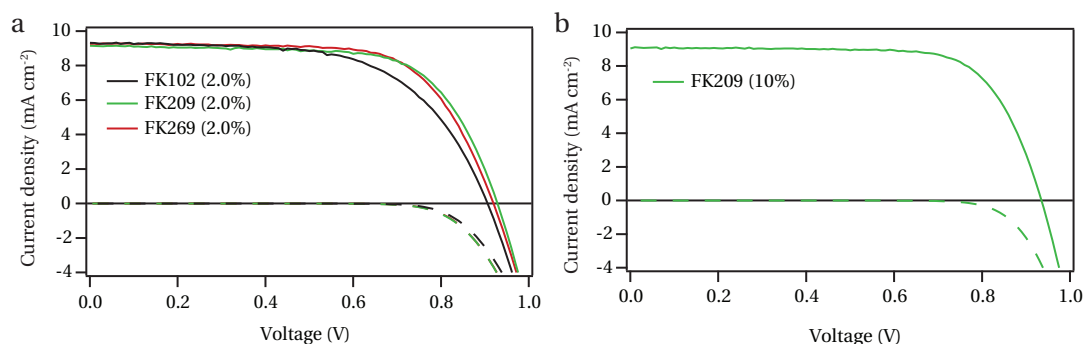


**Figure 2.15** — *J*-*V* Curves for photovoltaic devices based on the Y123 sensitizer and *p*-doped spiro-MeOTAD, measured under 100 mW cm<sup>-2</sup> simulated AM1.5G solar irradiance (solid line) and in the dark (dashed line). a) *J*-*V* Curves of devices containing different *p*-dopants FK102, FK209 and FK269 at a doping ratio of 2.0%. b) *J*-*V* Curve of a device doped at 10% using FK209.

the one-electron oxidation of spiro-MeOTAD, which is similar for FK102 and FK209, but much higher for FK269.

Overall, the findings suggest that the oxidation of spiro-MeOTAD using the proposed Co(III) complexes is an equilibrium reaction in solution, although the equilibrium constant is likely to be shifted for the doping of the solid-state hole-conductor. From the offset in redox potential I calculated equilibrium constants of  $3.3 \times 10^6$ ,  $2.7 \times 10^5$  and  $1.4 \times 10^{10}$  for FK102, FK209 and FK269, respectively. From these values one would expect a nearly quantitative reaction—contrary to the experimental findings. We attribute the discrepancy to uncertainties in the estimation of the redox potentials from the poorly reversible DPV polarograms and the extinction coefficient of spiro-MeOTAD<sup>•+</sup>.

#### 2.2.2.4 Influence of the type of dopant on PV performance

After the characterization of the two new Co(III) complexes FK209 and FK269, their beneficial influence on the photovoltaic device performance, especially compared to FK102, was established. Therefore solid-state dye-sensitized solar cells were fabricated using the organic D- $\pi$ -A sensitizer Y123 (cf. Section 1.5.4 and Figure 1.9) and spiro-MeOTAD as a HTM. *J*-*V* characteristics measured at 100 mW cm<sup>-2</sup> AM1.5G simulated solar irradiance for devices containing the three different dopants are shown in Figure 2.15 a. In all three cases 2.0% of dopant with respect to the molar concentration of spiro-MeOTAD was added to the spin-coating formulation. Photovoltaic parameters derived from the *J*-*V* characteristics are summarized in Table 2.2.

An undoped device that was fabricated under identical conditions, previously yielded values of 878 mV, 9.1 mA cm<sup>-2</sup> and 0.29 for  $V_{OC}$ ,  $J_{SC}$  and  $FF$ , respectively, corresponding to a *PCE* of 2.3% (Section 2.2.1.4). In the presence of the Co(III) complexes the  $FF$  increases to 0.62, 0.69 and 0.69, the  $V_{OC}$  to 896, 925 and 918 mV and the  $J_{SC}$  to 9.9, 9.4 and 9.6 mA cm<sup>-2</sup> for FK102,

## 2.3. Conclusion and perspective

**Table 2.2** — Photovoltaic parameters of *p*-doped devices derived from *J*–*V* measurements at 100 mW cm<sup>−2</sup> simulated AM1.5G irradiance.<sup>b</sup>

Doping level		Blank	FK102	FK209	FK269	FK209
		-	2.0%	2.0%	2.0%	10%
<i>V</i> <sub>OC</sub>	(mV)	878 <sup>a</sup>	896	925	918	941
<i>J</i> <sub>SC</sub>	(mA cm <sup>−2</sup> )	9.1 <sup>a</sup>	9.9	9.4	9.6	9.1
<i>FF</i>		0.29 <sup>a</sup>	0.62	0.69	0.69	0.73
<i>PCE</i>	(%)	2.3 <sup>a</sup>	5.5	6.0	6.0	6.2

<sup>a</sup> Values adapted from Section 2.2.1.4.

<sup>b</sup> The average and standard deviation of three devices is given for each condition.

FK209 and FK269, respectively, boosting the *PCE* to 5.5, 6.0 and 6.0% (Table 2.2). In general one would not expect the type of dopant to have an influence on the device performance when the same doping level is maintained. In this regard, the difference in *PCE* and mainly *FF* for devices doped with FK102 compared to FK209/FK269 is somewhat unexpected but is likely to arise from the difference in the nature of the counterion. On one hand, a strong influence on ssDSC performance has been reported for LiTFSI [33] and EMIM TFSI (EMIM = 1-ethyl-3-methylimidazolium) [110]. A more recent publication attributes this effect to the role of LiTFSI acting as a *p*-dopant in the presence of oxygen, its effect on charge-transport being negligible in the absence of oxygen [34]. On the other hand, the greatly enhanced solubility of FK209/FK269 compared to FK102 leads to a better dispersion of the remaining Co(II) complex in the spiro-MeOTAD matrix, enhancing charge transport within the HTM and avoiding the crystallization of the Co(II) salt during the solution-processing.

### 2.2.2.5 Investigation of high doping levels

To further support the benefit of FK209 over FK102 I also tested devices with much higher doping levels. Doping with 10% FK209, resulted in values of 941 mV, 9.1 mA cm<sup>−2</sup> and 0.73 for *V*<sub>OC</sub>, *J*<sub>SC</sub> and *FF*, yielding a *PCE* of 6.2%. The corresponding *J*–*V* curve is displayed in Figure 2.15 b. The increase of the doping level improves the *FF* and the *PCE*. It is important to note, that this efficiency is measured directly after device fabrication without the need of any additional ageing or light-soaking treatments.

## 2.3 Conclusion and perspective

In conclusion I presented a new class of Co(III) complexes as *p*-type dopants for triarylamine-based hole conductors such as spiro-MeOTAD and their application in ssDSCs. For this application, three different cobalt complexes were proposed and characterized by means of optical and electrochemical techniques. It was evidenced that the proposed compounds fulfill the necessary requirements for this application and that the discussed strategy is a promising tool to tune the conductivity of spiro-MeOTAD in ssDSCs, without having to rely on

the commonly employed photo-doping. Hereby the exact same trends of  $V_{OC}$ ,  $J_{SC}$ ,  $FF$  and  $PCE$  for different levels of chemical doping or photo-doping were observed, suggesting that both strategies have the same effects.

Using the first generation dopant FK102, a record power conversion efficiency of 7.2% was obtained after ageing under dark. Furthermore, preliminary reliability data showed, that the addition of a *p*-dopant is not harmful for the long-term stability of these devices, as 80% of the initial device performance could be maintained over a period of 40 days. One of the main drawbacks of the FK102 dopant was its rather low solubility in organic solvents, hampering the investigation of high doping concentrations.

Therefore we designed two new complexes having a much higher solubility in organic solvents. This was achieved by modifying the ligands and the counterion of the Co(III) complex. The high solubility of the second generation dopants FK209 and FK269 enabled doping levels of more than 10% and finally a  $PCE$  of up to 6.2% without any ageing. Moreover, the FK269 complex exhibits a higher oxidation potential, which helped to increase the Co(III)-to-spiro-MeOTAD<sup>+</sup> conversion yield and which also makes it more attractive for a larger number of host materials.

This data clearly shows the benefit and potential of these new dopants that we expect to find widespread application in organic electronic devices based on triarylamine-based semiconductors. Future studies should focus more on the optimization of the doping level as well as a device fabrication under inert atmosphere as the new dopants presented herein have the potential to obviate the necessity of any oxygen-induced doping for an efficient device functioning.

## 3 9,9'-spirobifluorene based hole-transporters for ssDSC applications

*This chapter presents a series of new triarylamine hole-conductors based on 9,9'-spirobifluorene and their application in solid-state dye-sensitized solar cells. All new materials presented in this chapter have been synthesized by Dr. Tom Holcombe, LPI, EPFL.*

### 3.1 Introduction

The hole-transporting material (HTM) is one of the key components of a solid-state dye-sensitized solar cell (ssDSC). The main task of the HTM is to reduce oxidized dye molecules after the excitation and the subsequent electron injection into the conduction band of the metal oxide semiconductor. Moreover, the HTM is responsible for transporting holes away from the sensitized junction to the back contact. In order to fulfill these requirements, the HTM has to be in close proximity to the sensitizer and infiltrate the mesoporous metal oxide scaffold as much as possible. The following introductory paragraph aims at providing a detailed overview of the various approaches that have been reported in order to select a material for its use as the HTM in ssDSCs. In general, the HTMs that have been employed in ssDSCs can be divided into two main categories: organic and inorganic hole transporting materials.

#### 3.1.1 Inorganic *p*-type semiconductors

The general motivation for the use of inorganic HTMs, is their potentially better long-term stability compared to organic HTMs as the latter are often prone to photodegradation. Another advantage of inorganic semiconductors is their charge-carrier mobility that is usually orders of magnitude higher. This results from the three dimensional crystal structure that enables better charge transport compared to organic semiconductors, which in most cases are amorphous and where carrier transport occurs via hopping between strongly localized electronic states.

However, the development of inorganic hole-conductor-based ssDSCs is hindered by the limited availability of solution-processable wide-bandgap inorganic *p*-type semiconductors.

In this manner only CuI and CuSCN yielded reasonable PCEs of up to 4.7% [24] and 3.4% [111, 112], respectively, in ssDSCs. CuI and CuSCN have bandgaps of 3.1 and 3.6 eV, respectively, and therefore do not compete with the sensitizer for light-harvesting. Both materials exhibit reasonable solubility and can be processed from acetonitrile or dipropyl sulfide solution [113]. The main drawback, however, is their uncontrolled crystallization during the solution-processing, preventing intimate contact with the sensitized metal oxide structure. This usually requires the addition of a crystal-growth inhibitor, such as 1-methyl-3-ethylimidazolium thiocyanate [114] or triethylammonium thiocyanate [115], which not only hinders the formation of large crystallites, but also might hamper charge transport. Apart from that, severe stability issues with CuI-based ssDSCs have been reported [116]. More recently, Chung et al. [117] studied the use of a solution-processable inorganic metal halide perovskite, CsSnI<sub>3</sub>, as a hole-conductor and reached a *PCE* of 8.5%. In this device, the material has been employed in combination with a molecular ruthenium-based sensitizer. However, the true origin of photogenerated charge carriers remained unclear, as the perovskite itself is strongly absorbing in the visible range and might contribute to photocurrent generation.

#### 3.1.2 Organic *p*-type semiconductors

In contrast to only a few existing inorganic solution-processable semiconductors, there is an almost unlimited number of organic *p*-type semiconductors available, that have primarily been developed for their application in organic electronic devices, such as light-emitting diodes (LEDs), field-effect transistors (FETs) or solar cells. In general, both molecular and polymeric *p*-type semiconductors have been investigated for their application as HTMs in ssDSCs.

**Polymeric *p*-type semiconductors.** The use of conducting polymers as HTMs in ssDSCs has mainly been inspired by classical organic bulk-heterojunction solar cells, where *p*-type conducting polymers are used for both light absorption and charge carrier transport. Poly(3-hexylthiophen-2,5-diyl) (P3HT) and poly[2,6-(4,4-bis-(2-ethylhexyl)-4*H*-cyclopenta[2,1-*b*;3,4-*b'*]dithiophene)-*alt*-4,7-(2,1,3-benzothiadiazole)] (PCPDTBT) are two very prominent examples. Their structures are depicted in Figure 3.1. Both materials have also been studied as HTMs in ssDSCs, reaching power conversion efficiencies up to 3.9% with P3HT and a molecular dye [61, 118, 119]. Higher *PCEs* could be obtained when the molecular sensitizer was replaced by inorganic pigments such as Sb<sub>2</sub>S<sub>3</sub> [139, 140] or CH<sub>3</sub>NH<sub>3</sub>PbI<sub>3</sub> [141]. The use of inorganic pigments in ssDSCs will be discussed in more detail at the beginning of Chapter 4.

Depending on the choice of the sensitizer and the device architecture, strongly absorbing polymers such as P3HT or PCPDTBT can act simultaneously as hole-conductor and light absorber. However, the efficient generation of free charge carriers at the TiO<sub>2</sub>/polymer heterojunction is usually not observed. The exact reason of this phenomenon is still poorly understood, but seems to be related to an unfavourable interaction between the polymer and TiO<sub>2</sub> [142, 143]. One possibility to overcome this problem is to modify the interface through



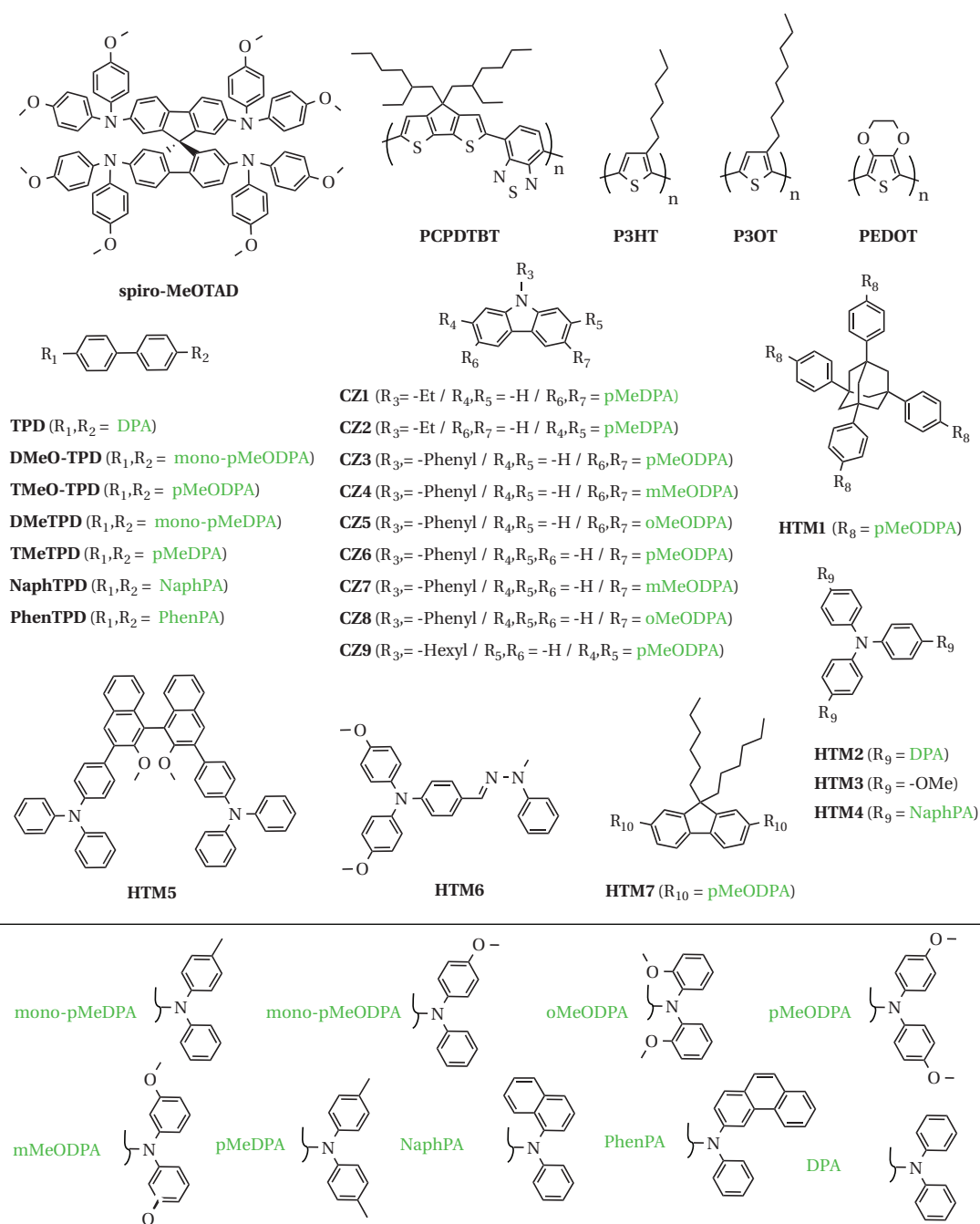


**Figure 3.1** — Structures of organic hole-transporting materials that have been used for ssDSCs. The corresponding references are: P3HT [61, 118, 119]; POPT [120, 121]; PCPDTBT [122]; PEDOT [123–127]; CZ1, CZ2 [128]; CZ3, CZ6 [129]; CZ4, CZ5, CZ7, CZ8 [130]; CZ9, HTM7 [131]; HTM1 [132]; HTM5 [133]; DMeTPD, TMeTPD, NaphTPD, PhenTPD [47]; TMeO-TPD [47, 134]; HTM6 [135]; TPD [47, 136]; HTM2 [136, 137]; HTM4 [47, 136]; HTM3 [138]; DMeO-TPD [52].

the adsorption of functional molecules on the metal oxide surface [122], e.g. a strong electron acceptor like [6,6]-phenyl- $\text{C}_{61}$ -butyric acid methyl ester—commonly known as PCBM. An-

other possibility is to properly tune the polymer and the sensitizer together in order to allow for light-harvesting via energy transfer. In the latter case, the photoexcitation of the polymer is followed by a resonant energy transfer from the polymer to the molecular sensitizer that is anchored to the  $\text{TiO}_2$  and capable of injecting electrons into the  $\text{TiO}_2$  conduction band (cf. Section 3.1.3.4). This concept has been proved several times in the literature, although the overall *PCE* remained relatively low ( $< 2.0\%$ ) [65, 144].

One of the major problems when using a polymer as the HTM is the infiltration of the rather large polymer chains into the nanoporous metal oxide structure. The in situ polymerization of the monomer within the pores of the metal oxide host has been proposed as a reasonable approach to overcome this issue. Yanagida et al. pioneered the use of electropolymerization and—more recently—photoelectropolymerization for the deposition of polypyrrole [145] or poly(3,4-ethylenedioxythiophene) (PEDOT) [146, 147]. Following these initial works, power conversion efficiencies as high as 7.1% could be achieved using photoelectropolymerized PEDOT [148]. In a similar manner, Kim et al. reported on the use of a heat-induced radical polymerization to polymerize the brominated 3,4-ethylenedioxythiophene monomer inside the mesoporous  $\text{TiO}_2$ , reaching a *PCE* of 6.8% [127].

**Molecular *p*-type semiconductors.** Extensive studies have been carried out on the use of molecular *p*-type semiconductors. Hagen et al. pioneered the use of triarylamine derivatives as HTMs in ssDSC by using thermally evaporated *N,N'*-bis(4-methoxyphenyl)-*N,N'*-diphenyl-[1,1'-biphenyl]-4,4'-diamine (DMeO-TPD) as the hole-conductor and reported a *PCE* of 0.2% [52]. The structure of DMeO-TPD is depicted in Figure 3.1. The breakthrough, however, occurred through the use of a solution-processable triarylamine derivative, 2,2',7,7'-tetrakis(*N,N*-di-*p*-methoxyphenyl-amine)-9,9'-spirobifluorene (spiro-MeOTAD, Figure 3.1). In 1998 Bach et al. were the first to report on the use of spiro-MeOTAD in ssDSCs, reaching a *PCE* of 0.7% [25]. Over the past decade the efficiency of this system was improved up to 7.2% (Section 1.5.4)—an achievement that can mainly be attributed to the development of new sensitizers with a broader absorption spectrum and/or higher molar extinction coefficient. Since the early days of ssDSCs no alternative that can compete with spiro-MeOTAD has been reported, although a variety of triarylamine-based molecular hole-conductors were investigated. In this regard, it is interesting to note that besides a few exceptions, e.g. pentacene [149], all materials that have been employed so far rely on triarylamine as the hole-transporting unit. An overview of the HTMs that have been used in ssDSCs so far is given in Figure 3.1.

In order to answer the question as to why no HTMs that can compete with spiro-MeOTAD have been found and in order to be able to develop efficient alternatives, the general requirements of the HTM in a ssDSC need to be identified.

### 3.1.3 Basic requirements for the HTM in ssDSCs

#### 3.1.3.1 Semiconducting properties

The basic function of the HTM in a DSC is to efficiently regenerate the oxidized sensitizer that underwent photoexcitation and injected an electron into the metal oxide conduction band. Moreover, after the electron transfer from the HTM to the oxidized dye or rather hole transfer from the oxidized dye to the HTM, the holes should quickly move away from the interface, in order to prevent the undesired back reaction, i.e. the recombination between them and electrons in the metal oxide (cf. Section 1.3). In comparison to conventional liquid DSCs, the interfacial recombination is about 100 times faster in spiro-MeOTAD based ssDSCs [150]. This leads to rather short electron diffusion lengths in the metal oxide semiconductor, limiting the total device thickness. Therefore, the optimal thickness of the mesoporous metal oxide lies in the range of 2–3  $\mu\text{m}$ —in contrast to liquid DSCs, where film thicknesses  $> 10 \mu\text{m}$  are common. The rate of the interfacial recombination strongly depends on the choice of the metal oxide and/or the HTM and is a property of the interface that is not easy to predict. However, it can be influenced by molecular engineering of the sensitizer [42–44, 151] or through a modification of the metal oxide surface. The latter can, for example, be achieved by coating the surface of the mesoporous semiconductor with a thin film of an insulating metal oxide such as  $\text{Al}_2\text{O}_3$ ,  $\text{ZrO}_2$  or  $\text{MgO}$  [15, 20, 22], or tailored through the adsorption of functional molecules [30].

The fundamental requirement for the hole injection to happen efficiently, is that the highest occupied molecular orbital (HOMO) level of the HTM must be lying energetically above the HOMO level of the sensitizer (cf. energy scheme in Section 1.3). The minimum driving force that is necessary for an efficient oxidized dye regeneration has not been determined in an ssDSC configuration so far—mainly due to lack of suitable HTMs with different HOMO levels—but has been found to be around 0.2 eV in liquid DSCs [97, 152]. Suitable energy levels, however, are not the only requirement for an efficient charge transfer, as the charge transfer might as well be hindered by unfavorable interaction between the two species (e.g. due to poor orbital overlap). The influence of a certain ‘chemical compatibility’ between spiro-MeOTAD and a series of dyes has recently been investigated by Kwon et al. [51]

Besides these energetic requirements, the HTM should exhibit good *p*-type conductivity in order to minimize the charge transport resistance in the bulk. Moreover, a high hole mobility is required to allow for a fast migration of holes away from the sensitized metal oxide surface. For spiro-MeOTAD hole mobilities on the order of  $1 \times 10^{-5}$  to  $1 \times 10^{-4} \text{ cm}^2 \text{ V}^{-1} \text{ s}^{-1}$  have been reported [33, 131, 153–155], which is within the typical range for disordered triarylamine-based organic semiconductors. In contrast, the conductivity of spiro-MeOTAD strongly depends on the charge carrier density and is very low for the pristine material. However, it can be influenced through the addition of ionic additives (cf. Section 1.5.3), the addition of chemical *p*-dopants or photo-doping, i.e. the photo-induced oxidation of spiro-MeOTAD by oxygen. The *p*-doping of spiro-MeOTAD and its influence on conductivity are discussed in detail in Chapter 2. The introductory section of Chapter 2 also gives a detailed explanation about the

relation between conductivity and charge carrier mobility. The importance of conductivity and mobility for an efficient functioning of the device has recently been investigated by Leijtens et al. [154] The charge carrier mobility of spiro-MeOTAD seems to be the crucial factor that limits the optimum thickness of ssDSCs, which makes it desirable to develop HTMs with a higher hole mobility.

#### 3.1.3.2 Processability and pore infiltration

The deposition of the hole transporting material and its infiltration into the porous network of the sensitized metal oxide is one of the most critical steps during cell fabrication. Spiro-MeOTAD is usually deposited by spin-coating a solution of 180–220 mg ml<sup>-1</sup> in chlorobenzene. Snaith et al. have explained in detail the process of pore-filling and solvent evaporation during the spin-coating procedure [156]. Briefly, upon the deposition of the HTM solution on the substrate, the solution infiltrates the pores of the metal oxide by capillary forces and forms an additional reservoir on top of the mesoporous structure. During the spinning, the solvent starts to evaporate, leading to an increase in solution concentration in the reservoir and the diffusion of additional spiro-MeOTAD molecules into the pores. At a certain point, spiro-MeOTAD starts to precipitate which finally limits the total amount of spiro-MeOTAD in the pores and results in the formation of a capping layer on top of the mesoporous structure.

The pore-filling fraction (*PFF*), i.e. the volume fraction of spiro-MeOTAD in the pores of the metal oxide semiconductor, achieved by this technique, has been measured to be around 60%, referring to the total pore volume [156, 157]. Several methods have been developed to determine the *PFF* in a ssDSC. The value of 60% seems to lie just above the threshold to achieve good cell performance, although the *PCE* is expected to improve further, if the *PFF* can be increased [158, 159]. The pore infiltration becomes even more of a problem when using a polymeric HTM. It has been shown that the pore infiltration strongly depends on the average molecular weight of the polymer [160, 161]. The *PFF* of a P3HT/TiO<sub>2</sub> composite has been determined to be around 6–24%, although this value was sufficient for an efficient charge collection [162]. One strategy to improve the *PFF* is to anneal the sample above the glass transition temperature or even the melting point of the HTM after its deposition. Numerous reports have shown that annealing helps to significantly increase the *PFF*, e.g. in the case of P3HT [161, 163], although the effect on device performance has not been investigated so far. Another strategy that has been proposed to increase the *PFF* is the solvent-free melt-infiltration of molecular HTMs [135, 137].

Besides the aforementioned pore-filling, good pore-wetting, i.e. the wetting of the sensitized metal oxide film with the HTM solution, is equally important to achieve high filling fractions [43, 164]. Whereas the pore-filling depends mainly on the solubility of the HTM in the chosen solvent as well as the volatility of this solvent during the spin-coating, the pore-wetting is expected to be influenced by the difference in hydrophobicity between the sensitized semiconductor's surface and the HTM solution.

### 3.1.3.3 Morphology

Concerning its solid-state morphology, the hole transporting material should preferably form an amorphous phase in order to assure good pore-filling and contact with the sensitized semiconductor. Although partial crystallization of organic semiconductors often helps to increase the electrical conductivity and charge carrier mobility of the material, the complete amorphous state is expected to be a key parameter for the application in ssDSCs. Crystallization of the material within the pores would prevent good interaction with the sensitizer due to the formation of grain boundaries in the bulk HTM and/or volume shrinkage. As mentioned in Section 3.1.1, the growth of large crystals has been found to influence the device performance, for example when using CuI or CuSCN as HTM.

After the deposition the HTM should remain stable in its amorphous state—a property that is practically achieved by choosing materials with high glass transition temperatures. In 1996 Salbeck et al. introduced the spiro concept in order to enhance the thermal and morphological stability of known organic hole-conductors, while maintaining their electronic properties [165]. Due to the spiro linkage, there is only little interaction between the two orthogonally oriented moieties. However, doubling of the molar mass and the hindrance of molecular packaging significantly increase the glass transition temperature and melting point of the material. Therefore, spiro compounds constitute a valuable class of materials for the application in ssDSCs. In case of spiro-MeOTAD, the values for glass transition temperature and melting point are 121°C and 246°C, respectively [101].

### 3.1.3.4 Optical properties

Two different strategies can be envisaged with respect to the optical properties of the HTM in an ssDSC. On one hand, the HTM can be chosen as colorless (such as spiro-MeOTAD), so that it does not compete with the sensitizer for light absorption. In this case, the HTM is only responsible for transporting charges and needs to be combined with a panchromatic sensitizer in order to maximize light-harvesting and photocurrent generation. The second approach is to employ a colored HTM that absorbs light in a region complementary to the sensitizer and that, at the same time, efficiently transfers its excitation energy to the latter. This concept has been reported and described in the literature by combining poly(3-hexylthiophene) (P3HT) as HTM and a near-IR absorbing squaraine or phthalocyanine dye as sensitizer [65, 144], where the energy transfer between the two compounds occurs via non-radiative Förster Resonance Energy Transfer (FRET). The efficiency of the FRET mainly depends on two parameters: the distance between both compounds and the overlap between the emission spectrum of the donor species (HTM) and the absorption spectrum of the acceptor species (dye). Due to the confinement of the HTM in nanometer-sized pores and the close proximity to the sensitizer, FRET is a promising concept for ssDSCs—if suitable materials can be found.

### 3.1.3.5 Stability

The long-term stability of solid-state DSCs is still an issue and stable photovoltaic devices of this type have rarely been reported, although the various components of the ssDSC are not expected to be unstable upon prolonged light exposure or thermal stress. One major problem that leads to a decrease of photovoltaic performance over time is likely to be the facile oxidation of spiro-MeOTAD through molecular oxygen and light, so-called photo-doping (cf. Section 2.1.2). However, photo-doping is necessary to some extent for a good cell performance, unless the spiro-MeOTAD is chemically *p*-doped. More detailed studies that investigate the photo-doping and its necessity for an efficient functioning of the device have been reported recently [34, 35].

### 3.1.4 Motivation and strategy

As is evident from the discussion presented above, finding an alternative to spiro-MeOTAD is not an easy task. Our strategy was to maintain the advantageous properties of spiro-MeOTAD such as a good solubility, amorphous nature and transparency in the visible region of the spectrum. At the same time we aimed at introducing small structural changes to the HTM in order to be able to elaborate a structure-property relationship. A basic question that we sought an answer for, was the influence of the different substituents on the triaryamine units on the charge transport properties and processability of the HTM. Besides that, our main goal was to design a material that exhibits better ambient stability and is less prone to photo-oxidation. To achieve this, we aimed at lowering the HOMO level of HTM by changing the substituents on the triarylamine units. Besides enhanced stability, a lower HOMO level should also lead to a higher  $V_{OC}$  as the latter is determined by the energy difference between the quasi Fermi level in the  $\text{TiO}_2$  and the HOMO level of the HTM.

## 3.2 Results and discussion

### 3.2.1 Design of new 9,9'-spirobifluorene based HTMs

In total seven new 9,9'-spirobifluorene derivatives were synthesized. Their molecular structures are presented in Figure 3.2. The main reason why spiro-MeOTAD has a relatively high HOMO level (i.e. low oxidation potential) is the electron-donating mesomeric effect of the methoxy substituents in the *para* position to the electron-rich nitrogen. Therefore, a removal of the methoxy groups stabilizes the HOMO level by about 0.12 eV, as has been shown previously [101]. However, we suspected the methoxy groups to be necessary for a good solubility of the material and preferred not to remove them, but rather shift them from the *para* to the *meta* position, i.e. out of resonance with the nitrogen atoms. The corresponding compound has been synthesized and is denoted as spiro-m-MeO. For further comparison we decided to synthesize the compound spiro-3,5-MeO that has methoxy groups on both *meta* positions.

The second idea was to replace the methoxy group in the *para* position by a group that is a weaker electron donor. A methyl group would be the simplest modification, but surprisingly it has been found that this substitution leads to an even lower oxidation potential [101]. We then chose spiro-p-tBut bearing a *tert*-butyl group in the *para* position to be of interest. This compound was successfully synthesized, but exhibited a very low solubility, rendering solution-processing impossible. Spiro-p-tBut was therefore not further investigated. On the contrary, the compound bearing *tert*-butyl groups in both *meta* positions, denoted as spiro-3,5-tBut, exhibited a greater solubility. Finally, we decided to investigate an unsymmetrically substituted molecule and synthesized the compound denoted as spiro-3,5-mixed that represents a combination of spiro-3,5-MeO and spiro-3,5-tBut.

With the exception of spiro-p-tBut, all above-mentioned materials follow the same strategy, i.e. removing the electron-rich methoxy groups from the *para* position. However, Zhao et al. proposed dimerization to be one of the main degradation pathways of triarylamine-based hole-conductors [166]. As the dimerization would preferentially occur in the *para* position, it might be necessary to chemically block this position or at least shield it with sterically demanding *meta*-substituents. Therefore we thought of designing an HTM that has a lower HOMO level compared to spiro-MeOTAD while keeping the *para*-methoxy substituents. We proposed spiro-MeO-TPA, which comprises an additional phenyl ring between the 9,9'-spirobifluorene core and the amine, to fulfill these requirements. Spiro-MeO-TPA is expected to exhibit a higher oxidation potential compared to spiro-MeOTAD due to the extended  $\pi$ -conjugation that is likely to stabilize the HOMO level.

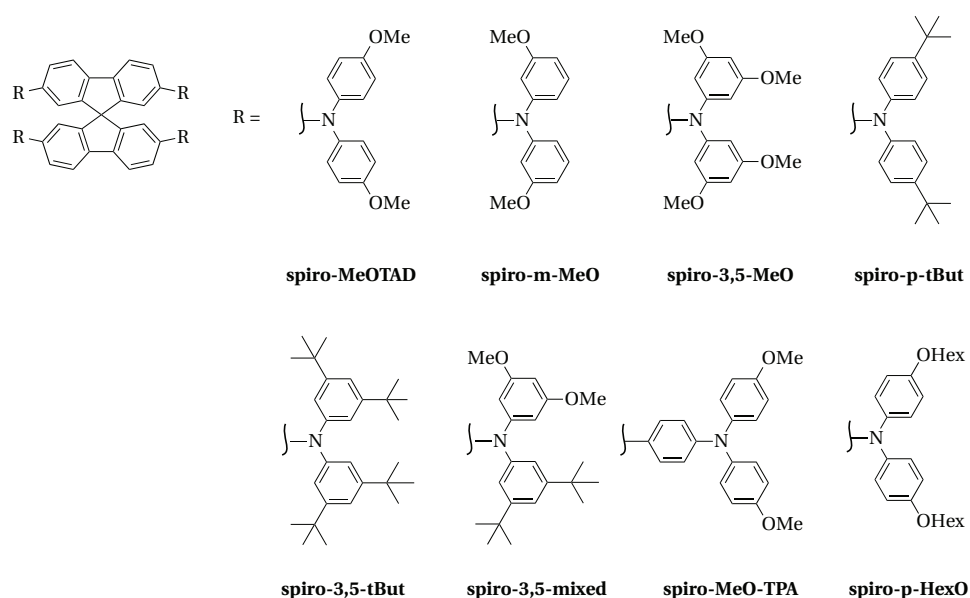


**Figure 3.2** — Molecular structures of the conventional hole-conductor spiro-MeOTAD and the new 9,9'-spirobifluorene derivatives discussed herein. Me = Methyl, Hex = *n*-Hexyl



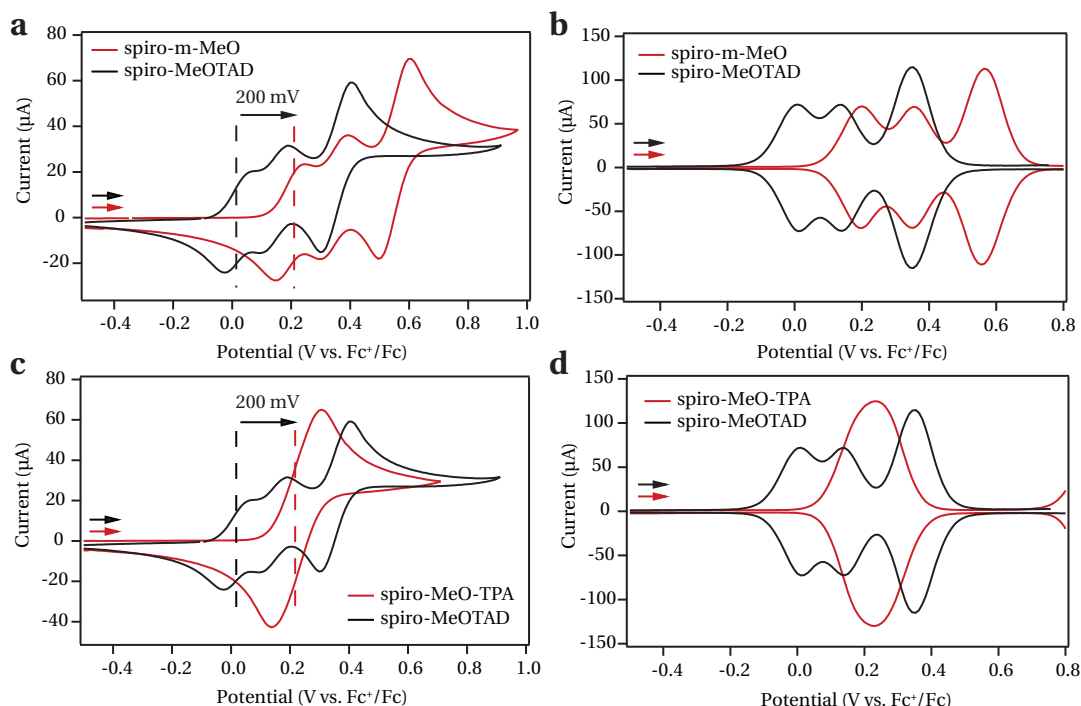


**Figure 3.3** — Electrochemical characterization of a, b) spiro-m-MeO and c, d) spiro-MeO-TPA using a, c) cyclic voltammetry and (b, d) differential pulse voltammetry in dichloromethane solution. 0.1 M tetrabutylammonium hexafluorophosphate has been added as a conduction salt. The applied potential was internally references vs. the  $\text{Fc}^+/\text{Fc}$  standard. CV and DPV curves of spiro-MeOTAD are shown for comparison.

A completely different approach has been realized with the compound spiro-p-HexO, where we replaced the methoxy groups by long *n*-hexyloxy chains. This modification is expected to have only a little effect on the energy levels of the material, but a possible steric influence in the ssDSC by keeping the HTM molecules at distance from the sensitized  $\text{TiO}_2$  surface.

All new materials mentioned above, were synthesized and purified as described in the experimental section (Section 6.1.1). In order to remove traces of palladium that is used as a catalyst during the synthesis and that might remain in the final materials as an impurity, functionalized polystyrene beads were employed as a metal scavenger. The effect of this purification treatment will be discussed in detail in Section 3.2.5. The results presented in this chapter have been obtained using the purified materials, unless stated otherwise.

### 3.2.2 Electrochemical characterization

Having synthesized the new materials, the first step was to characterize their electrochemical properties in order to confirm the lowering of the HOMO level.



### 3.2.2.1 Electrochemical measurements in solution

Electrochemical measurements were performed in dichloromethane solution containing 0.1 mol l<sup>-1</sup> tetrabutylammonium hexafluorophosphate as a supporting electrolyte. In all cases, the applied potential was internally referenced vs. the Fc<sup>+</sup>/Fc redox couple. Further experimental details can be found in the experimental section (Section 6.3). Oxidation potentials were extracted from differential pulse voltammetry (DPV) and confirmed by cyclic voltammetry (CV) measurements and averaged. To convert the obtained redox potentials to the vacuum scale, a value of -5.1 eV for the Fc<sup>+</sup>/Fc standard has been used.

For all materials—except spiro-3,5-MeO and spiro-MeO-TPA—three completely reversible oxidation/reduction waves were found, that correspond to the first, second and third/-fourth oxidation state of the molecule and that arise from the four triarylamine units. This is in agreement with what had previously been found for spiro-MeOTAD (Section 2.2.1.1). The results from the CV and DPV measurements are exemplary shown for spiro-m-MeO in Figure 3.3 a, b. Similar curves are also obtained for spiro-p-HexO, spiro-3,5-mixed and spiro-3,5-tBut. For spiro-3,5-MeO three distinct oxidation/reduction waves can be observed, but the cyclic voltammogram is not fully reversible and a clear DPV polarogramm could not be obtained. The voltammograms of spiro-p-HexO, spiro-3,5-mixed, spiro-3,5-tBut and spiro-3,5-MeO can be found in the Appendix (Figure A1). Concerning spiro-MeO-TPA, a single oxidation/reduction wave is obtained by both CV and DPV (Figure 3.3 c, d), suggesting that all four triarylamine units can be oxidized independently and therefore possess the same redox potential. This indicates that there is no electronic communication between the redox active units. Similar results have been obtained by Zhang et al. for an HTM that consists of four triarylamine units that are connected via an adamantane core (HTM1, Figure 3.1) [132]. Whereas the saturated adamantane core clearly separates the four triarylamine units from each other, electronic communication through the conjugated  $\pi$ -system of the 9,9'-spirobifluorene core would still be expected. A possible explanation is that the conjugation between the triarylamine units is interrupted due to the spatial configuration of the molecule. The electrochemical results also suggest that the triarylamine units are sufficiently far from each other so that there is no—or only little—electrostatic interaction between neighboring redox centers. The distance between the nitrogen atoms of two adjacent triarylamine units in spiro-MeO-TPA is about twice as large as in spiro-MeOTAD. According to Coulomb's law, this leads to a four-fold reduction in the electrostatic forces. The electrochemical properties of spiro-MeO-TPA might be interesting for solar cell applications, as the dismutation of spiro-MeOTAD (the reaction between two spiro-MeOTAD<sup>+</sup> molecules to yield spiro-MeOTAD<sup>0</sup> and spiro-MeOTAD<sup>2+</sup>) has been proposed as one of the possible degradation mechanisms.

The oxidation potentials of all six molecules that have been derived from CV and DPV measurements are summarized in Table 3.1. In agreement with our expectations, the displacement of the methoxy group from the *para* to the *meta* position stabilizes the HOMO level and increases the first oxidation potential by about 200 mV from 0.02 to 0.20 V vs. Fc<sup>+</sup>/Fc. The same trend is also observed for the second and third/fourth oxidation potential that shifts from 0.14 and

### Chapter 3. 9,9'-spirobifluorene based hole-transporters for ssDSC applications

**Table 3.1** — Redox potentials of the different HTMs derived from electrochemical measurements in solution.

Compound	$E_{ox}^1$	$E_{ox}^2$	$E_{ox}^{3/4}$
	V vs. $Fc^+/Fc$	V vs. $Fc^+/Fc$	V vs. $Fc^+/Fc$
spiro-MeOTAD	0.02	0.14	0.35
spiro-m-MeO	0.20	0.35	0.55
spiro-MeO-TPA	0.23	-	-
spiro-p-HexO	0.00	0.13	0.33
spiro-3,5-mixed	0.10	0.28	0.54
spiro-3,5-MeO	0.23	0.37	0.57
spiro-3,5-tBut	0.01	0.23	0.54

0.35 to 0.35 and 0.55 V vs.  $Fc^+/Fc$ , respectively. Likewise, an increase in oxidation potential by about 200 mV is observed for the introduction of an additional phenyl ring between the amine and the 9,9'-spirobifluorene core (spiro-MeO-TPA), resulting in a redox potential of 0.23 V vs.  $Fc^+/Fc$ . As expected, the substitution of the methoxy groups by hexyloxy groups does not change the oxidation potential dramatically. A small shift of about 20 mV towards less positive potentials is observed for spiro-p-HexO compared to spiro-MeOTAD, which can be rationalized by the slightly stronger electron-donating inductive effect of the longer alkyl chains. For the compound bearing a methoxy group in both *meta* positions (spiro-3,5-MeO) very similar redox properties were found as in the case of only one *meta*-methoxy group. The dominant effect of the methoxy group in the *meta* position is an electron-withdrawing inductive effect that stabilizes the HOMO level. Therefore, a small shift of about 20 mV towards more positive potential is observed for all four oxidation states when moving from one *meta*-methoxy to two *meta*-methoxy groups. In contrast to that, replacing methoxy by *tert*-butyl destabilizes the HOMO level due to the electron-donating inductive effect of the *tert*-butyl group. This is reflected in the redox properties of spiro-3,5-MeO, spiro-3,5-mixed and spiro-3,5-tBut as the first oxidation potential shifts from 0.01 to 0.10 and 0.23 V vs.  $Fc^+/Fc$  upon the gradual replacement of the methoxy groups in the *meta* positions by *tert*-butyl groups. The same trend is observed for the second oxidation potentials that lie at 0.23, 0.28 and 0.37 V vs.  $Fc^+/Fc$  for spiro-3,5-MeO, spiro-3,5-mixed and spiro-3,5-tBut, respectively, although the difference between the oxidation potentials is much smaller. Surprisingly, this difference becomes even smaller for the third/fourth oxidation state having oxidation potentials of 0.54, 0.54 and 0.57 V vs.  $Fc^+/Fc$  for spiro-3,5-MeO, spiro-3,5-mixed and spiro-3,5-tBut, respectively. In general, the shifts in redox potentials induced by the different substituents can be very well explained by their electronic effects. This is in good agreement with the findings of Bender et al. who studied the influence of a variety of substituents on the electrochemical properties of triphenylamine [167].

A graphical summary of the electrochemical properties of all compounds is given in Figure 3.4. For better clarity all values obtained from the electrochemical measurements

were converted to the vacuum scale using a conversion factor of  $-5.1$  eV for the  $\text{Fc}^+/\text{Fc}$  standard. For comparison, oxidation potentials of the three dopants FK102, FK209 and FK269 as well the two most commonly used dyes C220 and Y123 are included as well. From this comparison, it becomes clear that all three dopants exhibit a sufficiently large energy offset for the one-electron oxidation of the six new HTMs. Furthermore, the graphical representation shows that spiro-m-MeO, spiro-MeO-TPA and spiro-3,5-MeO are not able to regenerate the C220 dye as their redox potentials lie energetically below the HOMO level of this dye. However, the regeneration should be possible in the case of Y123 for all materials, although the energetic offset might be too small for the hole injection to happen efficiently.

### 3.2.2.2 Photoelectron spectroscopy in air (PESA)

In order to further investigate the position of the HOMO level of the different materials, photoelectron spectroscopy measurements were performed. Photoelectron spectroscopy in air (PESA) is a powerful technique that gives a straightforward access to the ionization

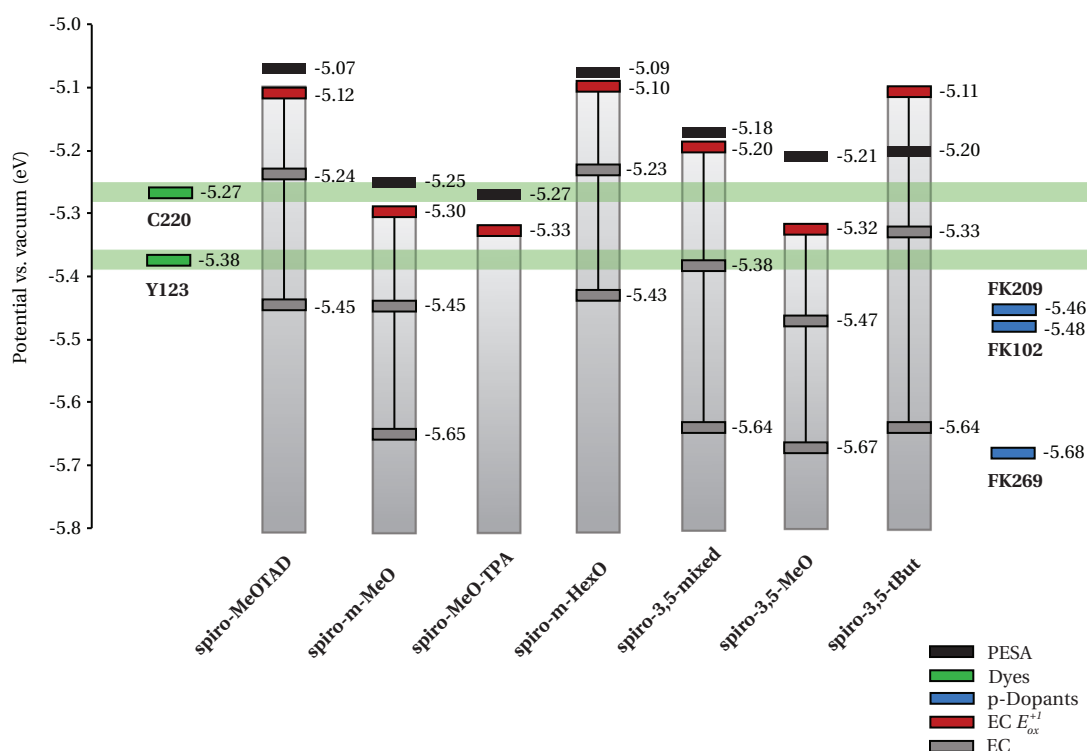


**Figure 3.4** — Summary of the electrochemical properties of all newly synthesized HTMs and spiro-MeOTAD derived from electrochemical measurements in solution (EC) and photoelectron spectroscopy in air (PESA). Redox potentials obtained from measurements in solution have been converted to the vacuum scale using a conversion factor of  $-5.1$  eV for the  $\text{Fc}^+/\text{Fc}$  standard. The first oxidation potentials ( $E_{ox}^{+1}$ ) are marked in red. The HOMO levels of the dyes Y123 and C220 as well as the redox potentials of the Co(III) dopants FK102, FK209 and FK269 have been added for comparison.

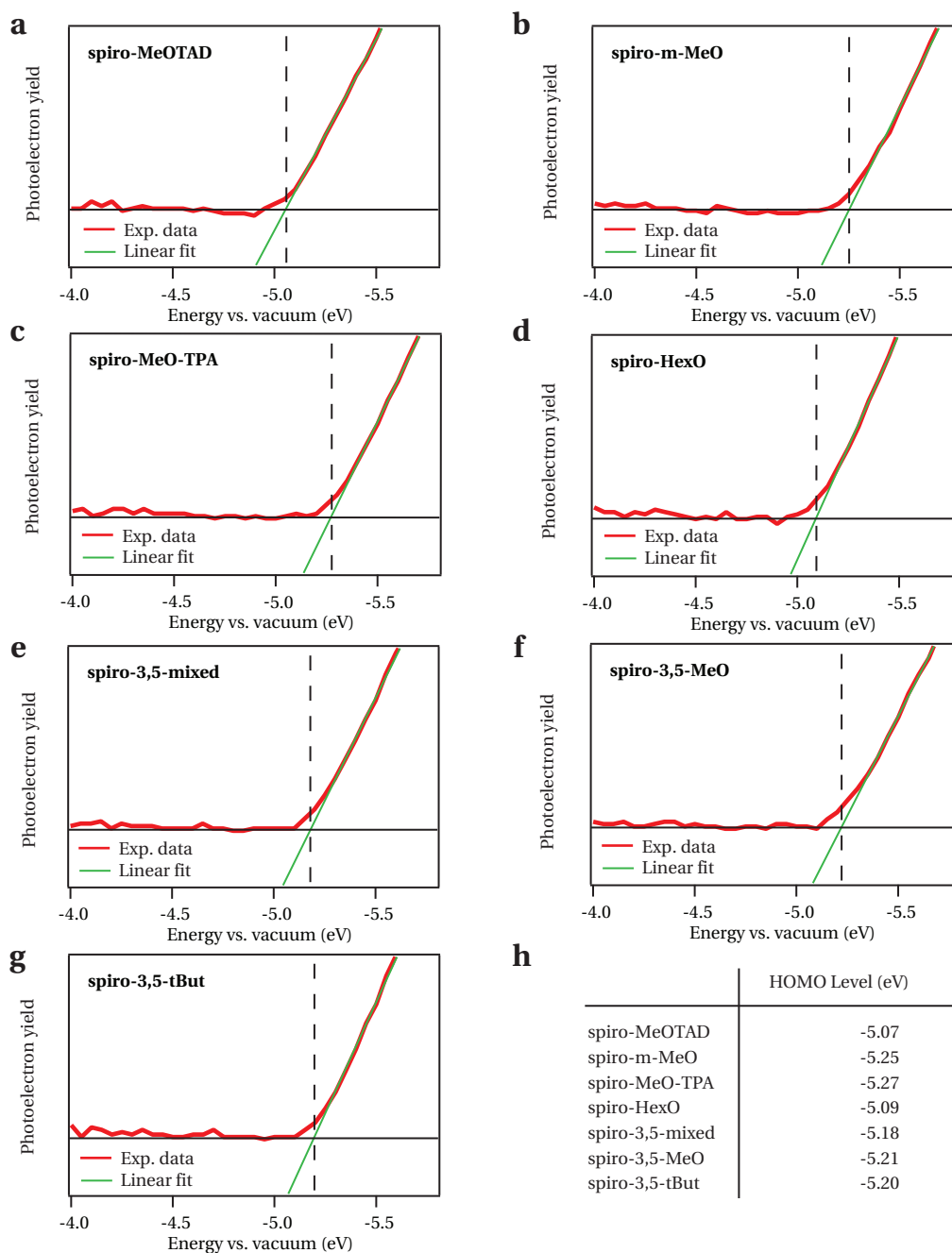


**Figure 3.5** — a–g) Results of photoelectron spectroscopy in air (PESA) measurements for the different HTMs. The graphs show the photoelectron yield as a function of ionization energy. The ionization potential (HOMO level) was determined from the intercept between the baseline and a linear fit to the steep rise in photoelectron yield. h) Summary of the HOMO levels derived from PESA measurements.

potential/work function/Fermi level of a material and in the present case to the HOMO level of the investigated molecules. Another advantage is that PESA allows the measurement to be performed in ambient atmosphere and on a thin film. Compared to electrochemical

measurements that are carried out in solution, this method lies closer to the final application in a solar cell. Due to the amorphous nature of the material, one would, however, expect only little interaction between the molecules in the solid-state and therefore similar results to be obtained by both techniques. A detailed description of the working principle of PESA can be found in the experimental section (Section 6.4).

The results obtained by PESA are presented in Figure 3.5 a–g, that shows plots of the photoelectron yield as a function of the incident photon energy. For all materials the PESA measurements yield a flat baseline for low photon energies and a sudden steep rise in photoelectron yield for photon energies between 5.0–5.3 eV, resulting from the ejection of photoelectrons. The intercept between the baseline and a linear fit to the steep rise in photoelectron yield represents the ionization potential, i.e. the position of the HOMO level of the sampled material. The HOMO levels of the different 9,9'-spirobifluorene derivatives measured by PESA are summarized in Figure 3.5 h and are also included in Figure 3.4 for a better comparison with results obtained by electrochemical measurements in solution. In general, a very good agreement between the two techniques is observed. For spiro-MeOTAD, spiro-m-MeO, spiro-MeO-TPA, spiro-p-HexO and spiro-3,5-mixed, the PESA measurements yield HOMO levels of –5.07, –5.25, –5.27, –5.09 and –5.18 eV, respectively. For these materials, the data obtained by electrochemistry and PESA differs only by 10–50 meV. A rather large discrepancy of about 0.1 eV is however found for spiro-3,5-MeO and spiro-3,5-tBut that yield HOMO values of –5.21 eV and –5.20 eV, respectively. The origin of this discrepancy remains unclear.

### 3.2.3 Charge transport properties investigated by FET measurements

One of the main tasks of the HTM is to transport holes from the sensitized metal oxide junction to the back contact. Hence, good charge transport properties of the HTM are crucial for an efficient functioning of the device. The charge transport is mainly governed by two parameters: the mobility and the conductivity. In Chapter 2 I have already shown that the conductivity of the HTM can be influenced through the addition of *p*-dopants. In contrast to the conductivity, the mobility is an intrinsic property of the HTM. Therefore, one of my main interests was to determine the hole mobility of the new HTMs.

#### 3.2.3.1 Techniques to determine charge carrier mobilities

Several methods have been used to determine the charge carrier mobility of organic semiconductors, but there are basically three techniques that are frequently used [168]: the extraction of the mobility from steady-state space-charge limited current (SCLC) measurements; from time of flight (TOF) measurements; from organic field-effect transistor (OFET) measurements. All three techniques will be explained briefly in the following paragraphs.

**Steady-state space charge-limited current (SCLC).** The SCLC technique is based on measuring the current–voltage characteristics of a thin film of the organic semiconductor sand-

wiched between two electrodes. Two assumptions have to be made: the contacts between the organic semiconductor and the electrodes have to be ohmic and the charge transport through the semiconductor has to arise from only one type of charge carrier (either holes or electrons). Both criteria are usually met through the choice of suitable charge-selective contacts. The current that flows through the device is then measured as a function of applied potential. At low potentials, the current is proportional to the applied voltage following Ohm's Law. At higher potentials, the current changes from injection-limited to transport-limited as the applied potential leads to the formation of a space-charge region within the bulk of the semiconductor. The space-charge limited current  $J_{SCLC}$  can then be described by Equation 3.1, which is a modified version of the Mott–Gurney equation considering the Poole–Frenkel Effect. The Poole–Frenkel Effect can be used to describe the temperature and electric field dependence of the mobility in disordered organic semiconductors. In Equation 3.1,  $\epsilon$  and  $d$  are the permittivity and thickness of the semiconductor,  $\mu_0$  is the zero-field mobility,  $F$  is the electric field,  $\beta$  is the Poole–Frenkel coefficient and  $\theta$  a factor that considers the presence of charge carrier traps. In many cases,  $\theta$  is approximated as 1 resulting in the trap-free SCLC model.

$$J_{SCLC} = \frac{9}{8}\epsilon\frac{1}{d}F^2\theta\mu(F, T) = \frac{9}{8}\epsilon\frac{1}{d}F^2\theta\mu_0(T)\exp(\beta F^{1/2}) \quad (3.1)$$

**Time of flight (TOF).** The TOF technique is based on measuring the transit time that carriers require to move through a semiconductor film in the presence of an electric field. The device architecture is similar as for the SCLC method: the organic semiconductor is sandwiched between two electrodes out of which one has to be transparent. While applying a potential between the two electrodes, a thin sheet of carriers is generated close to the transparent electrode by the aid of a short laser pulse. Under the applied electric field, the carriers move through the semiconductor to the back contact, which results in a transient current signal. The transit time  $\tau$  that can be extracted from the current transient is then used to calculate the charge carrier mobility for a given applied potential  $V$  and film thickness  $d$  according to Equation 3.2.

$$\mu = \frac{d^2}{V\tau} \quad (3.2)$$

**Organic-field effect transistor (OFET).** The third possibility is to extract the charge carrier mobility from an OFET configuration. In past decades, strong interest was placed on the development of field-effect transistors based on solution-processable organic semiconductors [169]. Due to the ease of fabrication, OFETs can also be used as a tool to determine electronic properties of materials that are not primarily developed for this application. Here, I followed this idea in order to determine the charge-carrier mobility of the newly synthesized HTMs in an OFET configuration.

### 3.2.3.2 Characterization of organic field-effect transistors

The device architecture of a typical bottom gate/bottom contact OFET is schematically depicted in Figure 3.6 a. The terms 'top' and 'bottom' refer to the order in which the semiconductor, the gate electrode and the source/drain electrodes are deposited. In the 'top' case, the electrodes are deposited onto the semiconductor, whereas in the 'bottom' case, the semiconductor is deposited onto the electrodes. The bottom gate/bottom contact configuration is the most simple one, as bottom gate/bottom contact transistor substrates are commercially available. Other device configurations that include bottom gate/top contact, top gate/bottom contact and top gate/top contact do exist, but will not be discussed here. A typical bottom gate/bottom contact OFET consists of highly doped  $n$ -type silicon that serves as both substrate and gate electrode. 100–500 nm of  $\text{SiO}_2$  are thermally grown on top of the  $n$ -Si, acting as a gate insulator and dielectric. Two indium tin oxide/gold electrodes, called source and drain, are then deposited on the gate insulator by lithography and/or shadow mask evaporation to form a channel of well-defined geometry. The organic semiconductor is finally deposited on the substrate by solution-processing or thermal evaporation and fills the channel between the source and drain electrodes, completing the OFET architecture.

The basic function of a transistor is to modulate the current that flows between source and drain, via a voltage that is applied between source and gate. The magnitude of the source–drain current,  $I_{DS}$ , thus depends on both the source–drain voltage,  $V_{DS}$ , and the source–gate voltage,  $V_{GS}$ . In the present case all studied materials are  $p$ -type semiconductors, therefore both  $V_{DS}$  and  $V_{GS}$  are negative. Herein, an increase in voltage always refers to an increase of the absolute value of the voltage.

At first we consider the *OFF state* of the transistor, i.e.  $V_{GS} = 0$ . Upon applying a negative voltage between source and drain, no or only little current flows through the device as the organic semiconductor is poorly conductive. The current that flows between source and drain when  $V_{GS} = 0$  is called the leakage current. However, when a negative source–gate voltage is applied, the polarization of the gate dielectric leads to an accumulation of positive charge carriers (holes) at the semiconductor/gate dielectric interface. These holes form a conductive channel that is uniformly distributed between the source and drain electrode at  $V_{DS} = 0$  and that allows current to flow between them when a negative source–drain voltage is applied. The transistor is now in the *ON state* and is said to work in *accumulation mode*. The minimum voltage that is necessary to turn on the transistor is called threshold voltage  $V_{Th}$ . The ratio between the current in the *ON state* and the current in the *OFF state* for a given source–drain voltage is called the ON/OFF ratio  $I_{ON/OFF}$ .

Depending on the magnitude of  $V_{DS}$ ,  $V_{GS}$  and  $V_{Th}$ , three different operational regions can be identified. For  $V_{DS} \ll (V_{GS} - V_{Th})$ , the source–drain current increases linearly with  $V_{DS}$ . Therefore, this region is called linear regime (Condition 1 in Figure 3.6 c, d). Upon a further increase in  $V_{DS}$ , the gradient of the electric field and the charge carrier density between source and drain becomes more and more prominent until a point is reached where the channel is

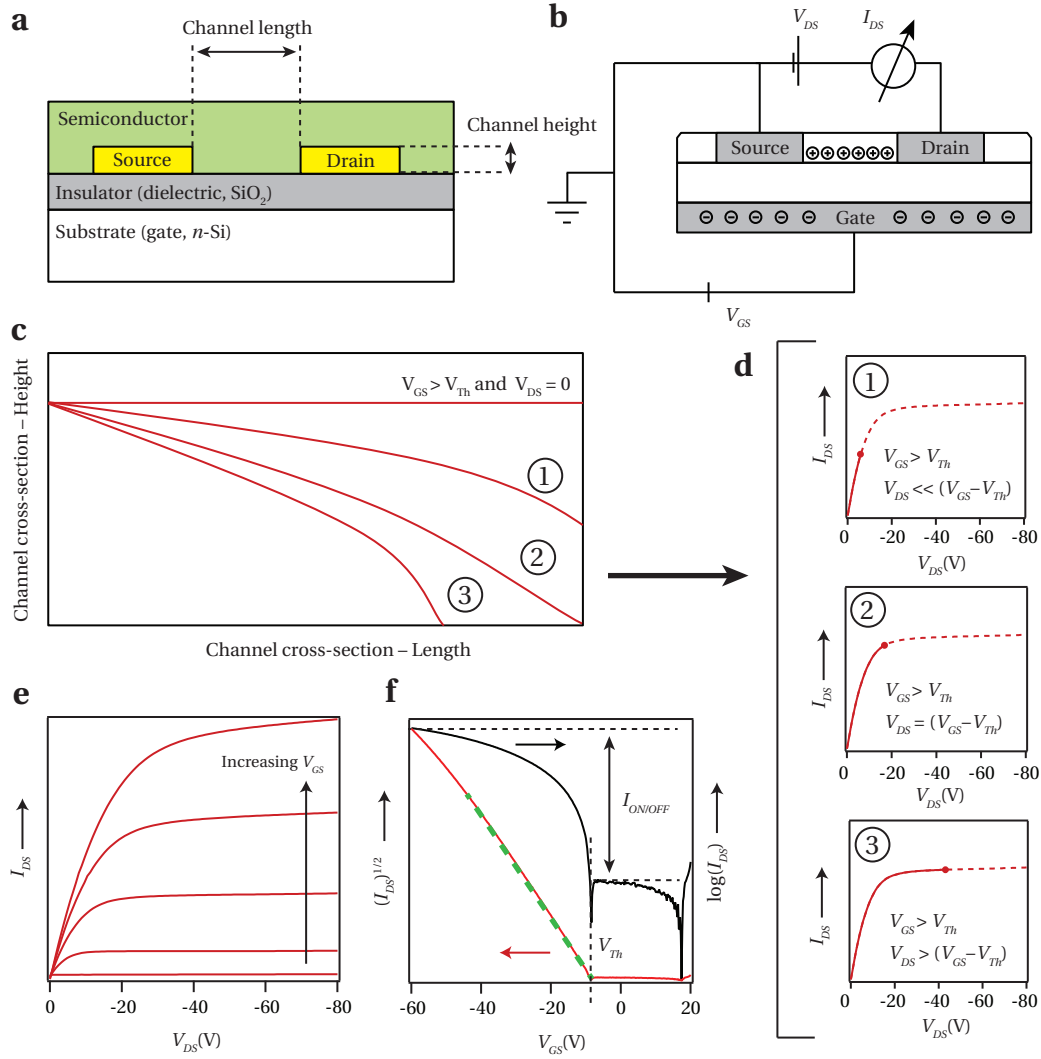


**Figure 3.6** — a) Device architecture of a typical bottom gate/bottom contact OFET. b) Electrical circuit of the OFET operation with  $I_{DS}$ —source–drain current,  $V_{DS}$ —source–drain voltage and  $V_{GS}$ —source–gate voltage. c) Channel cross section illustrating the charge distribution in the channel at different conditions indicated by numbers 1–3. The three different conditions 1 (linear regime), 2 (pinch-off point) and 3 (saturation regime) are detailed in panel d.  $V_{Th}$ —threshold voltage. e) Typical output characteristics measured at different source–gate voltages. f) Black curve: Typical transfer characteristics indicating the threshold voltage and the ON/OFF current ratio  $I_{ON/OFF}$ . Red curve: Plot of  $\sqrt{I_{DS}}$  vs.  $V_{GS}$ . Green dotted line: linear fit that gives access to the saturation mobility.

‘pinched off’ (Condition 2 in Figure 3.6 c, d). At this point  $V_{DS} = V_{GS} - V_{Th}$  and a depletion region of charge carriers starts to form close to the drain electrode. Current can still flow through the depletion region, but the source–drain current does not increase further with an increasing source–drain voltage. This condition is called the saturation regime (Condition 3 in Figure 3.6 c, d).

The current in the saturation regime can be expressed by Equation 3.3, where  $C_i$  is the capaci-



tance of the gate dielectric and  $W$  and  $L$  the channel width and length, respectively. Practically, the square root of the source–drain current is plotted against the source–gate voltage and the mobility is extracted from the slope of a linear fit.

$$I_{DS} = \frac{W}{2L} \mu_{sat} C_i (V_{GS} - V_{Th})^2 \quad (3.3)$$

Typically, two types of measurements are carried out. Firstly, the source–gate voltage is kept constant while sweeping the source–drain voltage. This measurement is repeated for various source–gate voltages and is referred to as *output characteristics* (Figure 3.6 e). Secondly, the source–drain voltage is fixed while sweeping the source–gate voltage. This measurement gives access to the saturation mobility according to Equation 3.3 and is referred to as *transfer characteristics* (Figure 3.6 f). Moreover,  $I_{ION/OFF}$  and  $V_{Th}$  can be derived from the transfer characteristics. A hysteresis measurement was performed in all cases.

### 3.2.3.3 OFETs based on spiro-MeOTAD

**Hole mobility of spiro-MeOTAD determined from OFET measurements.** The hole mobility of spiro-MeOTAD has been reported by several groups using a variety of techniques. Poplavskyy et al. found hole mobilities of roughly  $7 \times 10^{-5}$  and  $1 \times 10^{-4} \text{ cm}^2 \text{ V}^{-1} \text{ s}^{-1}$  at an electric field of about  $6 \times 10^4 \text{ V cm}^{-1}$  using the SCLC and TOF method, respectively [153]. Snaith et al. reported hole mobilities of  $2 \times 10^{-4}$  and  $1 \times 10^{-5} \text{ cm}^2 \text{ V}^{-1} \text{ s}^{-1}$  obtained by SCLC and TOF measurements at similar electric fields [33]. An SCLC mobility of about  $1 \times 10^{-4} \text{ cm}^2 \text{ V}^{-1} \text{ s}^{-1}$  has also been reported by Rana et al. for spiro-MeOTAD films deposited by thermal evaporation [155]. In all cases a rather weak electric field dependence of the charge carrier mobility has been observed. More recently, hole mobilities in the range of  $1 \times 10^{-5}$  to  $1 \times 10^{-4} \text{ cm}^2 \text{ V}^{-1} \text{ s}^{-1}$  have also been found by Leitjens et al. using transient conductivity measurements [154].

In order to prove the eligibility of the OFET measurements to estimate the hole mobility of disordered triarylamine based semiconductors, I first sought to determine the hole mobility of spiro-MeOTAD in order to compare it to the above-cited literature values. Other 9,9'-spirobifluorene based materials have previously been investigated in an OFET configuration by Saragi et al. [170–172], but in all cases the organic semiconductor had been deposited by thermal evaporation. Here, OFETs based on spiro-MeOTAD were prepared by spin-coating spiro-MeOTAD from a toluene solution onto commercially available OFET substrates. The substrates consist of highly doped  $n$ -type silicon as gate, 300 nm thick  $\text{SiO}_2$  as dielectric and 40 nm thick lithographically patterned source/drain electrodes made of 10 nm ITO (tin-doped indium oxide) and 30 nm Au. Each substrate bears 16 different transistor structures with four different channel lengths (20, 10, 5 and 2.5  $\mu\text{m}$ ). The channel width is 10 mm in all cases.

Transfer and output characteristics of spiro-MeOTAD-based OFETs with four different channel lengths are depicted in Figure 3.7. Typical FET behaviour is observed in all cases. However, for small channel lengths (5 and 2.5  $\mu\text{m}$ ) a strong parasitic leakage current is obtained in

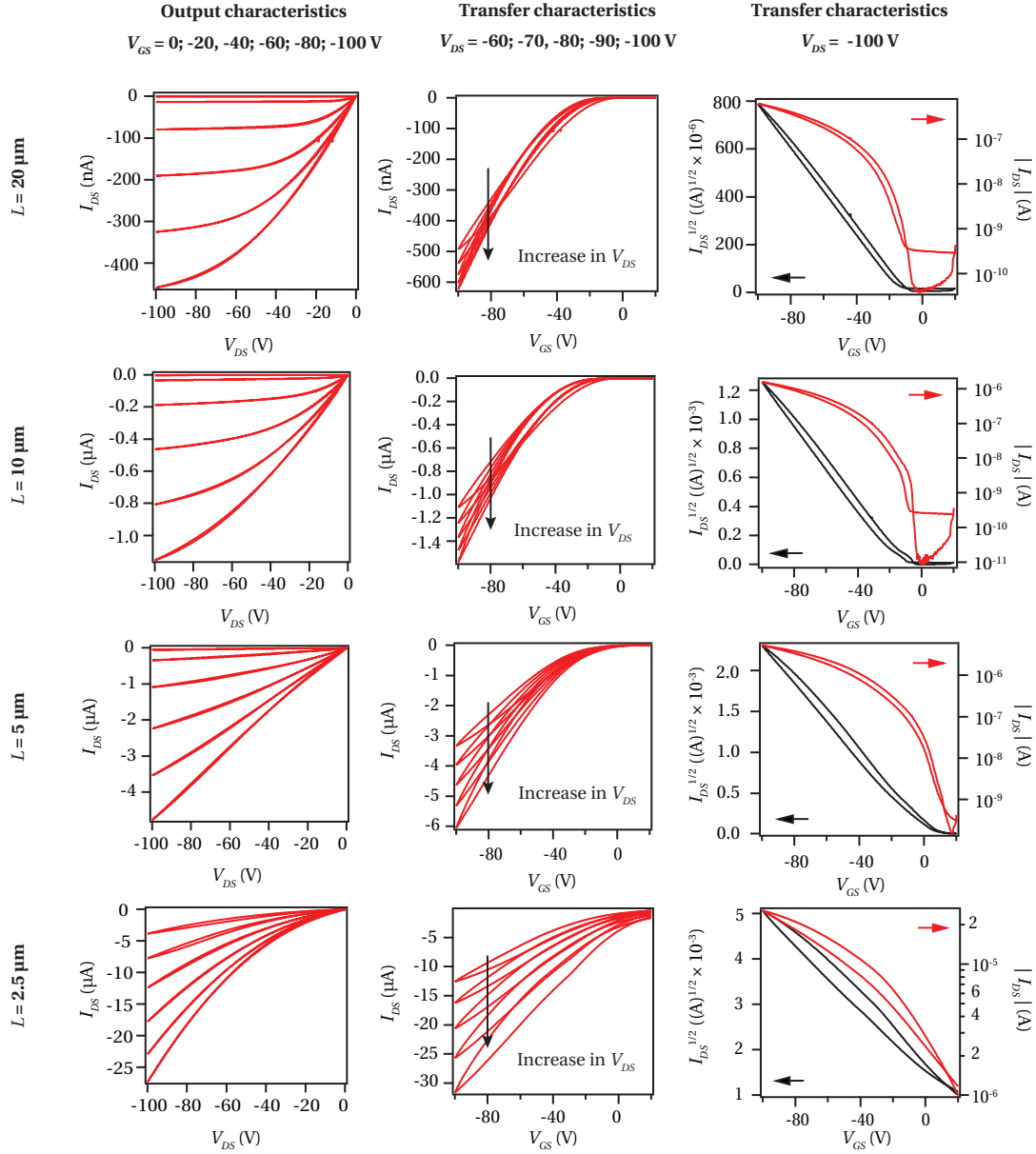


**Figure 3.7** — Output characteristics at  $V_{GS} = 0; -20; -40; -60; -80$  and  $-100$  V (left column), transfer characteristics at  $V_{DS} = -60; -70; -80; -90$  and  $-100$  V (middle column) and transfer characteristics at  $V_{DS} = -100$  V for OFETs based on spiro-MeOTAD and four different channel length  $L$  (20, 10, 5 and 2.5  $\mu\text{m}$ ) as indicated on the left-hand side of the figure. Spiro-MeOTAD was processed from toluene solution. No surface treatment has been applied to the OFET substrate.

the OFF state. Therefore,  $I_{DS}$  does not saturate for small channel length (Figure 3.7) even at high source–gate voltages. The leakage current suggests that the pristine material is already quite conductive which is likely to originate from intrinsic  $p$ -doping of spiro-MeOTAD. This hypothesis is further strengthened by the fact that for small channel lengths,  $I_{DS}$  continues to decrease when a positive source–gate voltage is applied, which means that positive charge

carriers can be depleted from the channel. Moreover, a significant hysteresis is observed in the transfer characteristics, especially for smaller channel lengths of 5 and 2.5  $\mu\text{m}$ . Such behaviour is usually attributed to the presence of charge carrier traps. In the present case, such traps might be located at the interface between the semiconductor and the gate dielectric. Interfacial trapping is a well-known problem and can usually be avoided by replacing terminating hydroxyl group on the  $\text{SiO}_2$  surface with a self-assembled monolayer of alkyl silanes. Such a treatment has not been employed in the case of the data presented in Figure 3.7 (This issue will be addressed and further discussed at the end of this section). Due to the above-mentioned problems at short channel lengths, I decided to focus only on a channel length of 20  $\mu\text{m}$ . From the transfer characteristics measured at  $V_{DS} = -100$  V a saturation mobility of  $2.2 \pm 0.1 \times 10^{-5} \text{ cm}^2 \text{ V}^{-1} \text{ s}^{-1}$ , a threshold voltage of  $-13 \pm 2$  V and an ON/OFF ratio of roughly  $10^3$  can be derived. This mobility is in good agreement with previously reported values obtained by TOF and SCLC measurements. To the best of my knowledge this is the first time that the mobility of spiro-MeOTAD has been determined in an FET configuration.

**Influence of the solvent on OFET behaviour.** OFET data presented so far has been obtained by spin-coating spiro-MeOTAD from a toluene solution, although initial experiments had been carried out by spin-coating from chlorobenzene, as this is the solvent of choice for the fabrication of ssDSC. For OFETs that have been prepared using chlorobenzene as a solvent for the solution-processing of the HTM, very high leakage currents in the OFF state are observed, even for a channel length of 20  $\mu\text{m}$ . The corresponding output and transfer characteristics are shown in Figure 3.8. This behaviour can be explained by a higher conductivity of the spiro-MeOTAD film. As spiro-MeOTAD is amorphous and does not form nanocrystalline domains, it is unlikely that this phenomenon is due to a difference in film morphology, which could be induced by the difference in the boiling points of the two solvents. It is suspected that the higher conductivity arises from partial oxidation of spiro-MeOTAD by the solvent, i.e. *p*-type doping. In fact, the instability of spiro-MeOTAD in other chlorinated solvents such as dichloromethane and chloroform was observed. Fresh solutions of spiro-MeOTAD in dichloromethane turn slightly reddish in colour within about 15–30 minutes, indicating the formation of the spiro-MeOTAD $^{\bullet+}$  cation radical. An even more drastic degradation is observed in the case of chloroform, as a color change from colorless to dark brown occurs within minutes. Chlorinated solvents are known to be unstable and dichloromethane and chloroform that are commercially available normally contain a stabilizer that is supposed to scavenge degradation products. Chlorobenzene is usually considered as stable and spiro-MeOTAD solutions in chlorobenzene do not change colour even on longer timescales. However, small amounts of impurities or degradation products might still be present, leading to a partial oxidation of spiro-MeOTAD and the aforementioned enhancement in conductivity. It is important to note that in all the above-described cases, the solutions were handled in an inert atmosphere using ultra dry solvents. Hence, any oxidation involving water or oxygen can be excluded. Due to problems that were encountered with chlorobenzene, I decided to carry out all future FET experiments using toluene as the solvent for the solution-processing. Toluene has very similar properties compared to chlorobenzene, but should be more stable and therefore suitable

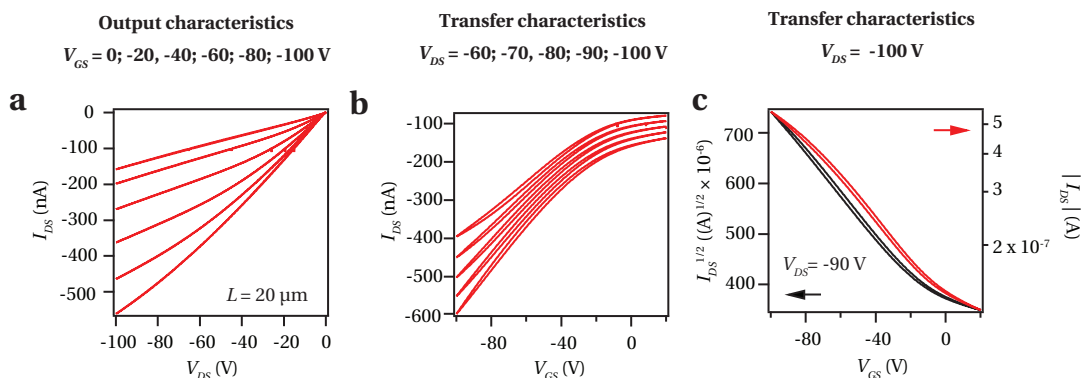


**Figure 3.8** — Characteristics of an OFET based on spiro-MeOTAD that was processed from chlorobenzene solution for a channel length of 20  $\mu\text{m}$ . a) Output characteristics at  $V_{GS} = 0; -20; -40; -60; -80$  and  $-100$  V. b) Transfer characteristics at  $V_{DS} = -60; -70; -80; -90$  and  $-100$  V. c) Transfer characteristics at  $V_{DS} = -100$  V.

for the fabrication of OFETs based on the HTMs described herein. However, chlorobenzene was still used for the fabrication of photovoltaic devices as will be described in Section 3.2.4, mainly due to the higher solubility of the HTMs in this solvent. In the case of ssDSCs, partial oxidation by the solvent is not expected to be a problem, as the HTMs are strongly doped via the addition of a chemical *p*-dopant.

**Influence of the surface treatment on OFET performance.** As already mentioned, charge carrier trapping at the interface between the organic semiconductor and the gate dielectric is a known issue in the OFET field. The main cause of this problem is the large number of terminating hydroxyl groups on the surface of  $\text{SiO}_2$ . A common procedure to overcome this issue is to replace the hydroxyl groups with hydrophobic alkyl chains. Practically this is achieved by treating the OFET substrate with a solution of hexamethyldisilazane or octyl(trichloro)silane, which form a self-assembled monolayer on the  $\text{SiO}_2$  surface [173].

It was found that these two materials are not suitable in this case as the silane treatment lead to non-uniform spiro-MeOTAD films due to poor surface wetting. Therefore, a more hydrophilic silane, namely phenyl(triethoxy)silane (PTES) [174], was employed for the surface modification, yielding much better quality films. Transfer characteristics at  $V_{DS} = -100$  V of a PTES-treated OFET as well as an untreated OFET based on spiro-MeOTAD are given in Figure 3.9 a, c, respectively. Figure 3.9 b, d shows the mobility that is calculated from the first derivative of the  $\sqrt{I_{DS}}$  vs.  $V_{GS}$  plot. Without PTES, the measured mobility was  $2.2 \pm 0.1 \times 10^{-5} \text{ cm}^2 \text{ V}^{-1} \text{ s}^{-1}$  as mentioned previously. This value increases to about  $4.6 \pm 0.5 \times 10^{-5} \text{ cm}^2 \text{ V}^{-1} \text{ s}^{-1}$  when the  $\text{SiO}_2$  substrate is covered with a self-assembled monolayer of PTES prior to the deposition of spiro-MeOTAD. In agreement with the assumption that the silane treatment prevents interfacial trapping, the PTES-treated OFET yields a weaker hysteresis as well as a lower threshold voltage of about  $-5.0 \pm 2$  V.

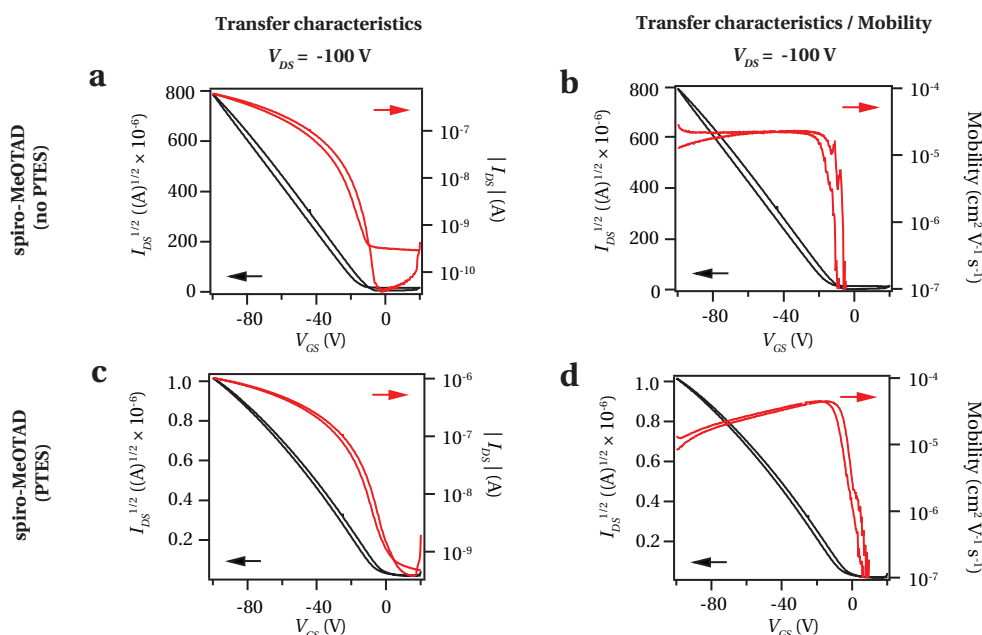


**Figure 3.9** — Transfer characteristics measured at  $V_{DS} = -100$  V for two OFETs based on spiro-MeOTAD and a channel length of  $20\ \mu\text{m}$ . In the case of a, b) no surface treatment has been applied whereas in the case of c, d) the OFET substrate was treated with a solution of phenyl(triethoxy)silane (PTES) prior to the deposition of spiro-MeOTAD.

### 3.2.3.4 OFETs based on new 9,9'-spirobifluorene derivatives

OFETs using the above-described procedure were also fabricated with the newly synthesized HTMs. All materials were deposited by spin-coating from toluene on PTES-treated OFET substrates and characterized as previously mentioned. The corresponding output and transfer characteristics for a channel length of  $20\ \mu\text{m}$  are depicted in Figure 3.10 and the results are summarized in Table 3.2. Surprisingly, spiro-p-HexO did not show any electric conduction independent from  $V_{DS}$  and  $V_{GS}$ . Therefore, FET data could not be obtained for this material. Additionally, spiro-p-HexO thin films crystallized during the annealing at  $100^\circ\text{C}$  after the solution-processing. Whether this was the reason for the insulating properties of the thin film could not be resolved at this stage of research. It can be hypothesized that the long hexyloxy chains shield the molecules from each other and therefore impede charge transport.

Apart from spiro-p-HexO typical FET behaviour is observed for all new materials. From the transfer characteristics at  $V_{DS} = -100$  V hole mobilities of  $9.1 \pm 0.3 \times 10^{-6}$ ,  $2.9 \pm 0.2 \times 10^{-5}$ ,  $8.4 \pm 0.6 \times 10^{-7}$ ,  $3.0 \pm 0.1 \times 10^{-6}$  and  $6.0 \pm 0.9 \times 10^{-7}\ \text{cm}^2\ \text{V}^{-1}\ \text{s}^{-1}$  could be derived for spiro-m-MeO, spiro-MeO-TPA, spiro-3,5-mixed, spiro-3,5-MeO and spiro-3,5-tBut, respectively. All new materials exhibit lower hole mobilities than what had been found for spiro-MeOTAD. Exceptionally low hole mobilities were found for the three compounds that bear substituents in both *meta* positions on the triarylamine units, namely spiro-3,5-mixed, spiro-3,5-MeO and spiro-3,5-tBut. OFETS of these materials also exhibit very large threshold voltages of 23–27 V. The highest hole mobility was obtained for spiro-MeO-TPA with a value of

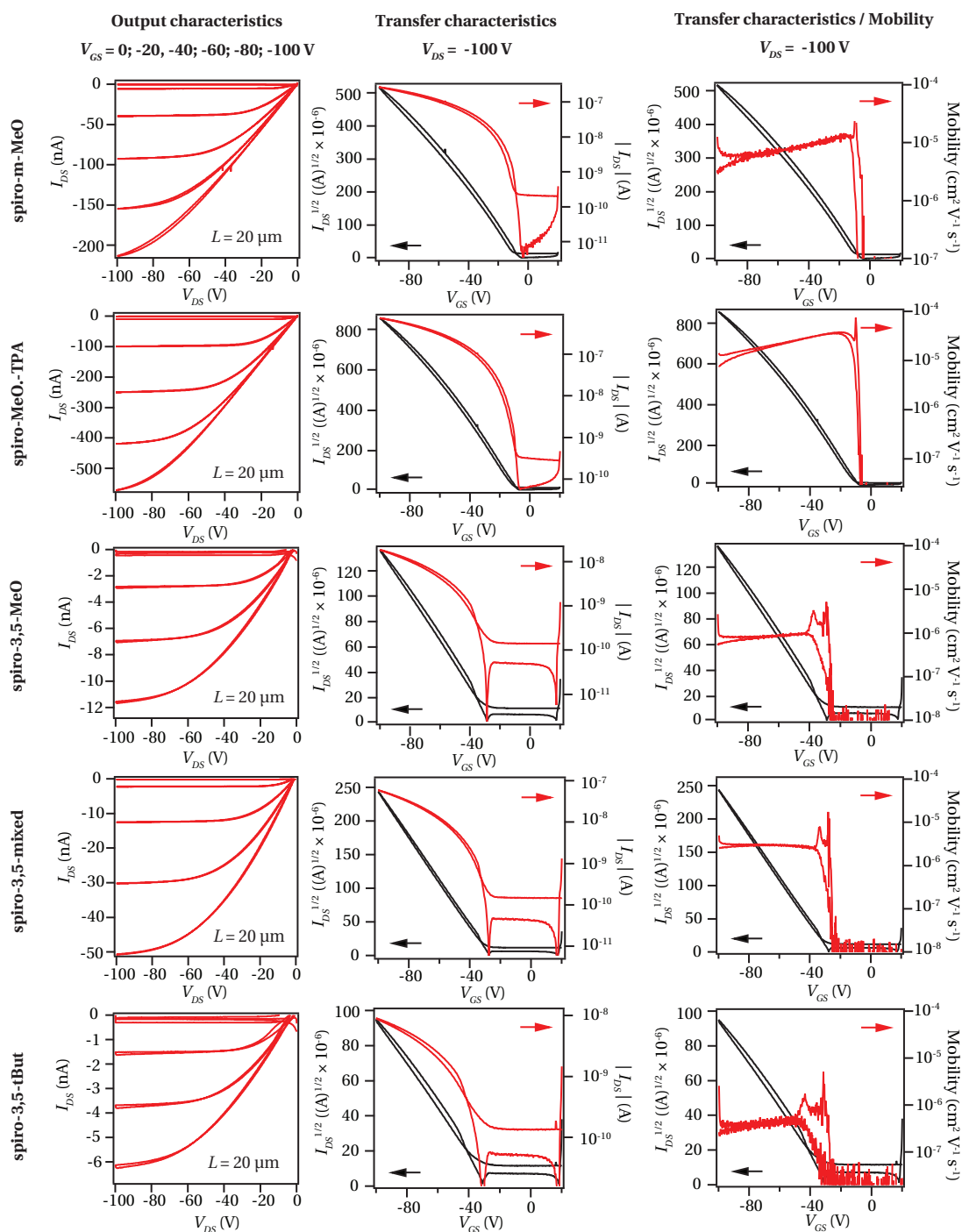


**Figure 3.10** — Output characteristics at  $V_{GS} = 0; -20; -40; -60; -80$  and  $-100$  V (left column) and transfer characteristics at  $V_{DS} = -100$  V (middle and right column) for OFETs based on spiro-m-MeO, spiro-Me-TPA, spiro-3,5-mixed, spiro-3,5-MeO and spiro-3,5-tBut, as indicated on the left-hand side of the figure. The channel length was  $20 \mu\text{m}$  in all cases. The plots in the right column show the mobility after the differentiation of the  $\sqrt{I_{DS}}$  vs.  $V_{GS}$  plot. It is worth mentioning that the negative and positive spikes that are observed in the transfer characteristics and mobility plots at very low current, are artifacts that result from capacitive charging.

$2.9 \pm 0.2 \times 10^{-5} \text{ cm}^2 \text{ V}^{-1} \text{ s}^{-1}$  that is only marginally lower than the mobility found for spiro-MeOTAD.

From the comparison of the different 9,9'-spirobifluorene derivatives it becomes evident that the substituents on the peripheral triarylamine units have a tremendous influence on the charge transport properties of the materials. Carrier transport and mobility in disordered organic semiconductors is strongly related to the degree of molecular and energetic disorder. Whereas the molecular disorder results from the random orientation of the organic molecules, the energetic disorder is described by the width of the density of states that is usually assumed to be of Gaussian shape. Due to the energy-activated charger transport that occurs between strongly localized states, the carrier mobility usually exhibits a strong dependence on temperature, charge density and electric field. Another factor that influences the carrier transport—theoretically even in the absence of molecular or energetic disorder—is the electronic coupling between adjacent hopping sites, i.e. their distance and orbital overlap.

Due to the similar size and structure of the new HTMs one would not expect them to differ much in terms of molecular or energetic disorder. In contrast to that, the electronic coupling between neighbouring molecules might be significantly affected by the size and position of the substituents. Especially the bulky *tert*-butyl groups are likely to increase the spacing between the triarylamine hopping sites, therefore hindering carrier movement. In agreement with that assumption the data reveals a decrease in mobility when gradually replacing the two *meta*-methoxy groups in spiro-3,5-MeO ( $3.0 \pm 0.1 \times 10^{-6} \text{ cm}^2 \text{ V}^{-1} \text{ s}^{-1}$ ) by *tert*-butyl groups, leading to mobilities of  $8.4 \pm 0.6 \times 10^{-7}$  and  $6.0 \pm 0.9 \times 10^{-7} \text{ cm}^2 \text{ V}^{-1} \text{ s}^{-1}$  for spiro-3,5-mixed and spiro-3,5-tBut, respectively. A threefold reduction in mobility from  $9.1 \pm 0.3 \times 10^{-6}$  to  $3.0 \pm 0.1 \times 10^{-6} \text{ cm}^2 \text{ V}^{-1} \text{ s}^{-1}$  is also observed when moving from one *meta*-methoxy to two *meta*-methoxy groups.

**Table 3.2** — Saturation mobilities extracted from FET measurements at  $V_{DS} = -100 \text{ V}$  for various HTMs.

Compound	Saturation mobility <sup>a,b</sup> $\text{cm}^2 \text{ V}^{-1} \text{ s}^{-1}$	Threshold voltage <sup>b</sup> V
Spiro-MeOTAD (no PTES)	$2.2 \pm 0.1 \times 10^{-5}$	$-13 \pm 2$
Spiro-MeOTAD	$4.6 \pm 0.5 \times 10^{-5}$	$-5 \pm 2$
Spiro-m-MeO	$9.1 \pm 0.3 \times 10^{-6}$	$-7 \pm 2$
Spiro-MeO-TPA	$2.9 \pm 0.2 \times 10^{-5}$	$-11 \pm 3$
Spiro-3,5-mixed	$8.4 \pm 0.6 \times 10^{-7}$	$-25 \pm 2$
Spiro-3,5-MeO	$3.0 \pm 0.1 \times 10^{-6}$	$-27 \pm 1$
Spiro-3,5-tBut	$6.0 \pm 0.9 \times 10^{-7}$	$-23 \pm 5$

<sup>a</sup> Saturation mobilities were determined from a linear fit of the  $\sqrt{I_{DS}}$  vs.  $V_{GS}$  plot at moderate source-gate voltages of  $V_{GS} + V_{Th} \approx 10 - 30 \text{ V}$ .

<sup>b</sup> The average mobility and threshold voltage of three OFETs is given.



The pronounced decrease in mobility from  $4.6 \pm 0.5 \times 10^{-5}$  to  $9.1 \pm 0.3 \times 10^{-6} \text{ cm}^2 \text{ V}^{-1} \text{ s}^{-1}$  when shifting the methoxy group from the *para* (spiro-MeOTAD) to the *meta* position (spiro-m-MeO) turned out to be somewhat unexpected. The different position of the methoxy group could lead to a different configuration of the triarylamine units, which in turn could hinder the intermolecular electronic coupling. However, this stands in contradiction to the findings of Saragi et al. who investigated the methyl analogous of spiro-MeOTAD and spiro-m-MeO and found a higher saturation mobility for the compound bearing a methyl group in the *meta* position than for the one bearing a methyl group in the *para* position [170].

### 3.2.4 ssDSC device performance of new HTMs

In order to investigate their usefulness for practical applications, the new hole-transporting materials were employed in ssDSCs. Considering the charge transport properties of the various materials that have been extracted from the OFET measurements, spiro-m-MeO and spiro-MeO-TPA are the two most promising candidates as they exhibit the highest hole mobilities. ssDSCs based on the two HTMs were fabricated in the same manner as for spiro-MeOTAD using the Y123 sensitizer. From the electrochemical measurements a driving force of 50–80 mV for the regeneration of the oxidized dye can be derived—a value that might be too small for the hole injection to occur efficiently. Besides the common additives—TBP and LiTFSI—3.2% of FK269 was added to the HTM spin-coating formulation as a *p*-type dopant.

*J*–*V* curves for devices based on spiro-MeOTAD, spiro-m-MeO and spiro-MeO-TPA measured under simulated AM1.5G irradiance at two different light intensities and in the dark are shown in Figure 3.11. The photovoltaic parameters that have been extracted from the *J*–*V* characteristics are summarized in Table 3.3. Significant differences between the three materials can already be observed in the dark as evident from Figure 3.11 c. Both of the new materials show much smaller dark current flow under forward bias.

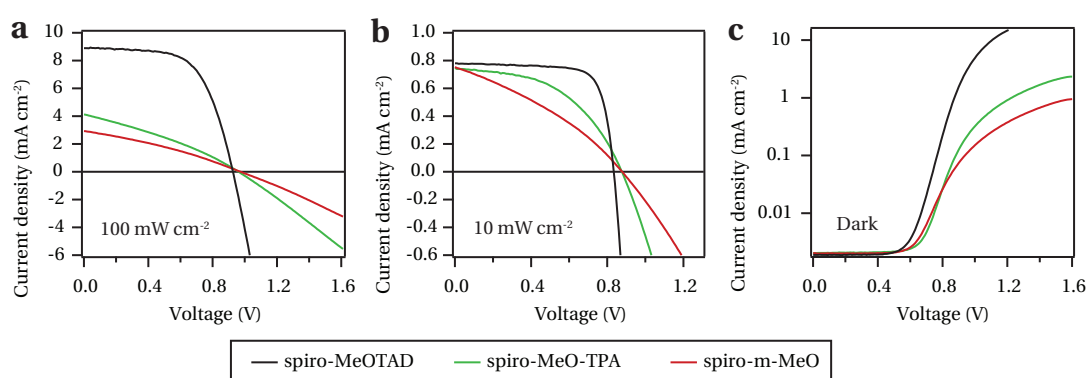


**Figure 3.11** — *J*–*V* curves measured at approximately a) 100 mW cm<sup>-2</sup>, b) 10 mW cm<sup>-2</sup> and c) in the dark for the HTMs spiro-MeOTAD, spiro-m-MeO and spiro-MeO-TPA. All devices were based on the Y123 sensitizer and contained 3.2% of the FK269 Co(III) dopant. Please note that c) is a semi logarithmic plot.



Under applied forward bias in the dark, electrons flow from the FTO substrate through the mesoporous  $\text{TiO}_2$ , to the HTM, through the HTM and to the back contact. Under such conditions, four different possibilities that could hinder the dark current flow can be envisaged.

- The transport through the mesoporous  $\text{TiO}_2$  could be hindered. In the present case, all photovoltaic devices were fabricated using the same type of mesoporous  $\text{TiO}_2$ . Therefore, a difference in the transport properties of the  $\text{TiO}_2$  is unlikely.
- The electron transfer from the mesoporous  $\text{TiO}_2$  to the HTM could be hindered. Firstly, the electron transfer strongly depends on the sensitizer that is employed as it keeps the HTM molecules at distance from the  $\text{TiO}_2$  surface. Here, one expects the interface to be the same, as the same sensitizer is used in all cases. Secondly, the electron transfer depends on the total interfacial area between the  $\text{TiO}_2$  and the HTM. Assuming the same  $\text{TiO}_2$  morphology and thickness, the total interfacial area could only change if the pore-filling changes. The HTMs compared here all have a very high solubility and similar properties to spiro-MeOTAD. Hence, a significant difference in pore-filling is not expected.
- The charge transport through the HTM could be hindered. The charge transport is strongly related to the conductivity of the HTM. As the conductivity depends on the charge carrier mobility, this could be an issue, as the charge carrier mobility of the new HTMs is lower than that of spiro-MeOTAD.
- The charge transfer across the interface between the HTM and the back contact could be hindered. In the photovoltaic devices, all HTMs are highly doped and are expected to form ohmic contacts to the metallic back electrode, as this is the case for spiro-MeOTAD.

From a comparison of the different possibilities listed above, it can be concluded that the lower dark current, that is observed for spiro-m-MeO and spiro-MeO-TPA compared to spiro-MeOTAD, is most likely to result from the lower hole mobilities of these materials. The lower hole mobility leads to a lower conductivity of the HTM, a higher series resistance of the solar cell and hence a smaller dark current. The series resistance of the solar cell  $R_s$  can be crudely estimated from the linear part of the dark  $J-V$  curve at high forward bias using Ohm's Law. In the present case this method yields values of 20, 645 and  $252 \Omega \text{ cm}^2$  for spiro-MeOTAD, spiro-m-MeO and spiro-MeO-TPA, respectively.

Measurements under full sunlight illumination of approximately  $100 \text{ mW cm}^{-2}$ , yield values of 834 mV,  $0.78 \text{ mA cm}^{-2}$  and 0.75 for  $V_{OC}$ ,  $J_{SC}$  and  $FF$ , respectively, corresponding to a  $PCE$  of 5.3% for the reference device based on spiro-MeOTAD. Upon replacing spiro-MeOTAD by either spiro-m-MeO or spiro-MeO-TPA, one observes an increase in  $V_{OC}$  to 974 and 961 mV, a decrease in  $J_{SC}$  to 2.9 and  $4.1 \text{ mA cm}^{-2}$  and a decrease in  $FF$  to 0.32 and 0.31, yielding  $PCE$ s of 0.9 and 1.3%, respectively. The increase in  $V_{OC}$  can be rationalized by the lower HOMO level of the two new materials compared to spiro-MeOTAD, although the shift in  $V_{OC}$

### Chapter 3. 9,9'-spirobifluorene based hole-transporters for ssDSC applications

(30–50 mV) is small compared to the shift in HOMO level (200 mV, determined by PESA and electrochemistry). As the  $V_{OC}$  is dictated by the position of the HOMO level of the HTM and the quasi Fermi level in the  $\text{TiO}_2$ , this indicates that there must be a difference in the position of the quasi Fermi level.

The very low FF of the devices based on spiro-m-MeO or spiro-MeO-TPA clearly results from a low conductivity and high series resistance as is evident from the slope of the  $J$ - $V$  curves at  $V_{OC}$ . This finding is in good agreement with the dark current  $J$ - $V$  curves and also with the lower hole mobilities found by FET measurements. I also attribute the variation in  $J_{SC}$  to the difference in hole mobility, especially as spiro-MeO-TPA—that has a higher mobility compared to spiro-m-MeO—gives a slightly higher photocurrent under full sun illumination. The total amount of generated photocurrent can generally be described as the product of light-harvesting efficiency, electron injection efficiency and charge collection efficiency (cf. Section 1.4.3). As all devices compared here are based on the same sensitizer and  $\text{TiO}_2$  structure, one would neither expect a difference in light-harvesting efficiency nor the electron injection efficiency, rendering the charge collection efficiency responsible for the low photocurrents.

In fact, a lower hole mobility could lead to increased electron–hole recombination, a shorter carrier diffusion length and hence a lower charge collection efficiency. As an increased electron–hole recombination rate would lead to a lower charge density and therefore quasi Fermi level in the  $\text{TiO}_2$ , this could also explain the rather small shift in  $V_{OC}$  that is observed,

**Table 3.3** — Photovoltaic parameters derived from  $J$ - $V$  characteristics measured at two different light intensities.

Compound	Doping <sup>a</sup> mol%	$P_{in}$ $\text{mW cm}^{-2}$	$V_{OC}$ mV	$J_{SC}$ $\text{mA cm}^{-2}$	FF -	PCE %	$R_s^b$ $\Omega \text{ cm}^2$
spiro-MeOTAD	3.2	9.2	834	0.78	0.75	5.3	20
		98.3	926	8.9	0.62	5.2	
spiro-MeO-TPA	3.2	9.30	877	0.75	0.49	3.4	252
		98.7	961	4.1	0.31	1.3	
spiro-m-MeO	3.2	9.4	878	0.75	0.33	2.3	645
		99.7	974	2.9	0.32	0.9	
spiro-m-MeO	10	9.7	784	0.68	0.36	2.0	119
		101	879	2.6	0.39	0.9	
spiro-m-MeO	20	9.8	736	0.59	0.37	1.7	87
		101	789	2.3	0.41	0.7	
spiro-m-MeO	40	9.8	708	0.72	0.39	2.0	32
		101	767	2.8	0.42	0.9	

<sup>a</sup> In all cases FK269 has been used as a  $p$ -type dopant.

<sup>b</sup> Values are derived from the linear part of the dark current  $J$ - $V$  curves at high forward bias.

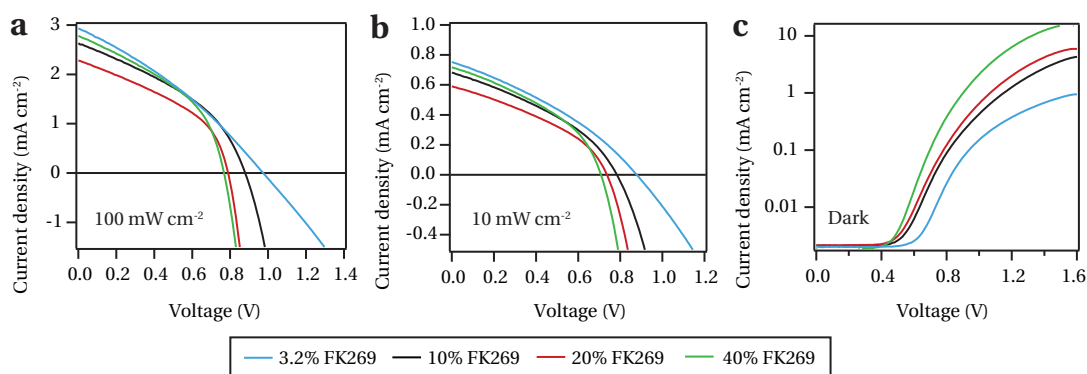


**Figure 3.12** —  $J$ - $V$  curves measured at approximately a) 100 mW cm<sup>-2</sup>, b) 10 mW cm<sup>-2</sup> and c) in the dark for the devices based on spiro-m-MeO containing different amounts of the FK269 Co(III) dopant. Please note that c) is a semi logarithmic plot.

despite the large difference in the HOMO levels of the HTMs. Alternatively, the lower charge collection efficiency could also be caused by a slower regeneration of oxidized dye molecules, resulting from the small energy offset between the HOMO level of the dye and the HTM, leading to increased recombination kinetics.

$J$ - $V$  measurements at a low light intensity of approximately 10 mW cm<sup>-2</sup> (Figure 3.11 b) reveal very similar trends in terms of  $V_{OC}$ ,  $FF$  and  $PCE$  compared to what has been found under full sunlight illumination. Accordingly, the data reveals an increase in  $V_{OC}$  from 834 mV to 878 and 877 mV, a decrease in  $FF$  from 0.75 to 0.33 and 0.49 as well as a decrease in  $PCE$  from 5.2 to 2.3 and 3.4% when replacing spiro-MeOTAD by spiro-m-MeO or spiro-MeO-TPA, respectively. A difference is, however, observed in terms of the  $J_{SC}$ , which is surprisingly very similar for all three materials. This suggests that the hole injection cannot be the problem here and that the regeneration of the oxidized dye works efficiently—at least at low light conditions—despite the small energy offset of only 50–80 mV. Yet, the extrapolation of this finding to the full sunlight condition is not straightforward as the kinetics of the regeneration of oxidized dye molecules might be light intensity dependent.

It has been previously observed that in some cases the short-circuit photocurrent can be limited by the series resistance, e.g. in the case of ssDSCs based on undoped spiro-MeOTAD (Figure 2.2 in Section 2.1.2). In order to probe the effect of the series resistance on the  $J_{SC}$ , ssDSCs were fabricated based on spiro-m-MeO as mentioned before, but employing much higher levels of the chemical  $p$ -dopant. The higher doping is expected to increase the conductivity of the HTM, decrease the series resistance of the solar cell and increase the dark current. Figure 3.12 shows  $J$ - $V$  curves measured at different light intensities and in the dark for devices that were doped at 3.2, 10, 20 and 40% using FK269. The corresponding photovoltaic parameters are summarized in Table 3.3. It is worth mentioning that the  $p$ -dopant does still dissolve in the HTM spin-coating formulation, even at such high concentrations, although crystallization of the remaining Co(II) salt during the solution-processing is clearly visible.

As expected, one observes a significant increase in dark current density when increasing the amount of FK269 from 3.2 to 10, 20 and 40%, respectively, as is evident from Figure 3.12 c. This is consistent with an increase in the conductivity of the HTM/Co(III) composite and a concomitant decrease of the series resistance. The latter is estimated from the linear part of the dark  $J$ - $V$  curve at high forward bias, yielding values of 645, 119, 87 and 32  $\Omega\text{ cm}^2$  for 3.2, 10, 20 and 40% FK269, respectively. Under illumination, at both low and high light intensity, this trend is reflected in an increase of the  $FF$  with doping ratio (Table 3.3). A clear trend is also visible for the  $V_{OC}$  that decreases significantly for the higher doping ratios. This is most likely a result of the higher hole density in the HTM that leads to increased electron-hole recombination. More important, however, is the observation that the  $J_{SC}$  does not seem to be significantly affected by the change in doping level and series resistance. The small differences in the  $J_{SC}$  that are observed, are attributed to experimental variations. From this data it seems that the  $J_{SC}$  of the devices based on the new HTMs is not limited by the series resistance, but that it is a direct result of the lower hole mobility. Further investigations are required to confirm this theory.

ssDSCs have also been fabricated using the remaining materials spiro-p-HexO, spiro-3,5-mixed, spiro-3,5-MeO and spiro-3,5-tBut. In agreement with what has been found in a transistor configuration, spiro-p-HexO exhibited completely insulating properties, both in the dark and under illumination. Regarding spiro-3,5-tBut, standard ssDSCs could not be fabricated due to very poor surface wetting of the sensitized nanoporous  $\text{TiO}_2$  film with the HTM solution, leading to inhomogeneous film formation. Photovoltaic devices could be fabricated using spiro-3,5-mixed and spiro-3,5-MeO but suffered from very high series resistances and  $PCE$ s below 0.1%. As this behaviour clearly results from the low hole mobility, this data will not be further discussed.

#### 3.2.5 Influence of the material's purity

Purity of the materials is one of the key parameters for high performance electronic devices. Although the purity of organic semiconductors is assumed to be far less critical compared to inorganic semiconductors, trace amounts of impurities might still affect the properties of a material. Particularly, charge carrier transport can be hindered by impurities as they often form deep traps in the density of states, leading to a lower charge carrier mobility.

The purity of the new HTMs presented in this chapter has been primarily determined by  $^1\text{H}$  and  $^{13}\text{C}$  nuclear magnetic resonance (NMR) spectroscopy, although this technique is not ideal due to a relatively high limit of detection. Moreover, NMR spectroscopy would not detect any impurities that are of inorganic nature.

In order to probe the effect of the HTM purity, we synthesized spiro-MeOTAD using the exact same procedure as for the new HTMs and compared it to a batch of commercial spiro-MeOTAD. The high purity of the commercially available product can usually be assumed because of the sublimation purification step that the supplier employs in their procedure. In contrast to that,

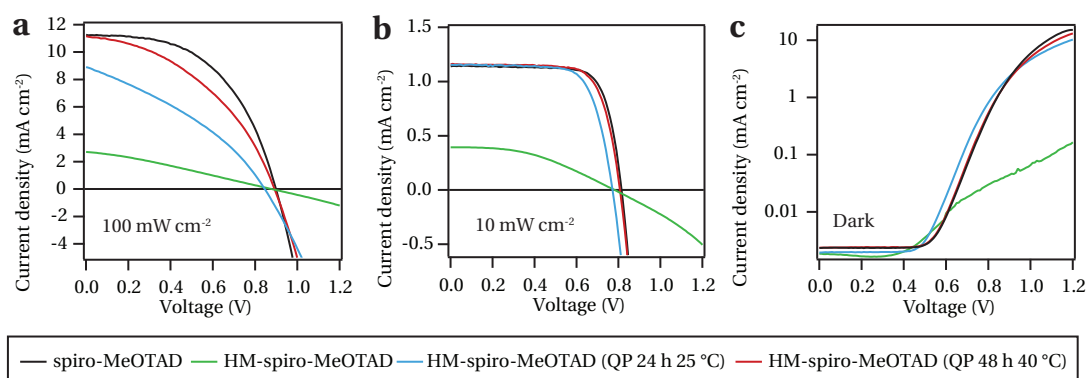


**Figure 3.13** —  $J$ - $V$  curves measured at approximately a)  $100 \text{ mW cm}^{-2}$ , b)  $10 \text{ mW cm}^{-2}$  and c) in the dark for the devices based on commercial spiro-MeOTAD and homemade spiro-MeOTAD at different purity levels. All devices contained 1.6% of the FK209 Co(III) dopant. The devices based on spiro-MeOTAD and HM-spiro-MeOTAD employ the C220 sensitizer, whereas the devices based on the QP treated HM-spiro-MeOTAD employ the Y123 sensitizer. Please note that c) is a semi logarithmic plot.

materials synthesized in our lab have been purified only by column chromatography, which makes trace amounts of impurities more likely.

**Effect of Quadrapure<sup>TM</sup> (QP) treatment on ssDSC performance.** In order to evaluate its quality, the homemade spiro-MeOTAD (HM-spiro-MeOTAD) was used to fabricate ssDSCs in order to compare it to the one that is commercially available.  $J$ - $V$  curves measured at different light intensities and in the dark are shown in Figure 3.13. The corresponding photovoltaic parameters that have been derived from the  $J$ - $V$  curves are summarized in Table 3.4. When compared to spiro-MeOTAD, the device based on HM-spiro-MeOTAD suffers from a very low FF and  $J_{SC}$  at both high and low light intensity and also from a significantly lower dark current at high forward bias. Due to the identical fabrication procedure in both cases, one can infer that there must be a difference in the chemical purity between both materials.

As one of the most probable impurities we suspected trace amounts of palladium in the homemade (HM) materials. Palladium, that is used as a catalyst for the coupling reaction between the amine and the 9,9'-spirobifluorene core, is known to be difficult to separate by column chromatography. One way to remove trace amounts of heavy metals from soluble organic molecules is the use of a metal scavenger that binds to the metal and allows its separation. We chose to employ commercially available functionalized polystyrene beads (Quadrapure<sup>TM</sup>, QP) as a suitable scavenger. The micrometer-sized QP beads can be added to a solution of the HTM in organic solvent and easily be removed after the reaction with the metallic impurities by simple filtration. One of the most common functionalities on the polystyrene beads and also the one that has been used here is a thiourea (TU) unit.

After the treatment of HM-spiro-MeOTAD with the QP TU beads at  $25^\circ\text{C}$  for 24 h (cf. Section 6.1.1), I used the material to fabricate ssDSCs. As shown in Figure 3.13 and Table 3.4, this simple treatment resulted in a significant increase in device performance at

### Chapter 3. 9,9'-spirobifluorene based hole-transporters for ssDSC applications

**Table 3.4** — Photovoltaic parameters derived from  $J$ - $V$  characteristics measured at two different light intensities.

Compound	$P_{in}$ mW cm <sup>-2</sup>	$V_{OC}$ mV	$J_{SC}$ mA cm <sup>-2</sup>	$FF$ -	$PCE$ %	$R_s^c$ $\Omega$ cm <sup>2</sup>
spiro-MeOTAD <sup>a</sup>	9.6	814	1.1	0.76	7.3	18
	99.5	898	11.3	0.52	5.3	
HM-spiro-MeOTAD <sup>b</sup>	9.7	782	0.4	0.43	1.4	1253
	99.9	881	2.7	0.29	0.7	
HM-spiro-MeOTAD (QP 24 h 25°C) <sup>b</sup>	9.7	771	1.2	0.72	6.7	34
	99.7	846	8.9	0.35	2.6	
HM-spiro-MeOTAD (QP 48 h 40°C) <sup>a</sup>	9.6	807	1.2	0.74	7.2	23
	99.2	892	11.2	0.42	4.3	

<sup>a</sup> Device based on Y123 dye.

<sup>b</sup> Device based on C220 dye.

<sup>c</sup> Values are derived from the linear part of the dark current  $J$ - $V$  curves at high forward bias.

both high and low light intensity, which is mainly due to an increase in  $FF$  and  $J_{SC}$ . At low light intensity, HM-spiro-MeOTAD (QP 24 h 25°C) reached almost the same device performance as the commercially available spiro-MeOTAD. The difference in  $V_{OC}$  originates from the use of two different dyes (cf. caption Figure 3.13). In order to further improve the metal scavenging, we increased the reaction temperature and time to 40°C for 48 h. The photovoltaic characterization of devices based on HM-spiro-MeOTAD (QP 48 h 40°C) is included in Figure 3.13 and Table 3.4. A further improvement in  $FF$  and  $J_{SC}$  is observed for the prolonged QP treatment, finally leading to a performance that was close to the one of the commercial product, even at the full sunlight intensity. For a better comparison of the different batches, the series resistance of the devices based on different spiro-MeOTAD batches is crudely estimated from the linear part of the dark-current  $J$ - $V$  curves at high forward bias. This procedure yields values of 18, 1253, 34 and 23  $\Omega$  cm<sup>2</sup> for the different batches spiro-MeOTAD, HM-spiro-MeOTAD, HM-spiro-MeOTAD (QP 24 h 25 °C) and HM-spiro-MeOTAD (QP 48 h 40°C), respectively.

This data clearly shows the benefit of the QP treatment for the device performance and suggest that the as-synthesized materials indeed contain trace amounts of palladium that affect the charge transport properties. Following the promising results obtained for HM-spiro-MeOTAD after the QP treatment at 40 °C for 48 h, this treatment has been also applied to all other HTMs presented here. All PV and OFET data presented in this chapter is based on the use of QP treated materials, using the the QP purification at 40°C for 48 h. It is important to note that, despite the optimized QP purification, HM-spiro-MeOTAD (QP 48 h 40°C) does not reach the same photovoltaic performance under full sun illumination, as the commercial spiro-MeOTAD.

**Table 3.5** — Saturation mobilities extracted from FET measurements at  $V_{DS} = -100$  V for commercial spiro-MeOTAD and QP-treated HM-spiro-MeOTAD.

Compound	Saturation mobility $\text{cm}^2 \text{V}^{-1} \text{s}^{-1}$	Threshold voltage V
Spiro-MeOTAD	$4.6 \pm 0.5 \times 10^{-5}$	$-5 \pm 2$
HM-Spiro-MeOTAD (QP 48 h 40 °C)	$2.9 \pm 0.2 \times 10^{-5}$	$-24 \pm 6$

**Effect of QP treatment on OFET performance.** From the photovoltaic data it seems evident that the Pd contamination has an effect on the conductivity of the HTMs. In order to further investigate this hypothesis OFETs were fabricated based on HM-spiro-MeOTAD (QP 48 h 40°C) using the same procedure as reported in Section 3.2.3. From the transfer characteristics at  $V_{DS} = -100$  V a saturation mobility of  $2.9 \pm 0.2 \times 10^{-5} \text{ cm}^2 \text{V}^{-1} \text{s}^{-1}$  can be derived for HM-spiro-MeOTAD (QP 48 h 40°C). This value is lower than that found under identical conditions for commercial spiro-MeOTAD, which yielded a hole mobility of  $4.6 \pm 0.5 \times 10^{-5} \text{ cm}^2 \text{V}^{-1} \text{s}^{-1}$ . Additionally, the measurements reveal an increased threshold voltage of  $-24 \pm 6$  V for HM-spiro-MeOTAD (QP 48 h 40°C) compared to  $-5 \pm 2$  V found in the case of spiro-MeOTAD. The results are summarized in Table 3.5.

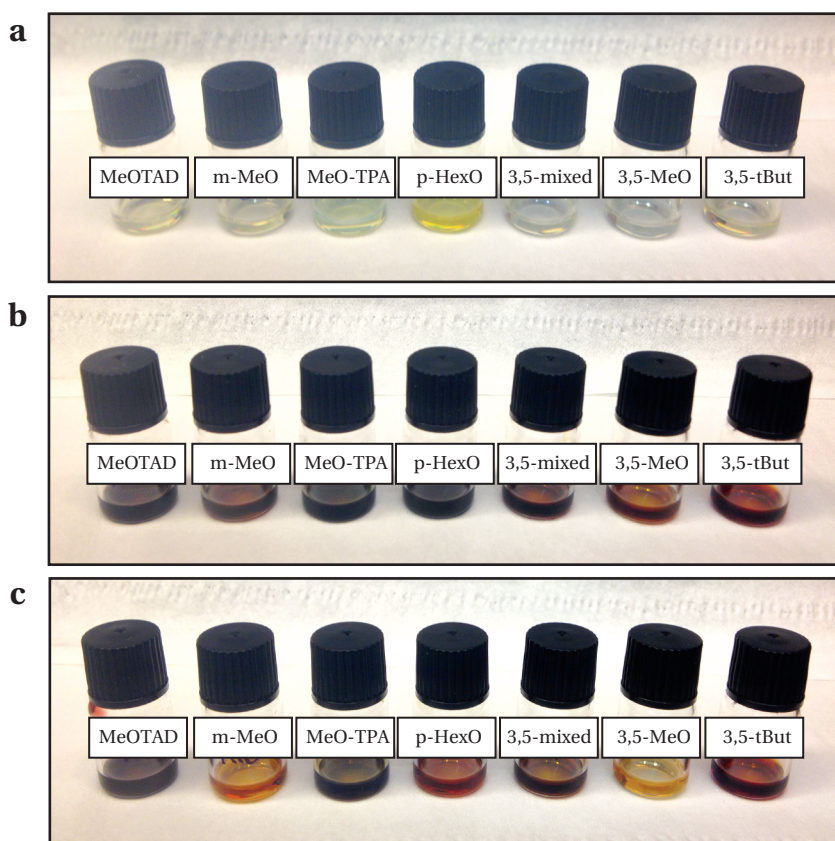
**Effect of 4-*tert*-butylpyridine on oxidized HTM solutions.** As explained in Section 1.5.3, LiTFSI and 4-*tert*-butylpyridine are the two additives that are commonly added to the HTM spin-coating formulation to ensure an efficient device functioning. These two additives have therefore been employed in all ssDSCs based on the new HTMs presented in this chapter. Nevertheless, for many of the new HTMs I observed an unusual behaviour when preparing the spin-coating solution: a decolouration of the oxidized HTM solution upon the addition of TBP. This effect is illustrated in Figure 3.14.

Figure 3.14 a shows a set of chlorobenzene solutions of spiro-MeOTAD and the six new HTMs spiro-m-MeO, spiro-MeO-TPA, spiro-HexO, spiro-3,5-mixed, spiro-3,5-MeO and spiro-3,5-tBut. Due to their large bandgap, all materials appear as almost colourless, pale yellow when in solutions. Neither of the additives was added at this stage. The slight variation in colour can be attributed to small differences in the bandgap of the materials. Upon the addition of the Co(III) oxidant FK269 (3.2%), an immediate colour change to dark red/orange was observed for all materials, which confirms the formation of the oxidized species (Figure 3.14 b). The coloration of the solutions persists for at least 3 h, indicating that the cation radical is (at least kinetically) stable in all cases. However, upon the addition of TBP, a quick decolouration of the solution, that occurs within minutes, can be observed for some of the materials (Figure 3.14 c). Strong colour changes are especially noticeable for spiro-m-MeO, spiro-3,5-MeO and spiro-HexO. It is important to note that no colour change occurs even after several days for a solution of spiro-MeOTAD and that no trend can be identified that links the decolouration to a specific type or position of the substituents on the triarylamine units. It is also worth mentioning that the subsequent addition of LiTFSI does not have any visible effect and that the decolouration



occurs only upon the addition of TBP. From this data it is not clear whether the disappearance of the intense colour is related to the reversible reduction of the cation radical, which would lead to 'de-doping', or to its degradation. However, as TBP is a nucleophile it seems plausible that it could act as a reducing agent for the oxidized HTM—a reaction that seems to take place only in the presence of the palladium impurities, which could act as a catalyst.

The same experiment was carried out for the different batches of HM-spiro-MeOTAD. Surprisingly, one can observe a similar colour change for HM-spiro-MeOTAD as in the case of the new HTMs, which suggest that the decolouration must be linked to the presence of impurities. The cation radical of spiro-MeOTAD is known to be stable and solutions of the commercial spiro-MeOTAD do not show any evidence of degradation. A decolouration is also observed in the case of the QP-treated HM-spiro-MeOTAD (QP 48 h 40°C), suggesting that a fraction of the impurities must still be present after the QP purification.



**Figure 3.14** — Influence of the addition of TBP on the color of oxidized HTM solutions. On the labels, the 'spiro-' prefix has been omitted in all cases. a) HTM solutions in chlorobenzene. b) HTM solutions after the addition of 3.2% FK269 oxidant. c) Oxidized HTM solution after the addition of TBP.



### 3.3 Conclusion and perspective

We successfully synthesized seven new 9,9'-spirobifluorene derivatives as potential replacements for spiro-MeOTAD in ssDSCs. One of the materials, spiro-p-tBut, exhibited a very low solubility in organic solvent and was therefore not investigated further.

All six remaining materials were characterized by electrochemical measurements in solution and photoelectron spectroscopy in air. Both techniques confirmed a lower HOMO level of about 0.2 eV compared to spiro-MeOTAD for two of the materials, spiro-m-MeO and spiro-MeO-TPA, which was one of the primary goals of the design of these compounds. Interestingly, by means of cyclic voltammetry and differential pulse voltammetry it was found that in the case of spiro-MeO-TPA, all four oxidation states possess the same redox potential. This might be a valuable property for solar cell application, as in the case of spiro-MeOTAD the dismutation has been proposed as one of the possible degradation mechanisms.

In order to evaluate the hole mobilities of the new materials, solution-processed organic field-effect transistors were fabricated and characterized. From these measurements it was evidenced that all six materials exhibit lower hole mobilities compared to spiro-MeOTAD. This trend was attributed to the influence of the different substituents on the triarylamine moieties that hinder charge transport due to larger intermolecular distances. The highest mobilities amongst the series of new materials were achieved with spiro-m-MeO and spiro-MeO-TPA. One of the materials, spiro-p-HexO, did not show any electric conduction and, moreover, readily crystallized during a low temperature annealing at 100°C.

The two most promising materials, spiro-m-MeO and spiro-MeO-TPA, were investigated in a typical solid-state dye-sensitized solar cell configuration using the Y123 sensitizer. These devices exhibited a very high series resistance, leading to low fill factors and power conversion efficiencies. The high series resistance is likely to result from the lower hole mobility. Whereas the short-circuit photocurrents obtained at high light intensities were significantly lower compared to spiro-MeOTAD, very similar photocurrents were found for spiro-m-MeO and spiro-MeO-TPA under low light conditions. This suggests that the regeneration of oxidized dye molecules occurs efficiently, despite an energy driving force of only 50–80 meV. It was postulated that the low photocurrents observed at full sunlight intensity are a direct result of the lower charge carrier mobility and not the high series resistance. This argumentation was strengthened by the fact that the series resistance of the devices could be lowered by the use of large amounts of a *p*-dopant, which, however, did not affect the short-circuit photocurrent.

The influence of the purity of the hole-transporting material was investigated by using a batch of spiro-MeOTAD that was synthesized in our lab for the fabrication of solid-state dye-sensitized solar cells. The characterization of these devices revealed a very low performance of the homemade spiro-MeOTAD compared to commercial spiro-MeOTAD, indicating the presence of impurities in our materials. Part of the impurities could be removed by purification using thiourea-functionalized polystyrene beads as a metal scavenger. This purification led to a solar cell performance of the homemade spiro-MeOTAD close to the one of commercial

spiro-MeOTAD. However, transistor measurements showed that the purified homemade spiro-MeOTAD still has a lower hole mobility than the commercial spiro-MeOTAD. This suggests that the impurities could not be removed completely by the purification step using the metal scavenger. It is important to note that mobility that was achieved with spiro-MeO-TPA is in the same range as the one obtained for the purified homemade spiro-MeOTAD.

The purity of the materials could also be related to a decolouration of the oxidized HTM solution upon the addition of 4-*tert*-butylpyridine that was observed in some cases.

In conclusion, spiro-MeO-TPA showed the highest potential to replace spiro-MeOTAD in solid-state dye-sensitized solar cells, although its initial photovoltaic performance was low. However, before further studies on the device performance can be carried out, the purity of the material needs to be scrutinized. Due to the benefit of the purification using a metal scavenger, we suspect palladium that is used during the synthesis to be the major impurity. Trace metal analysis by inductively coupled plasma mass spectroscopy could help to quantify the amount of palladium in the material and help to solve the purity issue.

## 4 Mesoscopic perovskite-sensitized solar cells

*The following chapter describes the use of a sequential deposition technique for the fabrication of perovskite-based mesoscopic solar cells. The work presented in this chapter is partially based on an article that has been published in a peer-reviewed journal [175]. The photovoltaic data presented in this chapter has been obtained partly in a joint collaboration with Norman Pellet, LPI, EPFL.*

### 4.1 Introduction

Despite achieving remarkable power conversion efficiencies (*PCEs*) of up to 7.2% for the spiro-MeOTAD-based system [59], the performance of solid-state dye-sensitized solar cells (ssDSCs) has always been much lower compared to their liquid counterparts, that presently reach power conversion efficiencies of over 12% [94]. This difference arises mainly from the 10–100 times faster charge carrier recombination in the solid-state device compared to the liquid DSC [150]. In order to reduce the recombination and collect the majority of the photogenerated charge carriers, the thickness of the nanocrystalline oxide film is usually kept below 3  $\mu\text{m}$ , limiting the amount of light harvested by the molecular sensitizer and hence the short-circuit photocurrent of the device. One possibility to overcome the problem of light-harvesting is the development of organic sensitizers with a very high molar extinction coefficient that allow for complete absorption, even in the case of thin metal oxide films. In fact, the progress in terms of power conversion efficiency, that has been achieved in recent years in the field of ssDSCs is mainly due to the development of new dyes. However, despite quantitative absorbance, the incident photon-to-electron conversion efficiency of such devices rarely exceeds peak values of 70%, suggesting that the issue of charge collection is still not fully resolved. This can, for instance, be observed in the currently best performing ssDSC system based on a molecular dye (Y123) and a 2  $\mu\text{m}$  thick mesoporous  $\text{TiO}_2$  film as presented in Section 2.2.1.4.

To further increase the power conversion efficiency, the charge collection efficiency needs to be improved. This can be done either by slowing down the electron-hole recombination rate or by reducing the film thickness. This chapter focuses on the latter strategy that demands the

development of light absorbers with a higher absorption coefficient.

### 4.1.1 Inorganic absorbers in ssDSCs

Inspired by inorganic thin-film photovoltaics, many attempts have been made to increase the optical absorption cross-section of the light-harvesters in the solid-state DSC, by replacing the molecular sensitizer with an inorganic absorber. In particular, metal chalcogenides have gained notable attention due to their high absorption coefficient and suitable bandgap.

Semiconductor quantum dots (QDs) such as PbS [23, 176–178], CdS [176, 179, 180], CdSe [181] or their combinations [182] have been used in a typical mesoscopic ssDSC configuration using spiro-MeOTAD as the hole-conductor. However, in most cases, the *PCE* remained below 1.0%. It is worth noting that the low efficiency seems to be somewhat related to an unfavourable interaction between the metal chalcogenide quantum dot layer and the spiro-MeOTAD hole-conductor, as *PCEs* of over 5.0% could be reached when using similar quantum dots in conjunction with a liquid redox electrolyte [183–185].

A problem that is frequently encountered in the field of QD-sensitized solar cells is the inefficient infiltration of the QDs into the mesoporous metal oxide structure. Moreover, QDs that are traditionally synthesized in solution—which allows for a better control of crystal shape and size—are usually protected by a capping agent that prevents agglomeration or Oswald ripening. Nevertheless, this capping layer has to be removed once the QDs have been deposited on the metal oxide film, as it would hinder an efficient charge transport through the QD layer. Therefore, the in situ formation of the metal chalcogenide absorber within the pores of the metal oxide host would be preferable. Indeed, most of the highly efficient QD-sensitized solar cells follow this strategy [183, 184] and employ the successive ionic layer adsorption and reaction (SILAR) technique for the deposition of the absorber, where a substrate is alternately dipped in two precursor solutions. During SILAR the solution concentration, the dipping time and the number of dipping cycles allow for a relative good control of the quantum dot size.

In 2010, Moon et al. [186] reported on the use of  $\text{Sb}_2\text{S}_3$  as an absorber.  $\text{Sb}_2\text{S}_3$  was deposited onto 1  $\mu\text{m}$  thick mesoporous  $\text{TiO}_2$  films by chemical bath deposition, yielding a *PCE* of 3.1% with spiro-MeOTAD as the hole-transporting material (HTM). This value was later improved to up to 6.3% by replacing spiro-MeOTAD with poly(3-hexylthiophene) (P3HT) [140, 187].

More recently, Kojima et al. [188] introduced solution-processable hybrid organic–inorganic perovskites of the formula  $\text{CH}_3\text{NH}_3\text{PbX}_3$  ( $\text{X} = \text{Br}, \text{I}$ ) as sensitizers for DSCs reaching a *PCE* of 3.8% in conjunction with mesoporous  $\text{TiO}_2$  and a triiodide/iodide-based liquid electrolyte. Im et al. [189] later improved the *PCE* to 6.5% by optimizing the composition of the redox electrolyte. In both cases the photovoltaic devices suffered from poor stability due to the rapid dissolution of the perovskite in the liquid electrolyte. This problem could be overcome by using a solid-state configuration, employing spiro-MeOTAD as a hole-transporter. In this manner Kim et al. [190] achieved a *PCE* of 9%. At the same time, Lee et al. [191] showed that

such a device works even better when the semiconducting mesoporous  $\text{TiO}_2$  film was replaced by an insulating  $\text{Al}_2\text{O}_3$  scaffold, indicating rapid electron transport through the perovskite phase. With a champion cell, Lee et al. reached an impressive *PCE* of 10.3%, a value that was later improved by the same group to 12.3% [192]. Since these pioneering works, numerous reports have followed this concept [193–196].

#### 4.1.2 Organic–inorganic hybrid perovskites

Perovskites constitute a class of materials that all possess the same type of crystal structure as their parent compound, calcium titanate  $\text{CaTiO}_3$ . They have the general formula  $\text{ABX}_3$ , where A and B are cations—A is larger than B—and X are the anions. The ideal perovskite structure has a cubic symmetry, where the B cation is 6-fold coordinated by X in an octahedral configuration. Likewise, the A cation is 12-fold coordinated by X in a cuboctahedral configuration and is situated in the center of a cube formed by corner-sharing  $\text{BX}_6$  octahedra as illustrated in Figure 4.1 a.

The organic–inorganic hybrid perovskites are a special class of perovskites, where A is a small, monovalent organic cation such as methylammonium ( $\text{CH}_3\text{NH}_3^+$ ) [197, 198], ethylammonium ( $\text{CH}_3\text{CH}_2\text{NH}_3^+$ ) [199], tetramethylammonium ( $\text{N}(\text{CH}_3)_4^+$ ) [200, 201], formamidinium ( $\text{NH}_2\text{CHNH}_2^+$ ) [202, 203] or guanidinium ( $\text{C}(\text{NH}_2)_3^+$ ) [204, 205]. B is a divalent group 14 metal (Ge, Sn or Pb) and X are halides (Cl, Br or I). Not all possible combinations of the aforementioned cations and anions have been reported yet and not all of the existing hybrid perovskites have an ideal perovskite structure with cubic symmetry.

Depending on the size of the two cations, the three-dimensional (3D) ideally cubic perovskite structure of the formula  $\text{ABX}_3$  stands in competition with a two-dimensional (2D) layered structure of the general formula  $\text{A}_2\text{BX}_4$ . The 2D layered perovskite structure is composed of layers of corner-sharing  $\text{BX}_6$  octahedra that are separated by a double layer of organic cations.

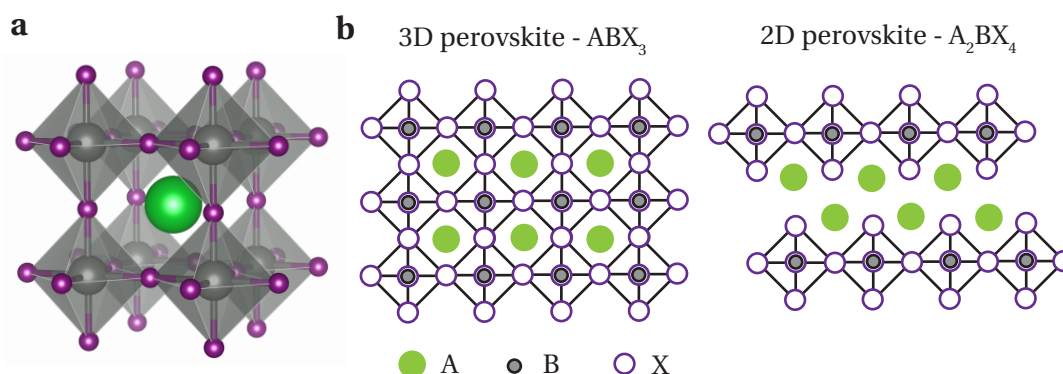


**Figure 4.1** — a) Perspective view of the  $\text{ABX}_3$  perovskite crystal structure. b) Projected view of the 3D perovskite ( $\text{ABX}_3$ ) and the 2D layered perovskite ( $\text{A}_2\text{BX}_4$ ),

Projected views of the two structures are illustrated in Figure 4.1 b. For several of the above-mentioned hybrid perovskites, both phases—the 2D phase and the 3D phase—may coexist, which sometimes renders the synthesis of phase-pure materials difficult. Organic cations that are larger than the ones mentioned before exclusively form the 2D layered perovskite structure. The 2D structure basically does not limit the size of the organic cation and also allows to replace the two monovalent organic cations by a divalent organic cation. The 2D layered perovskites have been extensively studied and reviewed by Mitzi et al. [206].

Regarding the 3D hybrid perovskites, especially the iodoplumbates ( $B = \text{Pb}^{2+}$ ,  $X = \text{I}^-$ ) and iodostannates ( $B = \text{Sn}^{2+}$ ,  $X = \text{I}^-$ ) have gained particular interest due to their low bandgaps and unusually high electronic conductivity. Even more astonishing is their good solubility in polar organic solvents that makes them very attractive for solution-processed electronics.

### 4.1.3 Methyl ammonium lead iodide – $\text{CH}_3\text{NH}_3\text{PbI}_3$

Methyl ammonium lead iodide  $\text{CH}_3\text{NH}_3\text{PbI}_3$  has received the most attention for solar cell applications, mainly due to having a suitable bandgap, its ease of processing and air stability. Pb is the only element of the group 14 metals that is stable in its +2 oxidation state. In contrast, the tin analogues of  $\text{CH}_3\text{NH}_3\text{PbI}_3$  are oxygen sensitive due to the facile oxidation of  $\text{Sn}^{2+}$  to  $\text{Sn}^{4+}$ , which hampers the practical application of this material. Although  $\text{CH}_3\text{NH}_3\text{PbI}_3$  is stable towards oxidation, it degrades within days when exposed to humid air because of the presence of the hygroscopic organic cation. However, this degradation process is rather slow which allows for a characterization and handling of the material in ambient conditions.

$\text{CH}_3\text{NH}_3\text{PbI}_3$  has a direct bandgap of 1.54 eV, corresponding to an absorption onset of about 800 nm. This can be seen in Figure 4.2 a, which shows the scatter-free absorption spectrum of a thin  $\text{CH}_3\text{NH}_3\text{PbI}_3$  film. Figure 4.2 a also displays the room-temperature photoluminescence of the same film that peaks at about 775 nm (excitation at 460 nm).

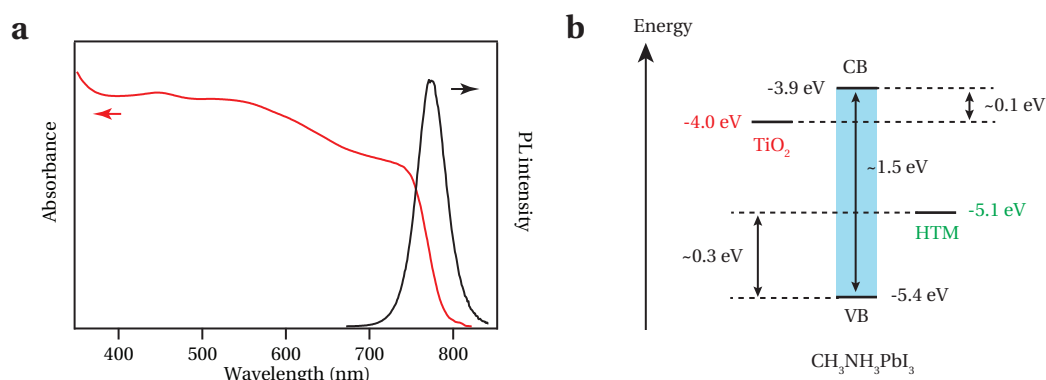


**Figure 4.2** — a) Scatter-free absorption and photoluminescence (PL) spectra of a thin film of  $\text{CH}_3\text{NH}_3\text{PbI}_3$ . The excitation wavelength was 460 nm. b) Energy scheme illustrating the position of the conduction band (CB) and valence band (VB) of  $\text{CH}_3\text{NH}_3\text{PbI}_3$  with respect to the conduction band of  $\text{TiO}_2$  and the HOMO of the HTM.

The position of the valence band (VB) of the  $\text{CH}_3\text{NH}_3\text{PbI}_3$  perovskite has been found at  $-5.4$  eV vs. vacuum by ultraviolet photoelectron spectroscopy [190]. With a bandgap of  $1.54$  eV, the conduction band (CB) lies at about  $-3.9$  eV. A scheme that depicts the energetic levels of the perovskite compared to  $\text{TiO}_2$  and spiro-MeOTAD is shown in Figure 4.2 b. Based on the aforementioned values for the CB and the VB of  $\text{CH}_3\text{NH}_3\text{PbI}_3$  the driving forces for the electron injection into the  $\text{TiO}_2$  CB and the hole injection into the HOMO level of the HTM are  $0.1$  and  $0.3$  eV, respectively. It is worth mentioning, that the VB and the CB of the organic–inorganic hybrid perovskite  $\text{CH}_3\text{NH}_3\text{PbI}_3$ , are formed exclusively from atomic orbitals belonging to the Pb and I atoms. The organic cation does not participate electronically, but directs the formation of the perovskite crystal structure and is therefore responsible for the optical and electric properties of the material.

Three different crystal phases have been observed for  $\text{CH}_3\text{NH}_3\text{PbI}_3$  [207]. At elevated temperature ( $T > 54^\circ\text{C}$ ),  $\text{CH}_3\text{NH}_3\text{PbI}_3$  crystallizes in the ideal cubic perovskite phase. In the cubic phase the  $\text{CH}_3\text{NH}_3^+$  cation can occupy 24 different disordered states, but undergoes rapid reorientation [208]. In the temperature range of  $54^\circ\text{C} > T > -112^\circ\text{C}$ , the symmetry of the perovskite structure reduces to a tetragonal phase due to a tilting of the  $\text{PbI}_2$  octahedra around the  $c$ -axis. In this phase the number of disordered states for the  $\text{CH}_3\text{NH}_3^+$  cation is reduced to 8. At low temperature ( $T < -112^\circ\text{C}$ ) the  $\text{CH}_3\text{NH}_3\text{PbI}_3$  perovskite adopts a crystal phase of orthorhombic symmetry, in which the  $\text{CH}_3\text{NH}_3^+$  cation is fixed. A 2D layered perovskite phase of the type  $\text{A}_2\text{BX}_4$  has not been reported for  $\text{CH}_3\text{NH}_3\text{PbI}_3$ , which is advantageous for practical applications as the phase purity becomes less of an issue.

In general, the hybrid perovskites have a very strong tendency to form and crystallize, even at room temperature. This enables the convenient deposition of the perovskite by solution-processing, using a solution of two precursors, e.g.  $\text{PbI}_2$  and  $\text{CH}_3\text{NH}_3\text{I}$  in the case of  $\text{CH}_3\text{NH}_3\text{PbI}_3$ . During the solution-processing the perovskite crystallizes on the substrate due to the evaporation of the organic solvent. A low temperature annealing is subsequently

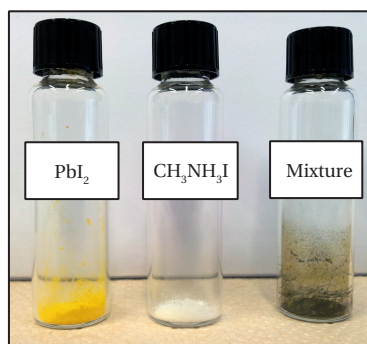


**Figure 4.3** — Formation of  $\text{CH}_3\text{NH}_3\text{PbI}_3$  in a solid-state reaction by a simple mixing of the two precursors:  $\text{PbI}_2$  and  $\text{CH}_3\text{NH}_3\text{I}$ .



employed in some cases, which serves only to facilitate the solvent evaporation, but is not necessary to obtain the perovskite in its crystalline form. Due to the high energy of formation, the hybrid perovskites form even in a solid-state reaction, when the two precursors are brought into contact. This is illustrated in Figure 4.3—upon the simple mixing of the two solid precursors, a colour change to dark brown is observed, indicating the formation of the  $\text{CH}_3\text{NH}_3\text{PbI}_3$  perovskite.

### 4.1.4 Motivation and strategy

As discussed above, one of the main advantages of  $\text{CH}_3\text{NH}_3\text{PbI}_3$  is its solubility in organic solvents that allows for a deposition by solution-processing. In all previous work that has been cited in the introductory paragraph, the perovskite pigment was applied by spin-coating a solution of the two precursors,  $\text{PbX}_2$  ( $X = \text{I}, \text{Br}$  or  $\text{Cl}$ ) and  $\text{CH}_3\text{NH}_3\text{I}$ , in a common solvent, i.e. *N,N*-dimethylformamid (DMF) or  $\gamma$ -butyrolactone (GBL). Although remarkable power conversion efficiencies have been obtained following this procedure, we find that it leads to rather large variations in the crystal morphology, as the perovskite crystallization during the solution-processing is poorly controlled. This variation in film morphology might be one of the reasons why the reproducibility of the device performance has been reported to be an

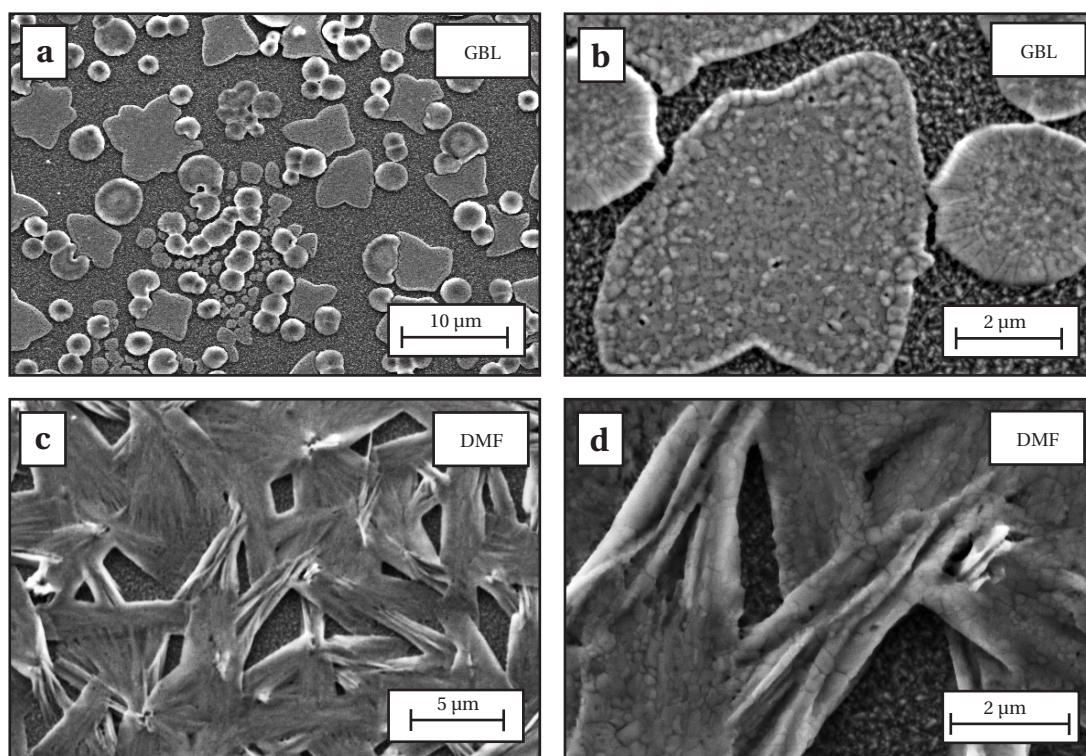


**Figure 4.4** — Perovskite thin films deposited by spin-coating from a solution of  $\text{PbI}_2$  and  $\text{CH}_3\text{NH}_3\text{I}$  in a, b)  $\gamma$ -butyrolactone (GBL) and c, d) *N,N*-dimethylformamide (DMF). The structure that is visible between the islands/needles is the  $\text{TiO}_2$ -coated FTO substrate.



issue.

The variation of the crystal morphology is illustrated in Figure 4.4. The figure shows scanning electron microscopy (SEM) images of  $\text{CH}_3\text{NH}_3\text{PbI}_3$  thin films on flat  $\text{TiO}_2$  coated fluorine doped tin-oxide (FTO) glass substrates, deposited by spin-coating from two different solvents: GBL and DMF. In the case of GBL, perovskite islands of different sizes and shapes are obtained (Figure 4.4 a, b), whereas the solution-processing from DMF yields large needle-shaped crystals that grow from the substrate (Figure 4.4 c, d). In both cases, large areas of the  $\text{TiO}_2$ /FTO substrate are exposed. Although the formation of large crystals might be hindered when the perovskite is deposited onto a mesoscopic metal oxide film, very similar morphologies are still observed on top of the porous structure [141, 196].

We suspected that for solar cell applications the ideal morphology of the perovskite absorber would be a conformal film that fully covers the internal surface of the porous  $\text{TiO}_2$  structure. In the photovoltaic device any exposed  $\text{TiO}_2$  that is in contact with the hole-transporting material leads to undesired electron–hole recombination and the loss of photogenerated charge carriers. Therefore, we sought to develop a technique that allows for a better control over the perovskite morphology during the solution-processing, finally aiming for a better reproducibility of the photovoltaic device performance.

## 4.2 Results and discussion

### 4.2.1 $\text{CH}_3\text{NH}_3\text{PbI}_3$ formed by sequential deposition

Inspired by the possibility to synthesize  $\text{CH}_3\text{NH}_3\text{PbI}_3$  in a simple solid-state reaction, we employ a technique that is based on the formation of the perovskite in two steps. Such a technique has previously been reported by Liang et al. [209]. The procedure that we employ is illustrated in Figure 4.5. First,  $\text{PbI}_2$  is deposited on a substrate by spin-coating from a DMF solution. Notably, I found that due to the coordinating nature of DMF,  $\text{PbI}_2$  solutions of very high concentration can be prepared using this solvent. The dry  $\text{PbI}_2$  film is then dipped into a solution of  $\text{CH}_3\text{NH}_3\text{I}$  in a solvent that does not readily dissolve the  $\text{PbI}_2$ , e.g. 2-propanol. Within a few seconds of bringing the two materials into contact, a color change from yellow to dark brown occurs, indicating the rapid formation of  $\text{CH}_3\text{NH}_3\text{PbI}_3$ .

The literature describes several examples in which a two-step procedure is used to fabricate nanostructures that are not easily—or not at all—accessible by a direct synthetic route. For example, ion exchange reactions have been used to convert dispersed II–V semiconductor nanocrystals into the corresponding III–V analogues while preserving particle size and distribution as well as the initial nanomorphology [210–212]. As reported, the thermodynamic driving force of such a reaction is the difference in bulk lattice energy for the two materials and the crystal morphology of the starting material serves as a template for the formation of the desired compound. As for  $\text{PbI}_2$ , the insertion of the organic cation is facilitated through the layered  $\text{PbI}_2$  structure, which consists of three spatially repeating planes, I–Pb–I, that form

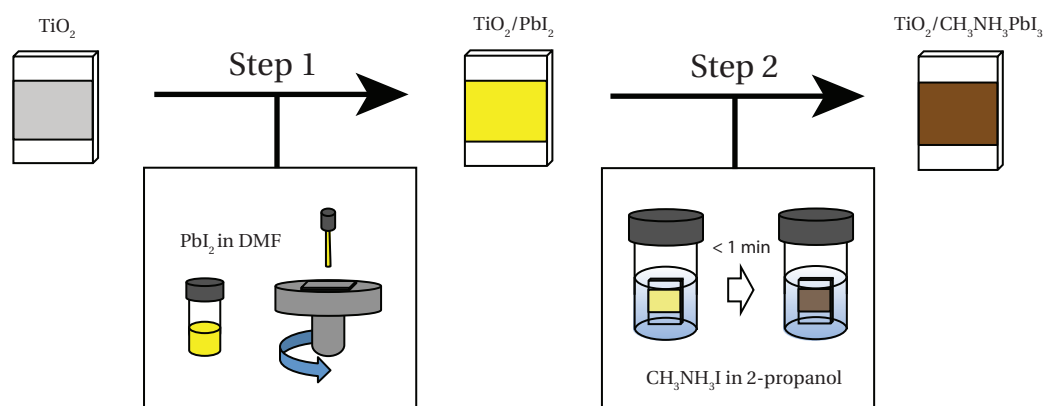


**Figure 4.5** — Scheme that illustrates the deposition of the  $\text{CH}_3\text{NH}_3\text{PbI}_3$  perovskite via the sequential deposition technique.  $\text{PbI}_2$  is first deposited via spin-coating (Step 1) and subsequently transformed into  $\text{CH}_3\text{NH}_3\text{PbI}_3$  by dipping in a solution of  $\text{CH}_3\text{NH}_3\text{I}$  (Step 2).

layers of edge-sharing  $\text{PbI}_6$  octahedra (Figure 4.6). Numerous literature reports show that a strong intralayer chemical bonding combined with only weak interlayer van der Waals interactions allows for an easy insertion of guest molecules between these layers [213–215]. I believe this to be one of the reasons for the surprisingly fast reaction kinetics of the transformation.

Due to the weak interlayer bonding, the I–Pb–I layers can stack in several arrangements, leading to a large number of different polytypes [216]. The most simple and also most common polytype of  $\text{PbI}_2$  is denoted as 2H. The letter H stands for hexagonal, which refers to the symmetry of the stacking arrangement, not the unit cell. The number 2 refers to twice the number of I–Pb–I layers that is necessary to reproduce the stacking sequence.

It is important to note, that the insertion of  $\text{CH}_3\text{NH}_3\text{I}$  into  $\text{PbI}_2$  results in an expansion of the crystal structure. From the lattice parameters (Table 4.1), a two-fold increase in volume

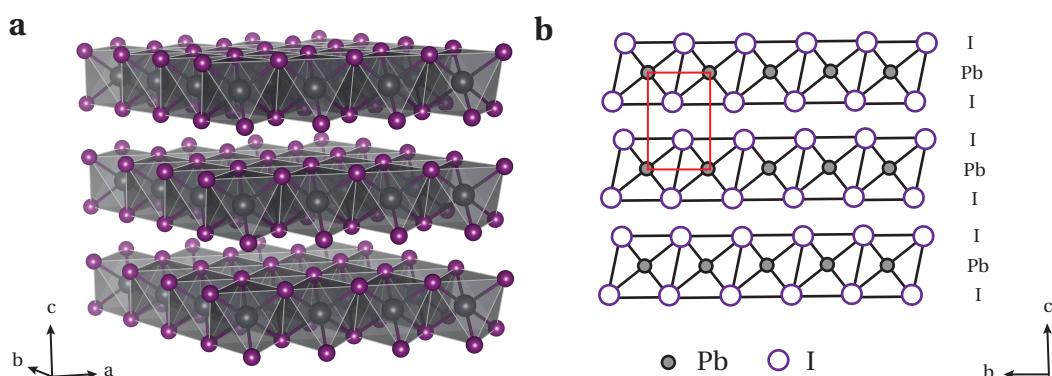


**Figure 4.6** — Crystal structure of  $\text{PbI}_2$ . a) 3D view and b) projected view along the  $a$ -axis. The displayed structure corresponds to the hexagonal 2H polytype. The red rectangle in panel b marks the unit cell.

**Table 4.1** — Comparison of  $\text{PbI}_2$  and  $\text{CH}_3\text{NH}_3\text{PbI}_3$ : crystal lattice parameters and values derived thereof.

		$\text{PbI}_2^a$	$\text{CH}_3\text{NH}_3\text{PbI}_3^b$
Crystal system		Trigonal	Tetragonal
Space group		P3m1	I4/mcm
Lattice parameters (Å)	$a$	4.558	8.874
	$b$	4.558	8.874
	$c$	6.986	12.67
Formula for unit cell volume		$a^2 c \sin(60^\circ)$	$a^2 c$
Unit cell volume (Å <sup>3</sup> )	$V$	125.7	997.9
Formula units per unit cell	$Z$	1	4
Volume per formula unit	$V/Z$	125.7	249.5
Molecular weight (g mol <sup>-1</sup> )	$M$	461.0	620.0
Density <sup>c</sup> (g cm <sup>-3</sup> )	$\rho$	6.090 (6.16)	4.127 (4.22)

<sup>a</sup> Lattice parameters taken from the Inorganic Crystal Structure Database, collection code 68819;

<http://www.fiz-karlsruhe.com/icsd.html>.

<sup>b</sup> Lattice parameters taken from [207].

<sup>c</sup> Density calculated from the lattice parameters. Values in brackets are taken from the literature:  $\text{PbI}_2$  [217] and  $\text{CH}_3\text{NH}_3\text{PbI}_3$  [197].

per formula unit can be estimated when transforming  $\text{PbI}_2$  to  $\text{CH}_3\text{NH}_3\text{PbI}_3$ . The calculated densities are 6.09 and 4.13 g cm<sup>-3</sup> for  $\text{PbI}_2$  and  $\text{CH}_3\text{NH}_3\text{PbI}_3$ , respectively. The different parameters are summarized in Table 4.1.

#### 4.2.2 Perovskite morphology investigated by scanning electron microscopy

In order to elucidate the changes in morphology during the insertion of  $\text{CH}_3\text{NH}_3\text{I}$  into the  $\text{PbI}_2$  structure,  $\text{PbI}_2$  was deposited by spin-coating on flat  $\text{TiO}_2/\text{FTO}$  substrates. The flat  $\text{TiO}_2$  layer had a thickness of 20–40 nm and was prepared by aerosol spray-pyrolysis as described in the experimental section (Section 6.7.2).

Figure 4.7 a, b shows cross-sectional SEM images of a typical  $\text{PbI}_2$  film obtained by spin-coating from DMF. The  $\text{PbI}_2$  film is composed of platelet-shaped  $\text{PbI}_2$  crystals that are between 50–200 nm in diameter and fully cover the  $\text{TiO}_2/\text{FTO}$  surface. The thin  $\text{TiO}_2$  layer that has been deposited on the FTO substrate is not resolved in these SEM images. The subsequent transformation of the as-deposited  $\text{PbI}_2$  film into  $\text{CH}_3\text{NH}_3\text{PbI}_3$  is achieved by dipping the film in a solution of  $\text{CH}_3\text{NH}_3\text{I}$  in 2-propanol. During the transformation the color of the film quickly (< 10 s) changes from yellow to dark brown, indicating the formation of the desired perovskite structure. Figure 4.7 c, d shows a SEM image taken after the transformation, employing a  $\text{CH}_3\text{NH}_3\text{I}$  solution concentration of 20 mg ml<sup>-1</sup> and a dipping time of about 10 minutes. Two main structural changes can be observed: on the one hand, large ribbon-structured as well as tetragonal-shaped crystals grow on top of the underlying  $\text{CH}_3\text{NH}_3\text{PbI}_3$  film, that somewhat maintained the initial  $\text{PbI}_2$  structure. But on the other hand, the latter becomes more and more porous as material is consumed during the crystal growth.

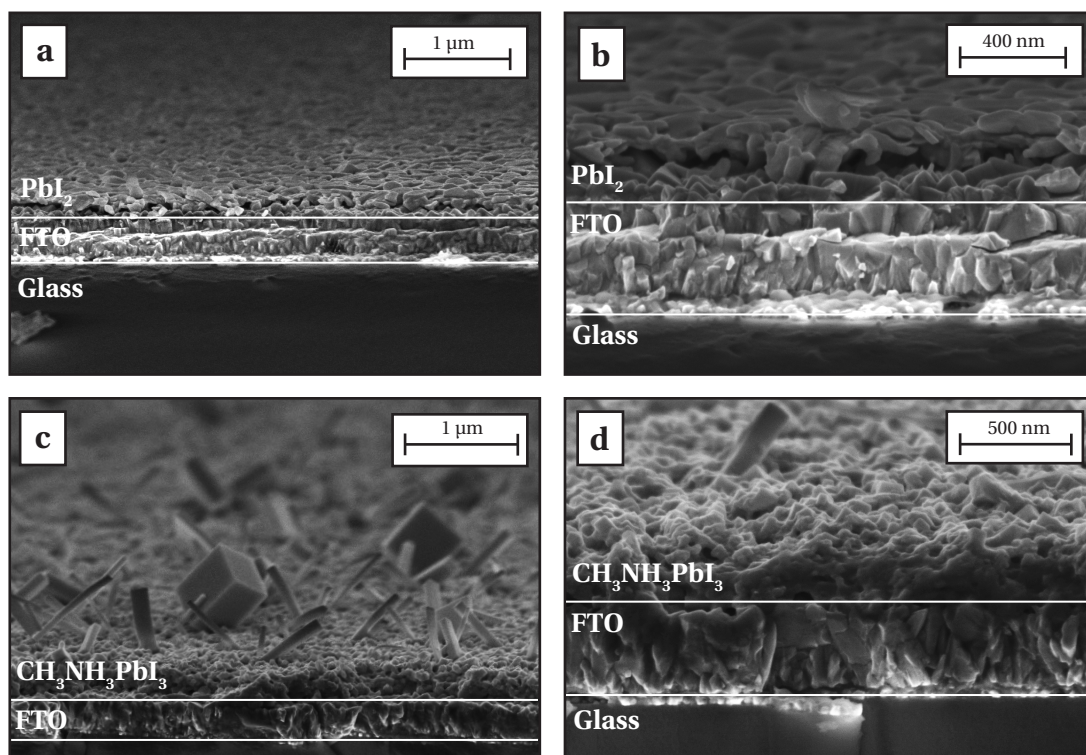


**Figure 4.7** — SEM images of a thin film of  $\text{PbI}_2$  deposited on a  $\text{TiO}_2$ -coated FTO substrate by spin-coating from a DMF solution a, b) before and c, d) after the dipping in a  $\text{CH}_3\text{NH}_3\text{I}$  solution in 2-propanol ( $20 \text{ mg ml}^{-1}$ ) for 10 min.

SEM images taken after varying dipping times that show how the number and size of the larger crystals changes are presented in Figure 4.8. The figure shows a top-view image of the bare  $\text{PbI}_2$  film (Figure 4.8 a) as well as images of similar films that have been dipped in a  $20 \text{ mg ml}^{-1}$   $\text{CH}_3\text{NH}_3\text{I}$  solution for 0.5, 2.0 and 45 min, respectively (Figure 4.8 b–d). From this data it is clear that the size of the larger crystals, as well as the porosity of the formerly relatively compact film, strongly depend on the dipping time. Moreover, it becomes evident that the crystal growth is slow compared to the actual insertion reaction, which is complete after less than 30 s. The kinetics of the reaction will be discussed in more detail in section 4.2.3.1. From the SEM images shown in Figure 4.8, it can be concluded that the unwanted growth of large perovskite crystals can be avoided when the dipping time is kept short, which is important for practical applications. It is worth mentioning that on the timescale of the reaction a significant dissolution of  $\text{PbI}_2$  into the  $\text{CH}_3\text{NH}_3\text{I}$ /2-propanol solution is not observed, which otherwise happens when the sample is left in the solution for several hours.

All SEM images that have been discussed so far were based on samples that have been prepared by employing a  $\text{CH}_3\text{NH}_3\text{I}$  solution concentration of  $20 \text{ mg ml}^{-1}$ . However, I found that the concentration of the  $\text{CH}_3\text{NH}_3\text{I}$  solution has a tremendous influence on the perovskite crystal morphology. Figure 4.9 shows SEM images of  $\text{CH}_3\text{NH}_3\text{PbI}_3$  films that were prepared by dipping in different  $\text{CH}_3\text{NH}_3\text{I}$  solutions, with concentrations ranging from 5 to  $40 \text{ mg ml}^{-1}$ .



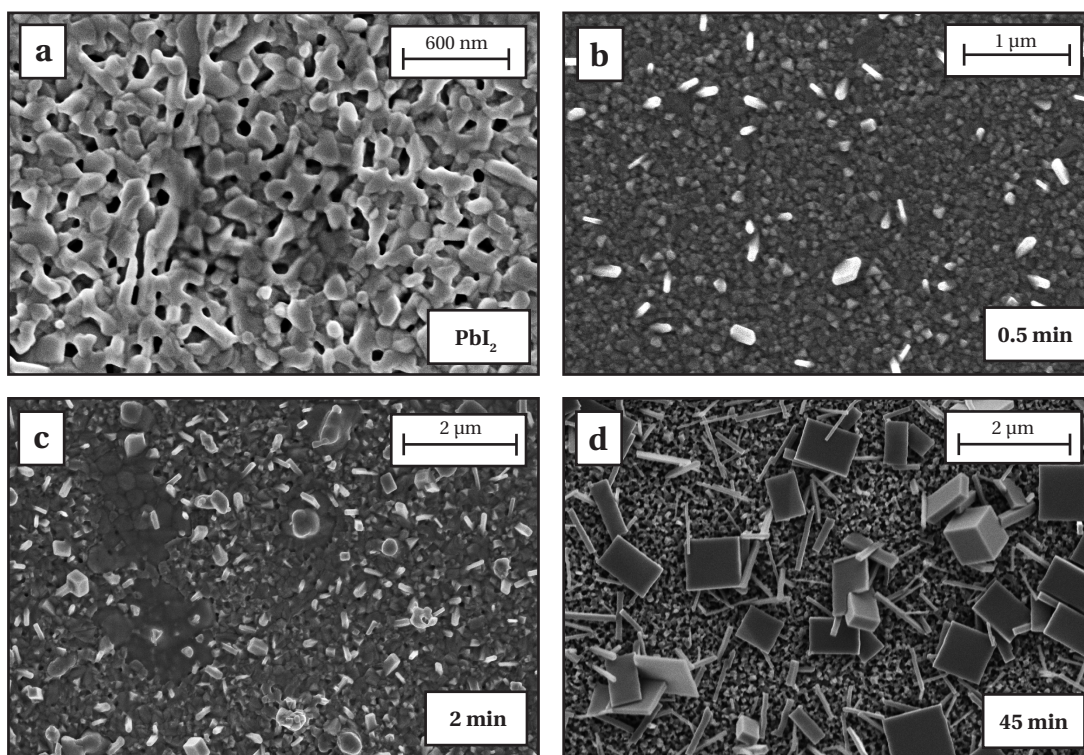


**Figure 4.8** — SEM images of thin films of  $\text{PbI}_2$  a) before and b-d) after dipping in a  $\text{CH}_3\text{NH}_3\text{I}$  solution in 2-propanol ( $20 \text{ mg ml}^{-1}$ ) for b) 0.5 min, c) 2 min and d) 45 min.

The dipping time was 60 s in all cases. From these images one can infer that the key parameter affecting the perovskite morphology is a change in the number of crystallization sites for the  $\text{CH}_3\text{NH}_3\text{PbI}_3$  crystal growth. I use the term ‘crystallization site’ instead of ‘nucleation site’, as the perovskite forms by insertion of  $\text{CH}_3\text{NH}_3\text{I}$  in an already existing  $\text{PbI}_2$  structure, and not by precipitation from solution. However, the exact mechanism that initiates the perovskite crystal growth is unclear.

A high  $\text{CH}_3\text{NH}_3\text{I}$  solution concentration generally results in a large number of crystallization sites, a small average crystal size and hence a smoother  $\text{CH}_3\text{NH}_3\text{PbI}_3$  surface. For a  $\text{CH}_3\text{NH}_3\text{I}$  solution concentration of  $40 \text{ mg ml}^{-1}$  we find a rather flat  $\text{CH}_3\text{NH}_3\text{PbI}_3$  surface from which larger ribbon- and tetragonal-shaped crystals protrude (Figure 4.9 b). Decreasing the concentration by a factor of two ( $20 \text{ mg ml}^{-1}$ ) has only little influence on the overall morphology, but affects the total number of  $\text{CH}_3\text{NH}_3\text{PbI}_3$  crystals protruding from the surface (Figure 4.9 c). Upon a further decrease of the  $\text{CH}_3\text{NH}_3\text{I}$  concentration to  $10 \text{ mg ml}^{-1}$  a significant change in the film morphology is observed: the obtained film is composed of much larger  $\text{CH}_3\text{NH}_3\text{PbI}_3$  crystals, resulting in a higher surface roughness (Figure 4.9 d). The trend of an increase in the crystal size and surface roughness with a decrease of the  $\text{CH}_3\text{NH}_3\text{I}$  solution concentration continues for concentrations of 8.75, 7.50 and  $6.25 \text{ mg ml}^{-1}$ , as depicted in Figures 4.9 e–g, respectively. It is observed that as the number of crystallization sites decreases

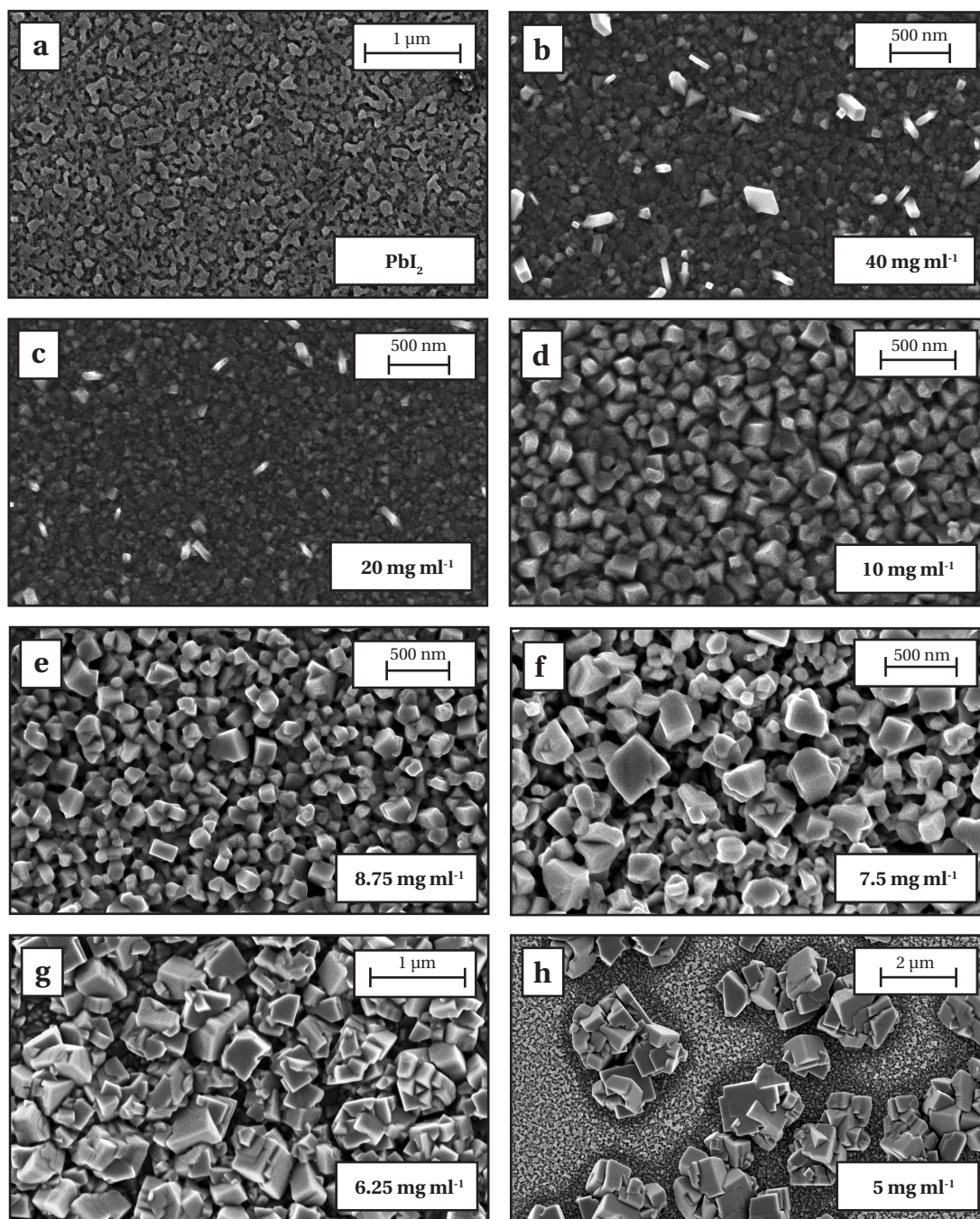


**Figure 4.9** — SEM images of thin films of  $\text{PbI}_2$  a) before and b–h) after dipping in a  $\text{CH}_3\text{NH}_3\text{I}$  solution in 2-propanol of varying concentration. The concentrations were: b) 40  $\text{mg ml}^{-1}$ , c) 20  $\text{mg ml}^{-1}$ , d) 10  $\text{mg ml}^{-1}$ , e) 8.75  $\text{mg ml}^{-1}$ , f) 7.5  $\text{mg ml}^{-1}$ , g) 6.25  $\text{mg ml}^{-1}$  and h) 5  $\text{mg ml}^{-1}$ . The dipping time was 60 s in all cases.

with the  $\text{CH}_3\text{NH}_3\text{I}$  solution concentration, the growth of larger crystals and the high surface roughness lead to the exposure of the  $\text{TiO}_2$ -coated FTO substrate. For a concentration of 5  $\text{mg ml}^{-1}$ , unreacted  $\text{PbI}_2$  that remains due to the large spacing between the perovskite



crystals is visible in the SEM (Figure 4.9 h). In Figure 4.9 h, the dark area around the perovskite crystals is the exposed  $\text{TiO}_2/\text{FTO}$  substrate, whereas the lighter area farther away from the crystals is the unreacted  $\text{PbI}_2$ . This becomes evident from the comparison with the bare  $\text{PbI}_2$  shown in Figure 4.9 a.

In order to obtain further insight into the mechanism of the perovskite crystal growth, the change in morphology was also investigated for much short dipping times and a  $\text{CH}_3\text{NH}_3\text{I}$  solution concentration of  $6.25 \text{ mg ml}^{-1}$ . SEM images for dipping times of 5, 10 and 20 s are shown in Figure 4.10. After a dipping time of 5 s, only part of the  $\text{PbI}_2$  is transformed into  $\text{CH}_3\text{NH}_3\text{PbI}_3$  as can be seen from Figure 4.10 a that shows a few perovskite crystals and unreacted  $\text{PbI}_2$  between them. After 10 s (Figure 4.10 b) the number and size of the perovskite crystals has increased, but unreacted  $\text{PbI}_2$  is still visible. Only after a dipping time of 20 s does the  $\text{PbI}_2$  seem to be transformed completely, as no unreacted  $\text{PbI}_2$  is visible in the SEM (Figure 4.10 c) and the bare  $\text{TiO}_2/\text{FTO}$  substrate is exposed between the perovskite crystals.

It is important to note, that the rate of conversion depends on the concentration of the  $\text{CH}_3\text{NH}_3\text{I}$  solution. A lower solution concentration leads to slower reaction kinetics. Therefore, it is difficult to elucidate the growth of the perovskite crystals for high concentrations of the  $\text{CH}_3\text{NH}_3\text{I}$  solution, as the reaction is complete in less than ten seconds. It has to be considered that the dipping time is not only composed of the true dipping time, but also the time that is needed to remove the excess  $\text{CH}_3\text{NH}_3\text{I}$  solution by spin-coating.

In general I find small fractions of unreacted  $\text{PbI}_2$  by X-ray diffraction spectroscopy (XRD) for all samples on flat  $\text{TiO}_2/\text{FTO}$ . The exact amount of unreacted  $\text{PbI}_2$  is difficult to quantify by XRD and strongly depends on the  $\text{CH}_3\text{NH}_3\text{I}$  solution concentration. Moreover, the exact location of the unreacted  $\text{PbI}_2$  is still unclear. This data will be discussed in detail in Section 4.2.4.

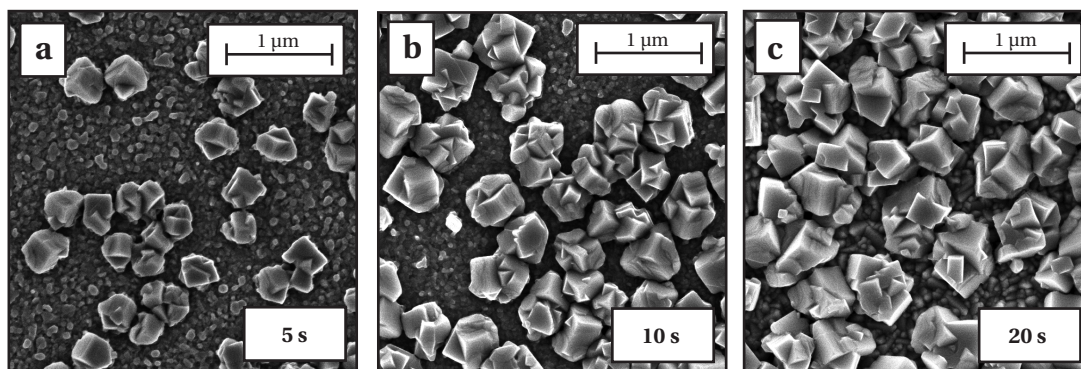


**Figure 4.10** — SEM images of thin films of  $\text{PbI}_2$  after dipping in a  $\text{CH}_3\text{NH}_3\text{I}$  solution in 2-propanol ( $5 \text{ mg ml}^{-1}$ ) for different times: a) 5 s, b) 10 s and c) 20 s.

### 4.2.3 Kinetics of the transformation reaction

In order to elucidate the kinetics of the transformation of  $\text{PbI}_2$  into  $\text{CH}_3\text{NH}_3\text{PbI}_3$ , we conducted optical absorption and emission spectroscopy measurements. A detailed description of the experimental conditions for these measurements can be found in the experimental section (Section 6.2). Briefly,  $\text{PbI}_2$  was deposited on either bare or mesoporous  $\text{TiO}_2$ -coated microscope glass slides. A sample was then placed vertically in a cuvette of 10 mm path length. Subsequently, a solution of  $\text{CH}_3\text{NH}_3\text{I}$  in 2-propanol ( $10 \text{ mg ml}^{-1}$ ) was rapidly injected into the cuvette while measuring the optical transmission or photoluminescence of the sample.

In general there are three different methods to monitor the kinetics of the transformation reaction: via the  $\text{CH}_3\text{NH}_3\text{PbI}_3$  absorption, via the  $\text{CH}_3\text{NH}_3\text{PbI}_3$  photoluminescence or via the  $\text{PbI}_2$  photoluminescence. The three approaches will be discussed in detail in the following paragraphs.

**$\text{CH}_3\text{NH}_3\text{PbI}_3$  absorption.** Firstly, the reaction can be monitored via the increase in the optical absorption due to the formation of the perovskite. The increase can be monitored at different wavelengths, preferably at a wavelength at which  $\text{PbI}_2$  does not absorb. The bandgap of  $\text{PbI}_2$  is about 2.5 eV, corresponding to an absorption onset of about 500 nm. Any wavelength between 500 nm and the absorption onset of the perovskite absorber (800 nm) should therefore be suitable to monitor the formation of  $\text{CH}_3\text{NH}_3\text{PbI}_3$ . The absorption spectra of thin films of  $\text{PbI}_2$  and  $\text{CH}_3\text{NH}_3\text{PbI}_3$  are shown in Figure 4.11 a, b. Practically, a change in the optical transmission is measured. Hence, the obtained signal is composed not only of real

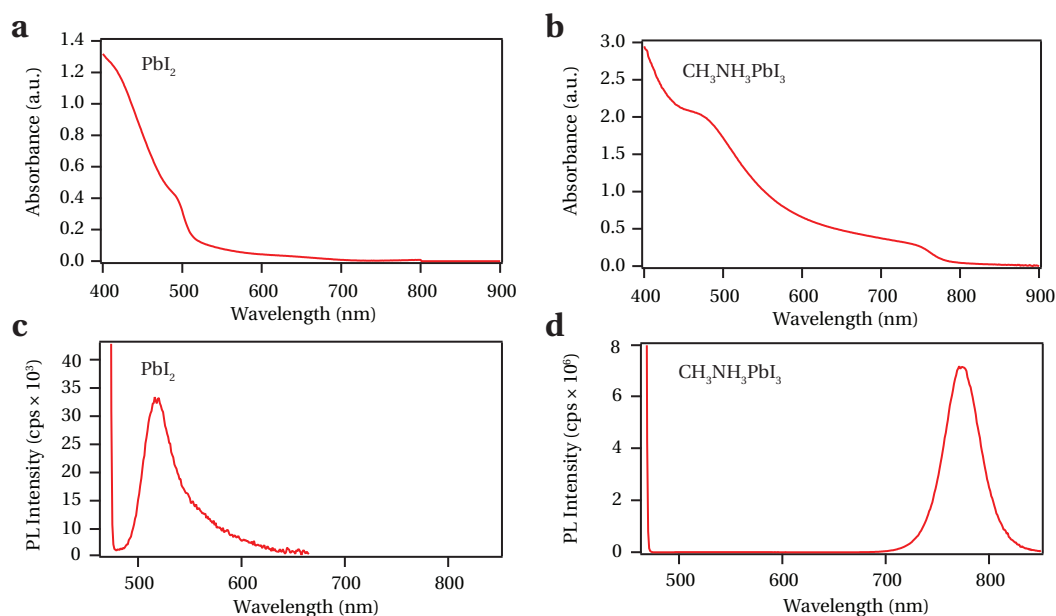


**Figure 4.11** — Steady-state absorption spectra of thin  $\text{PbI}_2$  films a) before and b) after the transformation to  $\text{CH}_3\text{NH}_3\text{PbI}_3$  and steady-state photoluminescence (PL) spectra of thin  $\text{PbI}_2$  films c) before and d) after the transformation. The excitation wavelength was 460 nm. cps—counts per second.



absorption, but also a change in the light-scattering properties of the film. Unfortunately, the disappearance of the  $\text{PbI}_2$  absorption during the transformation cannot be followed, as the  $\text{PbI}_2$  absorption spectrum overlaps completely with that of the perovskite.

**$\text{CH}_3\text{NH}_3\text{PbI}_3$  photoluminescence.** Secondly, the reaction kinetics can be monitored via the appearance of the perovskite photoluminescence (PL).  $\text{CH}_3\text{NH}_3\text{PbI}_3$  shows a strong PL band at about 775 nm, as already discussed in Section 4.1.3 and as shown in Figure 4.11 d. From a practical point of view, this method is convenient, as the PL signal arising from  $\text{CH}_3\text{NH}_3\text{PbI}_3$  does not interfere or overlap with the luminescence of  $\text{PbI}_2$ . Similar to the optical transmission, the observed signal might be related not only to the formation of  $\text{CH}_3\text{NH}_3\text{PbI}_3$ , but could also be affected by a change in the light-scattering properties of the film. Enhanced light-scattering can help to maximize the harvesting of the excitation light and therefore increase the emission intensity of the film without a change in absorption.

**$\text{PbI}_2$  photoluminescence.** Thirdly, the formation of the perovskite can be followed via the disappearance of the  $\text{PbI}_2$  photoluminescence located at around 525 nm. An emission spectrum of a thin  $\text{PbI}_2$  film is shown in Figure 4.11 c. However, several factors limit the accuracy of this method:

- The intensity of the  $\text{PbI}_2$  photoluminescence at room temperature is rather low—about 200 times lower than that of  $\text{CH}_3\text{NH}_3\text{PbI}_3$ .
- At the excitation wavelength chosen, the  $\text{PbI}_2$  PL band overlaps with an intense Raman peak arising from the solvent of the  $\text{CH}_3\text{NH}_3\text{I}$  solution, 2-propanol.
- The  $\text{PbI}_2$  PL band overlaps with another broad Raman peak, as determined from a series of PL spectra recorded at different excitation wavelengths. The origin of this peak is unclear, but it also appears for dry  $\text{PbI}_2$  films on microscope glass slides, suggesting that it may result from the  $\text{PbI}_2$  itself.

#### 4.2.3.1 Investigations on flat $\text{TiO}_2$ /FTO films

The kinetics of the transformation was first investigated on flat  $\text{TiO}_2$ /FTO films. Figure 4.12 a shows the gradual change of the absorption spectrum of a thin  $\text{PbI}_2$  film upon the addition of the  $\text{CH}_3\text{NH}_3\text{I}$  solution. In Figure 4.12 a the change as a function of time is illustrated by the colour gradient from red ( $\text{PbI}_2$ ) to black ( $\text{CH}_3\text{NH}_3\text{PbI}_3$ ). As expected, this data reveals an increase of the overall absorbance and the appearance of the typical absorption profile of the  $\text{CH}_3\text{NH}_3\text{PbI}_3$  perovskite with an onset at about 800 nm. Kinetic traces at different wavelength, showing the change in the absorbance as a function of time, are depicted in Figure 4.12 b. The colour code in Figure 4.12 b corresponds to the arrows in 4.12 a that indicate the position of the kinetic traces on the absorption spectrum. The data shows a steep rise of the absorbance upon the addition of the  $\text{CH}_3\text{NH}_3\text{I}$  solution, followed by a plateau that indicates that the conversion reaction is finished after less than 20 s. A small additional increase that occurs on a timescale

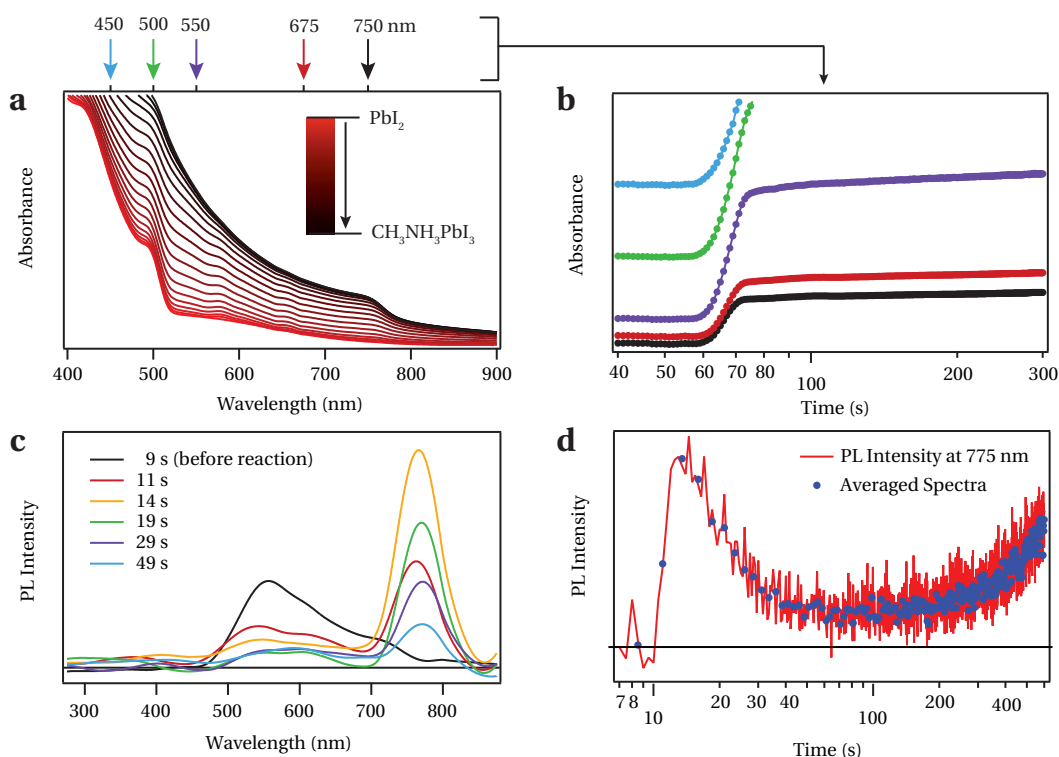


**Figure 4.12** — a) Change in the absorption spectrum of a thin  $\text{PbI}_2$  film during the transformation to  $\text{CH}_3\text{NH}_3\text{PbI}_3$ . The colour gradient from red ( $\text{PbI}_2$ ) to black ( $\text{CH}_3\text{NH}_3\text{PbI}_3$ ) indicates the change as a function of time. b) Kinetic traces at different wavelengths, showing the change in absorbance during the transformation as a function of time. The kinetic traces are also indicated in panel a) by coloured arrows. c) Change of the photoluminescence (PL) spectrum of a thin  $\text{PbI}_2$  film during the transformation. The excitation wavelength was 405 nm. d) Kinetic trace showing the change in PL intensity at 775 nm as a function of time. A spectrum was recorded every 0.5 s (red line). The spectra were later averaged over 2.5 s (blue dots) for a better signal-to-noise ratio.

of about 100 s contributes only little to the total change in absorbance and is attributed to a change in the light-scattering properties of the film. The enhanced light-scattering is likely to arise from the slow growth of large perovskite crystals, as has been evidenced by SEM in Section 4.2.2.

Complementary data on the reaction kinetics was also obtained by monitoring the change in photoluminescence during the conversion of  $\text{PbI}_2$  to  $\text{CH}_3\text{NH}_3\text{PbI}_3$ . The gradual change of the luminescence spectrum of a thin  $\text{PbI}_2$  film upon the addition of the  $\text{CH}_3\text{NH}_3\text{I}$  solution is shown in Figure 4.12 c. In this case the excitation wavelength was 405 nm. As expected and as described before, the conversion of  $\text{PbI}_2$  is accompanied by a quenching of the  $\text{PbI}_2$  luminescence at around 525 nm and a concomitant increase in the perovskite luminescence at 775 nm. From the emission spectra at different time points, one can observe that the maximum of the perovskite luminescence slightly shifts from 764 to 774 nm while the transformation proceeds. This shift might be related to a quantum size effect: the increase of the perovskite crystal size is accompanied by a decrease of the bandgap and therefore a redshift of the perovskite luminescence.

The shape and position of the  $\text{PbI}_2$  emission peak in Figure 4.12 c slightly differs from the one previously shown in Figure 4.11 c. I attribute this discrepancy to the difference in the excitation wavelength and also to the different experimental conditions that have been used to obtain the data shown in Figure 4.12 c. Details about these conditions can be found in the experimental section (Section 6.2).

A kinetic trace showing the change in the PL intensity at 775 nm as a function of time is depicted in Figure 4.12 d. We observe that the  $\text{CH}_3\text{NH}_3\text{PbI}_3$  luminescence sharply increases upon the addition of  $\text{CH}_3\text{NH}_3\text{I}$ , then passes through a maximum and finally decreases to a stationary value. The small increase that is observed on a timescale of several minutes is likely to result from changes in the film morphology and enhanced light-scattering, similar to what has been observed for the change in the absorption. We attribute the decrease that follows the initial rise to self-absorption of the luminescence by the perovskite formed during the reaction with  $\text{CH}_3\text{NH}_3\text{I}$ . Another parameter that could induce such behaviour is a change in the photoluminescence quantum yield. A size-dependent quantum yield has previously been observed for nanometer-sized quantum dots [218, 219].

#### 4.2.3.2 Investigations on porous $\text{TiO}_2$

In order to mimic the final architecture of a photovoltaic device,  $\text{PbI}_2$  was also deposited on porous  $\text{TiO}_2$  films and converted to  $\text{CH}_3\text{NH}_3\text{PbI}_3$  using the aforementioned procedure. The results of the corresponding measurements are illustrated in Figure 4.13. The figure shows kinetic traces following the increase in absorbance at 550 nm (Figure 4.13 a), the quenching of the  $\text{PbI}_2$  luminescence at 520 nm (Figure 4.13 b) and the appearance of the  $\text{CH}_3\text{NH}_3\text{PbI}_3$  luminescence at 775 nm (Figure 4.13 c). All kinetic traces resemble what has previously been observed on flat  $\text{TiO}_2$  films. The excitation wavelength was 460 nm in the case of Figure 4.13 b and 660 nm for Figure 4.13 c. In general, I find that the kinetics is independent of the excitation wavelength. The kinetic trace monitoring the absorption (Figure 4.13 a) was fitted to a biexponential function yielding the decay times stated in the

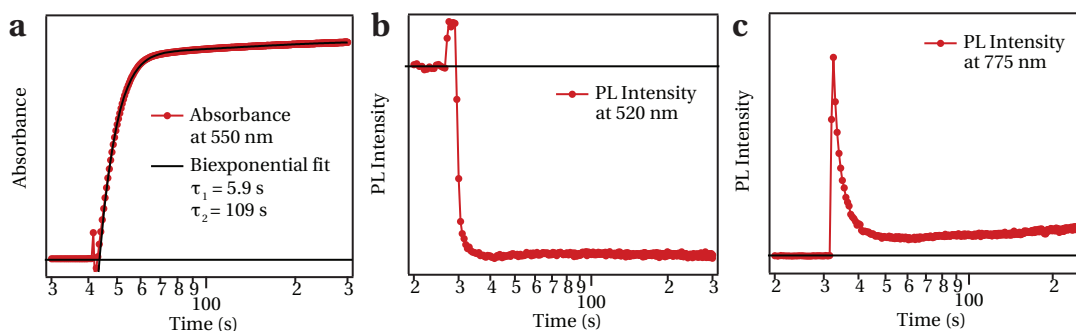


**Figure 4.13** — Kinetic traces following the a) absorbance at 550 nm, b) photoluminescence at 520 nm and c) photoluminescence at 775 nm of a mesoporous  $\text{TiO}_2/\text{PbI}_2$  composite upon the addition of the  $\text{CH}_3\text{NH}_3\text{I}$  solution. The excitation wavelength was b) 460 nm and c) 660 nm.

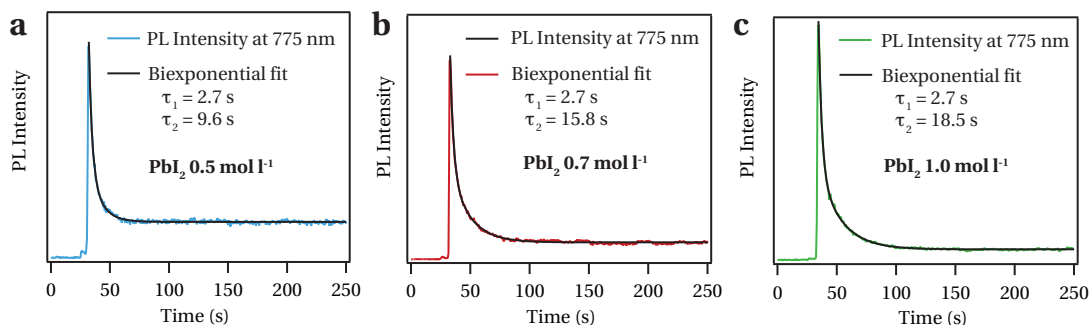


**Figure 4.14** — Kinetic traces following the photoluminescence at 775 nm during the transformation of three different  $\text{TiO}_2/\text{PbI}_2$  composites. The three samples were prepared using different  $\text{PbI}_2$  solution concentrations of a)  $0.5 \text{ mol l}^{-1}$ , b)  $0.7 \text{ mol l}^{-1}$  and c)  $1.0 \text{ mol l}^{-1}$  and a spinning rate of 1200 rpm. The excitation wavelength was 660 nm.

figure. As previously explained for data obtained on flat films, the two parts can be attributed to the transformation of  $\text{PbI}_2$  to  $\text{CH}_3\text{NH}_3\text{PbI}_3$  (fast component, time constant  $\tau_1$ ) and the growth of larger perovskite crystals (slow component, time constant  $\tau_2$ ). It is worth mentioning that the increase in the emission intensity before the quenching in Figure 4.13 b is an optical artefact that results from opening the sample compartment to add the  $\text{CH}_3\text{NH}_3\text{I}$  solution.

The data shown in Figure 4.13 has been obtained for a sample that was fabricated using optimized deposition conditions for  $\text{PbI}_2$ , i.e. a DMF solution concentration of  $1.0 \text{ mol l}^{-1}$  and a deposition by spin-coating at 6500 revolutions per minute (rpm). For a better understanding of the influence of the  $\text{PbI}_2$  loading on the reaction kinetics, I investigated samples that have been prepared using different  $\text{PbI}_2$  solution concentrations ( $0.5$ ,  $0.7$  and  $1.0 \text{ mol l}^{-1}$ ) and a spinning speed of 1200 rpm. The lower spinning speed has two consequences: it leads to a higher  $\text{PbI}_2$  loading and the formation of a  $\text{PbI}_2$  capping layer on top of the mesoporous structure. The formation of the capping layer will be further discussed in Section 4.20 that also contains SEM images of  $\text{TiO}_2/\text{PbI}_2$  composites with and without such a capping layer. The results of the kinetic measurements are shown in Figure 4.14 that shows kinetic traces following the appearance of the  $\text{CH}_3\text{NH}_3\text{PbI}_3$  luminescence at 775 nm for three samples that have been prepared using the three different solution concentrations mentioned before. The kinetic traces were fitted to a biexponential function yielding the decay times stated in the figure. The origin of the two decay times  $\tau_1$  and  $\tau_2$  is still unclear. However, it is observed that only  $\tau_2$  varies from 9.6 to 18.5 s when changing the deposition conditions of  $\text{PbI}_2$ . In contrast to that,  $\tau_1$  is unaffected and stays constant at 2.7 s. As this value is too short to be related to the main transformation reaction, I consider  $\tau_2$  to be more relevant.

Base on the data shown in Figure 4.14 three important observations can be made:

- Firstly, the reaction time increases with the  $\text{PbI}_2$  solution concentration, as evident from the longer decay times  $\tau_2$  that are stated in Figure 4.14 and that have been derived from the biexponential fits. This can be attributed to the higher loading of the  $\text{TiO}_2$

film with  $\text{PbI}_2$ . It is important to note that due to the higher loading, the fraction of the total pore volume that is filled with  $\text{PbI}_2$  might be larger. This could lead to a slower diffusion of  $\text{CH}_3\text{NH}_3\text{I}$  into the porous structure and hence slower transformation kinetics. Additionally, the solution concentration is likely to affect the thickness of the  $\text{PbI}_2$  capping layer, which might also retard the insertion of  $\text{CH}_3\text{NH}_3\text{I}$  into the  $\text{TiO}_2/\text{PbI}_2$  structure.

- Secondly, the data does not show the slow increase in the photoluminescence intensity that occurred on a timescale of several minutes in the case of  $\text{PbI}_2$  on flat  $\text{TiO}_2$  (Figure 4.12) and in the case of  $\text{PbI}_2$  on porous  $\text{TiO}_2$  in the absence of a  $\text{PbI}_2$  capping layer (Figure 4.13 c). Previously, I attributed this effect to a change in morphology that affects the light-scattering properties of the sample and therefore the harvesting of the excitation light. The absence of this effect suggests that in this case the change in morphology has no effect on the light-scattering properties of the sample. This assumption can be rationalized by the fact that films that do not possess a  $\text{PbI}_2$  capping layer appear translucent, as the  $\text{PbI}_2$  is confined in the pores of the metal oxide host. In contrast to that, the  $\text{PbI}_2$  capping layer that forms in the case of a slow spinning rate, is composed of large  $\text{PbI}_2$  crystals that scatter visible light, as can be seen from SEM images in Section 4.20. Such films are completely opaque. Hence, additional changes in the morphology do not influence the light-scattering properties of the sample.
- Thirdly, it is interesting to note that the PL intensity at the plateau, that is reached after the initial rise and the subsequent decay, decreases with an increasing  $\text{PbI}_2$  solution concentration. This trend is counterintuitive, as one would expect an increase in the PL intensity due to an increase in the total amount of  $\text{CH}_3\text{NH}_3\text{PbI}_3$  formed. However, an increase in the total amount of  $\text{CH}_3\text{NH}_3\text{PbI}_3$  also leads to a higher self-absorption, which, I believe, is the reason for the lower PL intensity at higher  $\text{PbI}_2$  loadings.

#### 4.2.4 X-ray diffraction spectroscopy

X-ray diffraction spectroscopy was used to investigate the crystal structure of the  $\text{CH}_3\text{NH}_3\text{PbI}_3$  perovskite obtained by the sequential deposition technique. The results are shown in Figure 4.15. The green and red curves in Figure 4.15 a show X-ray powder diffraction spectra measured before and after a  $\text{TiO}_2/\text{PbI}_2$  nanocomposite film is brought into contact with the  $\text{CH}_3\text{NH}_3\text{I}$  solution ( $20 \text{ mg ml}^{-1}$ ), respectively. The dipping time was 2 min. For comparison  $\text{PbI}_2$  was also spin-coated on a flat glass substrate and exposed to a solution of  $\text{CH}_3\text{NH}_3\text{I}$  in the same manner as the  $\text{TiO}_2/\text{PbI}_2$  nanocomposite. On the basis of literature data it becomes evident that the  $\text{PbI}_2$  deposited by spin-coating from DMF solution crystallizes in the form of the hexagonal 2H polytype, the most common  $\text{PbI}_2$  modification.<sup>1</sup> Moreover, the results show that on a flat glass substrate crystals grow in a preferential orientation along the c-axis, hence the appearance of only four diffraction peaks, corresponding to the (001), (002), (003)

<sup>1</sup>Inorganic Crystal Structure Database, collection code 68819; <http://www.fiz-karlsruhe.com/icsd.html>

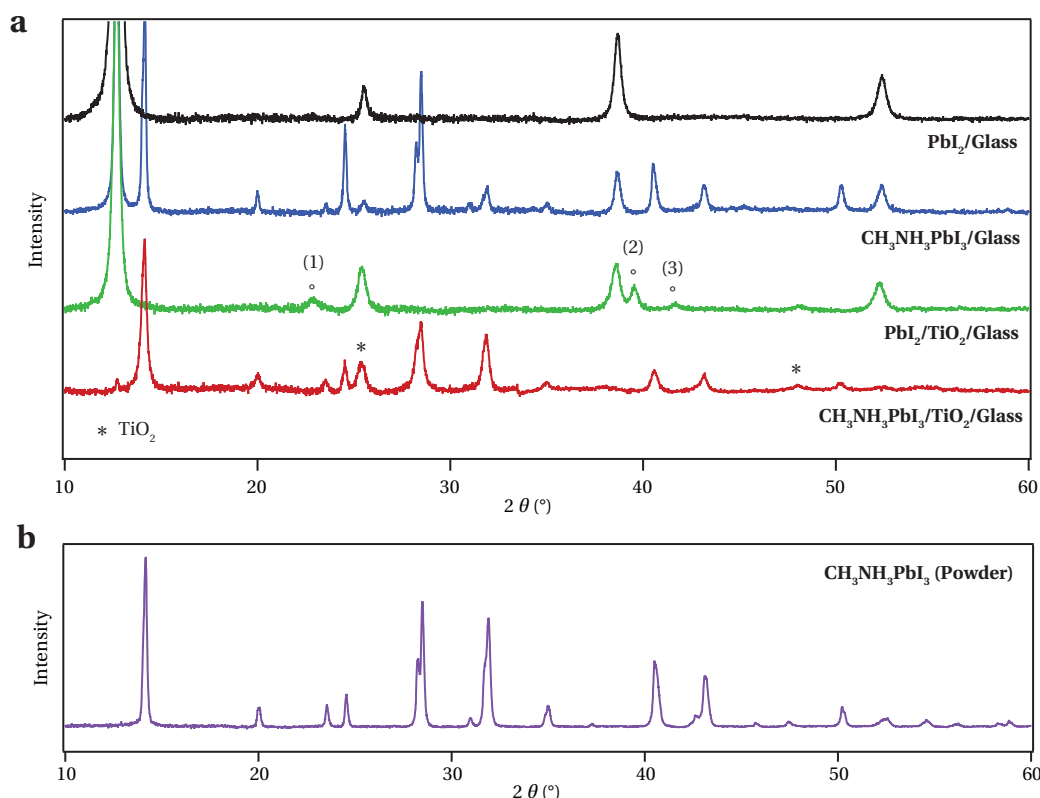


**Figure 4.15** — a) X-ray diffraction spectra of flat  $\text{PbI}_2$  films and  $\text{TiO}_2/\text{PbI}_2$  nanocomposites before and after the transformation to  $\text{CH}_3\text{NH}_3\text{PbI}_3$ . b) X-ray diffraction spectrum of a nanocrystalline powder of  $\text{CH}_3\text{NH}_3\text{PbI}_3$ .

and (004) lattice planes (Figure 4.15 a, black curve). For the  $\text{PbI}_2$  loaded on a mesoporous  $\text{TiO}_2$  film (Figure 4.15 a, green curve), three additional diffraction peaks are observed that do not originate from  $\text{TiO}_2$ , suggesting that the  $\text{TiO}_2$  anatase scaffold induces a different orientation for the  $\text{PbI}_2$  crystal growth. The peaks labelled (2) and (3) in Figure 4.15 a can be attributed to the (110) and (111) lattice planes of the 2H polytype. Peak (1) is assigned to a different  $\text{PbI}_2$  variant, which identification is difficult in view of the large number of polytypes that have been reported for  $\text{PbI}_2$  [216].

During the reaction with  $\text{CH}_3\text{NH}_3\text{I}$  several new diffraction peaks appear that are in good agreement with literature data on the tetragonal phase of the  $\text{CH}_3\text{NH}_3\text{PbI}_3$  perovskite [207]. For a better comparison, I show the X-ray diffraction spectrum of a crystalline  $\text{CH}_3\text{NH}_3\text{PbI}_3$  powder in Figure 4.15 b. When  $\text{PbI}_2$  is deposited on a flat film (Figure 4.15 a, blue curve) the conversion to perovskite upon exposure to the  $\text{CH}_3\text{NH}_3\text{I}$  solution is incomplete; a large amount of unreacted  $\text{PbI}_2$  remained even after a dipping time of 45 min. This agrees with the observation that the  $\text{CH}_3\text{NH}_3\text{I}$  insertion hardly proceeds beyond the surface of thin  $\text{PbI}_2$  films, and that the complete transformation of the crystal structure requires several hours as has previously been reported by Liang et al. [209]. A caveat associated with such long conversion times is that the perovskite dissolves in the methylammonium iodide solution over longer

periods, hampering the transformation.

In striking contrast to the behaviour of thin films of  $\text{PbI}_2$  deposited on a flat support, the conversion of  $\text{PbI}_2$  nanocrystals in the mesoporous  $\text{TiO}_2$  film is practically complete on a timescale of seconds, as is evident from the immediate disappearance of its most intense diffraction peak (the (001) peak) and the concomitant appearance of the XRD reflections for the tetragonal perovskite (Figure 4.15 a, red curve). Within the mesoporous  $\text{TiO}_2$  scaffold the size of the  $\text{PbI}_2$  crystals is constrained to about 22 nm by the pore size of the host. An important finding of this work is that confining the  $\text{PbI}_2$  crystals to such a small size drastically enhances their rate of conversion to perovskite: the reaction is complete within a few seconds of their coming into contact with the  $\text{CH}_3\text{NH}_3\text{I}$  solution. However, when deposited on a flat surface, larger  $\text{PbI}_2$  crystals in the size range of 50–200 nm are formed, resulting in incomplete conversion of the  $\text{PbI}_2$  on exposure to  $\text{CH}_3\text{NH}_3\text{I}$ , as shown by XRD.

It is worth mentioning that it is currently unclear where the remaining  $\text{PbI}_2$  is exactly located. More recent studies from our laboratory show that the amount of unreacted  $\text{PbI}_2$  depends strongly on the concentration of the  $\text{CH}_3\text{NH}_3\text{I}$  solution. I believe that this is related to change in surface roughness that occurs during the transformation: a high concentration of  $\text{CH}_3\text{NH}_3\text{I}$  leads to a quick coverage of the  $\text{PbI}_2$  film with a layer of  $\text{CH}_3\text{NH}_3\text{PbI}_3$ .  $\text{PbI}_2$  that is situated at the bottom of the film close to the substrate, is therefore not accessible anymore. A low concentration of  $\text{CH}_3\text{NH}_3\text{I}$  leads to the growth of large perovskite crystals and a higher surface roughness. Hence, more of the  $\text{PbI}_2$  can be transformed. However, for the concentration range investigated (5–40 mg  $\text{ml}^{-1}$ ) a certain amount of unreacted  $\text{PbI}_2$  always remained.

#### 4.2.5 Perovskite-sensitized solar cells

The above-discussed sequential deposition technique was used to fabricate mesoscopic solar cells employing spiro-MeOTAD (Figure 1.7 in Section 1.5.3) as the hole-transporting material. Following the concept that has been presented in Chapter 2, a Co(III) complex (FK209, cf. Section 2.2.2) is used as a p-type dopant for the HTM at a molar doping level of 10% to ensure a sufficient conductivity of the HTM and low series resistance of the solar cells.

The most important steps of the device fabrication are illustrated in Figure 4.16. The device fabrication can be divided into four main steps: a) deposition of the mesoporous (mp)  $\text{TiO}_2$ , b) infiltration of  $\text{PbI}_2$  into the mp- $\text{TiO}_2$ , c) conversion of  $\text{PbI}_2$  to  $\text{CH}_3\text{NH}_3\text{PbI}_3$  and d) deposition of the HTM. The coating of the FTO substrate with the compact  $\text{TiO}_2$  blocking layer via spray-pyrolysis (sp- $\text{TiO}_2$ ) that precedes the deposition of the mp- $\text{TiO}_2$ , as well as the evaporation of the back contact, are not detailed in the figure. In general it is worth mentioning that no post treatment was applied onto the mesoporous  $\text{TiO}_2$  film.



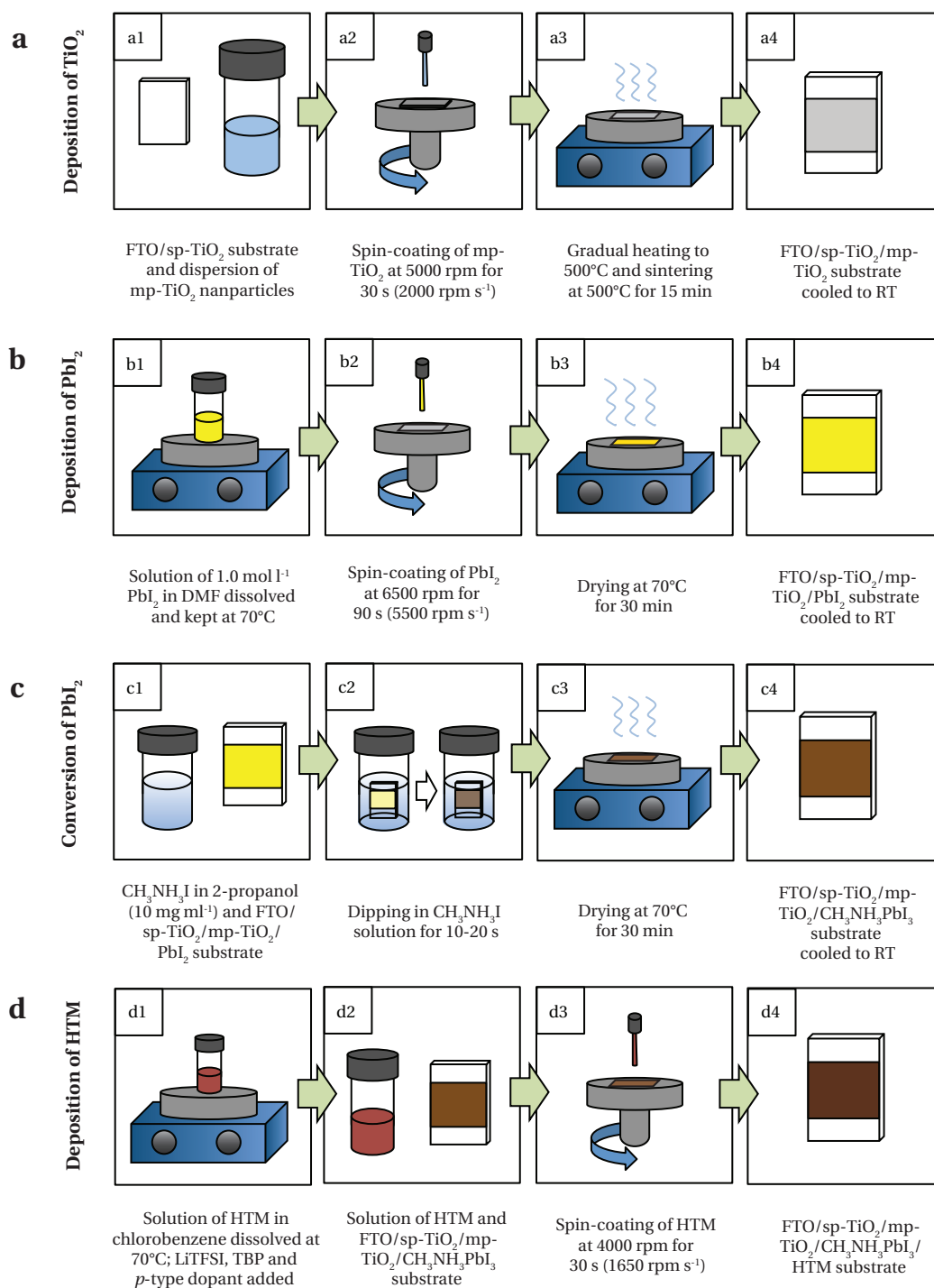


**Figure 4.16** — Scheme that illustrates the four most important steps of the fabrication of perovskite-based mesoscopic solar cells: a) deposition of the mesoporous  $\text{TiO}_2$ , b) deposition of  $\text{PbI}_2$ , c) conversion to  $\text{CH}_3\text{NH}_3\text{PbI}_3$  and d) deposition of the HTM. sp- $\text{TiO}_2$ —flat  $\text{TiO}_2$  deposited by spray-pyrolysis. mp- $\text{TiO}_2$ —mesoporous  $\text{TiO}_2$ .



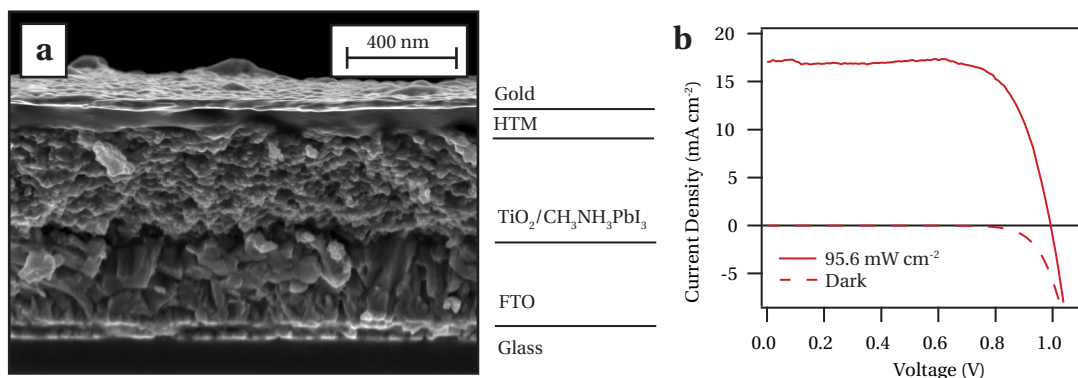


**Figure 4.17** — a) Cross-sectional scanning electron microscopy image of a typical photovoltaic device. Please note that the thin compact  $\text{TiO}_2$  layer that has been deposited on top of the FTO is not resolved in the image. b)  $J$ - $V$  curve of a typical photovoltaic device measured under  $95.6 \text{ mW cm}^{-2}$  simulated AM1.5G solar irradiation and in the dark.

Figure 4.17 a shows a cross-sectional SEM picture of a typical device. The mesoporous  $\text{TiO}_2$  film had an optimized thickness of around 350 nm and was infiltrated with the perovskite nanocrystals using the above-mentioned sequential deposition technique. The HTM was subsequently deposited by spin coating. It penetrates into the remaining available pore volume and forms a 100 nm thick layer on top of the composite structure. A thin gold layer was thermally evaporated under vacuum onto the HTM, forming the back contact of the device. The thin  $\text{TiO}_2$  compact layer, that has been deposited on top of the FTO substrate to avoid direct contact to the HTM, is not resolved in the SEM image depicted in Figure 4.17 a.

#### 4.2.5.1 Photovoltaic characterization

$J$ - $V$  characteristics of the solar cells were measured under simulated air mass 1.5 global (AM1.5G) solar irradiation and in the dark.  $J$ - $V$  curves of a typical device are shown in Figure 4.17 b. From the  $J$ - $V$  curve measured at a light intensity of  $95.6 \text{ mW cm}^{-2}$ , I derive values for the short-circuit photocurrent  $J_{SC}$ , the open-circuit voltage  $V_{OC}$  and the fill factor  $FF$  of  $17.1 \text{ mA cm}^{-2}$ , 992 mV and 0.73, respectively, yielding a solar-to-electric power conversion efficiency of 12.9%. The performance of the device at different light intensities is shown in Table 4.2. Statistical data on a larger batch of ten photovoltaic devices is shown in Table 4.3. From the average  $PCE$  value of  $12.0 \pm 0.5\%$  and the small standard deviation, we infer that photovoltaics with excellent performance and high reproducibility can be realized using the method discussed here.

In order to probe the origin of the generated photocurrent, the incident-photon-to-current conversion efficiency ( $IPCE$ ) spectrum was measured for the perovskite-based solar cell. The  $IPCE$  spectrum is depicted in Figure 4.18 a. Generation of the photocurrent starts at 800 nm, which is the bandgap of the  $\text{CH}_3\text{NH}_3\text{PbI}_3$  perovskite, and reaches peak values of over 90% in the short-wavelength region of the visible spectrum. Integrating the overlap of the  $IPCE$

## Chapter 4. Mesoscopic perovskite-sensitized solar cells

**Table 4.2** — Photovoltaic parameters of a typical photovoltaic device derived from  $J$ - $V$  measurements at different light intensities.

$P_{in}$ $\text{mW cm}^{-2}$	$V_{OC}$ $\text{mA cm}^{-2}$	$J_{SC}$ $\text{mV}$	$FF$ -	$PCE$ %
9.3	901	1.7	0.77	12.6
49.8	973	8.9	0.75	13.0
95.6	992	17.1	0.73	12.9

**Table 4.3** — Photovoltaic parameters of a larger batch of ten devices as derived from  $J$ - $V$  measurements at a light intensity of  $100 \text{ mW cm}^{-2}$ .

# Cell	$V_{OC}$ $\text{mV}$	$J_{SC}$ $\text{mA cm}^{-2}$	$FF$ -	$PCE$ %
1	990	17.8	0.70	12.2
2	996	17.7	0.72	12.6
3	971	17.1	0.71	11.7
4	992	17.9	0.73	12.9
5	978	16.3	0.71	11.4
6	962	16.9	0.73	11.9
7	972	18.1	0.68	12.0
8	986	17.4	0.71	12.2
9	963	17.5	0.69	11.5
10	959	17.6	0.66	11.2
<b>Average</b>	$977 \pm 14$	$17.4 \pm 0.5$	$0.70 \pm 0.02$	$12.0 \pm 0.5$

spectrum with the AM1.5G solar photon flux yields a current density of  $18.4 \text{ mA cm}^{-2}$ , which is in excellent agreement with the measured photocurrent density, extrapolated to  $17.9 \text{ mA cm}^{-2}$  at the standard solar AM1.5G intensity of  $100 \text{ mW cm}^{-2}$ . This confirms that any mismatch between the simulated sunlight and the AM1.5G standard is negligibly small. The integrated photocurrent is shown on the right-hand axis of the graph in Figure 4.18 a.

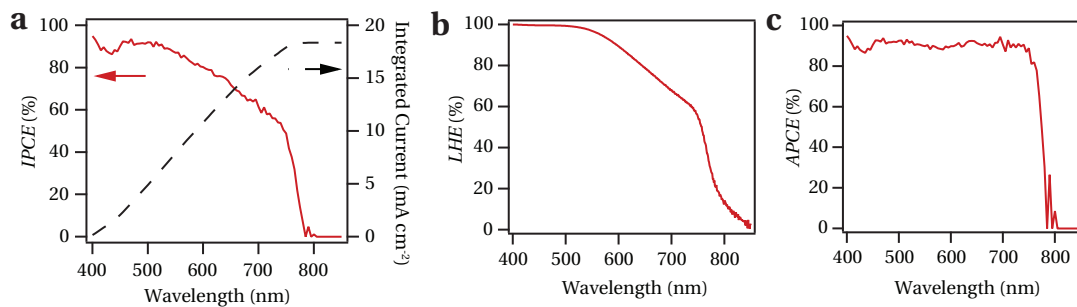


**Figure 4.18** — a)  $IPCE$  spectrum. The righthand axis indicates the integrated photocurrent that is expected to be generated under  $100 \text{ mW cm}^{-2}$  AM1.5G illumination. b)  $LHE$  spectrum. c)  $APCE$  spectrum that is derived from the  $IPCE$  and the  $LHE$ .

Despite values of over 90% in the blue, the *IPCE* drops significantly to about 50% in the red region of the visible spectrum. Comparison with the absorptance or light-harvesting efficiency (*LHE*) depicted in Figure 4.18 b reveals that the low *IPCE* values in the range of 600–800 nm result from the smaller absorption of the perovskite in this spectral region. This is also reflected in the spectrum of the absorbed-photon-to-current conversion efficiency (*APCE*), which can be derived from the *IPCE* and *LHE* (cf. Section 1.4.3) and is shown in Figure 4.18 c. The *APCE* is greater than 90% over the whole visible region, without correction for reflective losses, indicating that the device achieves near-unity quantum yield for the generation and collection of charge carriers. However, this data suggest that improving the light-harvesting in the red region of the visible spectrum could allow for a further increase of the photocurrent generated by the device and hence its *PCE*.

#### 4.2.5.2 Long-term stability

To test the stability of the perovskite-based photovoltaics, prepared using the aforementioned procedure, a sealed cell was subjected to long-term light-soaking at a light intensity of  $100 \text{ mW cm}^{-2}$  and a temperature of  $45^\circ\text{C}$ . The device was encapsulated under argon as described in the experimental section (Section 6.7.4) and maintained at the optimal electric power output during the ageing using maximum power point tracking. This is considered as the ideal way to test the stability of the device, as it is kept close to real operating conditions. The experiments reveal a very promising long-term stability: the photovoltaic device maintained more than 80% of its initial *PCE* after a period of 500 h. The evolution of the photovoltaic parameters ( $J_{SC}$ ,  $V_{OC}$ , *FF* and *PCE*) as a function of time is illustrated in Figure 4.19.

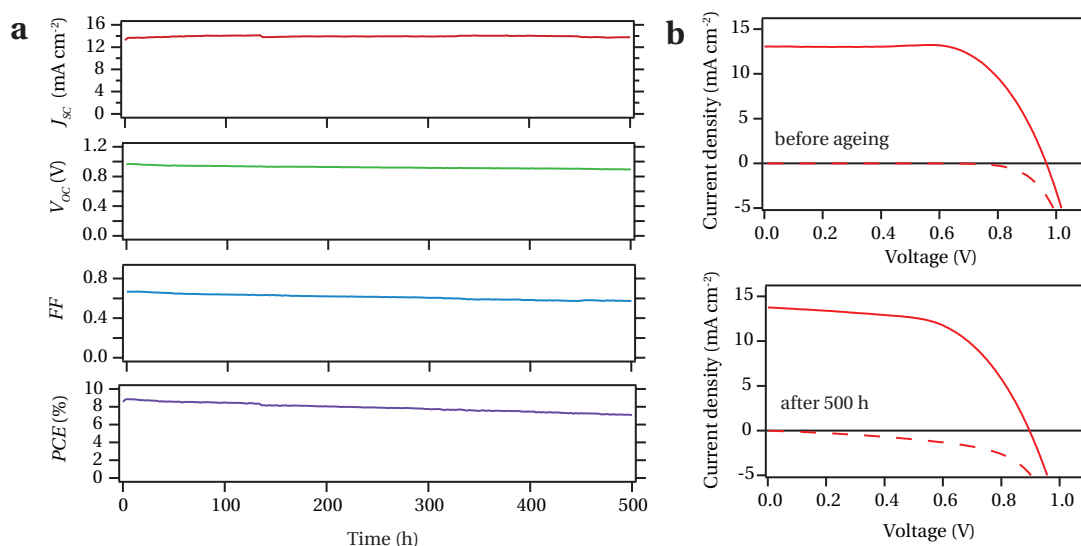


**Figure 4.19** — a) Evolution of photovoltaic parameters during the stability test under constant illumination of approximately  $100 \text{ mW cm}^{-2}$  and a temperature of  $45^\circ\text{C}$ . During the ageing the device was kept at its maximum power point using electronic control. An automatic measurement is performed every 2 h. b, c)  $J$ - $V$  characteristics measured under illumination (solid line) and in the dark (dotted line) b) before the ageing and c) after 500 h.

It is notable that no change in the  $J_{SC}$  is observed, indicating that there is no photodegradation of the perovskite light-harvester. The decrease in  $PCE$  is therefore only due to a decrease in both the  $V_{OC}$  and the  $FF$ , and the similar slope of the two decays suggests that they are linked to the same degradation mechanism. The change in these two parameters is mainly due to a decrease in the shunt resistance, as is apparent from Figure 4.19 b, c, where  $J-V$  curves of the device before and after the ageing process are shown. I suspect that this behavior arises from a defective compact blocking layer. If the blocking layer is not perfectly homogeneous, pinholes or cracks could develop during the ageing and lead to a contact between the TCO substrate and the HTM.

### 4.2.5.3 Optimization of photovoltaic performance

The data shown so far was obtained using a meticulously optimized device fabrication procedure (cf. Figure 4.16). During the optimization we found that several parameters are particularly important in order to achieve a good reproducibility and device performance. These parameters will be discussed in more detail in the following paragraphs.

**Deposition of  $PbI_2$ .** We use a solution concentration of  $462 \text{ mg ml}^{-1}$  ( $\sim 1 \text{ mol l}^{-1}$ )  $PbI_2$  in DMF for the deposition of  $PbI_2$ . This concentration exceeds the room temperature solubility limit of  $PbI_2$  in DMF, but is important to achieve a high loading of the mesoporous  $TiO_2$  film with  $PbI_2$ . To dissolve the  $PbI_2$  completely, the solution is heated to  $70^\circ\text{C}$  and kept at this temperature during its use. Supersaturated solution can easily be formed upon cooling the solution to room temperature, but spontaneous precipitation is observed. We find that the conditions for the spin-coating of  $PbI_2$  have a tremendous influence on the final film morphology. Slow spinning rates lead to the formation of a 300–400 nm thick  $PbI_2$  capping layer on top of the mesoporous structure. A cross sectional SEM picture of a film that was prepared using a spinning rate of 1200 rpm is shown in Figure 4.20 b. The capping layer is composed of large  $PbI_2$  crystals, as the crystal growth on top of the mesoporous structure is

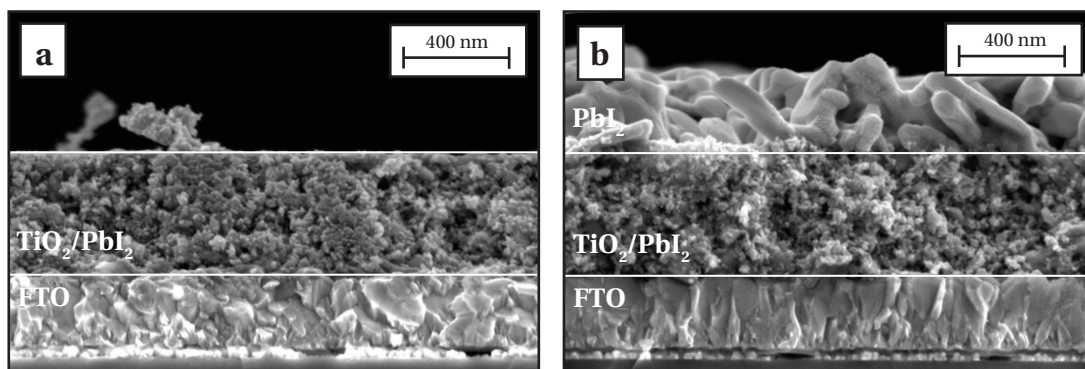


**Figure 4.20** — Cross-sectional SEM images of  $TiO_2/PbI_2$  composite that were prepared using different spinning rates for the  $PbI_2$  deposition: a) 6500 rpm and b) 1200 rpm. The slower spinning rate leads to the formation of a thick  $PbI_2$  capping layer on top of the mesoporous structure.

not limited by the pore diameter of the  $\text{TiO}_2$ . These large crystals scatter the light, therefore the corresponding films appear opaque. The formation of such a  $\text{PbI}_2$  capping layer can, however, be avoided when fast spinning rates are used during the solution-processing. A  $\text{TiO}_2/\text{PbI}_2$  composite that has been prepared by using a spinning rate of 6500 rpm is shown in Figure 4.20 a. The absence of a capping layer confirms that the  $\text{PbI}_2$  is entirely confined within the pores of the  $\text{TiO}_2$  host. Therefore, the resulting film appears translucent. It is worth mentioning that the precipitation of  $\text{PbI}_2$  during the spin-coating occurs within the first 3–5 s of the spinning process, which is why we use a rather fast acceleration of  $5500 \text{ rpm s}^{-1}$ . This ensures that the final spinning rate is reached before the actual precipitation occurs.

**Thickness of the mesoporous  $\text{TiO}_2$ .** We find that the thickness of the mesoporous  $\text{TiO}_2$  is a key parameter to achieve high power conversion efficiencies. Therefore, I fabricated and characterized perovskite-based solar cells using  $\text{TiO}_2$  films of different thickness, ranging from about 300 to 650 nm. The film thicknesses are determined by cross-sectional scanning electron microscopy. As this technique probes the film thickness only locally at a certain point and as it is not guaranteed that the film thickness is homogeneous over the whole substrate, I estimate the error for the given values to be at least  $\pm 50 \text{ nm}$ . Two different methods were used to influence the film thickness: a variation of the concentration of the  $\text{TiO}_2$  dispersion that is used to deposit the mp- $\text{TiO}_2$  film and a variation of the spinning rate for the deposition of  $\text{TiO}_2$ . Using two spinning rates (2000 and 5000 rpm) and three concentrations of the  $\text{TiO}_2$  dispersion, one obtains six different  $\text{TiO}_2$  thicknesses. The three concentrations were achieved by diluting a commercially available  $\text{TiO}_2$  dispersion with ethanol at three different weight ratios (1:2.5, 1:3.0 and 1:3.5).

The results are illustrated in Figure 4.21. The figure shows how the photovoltaic parameters ( $J_{SC}$ ,  $V_{OC}$ ,  $FF$  and  $PCE$ ) that were extracted from the  $J$ - $V$  characteristics measured at  $100 \text{ mW cm}^{-2}$  simulated AM1.5G irradiation change with varying  $\text{TiO}_2$  film thickness. The results shown in Figure 4.21 have been obtained for a  $\text{CH}_3\text{NH}_3\text{I}$  solution concentration of  $20 \text{ mg ml}^{-1}$ . This explains why the optimum thickness of 300–350 nm yields a  $PCE$  that is lower than what has been obtained earlier in this chapter. In general, decreasing trends are observed in terms of  $J_{SC}$ ,  $V_{OC}$  and  $PCE$  when the  $\text{TiO}_2$  film thickness is gradually increased from 300 to 600 nm. The  $FF$  steeply decreases when the  $\text{TiO}_2$  film thickness exceeds 350 nm but remains unaffected when the  $\text{TiO}_2$  thickness is increased further. The highest performance is achieved for a thickness of 300–350 nm.

The strong decrease in the photocurrent with the  $\text{TiO}_2$  film thickness is somewhat unexpected, as the stronger absorbance of the thicker films should lead to an increase in the photocurrent. The total amount of the generated photocurrent depends on three parameters: light-harvesting, charge separation and charge collection (cf. Section 1.4.3). As the light-harvesting increases with the  $\text{TiO}_2$  film thickness, the decrease in the  $J_{SC}$  must be related to a reduction in either the charge separation efficiency or the charge collection efficiency. Following light absorption, the charge separation occurs either via hole injection into the HTM or via electron injection into the  $\text{TiO}_2$ . One would not expect the electron injection

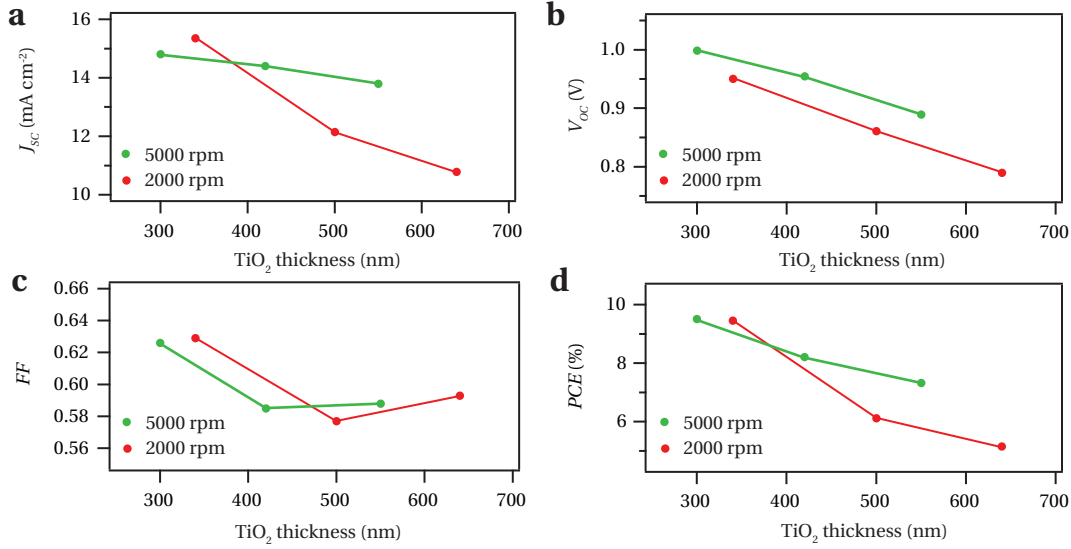


**Figure 4.21** — Photovoltaic parameters derived from  $J$ - $V$  measurements under  $100 \text{ mW cm}^{-2}$  simulated AM1.5G irradiation for devices based on  $\text{TiO}_2$  films of different thickness. The different thicknesses were achieved by changing the concentration of the  $\text{TiO}_2$  dispersion and the spinning rate during the spin-coating. Three different concentrations and two different spinning rates were investigated. The  $\text{CH}_3\text{NH}_3\text{I}$  solution concentration was  $20 \text{ mg ml}^{-1}$ .

to be influenced by the film thickness, as the interface between the perovskite and the  $\text{TiO}_2$  should be the same. The hole injection could be thickness-dependent, for instance if the pore infiltration of the HTM is an issue for thicker films. However, I believe, that the reduction of the  $J_{sc}$  is mainly related to a lower charge collection efficiency caused by enhanced electron-hole recombination.

In general, it is still unclear whether the recombination predominantly occurs between electrons in the  $\text{TiO}_2$  and holes in the perovskite, or electrons in the  $\text{TiO}_2$  and holes in the HTM. Which recombination pathway prevails, might strongly depend on the surface coverage of the mesoporous  $\text{TiO}_2$  with the perovskite absorber. Assuming that the  $\text{TiO}_2$  surface is not fully covered with  $\text{CH}_3\text{NH}_3\text{PbI}_3$ , one can postulate that the recombination of photogenerated charge carriers predominantly occurs between the  $\text{TiO}_2$  and the HTM. An increase in the film thickness leads to an increase in the interfacial area between the  $\text{TiO}_2$  and the HTM and hence a higher electron-hole recombination rate. This is in agreement with the trend observed for the  $V_{oc}$ , which shows a strong dependence on the  $\text{TiO}_2$  film thickness—a loss of 200 mV is observed when the  $\text{TiO}_2$  film thickness is doubled from 300 to 600 nm. Although more studies are required to elucidate the recombination mechanisms in the perovskite solar cells, it seems clear from the presented data that a low charge collection efficiency currently hinders the use of thicker  $\text{TiO}_2$  films.

**Concentration of the  $\text{CH}_3\text{NH}_3\text{I}$  solution.** As discussed in Section 4.2.2, the concentration of the  $\text{CH}_3\text{NH}_3\text{I}$  solution has a pronounced effect on the perovskite crystal growth. Therefore I

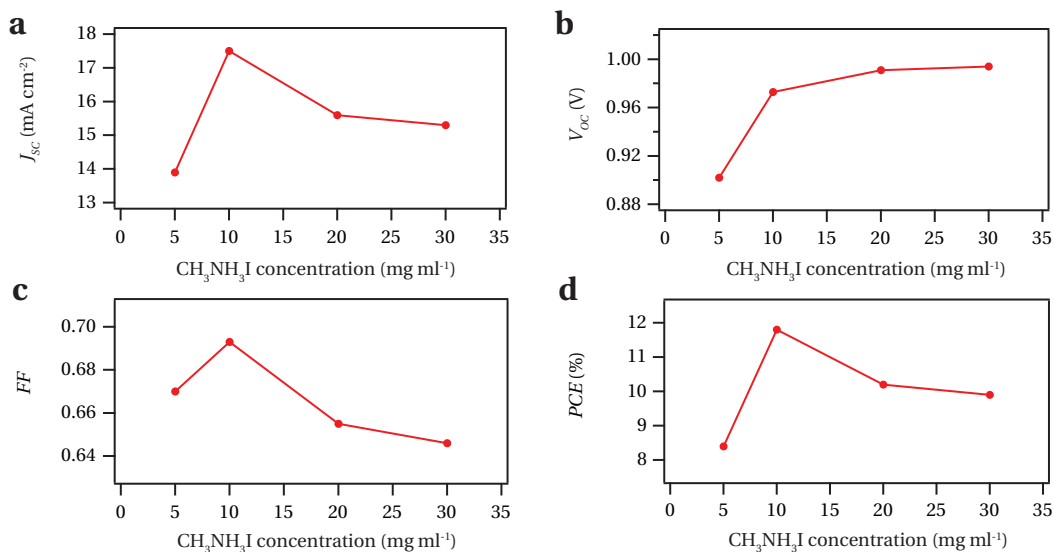


**Figure 4.22** — Photovoltaic parameters derived from  $J$ - $V$  measurements under  $100 \text{ mW cm}^{-2}$  simulated AM1.5G irradiation for devices that were fabricated using different  $\text{CH}_3\text{NH}_3\text{I}$  solution concentrations. The  $\text{TiO}_2$  film thickness was 350 nm.

investigated four different  $\text{CH}_3\text{NH}_3\text{I}$  solution concentrations (5, 10, 20 and  $30 \text{ mg ml}^{-1}$ ) for the fabrication of photovoltaic devices. The corresponding photovoltaic parameters ( $J_{SC}$ ,  $V_{OC}$ ,  $FF$  and  $PCE$ ) that were extracted from  $J$ - $V$  characteristics measured under simulated AM1.5G irradiation ( $100 \text{ mW cm}^{-2}$ ) are shown in Figure 4.22.

It is observed that the  $FF$ , the  $J_{SC}$  and the  $PCE$  increase when the  $\text{CH}_3\text{NH}_3\text{I}$  solution concentration is decreased from 30 to  $10 \text{ mg ml}^{-1}$ . The increase is followed by a sharp decrease when the concentration is lowered further to  $5 \text{ mg ml}^{-1}$ . This sharp decrease in performance is attributed to the incomplete conversion of  $\text{PbI}_2$  to  $\text{CH}_3\text{NH}_3\text{PbI}_3$  at such low concentration, as has been evidenced by scanning electron microscopy in Section 4.9. A clear trend is visible for the  $V_{OC}$ , that continuously drops when the  $\text{CH}_3\text{NH}_3\text{I}$  solution concentration is decreased from 30 to  $5 \text{ mg ml}^{-1}$ . This loss in  $V_{OC}$  may be related to a lower surface coverage of the  $\text{TiO}_2$  with the perovskite absorber, leading to enhanced electron-hole recombination. From the investigations on flat films it is known, that a lowering of the  $\text{CH}_3\text{NH}_3\text{I}$  solution concentration leads to larger  $\text{CH}_3\text{NH}_3\text{PbI}_3$  crystals and higher roughness of the  $\text{CH}_3\text{NH}_3\text{PbI}_3$  film. This could partly result in the exposure of the  $\text{TiO}_2$  surface. The highest  $PCE$  is obtained for a solution concentration of  $10 \text{ mg ml}^{-1}$ . However, a further optimization of the concentration might be possible, given the tremendous influence of  $\text{CH}_3\text{NH}_3\text{I}$  solution concentrations between 5 and  $10 \text{ mg ml}^{-1}$  on the perovskite crystal growth.

Although the influence of the  $\text{CH}_3\text{NH}_3\text{I}$  solution concentration on the perovskite morphology was studied in detail in Section 4.2.2, this data was obtained on flat  $\text{FTO/TiO}_2$  films. Therefore it is difficult and not entirely valid to use these findings to explain the trends in  $V_{OC}$ ,  $J_{SC}$  and  $FF$  observed here. Due to the small pore diameter of the mesoporous  $\text{TiO}_2$  scaffold, the



change in morphology within the pores cannot be investigated by SEM. Nevertheless, it is most probable that the solution concentration also has a significant effect on the morphology of the perovskite that is confined in the pores of the mesoporous host.

### 4.2.5.4 High performance devices

In an attempt to increase the light-harvesting of the solar cell and to obviate the lack of absorption in the long-wavelength region of the spectrum, we slightly modified the conditions for the device fabrication and introduced a 'pre-wetting' step. This additional step consists of dipping the dried  $\text{TiO}_2/\text{PbI}_2$  composite film in pure 2-propanol before dipping it in the  $\text{CH}_3\text{NH}_3\text{I}/2$ -propanol solution. Further details are provided in the experimental section (Section 6.7.2). The  $J$ - $V$  characteristics of the best-performing cell of the series that was fabricated in this manner are depicted in Figure 4.23. From this data we derive values of  $20.0 \text{ mA cm}^{-2}$ ,  $993 \text{ mV}$  and  $0.73$  for  $J_{\text{SC}}$ ,  $V_{\text{OC}}$  and  $FF$ , respectively, yielding a  $PCE$  of  $15.0\%$  measured at a light intensity of  $96.4 \text{ mW cm}^{-2}$ .

Several solar cells with remarkable  $PCE$ s between  $14\%$  and  $15\%$  were fabricated. One of these devices was sent to an accredited photovoltaic calibration laboratory (Newport, USA) for certification, where a power conversion efficiency of  $14.14\%$  measured under standard AM1.5G reporting conditions was confirmed. Detailed photovoltaics data for this device can be found in the Appendix (Figure A2). When compared to the devices discussed earlier in this chapter (Figure 4.17, Table 4.2 and Table 4.3), these top-performance devices benefit from a significantly higher photocurrent, which must result from the additional pre-wetting step. As the pre-wetting does not affect the loading of the mesoporous  $\text{TiO}_2$  with  $\text{PbI}_2$  and hence the amount of perovskite formed, we attribute this trend to increased light scattering, improving the long-wavelength response of the cell. The result of the pre-wetting is a film of pure solvent that covers the  $\text{TiO}_2/\text{PbI}_2$  composite. This solvent film locally decreases the methylammonium iodide concentration, inducing the growth of larger crystals. The effect becomes evident when

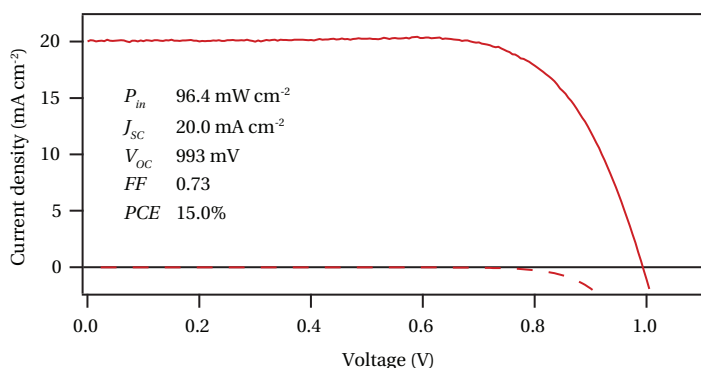


**Figure 4.23** —  $J$ - $V$  characteristics of the best performing device measured under  $96.4 \text{ mW cm}^{-2}$  AM1.5G illumination (solid line) and in the dark (dotted line). The device had been fabricated employing the pre-wetting step as detailed in the text and the experimental section (Section 6.7.2).



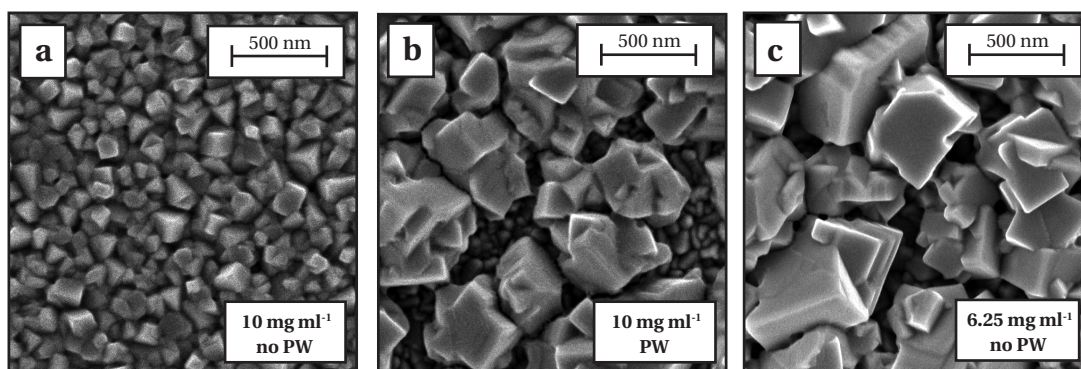


**Figure 4.24** — SEM images of  $\text{PbI}_2$  films on flat  $\text{TiO}_2$ -coated FTO substrates after the dipping in the  $\text{CH}_3\text{NH}_3\text{I}$  solution with a concentration of a, b)  $10 \text{ mg ml}^{-1}$  and c)  $6.25 \text{ mg ml}^{-1}$ . For sample b) a pre-wetting (PW) has been applied, i.e. the sample has been dipped in neat 2-propanol prior to the dipping in the  $\text{CH}_3\text{NH}_3\text{I}$  solution.

the pre-wetting is also carried out for the transformation of a flat  $\text{PbI}_2$  film. Figure 4.24 a, b shows SEM pictures of  $\text{PbI}_2$  films that were dipped in a solution of  $\text{CH}_3\text{NH}_3\text{I}$  ( $10 \text{ mg ml}^{-1}$ ) with and without pre-wetting. For a better comparison, the figure shows an SEM picture of a film that was obtained without the pre-wetting but with a  $\text{CH}_3\text{NH}_3\text{I}$  solution concentration of  $6.25 \text{ mg ml}^{-1}$  (Figure 4.24 c). Such a reduced concentration yields a perovskite morphology that is very similar to the one obtained with the pre-wetting and the standard concentration of  $10 \text{ mg ml}^{-1}$ . Although the SEM pictures clearly show the effect of the pre-wetting procedure, the extrapolation of these findings to the conversion of a mesoporous  $\text{TiO}_2/\text{PbI}_2$  composite is not straightforward. Preliminary studies from our laboratory indicate that the pre-wetting induces the growth of large perovskite crystals on top of the mesoporous  $\text{TiO}_2$  structure. Yet, it is not clear whether these large crystals contribute directly to the generation of photocurrent or only indirectly via enhanced light-scattering. Finally, it is worth mentioning that we observe a somewhat lower reproducibility and larger spread of photovoltaic device performance when the pre-wetting is employed. This can be attributed to the lack of control of the thickness of the solvent film that results from the pre-wetting and hence a variation in the perovskite morphology.

### 4.3 Conclusion and Perspective

I presented a very powerful technique to fabricate composite structures of  $\text{TiO}_2$  and the organic-inorganic hybrid perovskite  $\text{CH}_3\text{NH}_3\text{PbI}_3$  for photovoltaic applications. This technique is based on the sequential deposition and formation of the perovskite.  $\text{PbI}_2$  is first introduced from a solution into a nanoporous titanium dioxide film and subsequently transformed into the perovskite by exposing it to a solution of  $\text{CH}_3\text{NH}_3\text{I}$ . My findings show that the conversion occurs within the nanoporous host as soon as the two components come into contact, permitting much better control over the perovskite morphology than is possible with the previously employed single-step route.

The change in crystal morphology during the conversion, as well as the kinetics of the reaction, were investigated in detail using scanning electron microscopy, optical absorption and emission spectroscopy, and X-ray diffraction spectroscopy. Based on this data, I presented a comprehensive study on how the perovskite crystal growth is influenced by the dipping time and the  $\text{CH}_3\text{NH}_3\text{I}$  solution concentrations. However, more work is necessary to understand the exact mechanism of the perovskite crystallization.

Using the sequential deposition technique for the fabrication of solid-state mesoscopic solar cells greatly increases the reproducibility of their performance and allows us to achieve a power conversion efficiency of approximately 15% measured under standard AM1.5G test conditions. To the best of our knowledge, this is the highest power conversion efficiency reported so far for organic or hybrid inorganic–organic solar cells and one of the highest for any solution-processed photovoltaic device.

The use of organic–inorganic hybrid perovskites such as  $\text{CH}_3\text{NH}_3\text{PbI}_3$  in solar cells is a very recent concept. Therefore, several aspects of the basic device functioning are still poorly understood, amongst them the role of the mesoporous  $\text{TiO}_2$ . Snaith and coworkers have shown that the  $\text{TiO}_2$  can be replaced by an insulating wide-bandgap metal oxide scaffold, such as  $\text{Al}_2\text{O}_3$  [191]. In a very recent report, Bi et al. used the sequential deposition technique detailed herein for the fabrication of efficient mesoscopic solar cells based on  $\text{ZrO}_2$  as an insulating scaffold [220]. As the insulating scaffold does not participate electronically in the device functioning, these findings show that the perovskite itself can transport electrons. Additionally, this shows that efficient charge separation occurs at the  $\text{CH}_3\text{NH}_3\text{PbI}_3/\text{HTM}$  interface, without the need of a charge-collecting and charge-transporting metal oxide structure. The findings raise the questions whether the electron injection from the perovskite into the  $\text{TiO}_2$  conduction band occurs, especially considering the small energy offset between the two materials that is only about 0.1 eV. Recent studies from our group using time-resolved spectroscopy, however, revealed that the presence of a mesoporous  $\text{TiO}_2$  is indeed beneficial for retarding the recombination of photogenerated charge carriers, proving that charge injection into the  $\text{TiO}_2$  does take place.

Based on the studies presented in this chapter, I conclude that one of the parameters that currently limits the device performance seems to be the electron–hole recombination. If the recombination could be slowed down, the film thickness could be further increased, without losing photogenerated charge carriers. This would help to increase the light-harvesting in the long wavelength region of the visible spectrum, ultimately improving the  $J_{\text{SC}}$  and the  $PCE$  of the devices.

Another aspect that could not be elucidated so far due to the limited resolution of the scanning electron microscopy used herein, is the perovskite morphology within the pores of the mesoporous host. Transmission electron microscopy could help to determine the morphology and surface coverage of  $\text{CH}_3\text{NH}_3\text{PbI}_3$  on the  $\text{TiO}_2$ .

All in all, the findings presented in this chapter open new routes for the fabrication of

perovskite-based photovoltaic devices, because other preformed metal halide mesostructures may be converted into the desired perovskite by the simple insertion reaction detailed here. This provides new opportunities to realize solution-processed photovoltaic cells with unprecedented power conversion efficiencies and high stability equal to or even greater than those of today's best thin-film photovoltaic devices.



## 5 Conclusion & perspective

The studies discussed in this thesis aimed to achieve a higher performance, an improved reproducibility and a better understanding of solid-state mesoscopic solar cells. In order to achieve these goals and contribute to the development of a high-performance and stable photovoltaic device, I followed three different strategies: the use of chemical *p*-doping to control the charge transport properties of spiro-MeOTAD, the development of new molecular hole-transporting materials and the application of an organic-inorganic hybrid perovskite light absorber.

- In **Chapter 2** I presented a new class of *p*-type dopants based on Co(III) complexes. This is the first time that Co(III) complexes were used for such an application. It was shown that the complexes can be used to efficiently *p*-dope triarylamine-base hole-conductors such as spiro-MeOTAD. In total, we proposed three different complexes for the application as solution-processable dopants. All three materials were characterized by electrochemical and optical techniques and successfully employed in ssDSCs, reaching power conversion efficiencies of up to 7.2%. The presented studies showed that chemical *p*-doping can compete with the commonly employed oxygen-induced photo-doping and that it is a valuable tool to adjust the charge transport properties of spiro-MeOTAD in ssDSCs. I believe that controlled doping via the introduction of molecular *p*-dopants is favorable in terms of controllability and reproducibility of photovoltaic results and is expected to be indispensable if the devices are fabricated in an inert atmosphere. Moreover, preliminary reliability data showed that the *p*-dopants are not harmful for the long-term stability of the devices.

Since the development of these dopants, they have been routinely employed in our laboratory for the fabrication of mesoscopic solar cells based on spiro-MeOTAD [44, 69, 221]. Furthermore, the dopants were particularly helpful in the investigation of new hole-transporting materials presented in Chapter 3. More recently we also employed Co(III) dopants for the fabrication of perovskite-sensitized solar cells, reaching power conversion efficiencies of up to 15% [175]. This strategy has been followed by other groups, showing the value and advantage of our concept [222].

Future studies should focus more on the optimization of the doping level as well as a device fabrication under inert atmosphere, as the dopants have the potential to obviate the necessity of any oxygen-induced doping for an efficient device functioning. This would allow for a better comparison of chemical doping and photo-doping in terms of both photovoltaic performance and long-term stability.

- In **Chapter 3** I presented a series of new triarylamine-based molecular hole-conducting materials. In total we synthesized seven new materials. They were characterized by electrical and electrochemical techniques in order to evaluate their properties. One of our goals was to design an HTM that exhibits a higher oxidation potential compared to spiro-MeOTAD. This was achieved with two of the materials—spiro-m-MeO and spiro-MeO-TPA—that both exhibit an oxidation potential that is 200 mV higher compared to spiro-MeOTAD. Organic field-effect transistors were fabricated with the new materials in order to determine their hole mobilities. It was found that the hole mobility depends strongly on the peripheral substituents on the triarylamine moieties. Unfortunately, all new materials exhibited lower hole mobilities compared to commercial spiro-MeOTAD. The highest hole-mobility of  $2.9 \pm 0.2 \times 10^{-5} \text{ cm V}^{-1} \text{ s}^{-1}$  was obtained for spiro-MeO-TPA. This value is comparable to the mobility of a batch of spiro-MeOTAD that was synthesized in our laboratory. Spiro-MeO-TPA also showed another interesting phenomenon: all four oxidation states of spiro-MeO-TPA had the same redox potential, indicating that there is no electronic or electrostatic interaction between the redox-active units. In general, we found the purity of the new materials to be a key issue and proposed trace amounts of palladium as the possible impurity. A purification treatment using functionalized polystyrene beads as a metal scavenger helped to improve the purity of the materials.

The studies presented herein revealed the importance of the purity of the new materials on their performance in optoelectronic devices. An important finding was that only small structural changes on the hole-conducting triarylamine units can have a tremendous effect on the charge transport properties of the materials. Spiro-MeO-TPA was identified as the most promising candidate to rival spiro-MeOTAD as the HTM in mesoscopic solar cells. Unfortunately, preliminary photovoltaic results showed a very poor performance of spiro-MeO-TPA in ssDSCs. However, I believe that this is partly due to the purity issue that could not be resolved completely. Further in-depth studies that compare spiro-MeOTAD and spiro-MeO-TPA in more detail should help to identify other problems that might be linked to the poor performance of the photovoltaic devices.

- In **Chapter 4** I presented a new technique to realize nanocomposite structures based on a mesoscopic metal oxide and the organic-inorganic hybrid perovskite  $\text{CH}_3\text{NH}_3\text{PbI}_3$ . This technique is based on the sequential deposition of the perovskite absorber on mesoporous metal oxide films:  $\text{PbI}_2$  is first introduced from solution and subsequently exposed to a solution of  $\text{CH}_3\text{NH}_3\text{I}$ . It was shown that the desired perovskite forms within seconds after bringing the two materials into contact. Scanning electron microscopy

---

was used to investigate the changes in crystal morphology during the conversion of a  $\text{PbI}_2$  film into  $\text{CH}_3\text{NH}_3\text{PbI}_3$ . Notably, this data revealed that the concentration of the  $\text{CH}_3\text{NH}_3\text{I}$  solution has a tremendous influence on the perovskite morphology. From the results obtained by scanning electron microscopy we infer that the sequential deposition technique allows for a better control of the perovskite crystal morphology compared to the conventional single-step route. Using X-ray diffraction spectroscopy it was evidenced that the conversion of a flat film of  $\text{PbI}_2$  into  $\text{CH}_3\text{NH}_3\text{PbI}_3$  is incomplete: a large fraction of unreacted  $\text{PbI}_2$  remained. However, the confinement of the  $\text{PbI}_2$  in a mesoporous host greatly facilitates its conversion to  $\text{CH}_3\text{NH}_3\text{PbI}_3$ —the reaction being completed within less than 30 s. The kinetics of the transformation reaction was studied in detail using optical spectroscopy. Finally, the sequential deposition technique was employed for the fabrication of mesoscopic solar cells. For a best performing device we obtained a power conversion efficiency of 15%. To the best of my knowledge, this is the highest power conversion efficiency reported so far for organic or hybrid organic–inorganic solar cells and one of the highest for any solution-processed photovoltaic device in general.

Despite the excellent performance, several important aspects of the basic functioning of the device are still not entirely understood. Future studies should focus on elucidating the electron–hole recombination in the perovskite-based solar cells, that I believe to be a critical parameter. Moreover, it is equally important to identify the role of the charge-collecting metal oxide, as several studies from other laboratories have reported on efficient devices using an insulating metal oxide scaffold [191, 192, 220].

The investigations presented herein show that the potential of solid-state mesoscopic solar cells has not been exhausted yet. Especially the record power conversion efficiency of 15%, that was achieved by using a hybrid organic–inorganic perovskite sensitizer, sheds new light on the ssDSC technology. It is astonishing, how the use of the perovskite absorber could boost the power conversion efficiency to such high values within only 1–2 years of development. It is also surprising that the record PCEs have been obtained for solar cells that are still based on the molecular hole-transporter spiro-MeOTAD—a material that was developed 15 years ago and for which no competitors have been identified yet. Therefore, these recent developments demand once more to identify the 'magic' properties of spiro-MeOTAD. I believe that with the strategies presented herein, we are proceeding in the right direction, hoping that our contributions will aid the development of a clean and eco-friendly energy conversion device, that one day might rival conventional silicon-based solar cells.





## 6 Experimental Section

### 6.1 Materials and synthesis

Unless stated otherwise, all materials were purchased from Sigma-Aldrich or Acros Organics and used as received. Spiro-MeOTAD was purchased from Merck KGaA.  $\text{CH}_3\text{NH}_3\text{I}$  was synthesized according to a reported procedure [190]. The synthesis of the sensitizers C220 and Y123 followed our published methods [58, 103]. 4-*tert*-Butylpyridine was purified by distillation before use. The ligand 2-(1*H*-pyrazol-1-yl)-4-*tert*-butylpyridine was synthesized according to a published procedure [104]. 2,6-di(1*H*-pyrazol-1-yl)pyridine was synthesized in a similar manner reacting 2,6-dichloropyridine with 2 equivalents of pyrazole.

#### 6.1.1 Synthesis of new HTMs

With the exception of spiro-MeO-TPA, all new hole-transporting material were synthesized in a similar manner. The synthetic procedure is exemplary given for spiro-m-MeO, but is equivalent for spiro-MeOTAD, spiro-p-tBut, spiro-p-HexO, spiro-3,5-mixed, spiro-3,5-tBut and spiro-3,5-MeO. All final materials were purified by standard column chromatography using an optimized mixture of dichloromethane/hexanes as eluent. Yields were in the range of 20-40%.

**4,4',4'',4'''-(9,9'-spirobifluorene-2,2',7,7'-tetrayl) tetrakis(*N,N*-bis(4-methoxyphenyl)aniline) (spiro-MeO-TPA).** 0.65 g (1.03 mmol, 1.00 eq) of 2,2',7,7'-tetrabromo-9,9'-spirobifluorene, 2.00 g (4.64 mmol, 4.50 eq) of (4-(bis(4-methoxyphenyl)amino)phenyl)boronic acid, pinacol ester, and 1.31 g (6.18 mmol, 6.00 eq) of potassium phosphate tribasic were dissolved in 10 ml of *n*-butanol. The solution was degassed for 20 min with a stream of  $\text{N}_2$ . After stirring for 4 h, 15.0 mg (0.02 mmol, 0.02 eq) of tris(dibenzylideneacetone)dipalladium(0) and 60.0 mg (0.13 mmol, 0.13 eq) of 2-dicyclohexylphosphino-2',4',6'-triisopropylbiphenyl were added simultaneously. The reaction was then heated to 50°C for 1 h, prior to dilution with 30 ml of dichloromethane. The reaction mixture was filtered through a plug of  $\text{MgSO}_4$  with dichloromethane. The volatile organics were evaporated and the crude compound was

diluted with minimal dichloromethane in order to precipitate into 300 ml of hexanes. The precipitate was collected by filtration and dissolved in 50 ml of dichloromethane, which was then precipitated into methanol. Yield: 780 mg (0.50 mmol, 49%). Filtration yielded the final product.  $^1\text{H}$  NMR (400 MHz,  $\text{CH}_2\text{Cl}_2\text{-d}_2$ ):  $\delta$  7.93 (d,  $J$  = 8.0 Hz, 4H), 7.63 (dd,  $J$  = 8.0, 1.7 Hz, 4H, ArH), 7.33–7.25 (m, 8H, ArH), 7.09–6.93 (m, 20H, ArH), 6.90–6.79 (m, 24H, ArH), 3.80 (s, 24H, Me).

**Bis(3-methoxyphenyl)amine.** 2.00 g (16.2 mmol, 1.00 eq) of 3-methoxyaniline, 2.73 g (14.6 mmol, 0.90 eq) of 3-bromoanisole and 1.72 g (17.9 mmol, 1.10 eq) of sodium *tert*-butoxide were dissolved in 20 ml of toluene. The suspension was degassed for 20 min with a stream of  $\text{N}_2$ . Then, 39.0 mg (0.04 mmol, < 0.01 eq) of tris(dibenzylideneacetone)dipalladium(0) and 31.0 mg (0.06 mmol, < 0.01 eq) of bis(tri-*tert*-butylphosphine)palladium(0) were added simultaneously, in one batch. The reaction was then heated to 50°C for 1 h. After cooling to room temperature, the reaction mixture was diluted with 30 ml of dichloromethane and filtered through a plug of  $\text{SiO}_2$  with dichloromethane. The solvent was evaporated and the product obtained as a thick yellow oil. Yield: 3.00 g (13.1 mmol, 90%).  $^1\text{H}$  NMR (400 MHz,  $\text{CHCl}_3\text{-d}_1$ ):  $\delta$  7.21 (dd,  $J$  = 8.1, 8.1 Hz, 2H, ArH), 6.77–6.63 (m, 4H, ArH), 6.53 (m, 2H, ArH), 5.77 (s, 1H, NH), 3.81 (s, 6H, Me).

**2,2',7,7'-tetrakis-*N,N*-bis(4-methoxyphenyl)amine-9,9'-spirobifluorene (Spiro-m-MeO).**

1.65 g (2.62 mmol, 1.00 eq) of 2,2',7,7'-tetrabromo-9,9'-spirobifluorene, 2.70 g (11.8 mmol, 4.50 eq) of bis(4-methoxyphenyl)amine and 1.50 g (15.7 mmol, 6.00 eq) of sodium *tert*-butoxide were suspended in 20 ml of toluene. The suspension was degassed for 20 min with a stream of  $\text{N}_2$ . Then, 39 mg (0.04 mmol, 0.02 eq) of tris(dibenzylidene acetone)dipalladium(0) and 31 mg (0.06 mmol, 0.02 eq) of bis(tri-*tert*-butylphosphine)palladium(0) were added simultaneously. The reaction was then heated to 50°C for 1 h. After cooling to room temperature, the reaction mixture was diluted with 30 ml of dichloromethane and filtered through a plug of  $\text{MgSO}_4$  with dichloromethane. The volatile organics were evaporated and the crude compound was diluted with minimal dichloromethane in order to precipitate into 300 ml of hexanes. The precipitate was filtrated and dissolved in minimal dichloromethane, which was then precipitated into methanol. Filtration yielded the final product. Yield: 800 mg (0.66 mmol, 25%).  $^1\text{H}$  NMR (400 MHz,  $\text{CH}_2\text{Cl}_2\text{-d}_2$ ):  $\delta$  7.53 (d,  $J$  = 8.2 Hz, 4H, ArH), 7.24–7.06 (m, 8H, ArH), 6.97 (dd,  $J$  = 8.3, 2.1 Hz, 4H, ArH), 6.71–6.47 (m, 28H, ArH), 3.68 (s, 24H, Me).

**Quadrapure purification.** In a 20 ml glass vial, 0.3 g of material were dissolved in 6 ml dichloromethane. 0.3 g of thiourea functionalized polystyrene beads (Quadrapure TU, Sigma-Aldrich) were then added to the solution. The mixture was heated to 40°C for 48 h under continuous stirring. After cooling, the 6 ml of the solution of the hole-transporting material was filtered through a pipette fitted with a cotton plug and 10 cm of silica. The beads were physically retained at the top of the pipette column and the product was eluted with a further 3–6 ml of dichloromethane. A slight brown coloration was noticed at the top of the column. The eluent from the pipette was precipitated, drop by drop from the pipette, into vortexing

methanol (approximated 75–100 ml) in a 125 ml Erlenmeyer beaker. This precipitate was carefully collected by Buchner filtration, one pipette at a time, while a protective cone of nitrogen was held overhead.

### 6.1.2 Synthesis of cobalt complexes

**2-(1*H*-pyrazol-1-yl)pyridine.** To a suspension of 1*H*-pyrazole (4.0 g, 55.1 mmol) in dimethyl sulfoxide (40 ml) was added potassium *tert*-butoxide (1.2 eq). The mixture was stirred at room temperature until complete dissolution occurred. 2-fluoropyridine (1.2 eq) was then added and the mixture heated to 100°C for 4 h. After cooling down to room temperature, water was added and the mixture extracted with diethylether. The crude product was further purified by silica gel chromatography using dichloromethane/diethylether (49:1, volume percent) as eluent. 2-(1*H*-pyrazol-1-yl)pyridine was obtained as colorless oil that crystallized upon standing. Yield: 4.2 g (29.0 mmol, 53%). The results of the spectroscopic analysis were the same as previously reported [223].

**Tris(2-(1*H*-pyrazol-1-yl)pyridine)cobalt(II) bis(bis(hexafluorophosphate)).** 225 mg (1.55 mmol, 3.1 eq) of the 2-(1*H*-pyrazol-1-yl)pyridine ligand were dissolved in 20 ml of MeOH and then 119 mg (0.5 mmol, 1 eq) of CoCl<sub>2</sub> · 6H<sub>2</sub>O were added as a solid. The mixture was heated to reflux for 2 h. After cooling to room temperature excess of KPF<sub>6</sub> dissolved in MeOH was added to the mixture. The mixture was stored at 3°C for precipitation. After 3 h the product was collected on a sintered glass frit and dried in vacuum. The pure product was obtained as orange crystals. Yield: 246 mg (0.33 mmol, 66%). No peaks are visible in the <sup>1</sup>H NMR (400 MHz, Acetone-d<sub>6</sub>).

**Tris(1-(pyridin-2-yl)-1*H*-pyrazol)cobalt(III) tris(hexafluorophosphate (FK102)).** 218 mg (1.5 mmol, 3.0 eq) of the 2-(1*H*-pyrazol-1-yl)pyridine ligand were dissolved in 10 ml of water and heated to 75°C until complete solution occurred. Then 119 mg (0.5 mmol, 1 eq) of CoCl<sub>2</sub> · 6H<sub>2</sub>O were added to the colourless solution. To the pink solution H<sub>2</sub>O<sub>2</sub> (1 ml, 30%) and HCl (1 ml, 25%) were added to oxidize the cobalt. After 10 min 460 mg (2.5 mmol, 5 eq) of KPF<sub>6</sub> dissolved in 10 ml of hot water were added dropwise to the mixture. Precipitation occurred and the mixture was allowed to cool to room temperature. The product was collected on a sintered glass frit and dried in vacuum. The pure product was obtained as orange solid. Yield: 259 mg (0.28 mmol, 56%). <sup>1</sup>H NMR (400 MHz, Acetone-d<sub>6</sub>): δ 9.56–9.53 (m, 3H, ArH), 8.73–8.64 (m, 6H, ArH), 8.01–7.81 (m, 9H, ArH), 7.27–7.23 (m, 3H, ArH) ppm.

**Tris(2-(1*H*-pyrazol-1-yl)-4-*tert*-butylpyridine)cobalt(III) tris(bis(trifluoromethylsulfonyl)imide) (FK209).** 3.45 g (17.1 mmol, 3 eq) of 2-(1*H*-pyrazol-1-yl)-4-*tert*-butylpyridine was suspended in a 2:1 mixture of water (120 ml) and methanol (60 ml) and heated to 70°C. Then 1.36 g (5.7 mmol, 1 eq) of CoCl<sub>2</sub> · 6H<sub>2</sub>O was added and the mixture was stirred at the same temperature for 10 min. 10 ml of H<sub>2</sub>O<sub>2</sub> (30%) and 10 ml of HCl (25%) were added to oxidize the cobalt and the mixture was further heated to 70°C for 2 h. Then a concentrated

solution of 8.18 g (28.5 mmol, 5 eq) lithium bis(trifluoromethylsulfonyl)imide in water was added slowly at 50°C to precipitate the product. The mixture was allowed to cool to room temperature and the orange solid was collected on a sintered glass-frit and washed with water. The solid was dried in air and then in vacuum to obtain the pure product as an orange solid. Yield: 7.76 g (5.16 mmol, 91%). <sup>1</sup>H NMR (400 MHz, Acetone-D<sub>6</sub>): δ 9.87–9.64 (m, 3H, ArH), 8.79–8.65 (m, 3H, ArH), 8.00–7.79 (m, 6H, ArH), 7.78–7.62 (m, 3H, ArH), 7.37–7.17 (m, 3H, ArH), 1.72–1.15 (m, 27H, tBu).

**Tris(2-(1*H*-pyrazol-1-yl)-4-*tert*-butylpyridine)cobalt(II) bis(bis(trifluoromethylsulfonyl)imide)).** The Co(II) analog of FK209 was synthesized using the same procedure as described above, but omitting the oxidation step. No peaks are visible in the <sup>1</sup>H NMR (400 MHz, Acetone-d<sub>6</sub>).

**Bis(2,6-di(1*H*-pyrazol-1-yl)pyridine)cobalt(III) tris(bis(trifluoromethylsulfonyl)imide)) (FK269).** 0.26 g (1.23 mmol, 2 eq) of 2,6-di(1*H*-pyrazol-1-yl)pyridine was suspended in 30 ml of acetonitrile. Then 0.21 g (0.86 mmol, 1.4 eq) of CoCl<sub>2</sub> · 6H<sub>2</sub>O was added and the mixture was stirred at room temperature for 10 min. Upon adding a solution of 0.47 g (0.86 mmol, 1.4 eq) of ammonium cerium nitrate in acetonitrile the color of the solution changed and a pale orange precipitate formed. Then a concentrated solution of 0.62 g (2.15 mmol, 3.5 eq) of lithium bis(trifluoromethylsulfonyl)imide in water was added and the mixture was stirred at room temperature for 3 h. The solid cobalt complex was collected on a sintered glass-frit, washed with water and then dried in vacuum to obtain the pure product as a pale orange solid. Yield: 0.75 g (0.60 mmol, 70%). <sup>1</sup>H NMR (400 MHz, DMSO-d<sub>6</sub>): δ 9.65–9.53 (m, 4H, ArH), 9.34–9.24 (m, 2H, ArH), 8.86–8.71 (m, 4H, ArH), 7.90–7.85 (m, 4H, ArH), 6.97–6.87 (m, 4H, ArH).

**Bis(2,6-di(1*H*-pyrazol-1-yl)pyridine)cobalt(II) bis(bis(trifluoromethylsulfonyl)imide)).** The Co(II) analog of FK269 was synthesized using the same procedure as described above, but omitting the oxidation step. <sup>1</sup>H NMR (200 MHz, Acetone-d<sub>6</sub>) δ 76.36 (s, 4H, ArH), 75.39 (s, 4H, ArH), 60.38 (s, 4H, ArH), 56.62 (s, 4H, ArH), 14.73 (s, 2H, ArH).

## 6.2 Optical spectroscopy

Unless stated otherwise, steady-state absorption spectra were recorded in transmission mode on a Varian Cary 5 spectrophotometer using a 10 mm path length quartz cell. Likewise, emission spectra were recorded on a Horiba Jobin Yvon Fluorolog spectrofluorometer. Kinetics measurements were carried out as follows: Mesoporous TiO<sub>2</sub> films were deposited on microscope glass slides and infiltrated with PbI<sub>2</sub> following the sequential deposition procedure (Section 6.7.2). The samples were then placed vertically in a standard cuvette of 10 mm path length using a Teflon holder. A solution of CH<sub>3</sub>NH<sub>3</sub>I in 2-propanol was then rapidly injected into the cuvette while either the photoluminescence or the optical transmission was monitored.

For the kinetic measurements on flat  $\text{PbI}_2$  films shown in Figure 4.12, different experimental setups were used. Emission spectra were recorded using a CCD camera connected to an optical fiber and a 405 nm laser-pointer as the excitation source. The emitted light was focused into the optical fiber using an array of optical lenses. During the transformation of  $\text{PbI}_2$  into  $\text{CH}_3\text{NH}_3\text{PbI}_3$  a complete emission spectrum was recorded every 0.5 s. In order to improve the signal-to-noise ratio, the spectra were later averaged over 2.5 s. Complete Absorption spectra were recorded on a Hewlett Packard 8453 UV-vis spectrophotometer. The absorption and emission spectra shown in the figure have been smoothened mathematically.

## 6.3 Electrochemical characterization

The electrochemical characterization of the Co(III) complexes and the hole-transporting materials was performed on an Autolab potentiostat (PGSTAT30, Metrohm) in a classical three-electrode configuration using cyclic voltammetry (CV) and differential pulse voltammetry (DPV) procedures. Three platinum wires were used as working, counter and pseudo-reference electrode, respectively. The supporting electrolyte was  $0.1 \text{ mol l}^{-1}$  tetrabutylammonium hexafluorophosphate ( $\text{TBAPF}_6$ ) in dichloromethane. The measured potential was internally referenced vs. the  $\text{Fc}^+/\text{Fc}$  standard. The scanning rate was  $0.1 \text{ V s}^{-1}$ . To convert the obtained redox potentials to the vacuum scale, a value of  $-5.1 \text{ eV}$  for the  $\text{Fc}^+/\text{Fc}$  standard has been used.

## 6.4 Photoelectron spectroscopy in air

Photoelectron-spectroscopy in air (PESA) measurements were carried out using a Riken Keiki Surface Analyzer (Modl RC-2, Riken Keiki, Japan). Samples were prepared by spin-coating the HTM from chlorobenzene solution on microscope glass slides. The microscope glass slides were cleaned by ultrasonication in acetone and 2-propanol and an  $\text{O}_3$ /ultraviolet (UV) treatment for 15 min prior to their use. The operating principle of the PESA spectrometer is based on the detection of photoelectrons that are ejected from the surface of the sample upon the irradiation of the sample with monochromatic UV light. Due to the operation of the spectrometer in ambient air, ejected photoelectrons quickly react with atmospheric oxygen to form  $\text{O}_2^{\bullet-}$  radicals. The  $\text{O}_2^{\bullet-}$  radicals are detected by an open counter. During the measurement, the wavelength of the monochromatic UV light is scanned and the amount of photoelectrons (i.e. the amount of generated  $\text{O}_2^{\bullet-}$  radicals) is measured.

## 6.5 Conductivity measurements

Substrates used for two-probe electrical conductivity measurements consisted of highly doped Si with a 300 nm thermally grown  $\text{SiO}_2$  layer on which 5 nm Cr/30 nm Au electrodes were deposited and lithographically patterned to yield a channel length and width of  $20 \mu\text{m}$  and 1 mm, respectively. As a cleaning step, the substrates were sonicated in acetone and subse-

quently rinsed with 2-propanol, followed by the removal of residual organic traces via oxygen plasma treatment for 10 min. The hole conductor was subsequently deposited by spin-coating a solution of spiro-MeOTAD, TBP, LiTFSI and FK102 in  $\text{CHCl}_3$ , whereas the concentrations were the same as in case of photovoltaic devices (Section 6.7.1).  $J$ - $V$  characteristics were recorded on a Keithley 4200 Semiconductor Characterization System. Device fabrication and characterization were carried out in a glove box under nitrogen atmosphere.

### 6.6 OFET fabrication and characterization

**Fabrication of organic field-effect transistors.** OFET substrates were purchased from Fraunhofer Institute for Photonic Microsystems, Germany. The substrates consist of highly doped n-type silicon as a gate, 300 nm thick  $\text{SiO}_2$  as dielectric and 40 nm thick lithographically patterned source/drain electrodes made of 10 nm ITO (tin-doped indium oxide) and 30 nm Au. Each substrate bares 16 different transistor structures with four different channel lengths (20  $\mu\text{m}$ , 10  $\mu\text{m}$ , 5  $\mu\text{m}$  and 2.5  $\mu\text{m}$ ). First, the substrates are cleaned by rinsing and ultrasonication in actone and 2-propanol, followed by an oxygen plasma treatment for 5 min. Unless stated otherwise, the substrates are then immersed in a solution of 30  $\mu\text{l}$  phenyl(triethoxy)silane in 15 ml toluene for 2 h, rinsed with acetone and dried using compressed air. The HTM is then deposited onto the substrate by spin-coating a 40  $\text{mg ml}^{-1}$  solution of the HTM in toluene at 1500 rpm for 45 s in an argon filled glovebox. Finally, the substrates are placed on a hotplate at 100°C for 15 min in order to remove any remaining traces of solvent.

**Characterization of organic field-effect transistors.** OFETs are characterized inside an argon filled glovebox using a Keithley Sourcemeter (Model 2602A, Keithley) interfaced with a computer and a home-built software based on Wavemetrics Igor Pro (cf. following paragraph). Standard characterization includes measuring the output characteristics and transfer characteristics at different source-drain and source-gate voltages, respectively. Each condition is measured in hysteresis mode using a settling time of 120 ms. The saturation mobilities were determined from a linear fit of the  $I_{DS}^{1/2}$  vs.  $V_{GS}$  plot at moderate source-gate voltages of  $V_{GS} + V_{Th} \approx 10 - 30 \text{ V}$  and a given source-drain voltage.

**Software interface for the OFET characterization.** OFETs were characterized using a home-built software routine based on Wavemetrics Igor Pro. This routine was written entirely by the author of this thesis. A screenshot of the graphical user interface is shown in Figure 6.1. The interface is used to control the different parameters required to measure the output or transfer characteristics of a transistor. Pre-defined macros allow to measure the transfer and/or output characteristics at different source-drain and/or source-gate voltages. Additional parameters such as hysteresis measurements or repeated measurements are available. Furthermore, the interface allows for a convenient handling of the data obtained. Various graphs can be plotted automatically and the software can be used to calculate the saturation mobility and/or conductivity. All data can be saved automatically in Igor Pro text format. This includes all experimental parameters. Data previously obtained can be reloaded into the program for a

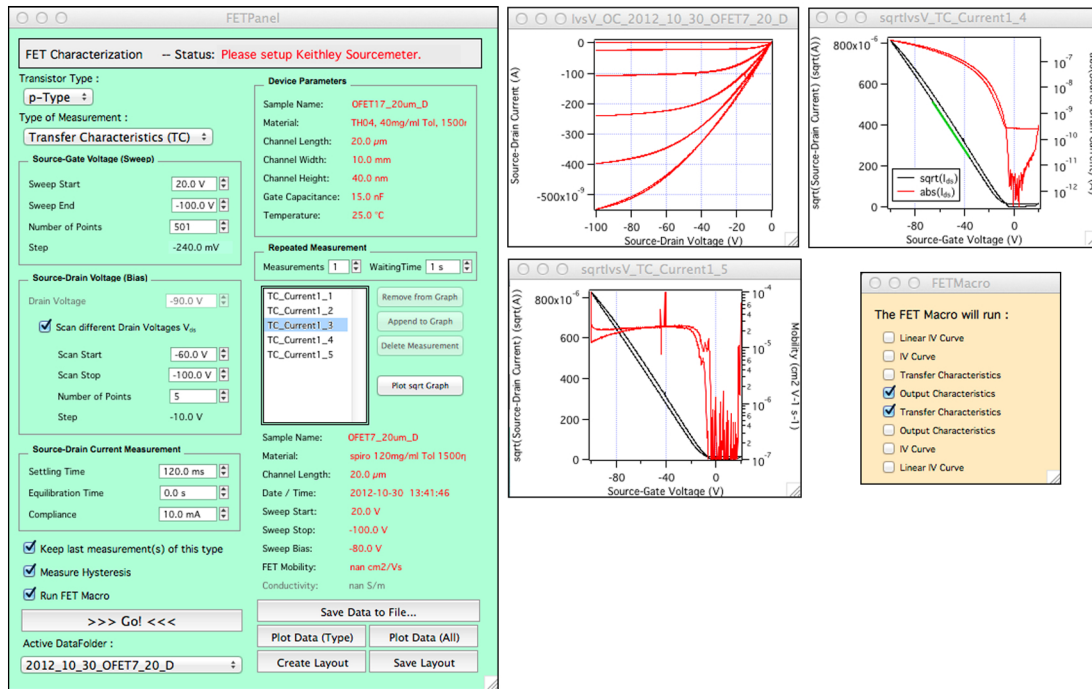


**Figure 6.1** — Screenshot of the graphical user interface of the software that was used to characterize the OFETs.

better comparison. Moreover, the program is capable of generating a PDF layout that contains the most important graphs and experimental parameters.

## 6.7 Fabrication and characterization of solar cells

### 6.7.1 Fabrication of solid-state dye-sensitized solar cells

First, fluorine-doped tin-oxide (FTO)-coated glass substrates (Tec15, Pilkington) were patterned by etching with zinc powder and 2 mol l<sup>-1</sup> hydrochloric acid. The substrates were cleaned by ultrasonication in an alkaline, aqueous washing solution, rinsed with deionized water, ethanol and acetone, and subjected to an O<sub>3</sub>/ultraviolet treatment for 30 min. After cleaning, a TiO<sub>2</sub> compact layer was deposited on the substrates by aerosol spray pyrolysis at 450°C using a commercial titanium diisopropoxide bis(acetylacetonate) solution (75% weight in 2-propanol) diluted in ethanol (1:10, volume ratio) as precursor and oxygen as carrier gas. After cooling to room temperature the substrates were treated in a 0.02 mol l<sup>-1</sup> aqueous solution of TiCl<sub>4</sub> for 30 min at 70°C, rinsed with deionized water and dried at 450°C during 15 min. A 2.5 μm thick mesoporous TiO<sub>2</sub> layer composed of 20 nm sized particles was then deposited on the substrates by screen-printing, dried at 125°C for 10 min, gradually heated to 500°C and then baked at this temperature for 15 min. The aforementioned treatment in aqueous TiCl<sub>4</sub> solution was repeated and the substrates again dried at 450°C during 15 min. Prior to sensitization the TiO<sub>2</sub> substrates were heated to 500°C during 30 min. After



cooling to approximately 70°C, the substrates were immersed into a  $10^{-4}$  mol l<sup>-1</sup> solution of the sensitizer (Y123 or C220) in a mixture of acetonitrile and *tert*-butyl alcohol (1:1, volume ratio) for 1 h. The hole-transporting material was deposited by spin-coating at 2000 rpm for 30 s using an acceleration of 770 rpm s<sup>-1</sup>. The formulation of the spin-coating solution was composed of 180 mg of spiro-MeOTAD, 17.5  $\mu$ l of 4-*tert*-butylpyridine (TBP) and 37.5  $\mu$ l of a stock solution of 170 mg ml<sup>-1</sup> lithium bis(trifluoromethylsulfonyl)imide (LiTFSI) in acetonitrile, in 1 ml chlorobenzene. When a chemical dopant was used, it was pre-dissolved in acetonitrile at a concentration of 100–200 mg ml<sup>-1</sup> and added to the spiro-MeOTAD solution prior to the spin-coating. The new hole-transporting materials were deposited using a similar spin-coating formulation and the the same weight concentration for the HTM as in the case of spiro-MeOTAD. Finally 200 nm of silver were thermally evaporated on top of the device to form the back contact. The devices were sealed using a 25  $\mu$ m thick polymer spacer (Surlyn, DuPont) and a microscope coverslip. The device fabrication was carried out under controlled atmospheric conditions, a humidity of 1% and under red light of  $\lambda > 600$  nm.

### 6.7.2 Fabrication of perovskite-based solar cells

The following procedure describes the fabrication of perovskite-based solar cells. The given experimental conditions are the standard conditions that were employed unless stated otherwise is the main text.

First, laser-patterned, fluorine-doped tin-oxide (FTO)-coated glass substrates (Tec15, Pilkington) were cleaned by ultrasonication in an alkaline, aqueous washing solution, rinsed with deionized water, ethanol and acetone, and subjected to an O<sub>3</sub>/ultraviolet treatment for 30 min. A TiO<sub>2</sub> compact layer was then deposited on the substrates by aerosol spray pyrolysis at 450°C using a commercial titanium diisopropoxide bis(acetylacetonate) solution (75% weight in 2-propanol) diluted in ethanol (1:39, volume ratio) as precursor and oxygen as carrier gas. After cooling to room temperature, the substrates were treated in an 0.04 mol l<sup>-1</sup> aqueous solution of TiCl<sub>4</sub> for 30 min at 70°C rinsed with deionized water and dried at 500°C for 20 min. The mesoporous TiO<sub>2</sub> layer composed of 20 nm sized particles was deposited by spin coating at 5000 rpm for 30 s using a commercial TiO<sub>2</sub> paste (Dyesol 18NRT, Dyesol) diluted in ethanol (2:7, weight ratio). After drying at 125°C the TiO<sub>2</sub> films were gradually heated to 500°C, baked at this temperature for 15 min and cooled to room temperature. Prior to their use, the films were again dried at 500°C for 30 min. PbI<sub>2</sub> was dissolved in *N,N*-dimethylformamide at a concentration of 462 mg ml<sup>-1</sup> (ca. 1 mol l<sup>-1</sup>) under stirring at 70°C. The solution was kept at 70°C during the whole procedure. The mesoporous TiO<sub>2</sub> films were then infiltrated with PbI<sub>2</sub> by spin coating at 6500 rpm for 90 s and dried at 70°C for 30 min. After cooling to room temperature, the films were dipped in a solution of CH<sub>3</sub>NH<sub>3</sub>I in 2-propanol (10 mg ml<sup>-1</sup>) for 20 s, rinsed with 2-propanol, dried by rapid spinning at 4000 rpm for 15 s and then dried fully at 70°C for 30 min. The HTM was then deposited by spin coating at 4000 rpm for 30 s. The spin-coating formulation was prepared by dissolving 72.3 mg spiro-MeOTAD, 28.8 ml 4-*tert*-butylpyridine (TBP), 17.5 ml of a stock solution of 520 mg ml<sup>-1</sup> lithium bis(trifluoromethylsulfonyl)imide



(LiTFSI) in acetonitrile and 29 ml of a stock solution of 300 mg ml<sup>-1</sup> tris(2-(1*H*-pyrazol-1-yl)-4-*tert*-butylpyridine)cobalt(III) bis(trifluoromethylsulfonyl)imide (FK209) in acetonitrile, in 1 ml chlorobenzene- Finally, 80 nm of gold was thermally evaporated on top of the device to form the back contact. The device fabrication was carried out under controlled atmospheric conditions and a humidity of 1%. For the fabrication of the best-performing devices exhibiting a PCE of 15%, slightly modified conditions were used. First, PbI<sub>2</sub> was spin-cast at 6500 rpm for 5 s. Second, the samples were subjected to a ‘pre-wetting’ by dipping in 2-propanol for 1–2 s before being dipped in the solution of CH<sub>3</sub>NH<sub>3</sub>I in 2-propanol.

### 6.7.3 Characterization of solar cells

Current–voltage characteristics were recorded by applying an external potential bias to the cell while recording the generated photocurrent with a digital source meter (Keithley Model 2400). The light source was a 450 W xenon lamp (Oriel) equipped with a Schott K113 Tempax sunlight filter (Prazisions Glas und Optik GmbH) to match the emission spectrum of the lamp to the AM1.5G standard. Before each measurement, the exact light intensity was determined using a calibrated Si reference diode equipped with an infrared cut-off filter (KG-3, Schott). IPCE spectra were recorded as functions of wavelength under a constant white light bias of approximately 5 mW cm<sup>-2</sup> supplied by an array of white light-emitting diodes. The excitation beam coming from a 300 W xenon lamp (ILC Technology) was focused through a Gemini-180 double monochromator (Jobin Yvon Ltd) and chopped at approximately 2 Hz. The signal was recorded using a Model SR830 DSP Lock-In Amplifier (Stanford Research Systems). All measurements were conducted using a non-reflective metal aperture of 0.2025 or 0.285 cm<sup>-2</sup> to define the active area of the device and avoid light scattering through the sides.

### 6.7.4 Long-term stability testing

**Solid-state dye-sensitized solar cells.** For stability tests under standard test conditions, devices were hermetically sealed with UV-curing epoxy glue, equipped with a  $\lambda < 420$  nm filter and kept in a solar simulator based on a Sun test CPS+ lamp (ATLAS). The devices were taken out regularly to measure the *J–V* characteristics. The devices used for stability tests were based on the C220 sensitizer and contained 0.7% FK102 dopant.

**Perovskite-based solar solar cells.** For long-term stability tests, the devices were sealed in argon using a 50 nm thick hot-melting polymer spacer (Surlyn, DuPont) and a microscope coverslip, and subjected to constant light soaking at approximately 100 mW cm<sup>-2</sup>. The light source was an array of white light-emitting diodes (LXM3-PW51 4000K, Philips). During the testing, the devices were maintained at their maximum power point using electronic control and at a temperature of about 45°C. An automatic *J–V* measurement at different light intensities (0%, 1%, 10%, 50% and 100% the solar value) was made every 2 h.

### 6.8 X-ray diffraction spectroscopy

For XRD measurements, flat  $\text{PbI}_2$  and  $\text{TiO}_2/\text{PbI}_2$  nanocomposites were deposited on microscope glass slides using the sequential deposition procedures (Section 6.7.2). X-ray powder diagrams were recorded on an X'Pert MPD PRO from PANalytical equipped with a ceramic tube (Cu anode,  $\lambda=1.54060 \text{ \AA}$ ), a secondary graphite (002) monochromator and a RTMS X'Celerator detector, and operated in BRAGG-BRENTANO geometry. The samples were mounted without further modification, and the automatic divergence slit and beam mask were adjusted to the dimensions of the thin films. A step size of  $0.008 \text{ deg}$  was chosen and an acquisition time of up to  $7.5 \text{ min deg}^{-1}$ . A baseline correction was applied to all X-ray powder diagrams to remove the broad diffraction peak arising from the amorphous glass slide.



# Appendix

**A1 — Additional electrochemical data**

**A2 — Certificate for perovskite-based solar cells**

## A1 — Additional electrochemical data

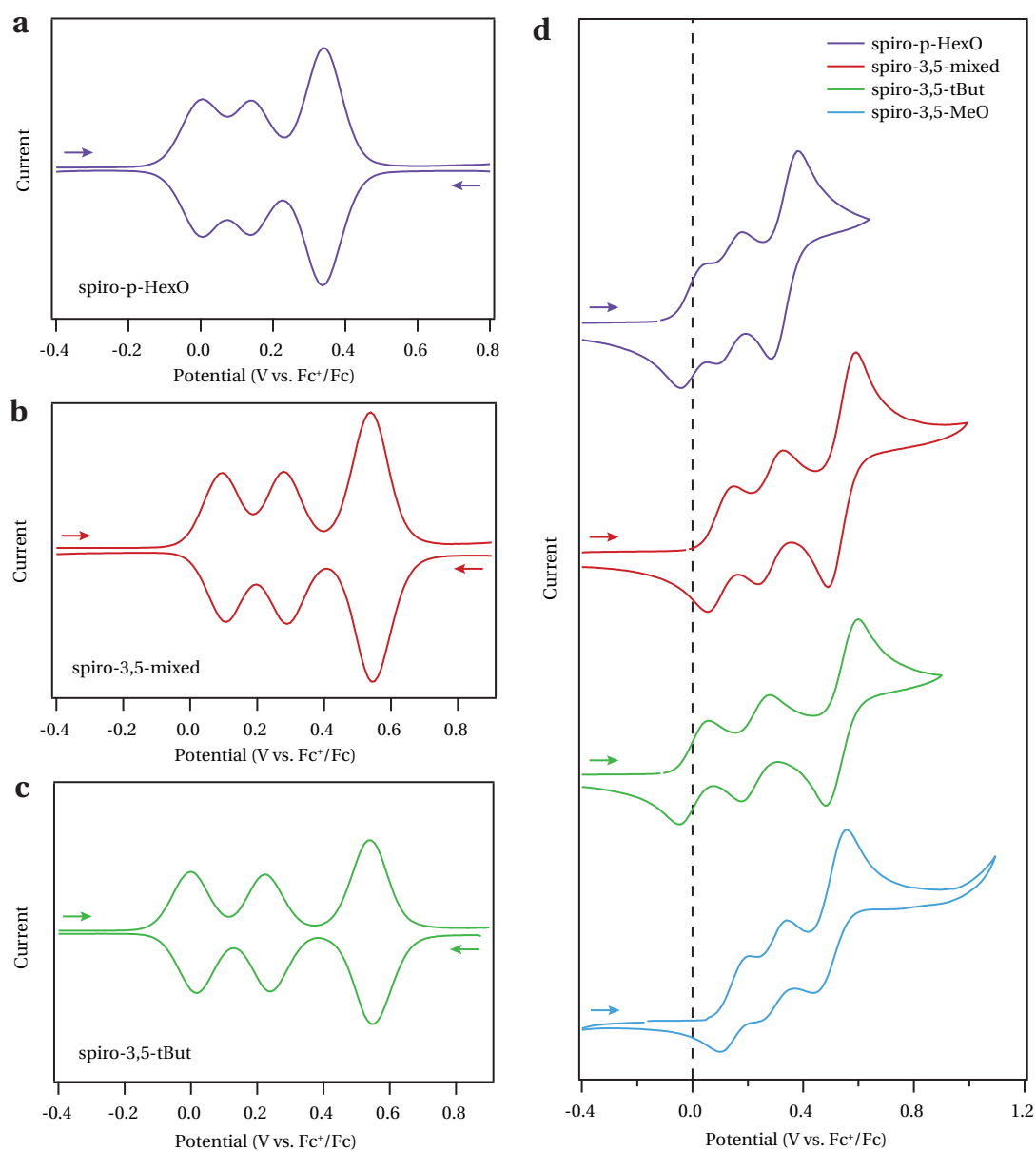


**Figure A1** — Electrochemical characterization of spiro-p-HexO, spiro-3,5-mixed, spiro-3,5-MeO and spiro-3,5-tBut by a–c) differential pulse voltammetry and d) cyclic voltammetry in dichloromethane solution. 0.1 M tetrabutylammonium hexafluorophosphate has been added as a conduction salt. The applied potential was internally references vs. the  $\text{Fc}^+/\text{Fc}$  standard. For spiro-3,5-MeO a clear differential pulse polarogram could not be obtained.

## A2 — Certificate for perovskite-based solar cells

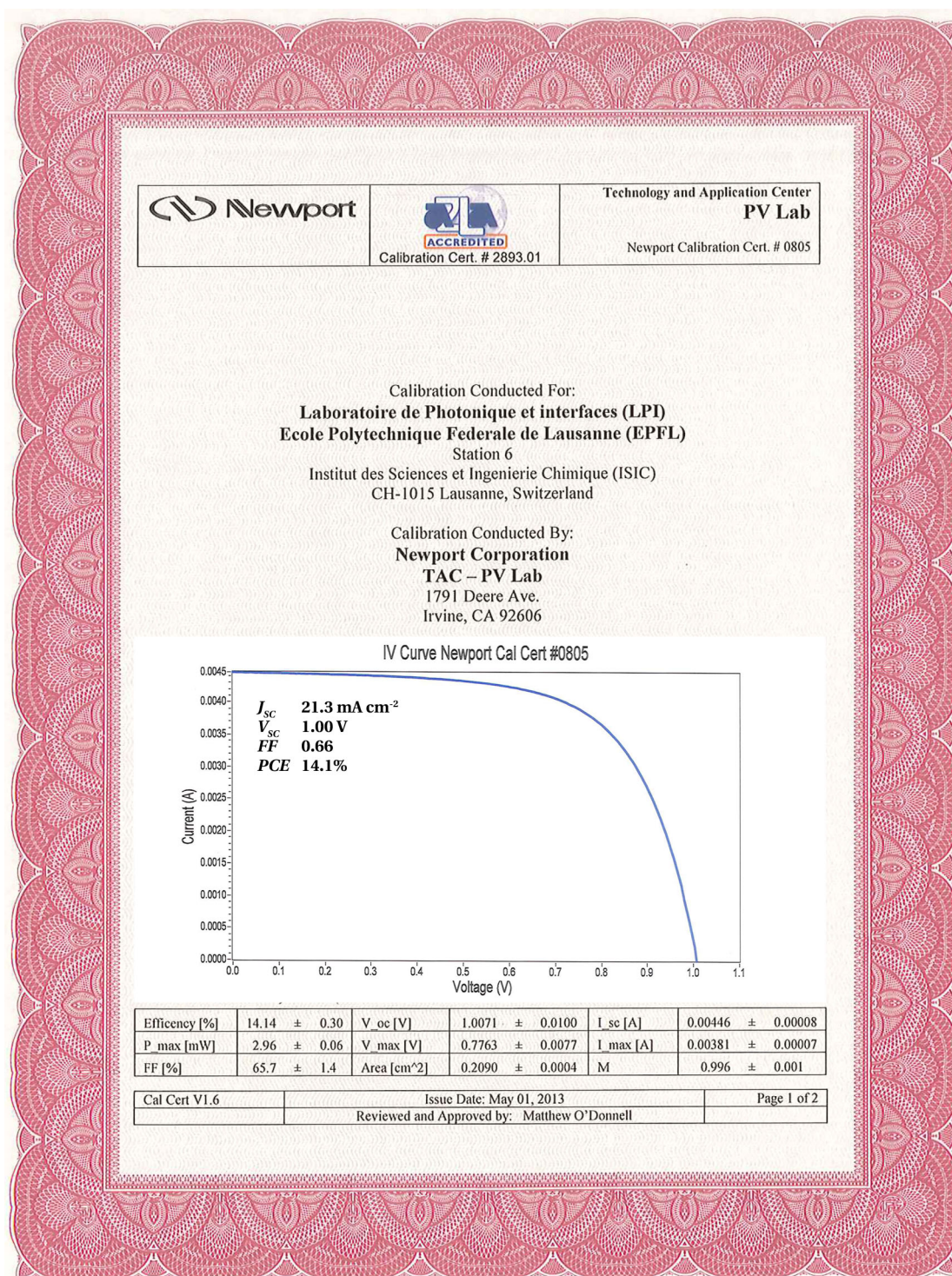


**Figure A2** — Photovoltaic performance of a perovskite-based mesoscopic solar cell as measured by an accredited PV calibration laboratory (Newport), confirming a power conversion efficiency of 14.14% measured under standard test conditions.



# Bibliography

- [1] O'Regan, B.; Grätzel, M. *Nature* **1991**, 353, 737–740.
- [2] Haid, S.; Marszalek, M.; Mishra, A.; Wielopolski, M.; Teuscher, J.; Moser, J.-E.; Humphry-Baker, R.; Zakeeruddin, S. M.; Grätzel, M.; Bäuerle, P. *Advanced Functional Materials* **2012**, 22, 1291–1302.
- [3] Bertoz, M. et al. *Dye-sensitized Solar Cells*, 1st ed.; EPFL Press: Lausanne, CH, 2010.
- [4] Green, M. A. *Solar Cells: Operating Principles, Technology, and System Applications*; Prentice-Hall, Inc.: Englewood Cliffs, N.J., USA, 1982.
- [5] Kavan, L.; Grätzel, M. *Electrochimica Acta* **1995**, 40, 643–652.
- [6] Jiang, C.; Koh, W. L.; Leung, M. Y.; Hong, W.; Li, Y.; Zhang, J. *Journal of Solid State Chemistry* **2013**, 198, 197–202.
- [7] Matteocci, F.; Mincuzzi, G.; Giordano, F.; Capasso, A.; Artuso, E.; Barolo, C.; Viscardi, G.; Brown, T. M.; Reale, A.; Di Carlo, A. *Organic Electronics* **2013**, 14, 1882–1890.
- [8] Peng, B.; Jungmann, G.; Jäger, C.; Haarer, D.; Schmidt, H.-W.; Thelakkat, M. *Coordination Chemistry Reviews* **2004**, 248, 1479–1489.
- [9] Jiang, C.; Leung, M. Y.; Koh, W. L.; Li, Y. *Thin Solid Films* **2011**, 519, 7850–7854.
- [10] Magne, C.; Dufour, F.; Labat, F.; Lancel, G.; Durupthy, O.; Cassaignon, S.; Pauporté, T. *"Journal of Photochemistry & Photobiology, A: Chemistry"* **2012**, 232, 22–31.
- [11] Lee, T.-H.; Sue, H.-J.; Cheng, X. *Nanoscale Research Letters* **2011**, 6, 517.
- [12] Xu, C.; Wu, J.; Desai, U. V.; Gao, D. *Nano Letters* **2012**, 12, 2420–2424.
- [13] Schlur, L.; Carton, A.; Lévêque, P.; Guillon, D.; Pourroy, G. *The Journal of Physical Chemistry C* **2013**, 117, 2993–3001.
- [14] Boucharef, M.; Di Bin, C.; Boumaza, M. S.; Colas, M.; Snaith, H.; Ratier, B.; Bouclé, J. *Nanotechnology* **2010**, 21, 205203.

## Bibliography

---

- [15] Docampo, P.; Tiwana, P.; Sakai, N.; Miura, H.; Herz, L.; Murakami, T.; Snaith, H. J. *The Journal of Physical Chemistry C* **2012**, *116*, 22840–22846.
- [16] Sadoughi, G.; Sivaram, V.; Gunning, R.; Docampo, P.; Bruder, I.; Pschirer, N.; Irajizad, A.; Snaith, H. J. *Physical Chemistry Chemical Physics* **2013**, *15*, 2075–2080.
- [17] Snaith, H. J.; Ducati, C. *Nano Letters* **2010**, *10*, 1259–1265.
- [18] Tiwana, P.; Docampo, P.; Johnston, M. B.; Snaith, H. J.; Herz, L. M. *ACS Nano* **2011**, *5*, 5158–5166.
- [19] Marchioro, A.; Dualeh, A.; Punzi, A.; Grätzel, M.; Moser, J.-E. *The Journal of Physical Chemistry C* **2012**, *116*, 26721–26727.
- [20] Li, T. C.; Góes, M. S.; Fabregat-Santiago, F.; Bisquert, J.; Bueno, P. R.; Prasittichai, C.; Hupp, J. T.; Marks, T. J. *The Journal of Physical Chemistry C* **2009**, *113*, 18385–18390.
- [21] Zhang, X.-T.; Sutanto, I.; Taguchi, T.; Tokuhito, K.; Meng, Q.-B.; Rao, T. N.; Fujishima, A.; Watanabe, H.; Nakamori, T.; Uragami, M. *Solar Energy Materials and Solar Cells* **2003**, *80*, 315–326.
- [22] Brennan, T. P.; Bakke, J. R.; Ding, I.-K.; Hardin, B. E.; Nguyen, W. H.; Mondal, R.; Bailie, C. D.; Margulis, G. Y.; Hoke, E. T.; Sellinger, A.; McGehee, M. D.; Bent, S. F. *Physical Chemistry Chemical Physics* **2012**, *14*, 12130–12140.
- [23] Brennan, T. P.; Trejo, O.; Roelofs, K. E.; Xu, J.; Prinz, F. B.; Bent, S. F. *Journal of Materials Chemistry A* **2013**, *1*, 7566–7571.
- [24] Kumara, G. R. A.; Okuya, M.; Murakami, K.; Kaneko, S.; Jayaweera, V. V.; Tennakone, K. *"Journal of Photochemistry & Photobiology, A: Chemistry"* **2004**, *164*, 183–185.
- [25] Bach, U.; Lupo, D.; Comte, P.; Moser, J. E.; Weissörtel, F.; Salbeck, J.; Spreitzer, H.; Grätzel, M. *Nature* **1998**, *395*, 583–585.
- [26] Bach, U. *Thesis, Swiss Federal Institute of Technology Lausanne, Switzerland* **2000**, 1–168.
- [27] Ding, I.-K.; Melas-Kyriazi, J.; Cevey Ha, N.-L.; Chittibabu, K. G.; Zakeeruddin, S. M.; Grätzel, M.; McGehee, M. D. *Organic Electronics* **2010**, *11*, 1217–1222.
- [28] Dürr, M.; Yasuda, A.; Nelles, G. *Applied Physics Letters* **2006**, *89*, 061110.
- [29] Koops, S. E.; O'Regan, B. C.; Barnes, P. R. F.; Durrant, J. R. *Journal of the American Chemical Society* **2009**, *131*, 4808–4818.
- [30] Krüger, J.; Plass, R.; Cevey, L.; Piccirelli, M.; Grätzel, M.; Bach, U. *Applied Physics Letters* **2001**, *79*, 2085–2087.
- [31] Jennings, J. R.; Wang, Q. *The Journal of Physical Chemistry C* **2010**, *114*, 1715–1724.



- [32] Cappel, U. B.; Smeigh, A. L.; Plogmaker, S.; Johansson, E. M. J.; Rensmo, H.; Hammarström, L.; Hagfeldt, A.; Boschloo, G. *The Journal of Physical Chemistry C* **2011**, *115*, 4345–4358.
- [33] Snaith, H. J.; Grätzel, M. *Applied Physics Letters* **2006**, *89*, 262114.
- [34] Abate, A.; Leijtens, T.; Pathak, S.; Teuscher, J.; Avolio, R.; Errico, M. E.; Kirkpatrick, J.; Ball, J. M.; Docampo, P.; McPherson, I.; Snaith, H. J. *Physical Chemistry Chemical Physics* **2013**, *15*, 2572–2579.
- [35] Cappel, U. B.; Daeneke, T.; Bach, U. *Nano Letters* **2012**, *12*, 4925–4931.
- [36] Schölin, R.; Karlsson, M. H.; Eriksson, S. K.; Siegbahn, H.; Johansson, E. M. J.; Rensmo, H. *The Journal of Physical Chemistry C* **2012**, *116*, 26300–26305.
- [37] Li, L.-L.; Diau, E. W.-G. *Chemical Society Reviews* **2012**, *42*, 291–304.
- [38] Yum, J.-H.; Hagberg, D. P.; Moon, S.-J.; Karlsson, K. M.; Marinado, T.; Sun, L.; Hagfeldt, A.; Nazeeruddin, M. K.; Grätzel, M. *Angewandte Chemie (International Edition)* **2008**, *48*, 1576–1580.
- [39] Moon, S.-J.; Yum, J.-H.; Humphry-Baker, R.; Karlsson, K. M.; Hagberg, D. P.; Marinado, T.; Hagfeldt, A.; Sun, L.; Grätzel, M.; Nazeeruddin, M. K. *The Journal of Physical Chemistry C* **2009**, *113*, 16816–16820.
- [40] Hagfeldt, A.; Boschloo, G.; Sun, L.; Kloo, L.; Pettersson, H. *Chemical Reviews* **2010**, *110*, 6595–6663.
- [41] Snaith, H. J.; Moulé, A. J.; Klein, C.; Meerholz, K.; Friend, R. H.; Grätzel, M. *Nano Letters* **2007**, *7*, 3372–3376.
- [42] Kroeze, J. E.; Hirata, N.; Koops, S.; Nazeeruddin, M. K.; Schmidt-Mende, L.; Grätzel, M.; Durrant, J. R. *Journal of the American Chemical Society* **2006**, *128*, 16376–16383.
- [43] Schmidt-Mende, L.; Kroeze, J. E.; Durrant, J. R.; Nazeeruddin, M. K.; Grätzel, M. *Nano Letters* **2005**, *5*, 1315–1320.
- [44] Nguyen, W. H.; Bailie, C. D.; Burschka, J.; Moehl, T.; Grätzel, M.; McGehee, M. D.; Sellinger, A. *Chemistry of Materials* **2013**, *25*, 1519–1525.
- [45] Snaith, H. J.; Zakeeruddin, S. M.; Schmidt-Mende, L.; Klein, C.; Grätzel, M. *Angewandte Chemie (International Edition)* **2005**, *117*, 6571–6575.
- [46] Peter, K.; Wietasch, H.; Peng, B.; Thelakkat, M. *Applied Physics A: Materials Science & Processing* **2004**, *79*, 65–71.
- [47] Karthikeyan, C. S.; Thelakkat, M. *Inorganica Chimica Acta* **2008**, *361*, 635–655.

## Bibliography

---

- [48] Snaith, H. J.; Karthikeyan, C. S.; Petrozza, A.; Teuscher, J.; Moser, J.-E.; Nazeeruddin, M. K.; Thelakkat, M.; Grätzel, M. *The Journal of Physical Chemistry C* **2008**, *112*, 7562–7566.
- [49] Karthikeyan, C. S.; Wietasch, H.; Thelakkat, M. *Advanced Materials* **2007**, *19*, 1091–1095.
- [50] Handa, S.; Wietasch, H.; Thelakkat, M.; Durrant, J. R.; Haque, S. A. *Chemical Communications* **2007**, 1725–1727.
- [51] Kwon, Y. S.; Lim, J.; Song, I.; Song, I. Y.; Shin, W. S.; Moon, S.-J.; Park, T. *Journal of Materials Chemistry* **2012**, *22*, 8641–8648.
- [52] Hagen, J.; Schaffrath, W.; Otschik, P.; Fink, R.; Bacher, A.; Schmidt, H. W.; Haarer, D. *Synthetic Metals* **1997**, *89*, 215–220.
- [53] Krüger, J.; Plass, R.; Grätzel, M.; Matthieu, H.-J. *Applied Physics Letters* **2002**, *81*, 367–369.
- [54] Schmidt-Mende, L.; Zakeeruddin, S. M.; Grätzel, M. *Applied Physics Letters* **2005**, *86*, 013504.
- [55] Wang, M.; Liu, J.; Cevey Ha, N.-L.; Moon, S.-J.; Liska, P.; Humphry-Baker, R.; Moser, J.-E.; Grätzel, M. G.; Wang, P.; Zakeeruddin, S. M.; Grätzel, M. *Nano Today* **2010**, *5*, 169–174.
- [56] Schmidt-Mende, L.; Bach, U.; Humphry-Baker, R.; Horiuchi, T.; Miura, H.; Ito, S.; Uchida, S.; Grätzel, M. *Advanced Materials* **2005**, *17*, 813–815.
- [57] Wang, M.; Xu, M.; Shi, D.; Li, R.; Gao, F.; Zhang, G.; Yi, Z.; Humphry-Baker, R.; Wang, P.; Zakeeruddin, S. M.; Grätzel, M. *Advanced Materials* **2008**, *20*, 4460–4463.
- [58] Cai, N.; Moon, S.-J.; Cevey-Ha, L.; Moehl, T.; Humphry-Baker, R.; Wang, P.; Zakeeruddin, S. M.; Grätzel, M. *Nano Letters* **2011**, *11*, 1452–1456.
- [59] Burschka, J.; Dualeh, A.; Kessler, F.; Baranoff, E.; Cevey Ha, N.-L.; Yi, C.; Nazeeruddin, M. K.; Grätzel, M. *Journal of the American Chemical Society* **2011**, *133*, 18042–18045.
- [60] Schmidt-Mende, L.; Campbell, W. M.; Wang, Q.; Jolley, K. W.; Officer, D. L.; Nazeeruddin, M. K.; Grätzel, M. *ChemPhysChem* **2005**, *6*, 1253–1258.
- [61] Moon, S.-J.; Baranoff, E.; Zakeeruddin, S. M.; Yeh, C.-Y.; Diau, E. W.-G.; Grätzel, M.; Sivula, K. *Chemical Communications* **2011**, 47, 8244–8246.
- [62] Reddy, P. Y.; Giribabu, L.; Lyness, C.; Snaith, H. J.; Vijaykumar, C.; Chandrasekharam, M.; Lakshmikantam, M.; Yum, J.-H.; Kalyanasundaram, K.; Grätzel, M. *Angewandte Chemie (International Edition)* **2007**, *46*, 373–376.
- [63] Driscoll, K.; Fang, J.; Humphry-Baker, N.; Torres, T.; Huck, W. T. S.; Snaith, H. J.; Friend, R. H. *Nano Letters* **2010**, *10*, 4981–4988.

- [64] Burke, A.; Schmidt-Mende, L.; Ito, S.; Grätzel, M. *Chemical Communications* **2007**, 234–236.
- [65] Mor, G. K.; Kim, S.; Paulose, M.; Varghese, O. K.; Shankar, K.; Basham, J.; Grimes, C. A. *Nano Letters* **2009**, 9, 4250–4257.
- [66] Shi, Y.; Hill, R. B. M.; Yum, J.-H.; Dualeh, A.; Barlow, S.; Grätzel, M.; Marder, S. R.; Nazeeruddin, M. K. *Angewandte Chemie (International Edition)* **2011**, 50, 6619–6621.
- [67] Cappel, U. B.; Karlsson, M. H.; Pschirer, N. G.; Eickemeyer, F.; Schöneboom, J.; Erk, P.; Boschloo, G.; Hagfeldt, A. *The Journal of Physical Chemistry C* **2009**, 113, 14595–14597.
- [68] Cappel, U. B.; Gibson, E. A.; Hagfeldt, A.; Boschloo, G. *The Journal of Physical Chemistry C* **2009**, 113, 6275–6281.
- [69] Dualeh, A.; Humphry-Baker, R.; Delcamp, J. H.; Nazeeruddin, M. K.; Grätzel, M. *Advanced Energy Materials* **2012**, 3, 496–504.
- [70] Yella, A.; Humphry-Baker, R.; Curchod, B. F. E.; Ashari Astani, N.; Teuscher, J.; Polander, L. E.; Mathew, S.; Moser, J.-E.; Tavernelli, I.; Rothlisberger, U.; Grätzel, M.; Nazeeruddin, M. K.; Frey, J. *Chemistry of Materials* **2013**, 25, 2733–2739.
- [71] Chiang, Y.-F.; Tsai, C.-H.; Chen, P.; Guo, T.-F. *Solar Energy* **2012**, 86, 1967–1972.
- [72] Hardin, B. E.; Gaynor, W.; Ding, I.-K.; Rim, S.-B.; Peumans, P.; McGehee, M. D. *Organic Electronics* **2011**, 12, 875–879.
- [73] Margulis, G. Y.; Christoforo, M. G.; Lam, D.; Beiley, Z. M.; Bowring, A. R.; Bailie, C. D.; Salleo, A.; McGehee, M. D. *Advanced Energy Materials* **2013**, n/a–n/a.
- [74] Xu, M.; Liu, G.; Li, X.; Wang, H.; Rong, Y.; Ku, Z.; Hu, M.; Yang, Y.; Liu, L.; Liu, T.; Chen, J.; Han, H. *Organic Electronics* **2013**, 14, 628–634.
- [75] Burschka, J.; Kessler, F.; Nazeeruddin, M. K.; Grätzel, M. *Chemistry of Materials* **2013**, 25, 2986–2990.
- [76] Walzer, K.; Maennig, B.; Pfeiffer, M.; Leo, K. *Chemical Reviews* **2007**, 107, 1233–1271.
- [77] Lüssem, B.; Riede, M.; Leo, K. *Physica Status Solidi A* **2012**, 210, 9–43.
- [78] Yoo, S.-J.; Lee, J.-H.; Lee, J.-H.; Kim, J.-J. *Applied Physics Letters* **2013**, 102, 183301.
- [79] Pingel, P.; Schwarzl, R.; Neher, D. *Applied Physics Letters* **2012**, 100, 143303.
- [80] Maennig, B.; Pfeiffer, M.; Nollau, A.; Zhou, X.; Leo, K.; Simon, P. *Physical Review B* **2001**, 64, 195208.
- [81] Arkhipov, V.; Heremans, P.; Emelianova, E.; Bäessler, H. *Physical Review B* **2005**, 71, 045214.

## Bibliography

---

- [82] Gao, W.; Kahn, A. *Journal of Applied Physics* **2003**, *94*, 359–366.
- [83] Chen, D.-Y.; Tseng, W.-H.; Liang, S.-P.; Wu, C.-I.; Hsu, C.-W.; Chi, Y.; Hung, W.-Y.; Chou, P.-T. *Physical Chemistry Chemical Physics* **2012**, *14*, 11689–11694.
- [84] Hock, R.; Mayer, T.; Jaegermann, W. *The Journal of Physical Chemistry C* **2012**, *116*, 18146–18154.
- [85] Meyer, J.; Hamwi, S.; Schmale, S.; Winkler, T.; Johannes, H.-H.; Riedl, T.; Kowalsky, W. *Journal of Materials Chemistry* **2009**, *19*, 702–705.
- [86] Hamwi, S.; Meyer, J.; Winkler, T.; Riedl, T.; Kowalsky, W. *Applied Physics Letters* **2009**, *94*, 253307.
- [87] Lehnhardt, M.; Hamwi, S.; Hoping, M.; Reinker, J.; Riedl, T.; Kowalsky, W. *Applied Physics Letters* **2010**, *96*, 193301.
- [88] Qi, Y.; Sajoto, T.; Barlow, S.; Kim, E.-G.; Marder, S. R.; Kahn, A. *Journal of the American Chemical Society* **2009**, *131*, 12530–12531.
- [89] Wong, H. M. P.; Wang, P.; Abrusci, A.; Svensson, M.; Andersson, M. R.; Greenham, N. C. *The Journal of Physical Chemistry C* **2007**, *111*, 5244–5249.
- [90] Yamamori, A.; Adachi, C.; Koyama, T.; Taniguchi, Y. *Applied Physics Letters* **1998**, *72*, 2147.
- [91] Jiang, X.; Karlsson, K. M.; Gabrielsson, E.; Johansson, E. M. J.; Quintana, M.; Karlsson, M.; Sun, L.; Boschloo, G.; Hagfeldt, A. *Advanced Functional Materials* **2011**, *21*, 2944–2952.
- [92] Cai, N.; Moon, S.-J.; Cevey-Ha, L.; Moehl, T.; Humphry-Baker, R.; Wang, P.; Zakeeruddin, S. M.; Grätzel, M. *Nano Letters* **2011**, *11*, 1452–1456.
- [93] Wang, H.; Xu, M.; Liu, G.; Li, X.; Xiang, P.; Ku, Z.; Rong, Y.; Liu, L.; Hu, M.; Yang, Y.; Han, H. *Electrochimica Acta* **2013**, *99*, 238–241.
- [94] Yella, A.; Lee, H. W.; Tsao, H. N.; Yi, C.; Chandiran, A. K.; Nazeeruddin, M. K.; Diau, E. W. G.; Yeh, C. Y.; Zakeeruddin, S. M.; Grätzel, M. *Science* **2011**, *334*, 629–634.
- [95] Tsao, H. N.; Burschka, J.; Yi, C.; Kessler, F.; Nazeeruddin, M. K.; Grätzel, M. *Energy & Environmental Science* **2011**, *4*, 4921–4924.
- [96] Yum, J.-H.; Baranoff, E.; Kessler, F.; Moehl, T.; Ahmad, S.; Bessho, T.; Marchioro, A.; Ghadiri, E.; Moser, J.-E.; Yi, C.; Grätzel, M.; Nazeeruddin, M. K. *Nature Communications* **2012**, *3*, 631–638.
- [97] Feldt, S. M.; Lohse, P. W.; Kessler, F.; Nazeeruddin, M. K.; Grätzel, M.; Boschloo, G.; Hagfeldt, A. *Physical Chemistry Chemical Physics* **2013**, *15*, 7087–7097.

- [98] Chan, C. K.; Zhao, W.; Barlow, S.; Marder, S.; Kahn, A. *Organic Electronics* **2008**, *9*, 575–581.
- [99] Kim, C. S.; Lee, S.; Tinker, L. L.; Bernhard, S.; Loo, Y.-L. *Chemistry of Materials* **2009**, *21*, 4583–4588.
- [100] Chan, C. K.; Kahn, A.; Zhang, Q.; Barlow, S.; Marder, S. R. *Journal of Applied Physics* **2007**, *102*, 014906.
- [101] Weissörtel, F. *Thesis, University of Regensburg, Germany* **1999**, 1–111.
- [102] Kröger, M.; Hamwi, S.; Meyer, J.; Riedl, T.; Kowalsky, W.; Kahn, A. *Organic Electronics* **2009**, *10*, 932–938.
- [103] Tsao, H. N.; Yi, C.; Moehl, T.; Yum, J.-H.; Zakeeruddin, S. M.; Nazeeruddin, M. K.; Grätzel, M. *ChemSusChem* **2011**, *4*, 591–594.
- [104] Shavaleev, N. M.; Scopelliti, R.; Baranoff, E.; Grätzel, M.; Nazeeruddin, M. K. *Inorganica Chimica Acta* **2012**, *383*, 316–319.
- [105] Jameson, D. L.; Blaho, J. K.; Kruger, K. T.; Goldsby, K. A. *Inorganic Chemistry* **1989**, *28*, 4312–4314.
- [106] Holland, J. M.; Kilner, C. A.; Thornton-Pett, M.; Halcrow, M. A. *Polyhedron* **2001**, *20*, 2829–2840.
- [107] Ayers, T.; Scott, S.; Goins, J.; Caylor, N.; Hathcock, D.; Slattery, S. J.; Jameson, D. L. *Inorganica Chimica Acta* **2000**, *307*, 7–12.
- [108] Saha, N.; Kar, S. K. *Journal of Inorganic & Nuclear Chemistry* **1977**, *39*, 1236–1238.
- [109] Cappel, U. B.; Gibson, E. A.; Hagfeldt, A.; Boschloo, G. *The Journal of Physical Chemistry C* **2009**, *113*, 6275–6281.
- [110] Abrusci, A.; Santosh Kumar, R. S.; Al-Hashimi, M.; Heeney, M.; Petrozza, A.; Snaith, H. J. *Advanced Functional Materials* **2011**, *21*, 2571–2579.
- [111] Premalal, E. V. A.; Dematage, N.; Kumara, G. R. R. A.; Rajapakse, R. M. G.; Shimomura, M.; Murakami, K.; Konno, A. *Journal of Power Sources* **2012**, *203*, 288–296.
- [112] Premalal, E. V. A.; Kumara, G. R. R. A.; Rajapakse, R. M. G.; Shimomura, M.; Murakami, K.; Konno, A. *Chemical Communications* **2010**, *46*, 3360–3362.
- [113] Kumara, G.; Konno, A.; Senadeera, G.; Jayaweera, P.; De Silva, D.; Tennakone, K. *Solar Energy Materials and Solar Cells* **2001**, *69*, 195–199.
- [114] Kumara, G. R. A.; Konno, A.; Shiratsuchi, K.; Tsukahara, J.; Tennakone, K. *Chemistry of Materials* **2002**, *14*, 954–955.

## Bibliography

---

- [115] Kumara, G. R. A.; Kaneko, S.; Okuya, M.; Tennakone, K. *Langmuir* **2002**, *18*, 10493–10495.
- [116] Sirimanne, P. M.; Jeranko, T.; Bogdanoff, P.; Fiechter, S.; Tributsch, H. *Semiconductor Science and Technology* **2003**, *18*, 708–712.
- [117] Chung, I.; Lee, B.; He, J.; Chang, R. P. H.; Kanatzidis, M. G. *Nature* **2013**, *485*, 486–489.
- [118] Zhang, W.; Zhu, R.; Li, F.; Wang, Q.; Liu, B. *The Journal of Physical Chemistry C* **2011**, *115*, 7038–7043.
- [119] Yang, L.; Cappel, U. B.; Unger, E. L.; Karlsson, M.; Karlsson, K. M.; Gabrielsson, E.; Sun, L.; Boschloo, G.; Hagfeldt, A.; Johansson, E. M. J. *Physical Chemistry Chemical Physics* **2011**, *14*, 779–789.
- [120] Lancelle-Beltran, E.; Prené, P.; Boscher, C.; Belleville, P.; Buvat, P.; Lambert, S.; Guillet, F.; Marcel, C.; Sanchez, C. *European Journal of Inorganic Chemistry* **2008**, *2008*, 903–910.
- [121] Gebeyehu, D.; Brabec, C. J.; Sariciftci, N. S. *Thin Solid Films* **2002**, *403*, 271–274.
- [122] Grancini, G.; Santosh Kumar, R. S.; Abrusci, A.; Yip, H.-L.; Li, C.-Z.; Jen, A. K. Y.; Lanzani, G.; Snaith, H. J. *Advanced Functional Materials* **2012**, *22*, 2160–2166.
- [123] Xia, J.; Masaki, N.; Lira-Cantu, M.; Kim, Y.; Jiang, K.; Yanagida, S. *Journal of the American Chemical Society* **2008**, *130*, 1258–1263.
- [124] Song, I. Y.; Park, S.-H.; Lim, J.; Kwon, Y. S.; Park, T. *Chemical Communications* **2011**, *47*, 10395–10397.
- [125] Manseki, K.; Jarernboon, W.; Youhai, Y.; Jiang, K.-J.; Suzuki, K.; Masaki, N.; Kim, Y.; Xia, J.; Yanagida, S. *Chemical Communications* **2011**, *47*, 3120–3122.
- [126] Liu, X.; Zhang, W.; Uchida, S.; Cai, L.; Liu, B.; Ramakrishna, S. *Advanced Materials* **2010**, *22*, E150–E155.
- [127] Kim, J.; Koh, J. K.; Kim, B.; Ahn, S. H.; Ahn, H.; Ryu, D. Y.; Kim, J. H.; Kim, E. *Advanced Functional Materials* **2011**, *21*, 4633–4639.
- [128] Degbia, M.; Schmaltz, B.; Van, F. T.; Melhem, H.; Bouclé, J.; Tomkeviciene, A.; Grazulevicius, J. V. *IEEE Proceedings, International Semiconductor Conference Dresden-Grenoble (ISCDG)* **2012**, 211–214.
- [129] Puckyte, G.; Schmaltz, B.; Tomkeviciene, A.; Degbia, M.; Grazulevicius, J. V.; Melhem, H.; Bouclé, J.; Tran-Van, F. *Journal of Power Sources* **2013**, *233*, 86–92.
- [130] Tomkeviciene, A.; Puckyte, G.; Grazulevicius, J. V.; Degbia, M.; Tran-Van, F.; Schmaltz, B.; Jankauskas, V.; Bouclé, J. *Synthetic Metals* **2012**, *162*, 1997–2004.
- [131] Leijtens, T.; Ding, I.-K.; Giovenzana, T.; Bloking, J. T.; McGehee, M. D.; Sellinger, A. *ACS Nano* **2012**, *6*, 1455–1462.

- [132] Zhang, K.; Wang, L.; Liang, Y.; Yang, S.; Liang, J.; Cheng, F.; Chen, J. *Synthetic Metals* **2012**, *162*, 490–496.
- [133] Zhao, Y.; Chen, W.; Zhai, J.; Sheng, X.; He, Q.; Wei, T.; Bai, F.; Jiang, L.; Zhu, D. *Chemical Physics Letters* **2007**, *445*, 259–264.
- [134] Yang, L.; Xu, B.; Bi, D.; Tian, H.; Boschloo, G.; Sun, L.; Hagfeldt, A.; Johansson, E. M. J. *Journal of the American Chemical Society* **2013**, *135*, 7378–7385.
- [135] Juozapavicius, M.; O'Regan, B. C.; Anderson, A. Y.; Grazulevicius, J. V.; Mimaite, V. *Organic Electronics* **2012**, *13*, 23–30.
- [136] Johansson, E. M. J.; Karlsson, P. G.; Hedlund, M.; Ryan, D.; Siegbahn, H.; Rensmo, H. *Chemistry of Materials* **2007**, *19*, 2071–2078.
- [137] Fredin, K.; Johansson, E. M. J.; Blom, T.; Hedlund, M.; Plogmaker, S.; Siegbahn, H.; Leifer, K.; Rensmo, H. *Synthetic Metals* **2009**, *159*, 166–170.
- [138] Johansson, E. M. J.; Yang, L.; Gabrielsson, E.; Lohse, P. W.; Boschloo, G.; Sun, L.; Hagfeldt, A. *The Journal of Physical Chemistry C* **2012**, *116*, 18070–18078.
- [139] Chang, J. A.; Rhee, J. H.; Im, S. H.; Lee, Y. H.; Kim, H.-J.; Seok, S. I.; Nazeeruddin, M. K.; Grätzel, M. *Nano Letters* **2010**, *10*, 2609–2612.
- [140] Im, S. H.; Lim, C.-S.; Chang, J. A.; Lee, Y. H.; Maiti, N.; Kim, H.-j.; Nazeeruddin, M. K.; Grätzel, M.; Seok, S. I. *Nano Letters* **2011**, *11*, 4789–4793.
- [141] Heo, J. H.; Im, S. H.; Noh, J. H.; Mandal, T. N.; Lim, C.-S.; Chang, J. A.; Lee, Y. H.; Kim, H.-J.; Sarkar, A.; Nazeeruddin, M. K.; Grätzel, M.; Il Seok, S. *Nature Photonics* **2013**, *7*, 486–491.
- [142] Bouclé, J.; Chyla, S.; Shaffer, M. S. P.; Durrant, J. R.; Bradley, D. D. C.; Nelson, J. *Advanced Functional Materials* **2008**, *18*, 622–633.
- [143] Bouclé, J.; Ravirajan, P.; Nelson, J. *Journal of Materials Chemistry* **2007**, *17*, 3141–3153.
- [144] Lee, H. J.; Leventis, H. C.; Haque, S. A.; Torres, T.; Grätzel, M.; Nazeeruddin, M. K. *Journal of Power Sources* **2011**, *196*, 596–599.
- [145] Murakoshi, K.; Kogure, R.; Wada, Y.; Yanagida, S. *Chemistry Letters* **1997**, 471–472.
- [146] Saito, Y.; Kitamura, T.; Wada, Y.; Yanagida, S. *Synthetic Metals* **2002**, *131*, 185–187.
- [147] Saito, Y.; Fukuri, N.; Senadeera, R.; Kitamura, T.; Wada, Y.; Yanagida, S. *Electrochemistry Communications* **2004**, *6*, 71–74.
- [148] Liu, X.; Cheng, Y.; Wang, L.; Cai, L.; Liu, B. *Physical Chemistry Chemical Physics* **2012**, *14*, 7098–7103.
- [149] Senadeera, G.; Jayaweera, P.; Perera, V.; Tennakone, K. *Solar Energy Materials and Solar Cells* **2002**, *73*, 103–108.

## Bibliography

---

- [150] Fabregat-Santiago, F.; Bisquert, J.; Cevey, L.; Chen, P.; Wang, M.; Zakeeruddin, S. M.; Grätzel, M. *Journal of the American Chemical Society* **2009**, *131*, 558–562.
- [151] Moon, S.-J.; Yum, J.-H.; Humphry-Baker, R.; Karlsson, K. M.; Hagberg, D. P.; Marinado, T.; Hagfeldt, A.; Sun, L.; Grätzel, M.; Nazeeruddin, M. K. *The Journal of Physical Chemistry C* **2009**, *113*, 16816–16820.
- [152] Daeneke, T.; Mozer, A. J.; Kwon, T.-H.; Duffy, N. W.; Holmes, A. B.; Bach, U.; Spiccia, L. *Energy & Environmental Science* **2012**, *5*, 7090–7099.
- [153] Poplavskyy, D.; Nelson, J. *Journal of Applied Physics* **2003**, *93*, 341–346.
- [154] Leijtens, T.; Lim, J.; Teuscher, J.; Park, T.; Snaith, H. J. *Advanced Materials* **2013**, *25*, 3227–3233.
- [155] Rana, O.; Srivastava, R.; Grover, R.; Zulfequar, M.; Husain, M.; Kamalasanan, M. N. *Synthetic Metals* **2011**, *161*, 828–832.
- [156] Snaith, H. J.; Humphry-Baker, R.; Chen, P.; Cesar, I.; Zakeeruddin, S. M.; Grätzel, M. *Nanotechnology* **2008**, *19*, 424003.
- [157] Ding, I.-K.; Tétreault, N.; Brillet, J.; Hardin, B. E.; Smith, E. H.; Rosenthal, S. J.; Sauvage, F.; Grätzel, M.; McGehee, M. D. *Advanced Functional Materials* **2009**, *19*, 2431–2436.
- [158] Melas-Kyriazi, J.; Ding, I.-K.; Marchioro, A.; Punzi, A.; Hardin, B. E.; Burkhard, G. F.; Tétreault, N.; Grätzel, M.; Moser, J.-E.; McGehee, M. D. *Advanced Energy Materials* **2011**, *1*, 407–414.
- [159] Docampo, P.; Hey, A.; Guldin, S.; Gunning, R.; Steiner, U.; Snaith, H. J. *Advanced Functional Materials* **2012**, *22*, 5010–5019.
- [160] Johansson, E. M. J.; Pradhan, S.; Wang, E.; Unger, E. L.; Hagfeldt, A.; Andersson, M. R. *Chemical Physics Letters* **2011**, *502*, 225–230.
- [161] Bartholomew, G. P.; Heeger, A. J. *Advanced Functional Materials* **2005**, *15*, 677–682.
- [162] Abrusci, A.; Ding, I.-K.; Al-Hashimi, M.; Segal-Peretz, T.; McGehee, M. D.; Heeney, M.; Frey, G. L.; Snaith, H. J. *Energy & Environmental Science* **2011**, *4*, 3051–3058.
- [163] Coakley, K. M.; Liu, Y.; McGehee, M. D.; Frindell, K. L.; Stucky, G. D. *Advanced Functional Materials* **2003**, *13*, 301–306.
- [164] Schmidt-Mende, L.; Grätzel, M. *Thin Solid Films* **2006**, *500*, 296–301.
- [165] Saragi, T. P. I.; Spehr, T.; Siebert, A.; Fuhrmann-Lieker, T.; Salbeck, J. *Chemical Reviews* **2007**, *107*, 1011–1065.
- [166] Zhao, H.; Tanjutco, C.; Thayumanavan, S. *Tetrahedron Letters* **2001**, *42*, 4421–4424.



- [167] Bender, T. P.; Graham, J. E.; Duff, J. M. *Chemistry of Materials* **2001**, *13*, 4105–4111.
- [168] Shirota, Y.; Kageyama, H. *Chemical Reviews* **2007**, *107*, 953–1010.
- [169] Zaumseil, J.; Sirringhaus, H. *Chemical Reviews* **2007**, *107*, 1296–1323.
- [170] Saragi, T. P. I. *Thesis, University of Kassel, Germany* **2004**, 1–197.
- [171] Saragi, T. P. I.; Fuhrmann-Lieker, T.; Salbeck, J. *Synthetic Metals* **2005**, *148*, 267–270.
- [172] Saragi, T. P. I.; Fuhrmann-Lieker, T.; Salbeck, J. *Advanced Functional Materials* **2006**, *16*, 966–974.
- [173] Veres, J.; Ogier, S.; Lloyd, G.; de Leeuw, D. *Chemistry of Materials* **2004**, *16*, 4543–4555.
- [174] Tsao, H. N.; Cho, D.; Andreasen, J. W.; Rouhanipour, A.; Breiby, D. W.; Pisula, W.; Müllen, K. *Advanced Materials* **2009**, *21*, 209–212.
- [175] Burschka, J.; Pellet, N.; Moon, S.-J.; Humphry-Baker, R.; Gao, P.; Nazeeruddin, M. K.; Grätzel, M. *Nature* **2013**, *499*, 316–319.
- [176] Lee, H.; Leventis, H. C.; Moon, S.-J.; Chen, P.; Ito, S.; Haque, S. A.; Torres, T.; Nüesch, F.; Geiger, T.; Zakeeruddin, S. M.; Grätzel, M.; Nazeeruddin, M. K. *Advanced Functional Materials* **2009**, *19*, 2735–2742.
- [177] Snaith, H. J.; Stavrinadis, A.; Docampo, P.; Watt, A. A. R. *Solar Energy* **2011**, *85*, 1283–1290.
- [178] Plass, R.; Pelet, S.; Krueger, J.; Grätzel, M.; Bach, U. *The Journal of Physical Chemistry B* **2002**, *106*, 7578–7580.
- [179] Brennan, T. P.; Ardalan, P.; Lee, H.-B.-R.; Bakke, J. R.; Ding, I.-K.; McGehee, M. D.; Bent, S. F. *Advanced Energy Materials* **2011**, *1*, 1169–1175.
- [180] Ardalan, P.; Brennan, T. P.; Lee, H.-B.-R.; Bakke, J. R.; Ding, I.-K.; McGehee, M. D.; Bent, S. F. *ACS Nano* **2011**, *5*, 1495–1504.
- [181] Lee, H.; Wang, M.; Chen, P.; Gamelin, D. R.; Zakeeruddin, S. M.; Grätzel, M.; Nazeeruddin, M. K. *Nano Letters* **2009**, *9*, 4221–4227.
- [182] Chi, C.-F.; Chen, P.; Lee, Y.-L.; Liu, I.-P.; Chou, S.-C.; Zhang, X.-L.; Bach, U. *Journal of Materials Chemistry* **2011**, *21*, 17534–17540.
- [183] Santra, P. K.; Kamat, P. V. *Journal of the American Chemical Society* **2012**, *134*, 2508–2511.
- [184] Lee, J.-W.; Son, D.-Y.; Ahn, T. K.; Shin, H.-W.; Kim, I. Y.; Hwang, S.-J.; Ko, M. J.; Sul, S.; Han, H.; Park, N.-G. *Scientific Reports* **2013**, *3*, 1050.
- [185] Pan, Z.; Zhang, H.; Cheng, K.; Hou, Y.; Hua, J.; Zhong, X. *ACS Nano* **2012**, *6*, 3982–3991.

## Bibliography

---

- [186] Moon, S.-J.; Itzhaik, Y.; Yum, J.-H.; Zakeeruddin, S. M.; Hodes, G.; Grätzel, M. *The Journal of Physical Chemistry Letters* **2010**, *1*, 1524–1527.
- [187] Chang, J. A.; Im, S. H.; Lee, Y. H.; Kim, H.-J.; Lim, C.-S.; Heo, J. H.; Seok, S. I. *Nano Letters* **2012**, *12*, 1863–1867.
- [188] Kojima, A.; Teshima, K.; Shirai, Y.; Miyasaka, T. *Journal of the American Chemical Society* **2009**, *131*, 6050–6051.
- [189] Im, J.-H.; Lee, C.-R.; Lee, J.-W.; Park, S.-W.; Park, N.-G. *Nanoscale* **2011**, *3*, 4088–4093.
- [190] Kim, H.-S.; Lee, C.-R.; Im, J.-H.; Lee, K.-B.; Moehl, T.; Marchioro, A.; Moon, S.-J.; Humphry-Baker, R.; Yum, J.-H.; Moser, J.-E.; Grätzel, M.; Park, N.-G. *Scientific Reports* **2012**, *2*, 591.
- [191] Lee, M. M.; Teuscher, J.; Miyasaka, T.; Murakami, T. N.; Snaith, H. *Science* **2012**, *338*, 643–647.
- [192] Ball, J. M.; Lee, M. M.; Hey, A.; Snaith, H. J. *Energy & Environmental Science* **2013**, *6*, 1739–1743.
- [193] Etgar, L.; Gao, P.; Xue, Z.; Peng, Q.; Chandiran, A. K.; Liu, B.; Nazeeruddin, M. K.; Grätzel, M. *Journal of the American Chemical Society* **2012**, *134*, 17396–17399.
- [194] Edri, E.; Kirmayer, S.; Cahen, D.; Hodes, G. *The Journal of Physical Chemistry Letters* **2013**, *4*, 897–902.
- [195] Qiu, J.; Qiu, Y.; Yan, K.; Zhong, M.; Mu, C.; Yan, H.; Yang, S. *Nanoscale* **2013**, *5*, 3245–3248.
- [196] Noh, J. H.; Im, S. H.; Heo, J. H.; Mandal, T. N.; Seok, S. I. *Nano Letters* **2013**, *13*, 1764–1769.
- [197] Weber, D. *Zeitschrift für Naturforschung* **1978**, *33b*, 1443–1445.
- [198] Weber, D. *Zeitschrift für Naturforschung* **1979**, *34b*, 939–941.
- [199] Im, J.-H.; Chung, J.; Kim, S.-J.; Park, N.-G. *Nanoscale Research Letters* **2012**, *7*, 1–7.
- [200] Yamada, K.; Isobe, K.; Okuda, T.; Furukawa, Y. *Zeitschrift für Naturforschung* **1994**, *49A*, 258–266.
- [201] Fütterer, K.; Depmeier, W.; Petricek, V. *Acta Crystallographica* **1995**, *B51*, 768–779.
- [202] Stoumpos, C. C.; Malliakas, C. D.; Kanatzidis, M. G. *Inorganic Chemistry* **2013**, *52*, 9019–9038.
- [203] Mitzi, D. B.; Liang, K. *Journal of Solid State Chemistry* **1997**, *134*, 376–381.
- [204] Szafranski, M.; Ståhl, K. *Journal of Solid State Chemistry* **2007**, *180*, 2209–2215.
- [205] Szafranski, M. *Thermochimica acta* **1997**, *307*, 177–183.

- [206] Mitzi, D. B. *Journal of the Chemical Society, Dalton Transactions* **2001**, 334, 1–12.
- [207] Baikie, T.; Fang, Y.; Kadro, J. M.; Schreyer, M.; Wei, F.; Mhaisalkar, S. G.; Graetzel, M.; White, T. J. *Journal of Materials Chemistry A* **2013**, 1, 5628–5641.
- [208] Kawamura, Y.; Mashiyama, H.; Hasebe, K. *Journal of the Physics Society Japan* **2002**, 71, 1694–1697.
- [209] Liang, K.; Mitzi, D. B.; Prikas, M. T. *Chemistry of Materials* **1998**, 10, 403–411.
- [210] Li, H.; Zanella, M.; Genovese, A.; Povia, M.; Falqui, A.; Giannini, C.; Manna, L. *Nano Letters* **2011**, 11, 4964–4970.
- [211] Beberwyck, B. J.; Alivisatos, A. P. *Journal of the American Chemical Society* **2012**, 134, 19977–19980.
- [212] Luther, J. M.; Zheng, H.; Sadtler, B.; Alivisatos, A. P. *Journal of the American Chemical Society* **2009**, 131, 16851–16857.
- [213] Warren, R. F.; Liang, W. Y. *Journal of Physics: Condensed Matter* **1993**, 5, 6407–6418.
- [214] Gurina, G. I.; Savchenko, K. V. *Journal of Solid State Chemistry* **2004**, 177, 909–915.
- [215] Preda, N.; Mihut, L.; Baibarac, M.; Baltog, I.; Lefrant, S. *Journal of Physics: Condensed Matter* **2006**, 18, 8899–8912.
- [216] Beckmann, P. A. *Crystal Research and Technology* **2010**, 45, 455–460.
- [217] Derenzo, S. E.; Weber, M. J.; Klintonberg, M. K. *Nuclear Instruments and Methods in Physics Research Section A* **2002**, 486, 214–219.
- [218] Martínez Maestro, L.; Jacinto, C.; Rocha, U.; Carmen Iglesias-de la Cruz, M.; Sanz-Rodriguez, F.; Juarranz, A.; García Solé, J.; Jaque, D. *Journal of Applied Physics* **2012**, 111, 023513.
- [219] de Mello Donegá, C.; Hickey, S. G.; Wuister, S. F.; Vanmaekelbergh, D.; Meijerink, A. *The Journal of Physical Chemistry B* **2003**, 107, 489–496.
- [220] Bi, D.; Moon, S.-J.; Häggman, L.; Boschloo, G.; Yang, L.; Johansson, E. M. J.; Nazeeruddin, M. K.; Grätzel, M.; Hagfeldt, A. *RSC Advances* **2013**, ???, ???–???
- [221] Dualeh, A.; De Angelis, F.; Fantacci, S.; Moehl, T.; Yi, C.; Kessler, F.; Baranoff, E.; Nazeeruddin, M. K.; Grätzel, M. *The Journal of Physical Chemistry C* **2012**, 116, 1572–1578.
- [222] Noh, J. H.; Jeon, N. J.; Choi, Y. C.; Mohammad K, N.; Grätzel, M.; Seok, S. I. *Journal of Materials Chemistry A* **2013**, 1, 11842–11847.
- [223] Elguero, J.; Fruchier, A.; De La Hoz, A.; Jalón, F. A.; Manzano, B. R.; Otero, A. *Chemische Berichte* **1996**, 129, 589–594.



# Acknowledgements

First of all I would like to thank my supervisor Prof. Michael Grätzel for giving me the possibility to work on such an interesting and multidisciplinary topic. I am grateful for the freedom and constant support that I was given throughout the time of my doctoral studies that significantly fostered my professional and personal development.

I am deeply grateful to all my colleagues from LPI for their support, enjoyable lunch and coffee breaks, laughs and scientific discussions. In particular I would like to thank: Magda for the inexhaustible supply with food, muffins and polish beverages as well as for the constant administrative, scientific and personal support; Manuel for his help in the lab and amazing technical knowledge; Aswani and Aravind for their cooking skills and enlightening scientific discussions; Nok for his sense of humor and for introducing me to the field of organic field-effect transistors; Norman for his motivation, scientific excellence and all the beers that we drank together; Simon for his reliability, open personality and skills as a bartender; the BCH crew Florian, Julien, Lauren, Simon and Tom for awesome barbecues; Pascal for his knowledge and the supply of metal oxide pastes; Paul for the laser-etching of the conductive substrates; Robin for his scientific support and knowledge as well as his programming skills; Magda, Juno and Francine for the friendly ambiance in the office; Francine for her old fridge that constantly provided us with cold drinks; Amalie, Magda, Nok and Aswani for delighting game and raclette nights; Tom for the synthesis of the hole-transporting materials; Florian for the synthesis of the cobalt complexes; Thomas for his help in organizing the ssDSC lab, very helpful scientific discussions and for introducing me to electrochemical impedance spectroscopy; Lê and Soo-Jin for their knowledge on ssDSCs; everyone from the ssDSC group who helped in keeping the lab clean and organized; Carole, Nazeer and Zakeer for their assistance and finally Magda, Robin and Simon for proof-reading my thesis.

I acknowledge Marie and Jacky from the chemical store as well as the team of the ISIC mechanical workshop. You really made my life easier!

Last but not least I would like to thank Ursula Gonthier, Nelly Gourdou, Antonella Ragnelli, Carmen Biagini and Anne Lene Odegaard for their superb administrative assistance.

Thank you all!



# Julian Burschka

---

Date / Place of birth: 01.02.1986 / Würzburg, Germany

Nationality: German

E-mail julian.burschka@gmail.com

## Education

---

- Nov. 2013 **Ph. D.** in Chemistry and Chemical Engineering from the Ecole Polytechnique Fédérale de Lausanne, Switzerland under the supervision of Prof. Michael Grätzel
- 2010 – 2013 **Doctoral studies** at the Ecole Polytechnique Fédérale de Lausanne, Switzerland under the supervision of Prof. Michael Grätzel
- Worked on the development, fabrication and characterization of high performance solid-state mesoscopic solar cells and the design, synthesis and characterization of associated organic, inorganic and hybrid materials*
- July 2010 **Diplomas** (M.Sc. equivalent) in **Chemistry** (University of Würzburg) and **Chemical Engineering** (CPE Lyon), **M.Sc.** in **Physical Chemistry and Catalysis** (UCB Lyon I)
- Feb. – July 2010 **Final year project** at the Ecole Polytechnique Fédérale de Lausanne, Switzerland under the supervision of Prof. Michael Grätzel
- Investigated the application of disulfide/thiolate-based redox electrolytes in nanocrystalline dye-sensitized solar cells*
- 2005 – 2010 **Full-time university education** (Double degree program) in chemistry and chemical engineering at the Julius-Maximilians-Universität Würzburg, Germany, the Ecole Supérieure de Chimie Physique Electronique de Lyon (CPE Lyon), France and the Université Claude Bernard Lyon I (UCB Lyon I), France
- June 2005 **Abitur** (university entrance qualification) in chemistry and physics

## Professional experience

---

- June – Sep. 2009 **Industrial placement** at Merck KGaA in Frankfurt, Germany
- Studied the influence of additional evaporated layers in solution-processed organic light-emitting diodes*
- Feb. – Apr. 2008 **Industrial placement** at BASF SE in Ludwigshafen, Germany
- Synthesized and explored borate-based ionic liquids*

## Additional skills

---

- Languages German (native), English (fluent), French (fluent)
- IT-Skills Microsoft Office, Adobe Photoshop/Illustrator/InDesign, PerkinElmer ChemBioDraw, Wavemetrics IgorPro, OriginLab Origin, Microsoft Windows, Apple MacOSX, Ubuntu Linux, LaTeX

#### List of publications

---

- (1) Burschka, J.; Pellet, N.; Moon, S.-J.; Humphry-Baker, R.; Gao, P.; Nazeeruddin, M. K.; Grätzel, M. *Nature* **2013**, 499, 316–319.
- (2) Burschka, J.; Kessler, F.; Nazeeruddin, M. K.; Grätzel, M. *Chemistry of Materials* **2013**, 25, 2986–2990.
- (3) Nguyen, W. H.; Bailie, C. D.; Burschka, J.; Moehl, T.; Grätzel, M.; McGehee, M. D.; Sellinger, A. *Chemistry of Materials* **2013**, 25, 1519–1525.
- (4) Burschka, J.; Brault, V.; Ahmad, S.; Breau, L.; Nazeeruddin, M. K.; Marsan, B.; Zakeeruddin, S. M.; Grätzel, M. *Energy & Environmental Science* **2012**, 5, 6089–6097.
- (5) Burschka, J.; Dualé, A.; Kessler, F.; Baranoff, E.; Cevey Ha, N.-L.; Yi, C.; Nazeeruddin, M. K.; Grätzel, M. *Journal of the American Chemical Society* **2011**, 133, 18042–18045.
- (6) Tsao, H. N.; Burschka, J.; Yi, C.; Kessler, F.; Nazeeruddin, M. K.; Grätzel, M. *Energy & Environmental Science* **2011**, 4, 4921–4924.

#### List of patents

---

- (1) Burschka, J.; Pellet, N.; Nazeeruddin, M. K.; Grätzel, M.; Ahmad, S. *High performance perovskite sensitized mesoscopic solar cells*, EP13166720.6.
  - (2) Burschka, J.; Kessler, F.; Baranoff, F.; Nazeeruddin, M. K.; Grätzel, M. *Metal complexes for use as dopants and other uses*, WO2012/114316.
- 
-



